IFAE

Universitat Autònoma
de Barcelona

TeV γ-ray observations of nearby Active Galactic Nuclei with the MAGIC telescope: exploring the high energy region of the multiwavelength picture

Diego Tescaro

— PhD Thesis —

June 1, 2010

Supervised by Dr. Abelardo Moralejo

Picture on the cover: The two MAGIC telescopes at the Observatory of Roque de los Muchachos in April 2009.

Contents

Introduction

The success of current generation of Cherenkov telescopes and the latest results from the Fermi γ-ray satellite have affirmed loudly the importance of γ-ray Astronomy for modern Astrophysics.

Photons are, since a long time, the messengers from the Cosmos. The optical frequencies have been widely exploited by astronomers to set the pillars of our knowledge of the Universe. In relatively recent times, the astronomers started to explore different regions of the electromagnetic spectrum. Each time a new waveband started to be exploited, important discoveries followed, thanks to the brand new 'perspective' from which the same astrophysical sources could be observed. These progresses answered many of the existing questions but a the same time, like always in science, opened new questions as well. But what makes photons so special? It is actually their neutral charge that turns the trick, together with their easy production in nature and detectability. To address the problem of the origin of Cosmic Rays, and in general of the mechanisms that accelerate the most energetic particles in the Universe, γ-rays have the advantage to trace back through their incoming direction, their production (or last interaction) site, since no magnetic field can modify their journey across the Universe. This is not the case for charged particles, whose trajectories, upon arrival on Earth, do not point back to the production site. In turn, gamma rays allow us to explore the most extreme processes of our Universe comfortably from our planet. Is not this a sufficiently good reason to study γ-rays?

High-energy γ-ray Astronomy is made even more attractive by the possibility to touch some of the most fundamental physics issues. Like the Lorentz invariance, which can be tested by γ-rays measurements, and the mystery of Dark Matter, which might be solved revealing the signature of the yet unknown weakly interacting particles annihilation or decay of.

Very interesting astrophysical sources have been detected in the gamma-band in the last years.

Supernova remnants are considered by many the acceleration site of the galactic Cosmic Rays and their morphology could be mapped in gamma rays at energies $> 10^{12}$ eV, demonstrating for the first time the association of supernova remnants shells with high energy particle acceleration.

Quasars are the most distant and powerful objects that we know and TeV radiation could be detected from one of them located at a redshift $z > 0.5$, a fact that has implication also about the density of background light in the Universe.

The center of our galaxy, where a black hole most likely resides and is also a potential region of accumulation of Dark Matter, has been also found to be a high energy gamma-ray emission region.

Pulsars are also considered efficient particle accelerators and for the first time pulsed γ-ray emission above 25 GeV could be detected by a ground-based instrument.

Starburst galaxies, the star factories, are also very recently discovered as gamma-ray production sites... in short the potential of this research field is huge.

On this thesis we will center on the study of active galaxies which are galaxies hosting in their nuclei what is considered the most powerful engine at work in nature. It is though that the gravitational potential of matter accumulated in an accretion disk is efficiently converted to energy while falling into the supermassive black hole located at the center of the active galaxy. There, we can test the physics laws in the most extreme conditions, in an environment that we can not artificially reproduce in laboratory facilities.

The studies reported in this thesis were carried on within the MAGIC collaboration during the last 4 and a half years, most of the time at the IFAE institute (Institut de Física d'Altes Energies) near Barcelona. The MAGIC telescope is a Cherenkov telescope for the detection of γ-rays in the energy range $\simeq 0.1$–10 TeV. MAGIC is a ground-based instrument, it detects gamma-rays indirectly, through the so-called Cherenkov imaging technique, contrary to space-born gamma-ray telescopes which directly detect the primary gammas. On the ground-based side, during the never-ending effort for a better sensitivity and lower energy threshold, several instruments played an important role. After the pioneering Whipple Chrenkov telescope, which in the 90's demonstrated the power of the ground-based observing technique detecting the first astrophysical sources at TeV energies, the HEGRA array system continued to explore the sky revealing several new TeV-gamma emitters. Nowadays, the most important instruments are the H.E.S.S., the MAGIC and the VERITAS telescopes. Looking at the future the CTA project, a huge array of Cherenkov telescopes of different sizes, promises new exciting times.
The high-energy γ-ray Universe is coming into focus!

Outline

The first three chapters of this thesis provide an introduction to the relevant physics topics discussed, starting from the basic notions and open questions about the Cosmic Rays (chapter 1), going through the achievements of the young branch of Astrophysics known as γ-ray Astronomy (chapter 2), and focusing finally on the astrophysical objects which are the subject of this thesis: the Active Galactic Nuclei (chapter 3).

We propose then three chapters that discuss the experimental approach to the subject. The γ-ray detection techniques and the type of detectors are first discussed (chapter 4), paying special attention to the explanation of the IACT technique. The MAGIC telescope(-s) (chapter 5) and its data analysis procedure (chapter 6) are then discussed in detail, since the astrophysical measurements shown on this thesis are obtained in this framework.

The next two chapters report on the physics results obtained in the course of my reserch. The measurement of the VHE gamma-ray flux of three famous extragalactic sources, namely Markarian 421 and Markarian 501, in the context of the up to date most complete multiwavelength campaigns ever organized on this type of objects (chapter 7), and Messier 87 during an important flaring activity (chapter 8).

Finally, two appendices describe the most relevant technical developments to which I was committed during my PhD. The first is the development of a novel method for the analysis of the MAGIC telescope data which makes use of the time information in the Cherenkov images (appendix A). The second is the development of the data acquisition software for MAGIC-II (appendix B), the second telescope of the MAGIC Florian Goebel Telescopes array.

Chapter 1

Cosmic rays

What is the origin of cosmic rays?

1.1 Cosmic rays

In 1912 Victor Hess discovered a penetrating radiation that originated in outer space (Hess, 1912). To date, almost hundred years later, a clear explanation about the origin of this radiation is still missing.

When the physicists of the epoch were charging their golden-leaf electroscopes, they noticed that the instruments were slowly and spontaneously discharging with time, even without any action from their side (Longair, 1992). They knew that the discharge was due to the presence of ionized gas around the charged conductor, but what was ionizing the gas? There must have been some kind of ionizing radiation continuously exciting the gas molecules inside the electroscopes. Surprisingly, the ionization level was varying in a very intriguing way with respect to the altitude: first slightly decreasing but then constantly increasing. Hess personally measured the ionizing effect at several altitudes, during a series of challenging balloon flights. The maximum altitude he reached was as high as 5 km above sea level. During these flights, he carried with him more refined ionizing effect detectors. Instead of gold-lead electroscopes he was using airtight vessels of glass enclosing two electrodes with a high voltage between them. Within two years Kolhöster confirmed the Hess results ascending in a open balloon flight up to 9 km and providing further evidences of the increase or ionizing radiation with respect to the altitude. Years later, in 1926, Millikan called this radiation cosmic rays. Even if now we know that cosmic rays are mainly charged particles, and not "rays", the name has survived since then. From now on in the text we will usually refer to Cosmic Rays with the acronym 'CR'.

The main references for this section are the review articles: Biermann and Sigl (2001) and Blümer et al. (2009).

1.2 Cosmic ray composition

All elements of the periodic table have been found in CR (Blümer et al., 2009), but by far the largest fraction is composed by protons and nuclei (98%). Protons p represent the 87% of this fraction, whereas 12% are He^{++}. The chemical abundances of protons and nuclei are in first approximation rather similar to those in the solar system (see figure 1.1). However, we can notice certain differences which reveal information on the acceleration

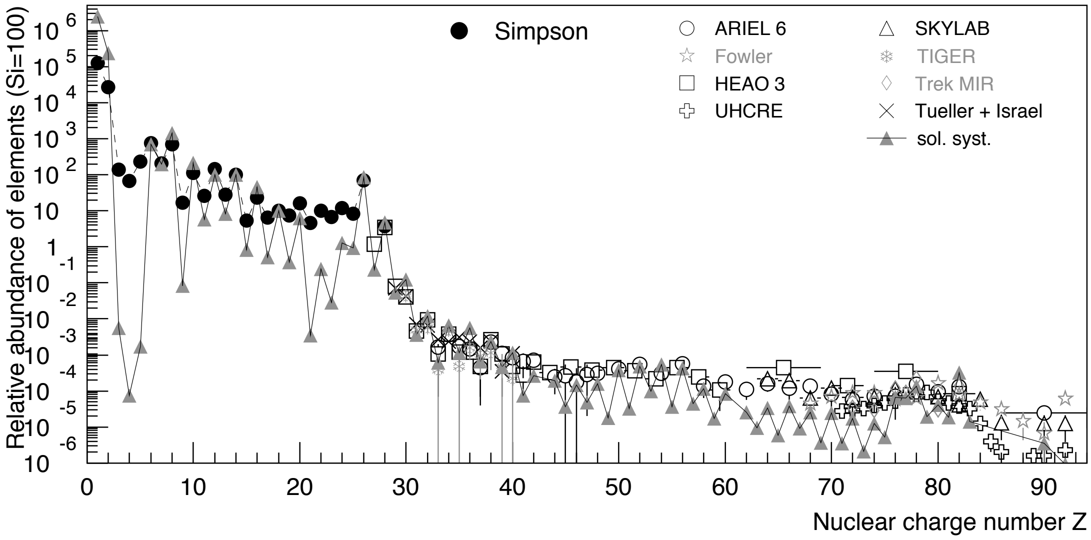

Figure 1.1: Abundance of elements in cosmic rays as function of their nuclear charge number Z at energies around 1 GeV/n. The solar system elements composition is also shown. From Blümer et al. (2009).

and propagation of CR, as for example the occurring of spallation processes for the lowest Z elements.

A smaller fraction (2%) of CR is given by electrons and positrons (e^+, e^-). The controversial peak in the e^+ plus e^- cosmic ray flux recently reported by the ATIC experiment, the PAMELA satellite e^+ excess and the new detailed measurements from the Fermi satellite are at the moment some of the hottest topics in the field, mainly because of its possible relation with the dark matter problem.

Least but not last, an even smaller fraction of the overall CR flux is given by high energy photons (γ-rays), which at these high energies is very convenient to treat as particles. Gamma rays play a very important role in the understanding of the origin on the cosmic rays in virtue of their neutral charge and because of their relatively easy production in nature. γ-rays are not isotropic as charged CR, they reveal instead their origin location because not deflected by the magnetic fields in the space[1].

Other neutral cosmic rays are neutrons n and neutrinos ν. The neutron lifetime is of the order of 900 s in the rest frame, so the fraction which arrive to the earth before decaying must be locally produced and can not bring information from the far universe. Regarding the neutrinos, a whole generation of huge detectors (as ICECUBE in the south pole) have been built to detect these elusive particles since they can also shed light over the mechanism of CR acceleration (ν-s are associated to hadronic interactions). Hopefully some interesting results will come soon also from this branch of astroparticle physics.

Cosmic rays are impinging the earth all the time[2] with a flux which depends strongly on the energy of the particles (see figure 1.2). Remarkably, the energy range of the cosmic rays spans through 13 decades, with their flux following (in first approximation) a simple

---

[1] Gammas might convert to e^+, e^- pairs when interacting with another photon or in the presence of the electric field of a nucleus. In the case that the $\pi^\pm$ radiate a secondary γ-ray it is like the primary is somehow sensitive to magnetic fields, but the fraction of gamma-rays affected is very small.

[2] Despite their stealth, they are thought to influence both the climate of our planet and the evolution of its inhabitants (Erlykin and Wolfendale, 2010).

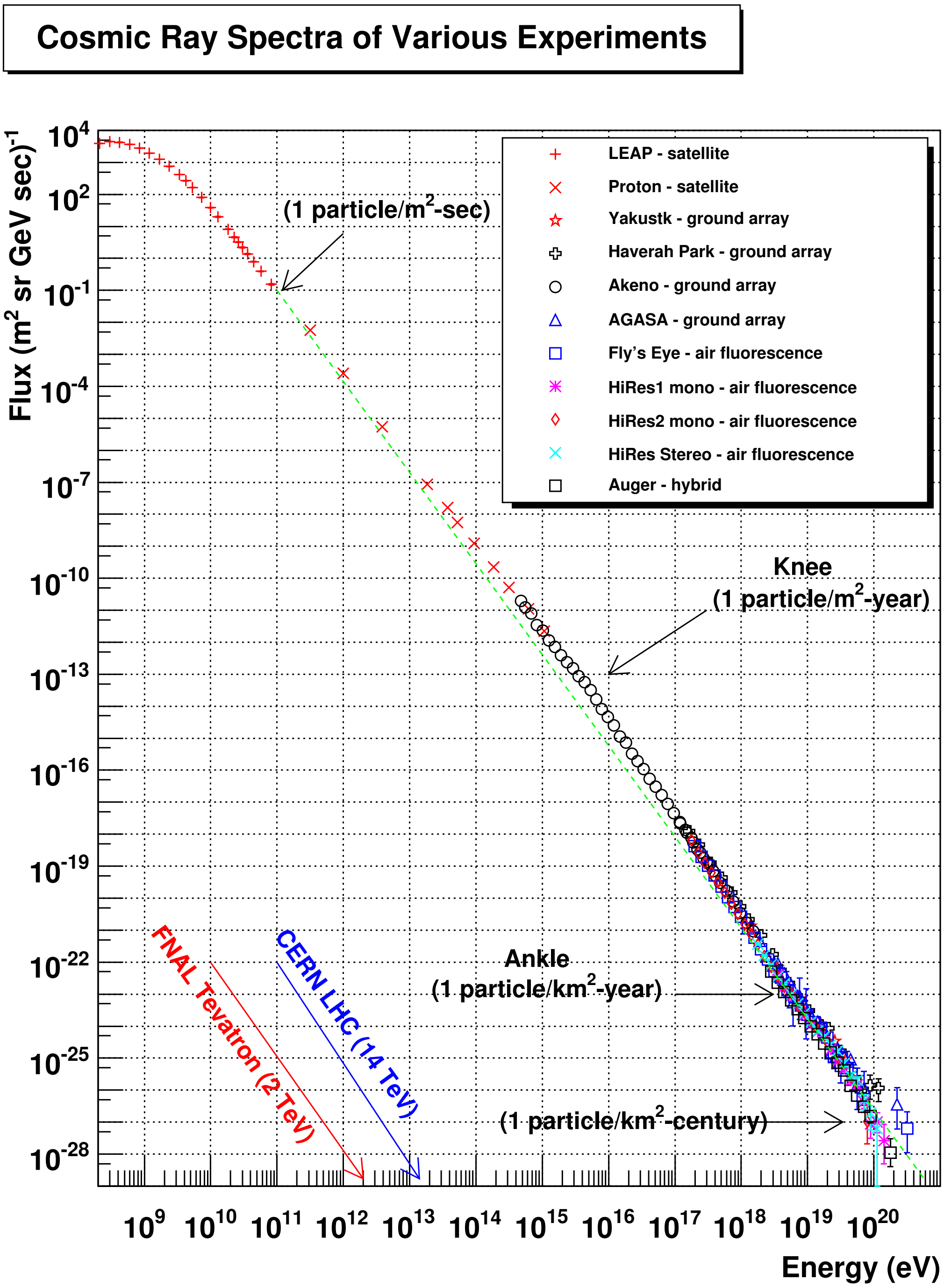

Figure 1.2: All-particle cosmic ray spectrum. Notice the “knee” and the “ankle” spectral features. The arrows marking the energies reached by the largest man-made particle accelerators. Plot from http://www.physics.utah.edu/~whanlon/spectrum.html.

power law, which is referred to as a *non-thermal*[3] behavior since non-thermal processes are thought to be producing such spectra. Digging a little bit more we can see that there are two breaks in the power law index. The first one, known as the 'knee', is located at roughly 5 PeV whereas the second break, at roughly 3 EeV (1 EeV = 10^{18} eV)[4]. Below the knee and beyond the ankle the cosmic-ray spectrum is described with a power law ($E^{-\Gamma}$) of index $\Gamma = 2.7$ whereas within the knee and the ankle the spectrum softens to $\Gamma = 3.1$.

The measure of the spectrum beyond the ankle becomes very difficult because of the extremely low flux: about 1 particle per square kilometer per century at $E = 10^{20}$ eV. Notice that the most powerful man-made particle accelerator, the brand new LHC, will reach energies of $\sim 10^{13}$ eV, seven orders of magnitude less than the most energetic cosmic ray recorded. From the experimental point of view this is relevant because the sensitivity is not expected to increase by R&D studies and new technologies. The only way to increase the sensitivity is to extend the collection area.

On the lower edge of the spectrum, the solar wind prevents low energy charged particles to come into the inner solar system, due to interaction with the magnetic field in the solar wind. This prevents us from knowing anything about the energies lower than about 300 MeV, only from about 10 GeV per charge unit Z of the particle the effect of the solar wind becomes negligible.

1.3 Cosmic rays origin

Cosmic rays are divided into two main classes according to their energy and probable acceleration sites: those below about 10^{18} eV in energy are called 'galactic' cosmic rays; above that energy, they are referred to as 'extragalactic' cosmic rays. The region within 10^{17} and 10^{18} is considered a 'transition' region.

Although galactic cosmic rays (protons and nuclei) are widely believed to be mainly accelerated by the winds and supernovae of massive stars (Biermann and Sigl (2001), Aharonian et al. (2004), Acciari et al. (2009*a*)), definitive evidence of this origin remains elusive nearly a century after their discovery (Butt, 2009).

The naming extragalactic comes from the fact that protons with energies above 3×10^{18} eV have Larmor radii in the galactic magnetic field ($\approx$ 3–6 μG, Blümer et al. (2009)) which are too large to be contained, and so such particles must come from outside our galaxy. The Larmor radius of a proton in the galactic magnetic field is actually:

$$r_L = 1.08\ pc\ \frac{E/PeV}{Z \cdot B/\mu G}$$

This classification is also corroborated by the different chemical composition and the change in the slope of the spectrum. Above the knee the fraction of heavy nuclei continuously increase up to the ankle where the composition becomes light again (Blümer et al., 2009). These considerations suggest somehow different origin for the two classes of cosmic rays, that is why they are normally treated separately when explanations of they origin are provided.

---

[3] *Thermal* emission is the electromagnetic radiation from a hot material produced by the transition of electrons among atoms shells. Photons produced by different emission processes are known as *non-thermal.*

[4] A cosmic-ray particle of this energy carries the same energy necessary to lift a light shopping bag form the ground floor to your first floor apartment.

On the low energy side we can say that the particles with energies lower than 10^{10} eV mainly come from the sun. The solar wind prevents particles in that energy range from reaching the earth from outside the solar system.

1.3.1 Cosmic rays acceleration

Before arriving to the earth, energetic cosmic rays must had been first injected and then accelerated up to the extremely high energy detected. In the case of galactic cosmic rays, although in the literature there are several possible suggestions, the source for the injection of the primary particles are thought to be star wind like emissions (Biermann and Sigl, 2001). Concerning the acceleration processes, the standard mechanism is know as 'Diffusive Shock Acceleration' (DSA) also known as 'Fermi acceleration'. We can differentiate within 'first order' and 'second order' Fermi acceleration depending on the characteristic of the moving plasma. In the basic scenario a charged particle gain energy through the stochastic interaction with a moving, magnetized, 'cloud' of material. In this case the mean energy gain of the particle per interaction is: $\langle \Delta E/E \rangle \propto \beta^2$, being $\beta = v_{cloud}/c$ and the mechanism is referred as second order Fermi acceleration (Fermi-II).

The scenario is more complicated when a shock wave is present. We talk about 'shock' when the velocity of the moving material (blob) is higher that the speed of sound in the medium. In this case a shock front is formed and the particle to be accelerated interact differently with the moving material. The particle, which gains energy at each passage through the shock, is accelerated in a way directly proportional to β: $\langle \Delta E/E \rangle \propto \beta$, so that in this case we talk of first order Fermi acceleration (Fermi-I). The greater the velocity difference, the greater the energy gain by the particle per shock crossing and the larger the magnetic field (and turbulence), the higher the particle crossing frequency.

Shocks play an important role in astrophysics. They are present in many astrophysical cases and are subject of intense study and discussion by the community. For example shocks waves are produced in the interstellar medium after a supernova explosion or in active galactic nuclei jets as consequence of ejection of material from the very core of the galaxy (see also section 2.3).

1.3.2 Galactic CRs

Galactic, or low energy, cosmic rays are thought to be accelerated over centuries in the shock waves of supernova explosions within our galaxy. Shock acceleration through the DSA mechanism (shortly described above) in isolated supernova remnants is suggested as the responsible for the acceleration of cosmic rays. However, we still have no proof for this scenario.

From the energetic point of view, the typical supernova rate of 3 SN/century/galaxy is more than sufficient to provide the energy density observed in CR. Actually just $\approx 10\%$ of the kinetic energy released by SN explosions is enough to cover the required energy budget. As mentioned before particle would be accelerated through diffusive, first-order, shock acceleration in the shock waves of supernova remnants. The finite lifetime of a shock front ($\sim 10^5$ years) limits the maximum energy attainable for particle with charge Z to $E_{max} \sim Z \cdot (0.1 - 5)$ PeV. A popular explanation for presence of the knee is associated with the upper limit of acceleration by galactic supernovae for the dominant light CR particles. Heavier nuclei can instead be accelerate to much higher energies, in some model till up to the ankle.

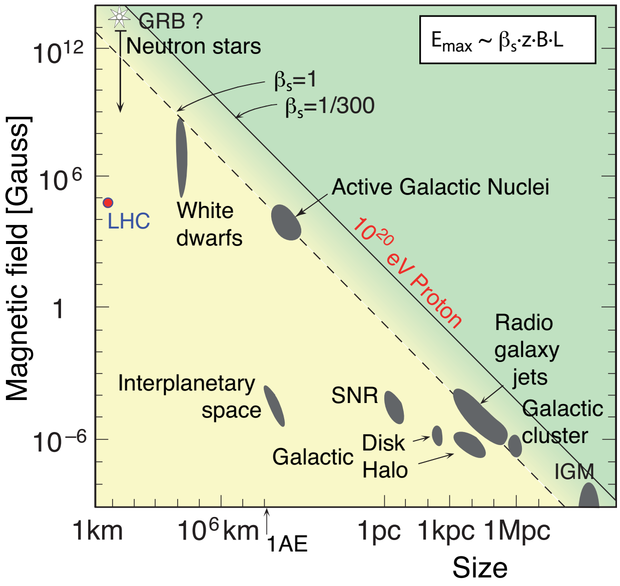

Figure 1.3: 'Hillas plot' of astrophysical sources in which cosmic rays could be accelerated up to UHE though the DSA mechanism. From Blümer et al. (2009).

Another popular explanation is the leakage of particles from the galaxy: above a certain energy cosmic rays are not contained in the galaxy (or its halo) anymore. These two explanation are not exclusive and a combination of the two is also possible and in some scenario even more likely.

1.3.3 Extragalactic CRs

There is no clear separation between galactic and extragalactic CR even if the ankle is considered as the marker within the two population. For energies higher than 10^{18} eV, a convincing explanation of the acceleration processes and sources is still unknown. As cosmic rays above these energies are no longer confined by galactic magnetic field, it is natural to think that they are produced by extragalactic sources.

In the framework of the DSA the magnetic filed strength B in the source and the size R of the emission region are related to the maximum acceleration energy by:

$$E_{max} \simeq 10^{18} eV Z \beta_s \left(\frac{R}{kpc}\right)\left(\frac{B}{\mu G}\right)$$

where β_s is the shock velocity and Z the particle charge. Given the above formula the list of viable astrophysical sources is (see also figure 1.3):

- Active Galactic Nuclei (AGNs, see chapter 3)
- Radio lobes of FR II galaxies
- Gamma-Ray Bursts (GRBs)

As alternative we have the so called top-down models which are 'non-acceleration' scenarios. In this case the Ultra High Energy Cosmic Rays (UHECRs) are produced in decays of super-heavy objects as might be dark matter particles. Measurement of the arrival direction, primary mass composition and flux will be the key ingredients to solving this puzzle.

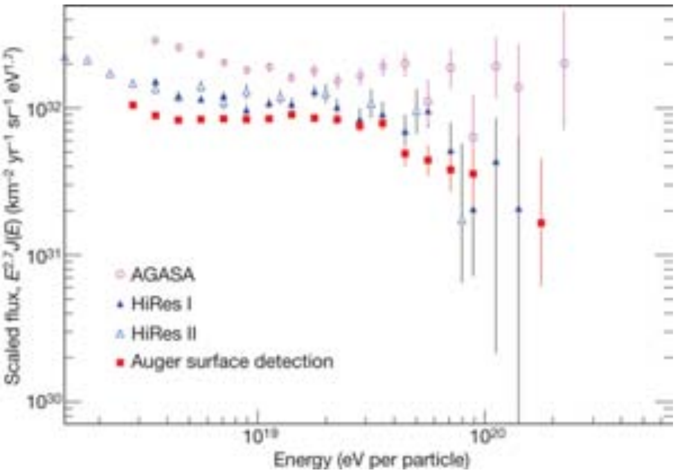

Figure 1.4: CR spectra in the GZK region from the AGASA, HIRES and AUGER experiment. Note the discrepancy in the highest energy region of the plot. From (Bauleo and Rodríguez Martino, 2009).

1.4 The GZK-cutoff

The interaction of cosmic rays with the 2.7 K microwave background radiation limits the upper edge of the cosmic ray spectrum:

$$\mathrm{p} + \gamma_{\mathrm{CMB}} \longrightarrow \Delta^{\star} \longrightarrow \mathrm{p} + \pi^{0}$$
$$\mathrm{p} + \gamma_{\mathrm{CMB}} \longrightarrow \Delta^{\star} \longrightarrow \mathrm{n} + \pi^{+}$$

The loss of energy by this process leads to the so-called Greisen-Zatsepin-Kuzmin (GZK) cutoff (Greisen, 1966; Zatsepin and Kuzmin, 1966). This limits the maximum distance that cosmic rays of $E \sim 10^{20}$ eV can travel to ~ 50 Mpc.

The observation of the GZK have been matter of disputation in the last years. The limited sample of cosmic rays in the GZK energy region, together with intrinsic differences in the way each experiment measure the CR energy set the stage for a controversial difference between the measure spectra (see figure 1.4). The recent result from the Pierre Auger Observatory (PAO), which nicely agree with the expected GZK cutoff curve, is a strong evidence of the existence of this effect.

1.5 Cosmic rays anisotropy

Given an expected angular deflection of only a few degrees for particles above $10^{19.5}$ eV in our galaxy and the existence of large cosmic voids with negligible magnetic fields, high statistics measurements should finally reveal correlations with source or source regions. The possibility to have a 'UHECR astronomy' is very appealing for the understanding of the origin of cosmic rays (Bauleo and Rodríguez Martino, 2009).

The search for anisotropy can be carried on different scales. To date, the search for large scale anisotropy in extragalactic cosmic rays have produced negative results. Some clustering on intermediate scale, with an angular separation of the order of 15° to 25°, was recently reported by the Auger collaboration, confirming a signal at a scale of 25°

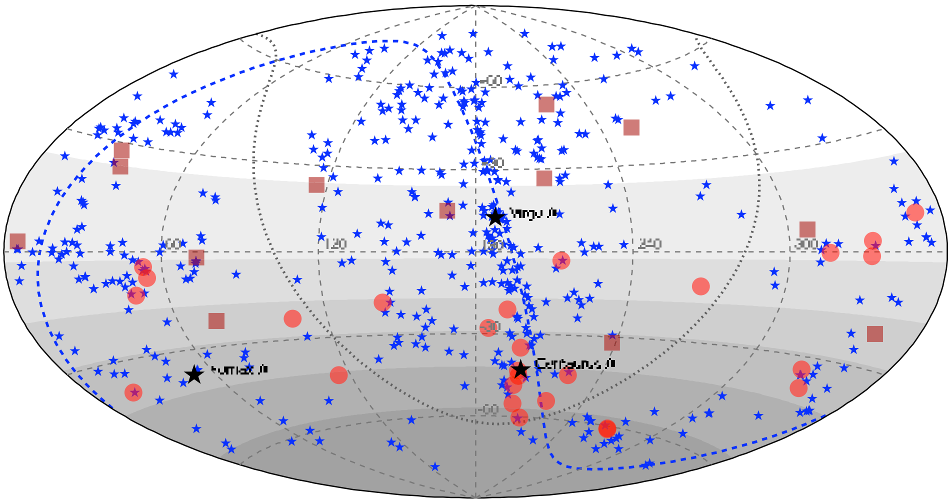

Figure 1.5: Map (equatorial coordinates) of the UHECRs detected by the Auger experiment (circles) and the HiRes telescopes (squares) superimposed to the location of the nearby AGNs (< 75 Mpc) of the Veron-Cetty Veron catalog (stars). The shaded area indicates the relative exposure of the Auger data set. The dotted line marks the galactic disk and the dashed curve is the super galactic plane. From Blümer et al. (2009).

obtained by the analysis of combined older data (AGASA, HiRes, SUGAR and Yakutsk). Although is impossible to asses unambiguously the chance probability of such correlations, the Auger collaboration obtained what can be considered a breakthrough in the small scale anisotropy searches. In a recent paper appeared in the Science magazine (Abraham et al., 2007), a correlation within their most energetic events ($E > 5.7 \times 10^{19}$ eV) and the nearby AGNs (Veron-Cetty & Veron catalog) was reported. Out of 35 events observed, 26 are correlated with AGNs with an angular distance of 3.1° with a chance probability to be incorrect in this hypothesis of less that 1%[5].

The analysis of correlation between the arrival direction of the highest energy CRs observed by the PAO and the position of nearby AGNs have been recently updated (Abraham et al., 2009) using the the data accumulated after the publication of the Science paper. The data sample now considered goes from 27 May, 2006 through 31 March, 2009. Their claim is that the subsequent data neither strengthen the case of anisotropy, nor do they contradict the earlier results. The current estimate, with 17 out of 44 events above 55 EeV that correlate, is more than two standard deviations from the value expected from a purely isotropic distribution of events (less than 1% probability to occur by chance).

Another interesting result mentioned in (Abraham et al., 2009) is an excess of events as compared to isotropic expectations observed in the sky region around the source Centaurus A (only 2% of isotropic realization have maximum departure greater than or equal to the observed one). Cen A is a very near (d$\sim$ 3.4 Mpc) radio-galaxy which has been recently established as TeV source (Aharonian et al., 2009). On the other hand, none of the UHECRs observed by Auger comes from the region around M 87, a source (see section 8.1.1) under many aspects very similar to Cen A, but the exposure of the Auger observatory is relatively low for that sky region (see figure 1.5).

---

[5] This results is not confirmed by the HiRes data, but the discrepancy might be explained by a different energy scale.

Chapter 2

Gamma-ray astronomy

What can we learn from γ-rays?

2.1 Gamma-ray astronomy

The γ-ray band is claimed to be the last frontier of astrophysics. The emission of the most extreme objects in our universe very often show their most interesting features in this part of the electromagnetic spectrum. Consequently, important astrophysical conclusions can be drawn from the study of the γ-ray component of the spectrum.

Gamma rays are also very important to solve the cosmic ray puzzle. The direct measurement of (charged) cosmic particles is in fact not the only approach to the study of CRs. Actually, as we will explain below, direct charged particles measurements is not even a viable approach when the aim is to determine their site of origin. Independent and complementary information about high energy CRs can be obtained by measurements of high energy gamma rays and neutrinos, which have the big advantage to be electrically neutral. Cosmic rays are produced far away from the earth, and galactic and intergalactic space is filled by magnetic fields. Consequently, the incoming directions of charged CRs do not point back to their production site since they are deflected by the Lorentz force which affect all the charges moving in a magnetic field. On the contrary, neutral CRs (as γ-s and ν-s) are not affected by the Lorentz force and therefore they keep information about their region of production. They come from the sky direction where the emitting source actually is.

Neutrinos are very light weakly interacting particles which can be detected only using detectors with very large volumes of interacting material. Neutrino physics is an established branch of research which led to important results in the last decades (the neutrino species oscillation just to give one example), but the experimental challenge of developing high-energy neutrino astronomy is tough. The expected neutrino flux from astrophysical sources is so low (and uncertain) that even the largest 'ν-astronomy' projects currently running could not detect, at least up to now, neutrino signal from any astrophysical source[1]. Nevertheless, big efforts are currently being done to make ν-astronomy possible, and a new generations of detectors is currently under development.

In conclusion, the "neutrino-way" is in principle viable to study both astrophysics and

---

[1] Excluding the sun, which is known to emit low energy neutrinos, and the detection from the supernova SN 1987A on February 23, 1987, when a "burst" of neutrinos (24 in total) was observed at three separate neutrino observatories (Kamiokande-II, IMB and Baksan).

cosmic rays but because of the still prevailing technical difficulties the most direct and proven way to find CR acceleration sites is to look for γ-rays instead, which are more abundant and more easily detectable.

In short, the γ-rays can bring us information about:

- The astrophysical sources where they are produced;
- The particle acceleration mechanisms at work in the universe;
- The characteristics of the medium crossed during their travel to the earth;

Conventionally, cosmic gamma rays are divided in the High Energy band (HE) with photon energy between 1 GeV and 100 GeV, the Very High Energy band (VHE) with photon energy between 100 GeV and 10 TeV and the Ultra High Energy band (UHE) with photon energy above 10 TeV. HE gammas are detected by satellite detectors (see section 4.1.1), the VHE gammas can be detected by ground-based experiments using Cherenkov telescopes (see chapter 4), whereas UHE gammas are also detected with ground-based experiments using mainly large arrays of particle detectors.

2.2 Gamma-ray production

The visible light photons are the messenger used by the classical astronomy to try to understand the universe. For many centuries the only detector available was the naked eye which is sensitive only in a very narrow band of the electromagnetic spectrum located at the peak of the sun emission spectra convolved with the transparency of the atmosphere (figure 4.1). Visible radiation is produced mainly by atomic excitation and has a black body spectra, dependent on the temperature of the emitting material. This is know as 'thermal' radiation and dominates the emission spectra of the stars, the most important component of the universe form the historical point of view[2]. During most of their lifetime stars are quite stable nuclear reactors converting H to He. VHE γ-rays are instead messengers of violent, non-thermal processes, happening at the location of the source or very close to it. With the expression 'non-thermal' we refer to the fact that the production of photons is in this case due to processes which are dominant at higher energy scales and which have as characteristic the non-equilibrium between matter and radiation. Particles of thermal radiating material follow a maxwell distribution.

From the VHE astrophysics point of view the most important γ-rays emission processes are described in the following (Longair (1992), Aharonian (2004)):

bremsstrahlung Bremsstrahlung is the radiation associated with the acceleration of electrons in the electrostatic field of ions and the nuclei of atoms. γ-rays production from bremsstrahlung requires astrophysics environments with matter. In a non relativistic regime, the bremsstrahlung γ-rays spectrum simply repeats the shape of the electron acceleration spectrum. In the case of a typical power law spectrum: $Q(\epsilon_e) \propto \epsilon_e^{-\Gamma}$. In the relativistic case instead, the bremsstrahlung γ-ray spectrum becomes flatter, with power law photon index $\Gamma - 1$. The process competes with

---

[2] From the energy point of view in our galaxy the energy density of cosmic rays is comparable to the energy density of starlight, of interstellar magnetic fields, and of the kinetic energy density of interstellar gas (http://www.mpi-hd.mpg.de/hfm/HESS/pages/about/physics/).

the ionization losses at low energies and becomes inefficient below a certain critical energy E_c (in hydrogen gas $E_c \sim 700 \cdot m_e c^2 \simeq 350$ MeV).

synchrotron radiation The synchrotron radiation is the emission of photons from electrons moving in a magnetic field. γ-ray production from synchrotron requires magnetized astrophysical environments. Generally the energy of synchrotron photons is much less than that of their parent electrons but in specific astrophysical environments energetic gammas can be generated.

inverse Compton Inverse Compton (IC) scattering provide one of the principal gamma rays production mechanism in astrophysics. It works effectively almost everywhere as in pulsars, active galactic nuclei o supernova remnants (see section 2.3). Contrary to the basic Compton mechanism, where photons scatter electrons increasing their energy, the IC produce HE photons as result of the scatter of an ultra-relativistic electron with a low energy photon seed. γ-ray production from IC requires astrophysics environments with a radiation field. This results in the production of VHE γ-rays from a population of accelerated electrons if ambient photons are available in the site and the environment is sufficiently transparent to gamma rays to allow them to escape from the production region. We can differentiate within two regimes depending on the energy of the electrons since the cross section for the production varies significantly. Given a power-law distributed population of accelerated electrons $dN_e/d\epsilon_e \propto \epsilon_e^{-\Gamma}$, below the so called Thomson limit ($a = 4\nu_0\epsilon_\gamma \ll 1$, with ν_0 the frequency of the seed photon) we will obtain gammas with a power low index $\alpha = (\Gamma+1)/2$. In the second case ($a \gg 1$) a much steeper spectrum is produced: $\alpha = \Gamma + 1$. The mechanism is specially efficient for electrons since the IC from protons is suppressed by a factor $(m_e/m_p)^4$.
According to the Synchrotron-Self-Compton emission models (see also section 3.4), seed photons to be subsequently up-scattered are self produced by the primary population of accelerated electrons through the synchrotron process.

π^0 **decay** In many astrophysical cases 'hadronic' scenarios are proposed as responsible for the emission of γ-rays (see also section 3.4). In this case a population of primary p and ions is assumed to interact through inelastic scattering with ambient gas and produce π mesons. The neutral π^0 (produced with $\simeq 33\%$ b.r.) has a very short lifetime ($\tau \approx 10^{-17}$ s) and its preferred decay channel is $\pi^0 \to \gamma + \gamma$. Since 2/3 of the energy of the primary proton goes in the production of charged pions ($\pi^\pm$), which decays leptonically the production of a large amount of HE neutrinos is expected in this scenario. Unfortunately, only $\sim$ km^3 size detectors can hopefully detect these neutrinos, making this very challenging from the experimental point of view.

Another mechanism, which actually does not produce photons but is closely related, is the pair production.

pair production It consists on the creation of a couple $e^- + e^+$ from a γ with $E_\gamma > 2m_e c^2$. Pair production cannot take place in free space because momentum and energy cannot be conserved simultaneously[3] without a third body, like an ambient nucleus. In a gas environment the radiation length for the pair production is the

---

[3] If a photon of energy $2\gamma m_e c^2$ and momentum $2\gamma m_e c$ produce a $e^\pm$ pair moving exactly on the same direction, their maximum momentum will be $2\gamma m_e v$, but $v < c$.

same as for bremsstrahlung, revealing their intimate quantum electrodynamics relation. Photon-photon pair production (inverse process of pair annihilation) is also possible. All the γ-ray production mechanism described above can compete with pair production. The energy range and environmental conditions determine the dominant processes. It is responsible for the source opacity and for the 'gamma-ray horizon' at large distance.

High energy astrophysical scenarios are more complex than scenarios in other wavelengths because all these several processes are possibly at work and in competition. Inverse Compton and synchrotron radiation may very well dominate, especially at VHE, over bremsstrahlung, depending on the ratio of the energy density of the radiation and magnetic fields to the number density of the ambient gas.

As final remark, we want to mention that is generally believed that efficient electron acceleration is actually in most cases limited by radiative losses. One can then make two general considerations. The first is that γ-rays are abundantly produced and it makes sense to seek them. The second is that protons and heavier nuclei can reach much higher energies that electrons in the VHE γ-rays production sites.

2.2.1 The gamma-ray horizon

Even if the density of matter and radiation in the universe is in average extremely low, the cosmological distances that γ-rays from extragalactic sources have to travel to reach the earth increases their probability of interaction. The important physical process involved is again the pair production, that leads to the annihilation of the primary gamma. The mean free path of VHE γ-rays in hydrogen gas is governed by the electron-positron pair

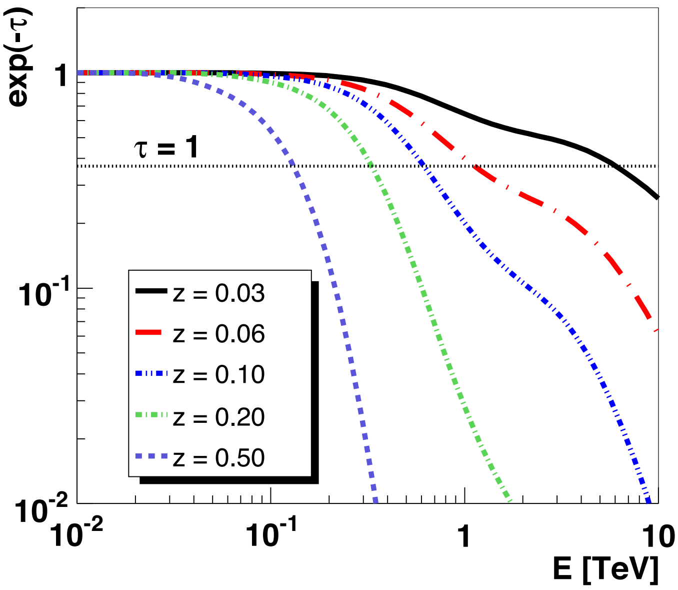

Figure 2.1: EBL attenuation coefficients as a function of γ-ray energy. The 'best fit' model from Kneiske et al. (2002) is used fro the EBL density. Plot from Mazin (2007).

production cross section and has a value of 80 $g \cdot cm^{-2}$ which for all practical purposes has no effect on the transparency of the universe in the VHE band (Hinton and Hofmann, 2009). More relevant is the absorption by pair production on ambient (CMB, IR, visible or X-ray) photons of energy E_T. The process acts above the threshold $E_\gamma E_T = m^2c^4$ or $E_\gamma, TeV = 0.26/E_T, eV$ and the absorption cross section for an isotropic photon field $\sigma_{\gamma\gamma}$ (see, Aharonian et al. (2008*b*)) peaks close to threshold at $E_\gamma, TeV = 0.9/E_T, eV$ (Hinton and Hofmann, 2009).

The attenuation of the original γ-ray flux depends on the distance of the source (typically measured in redshift units), on the energy of the primary VHE γ-rays and on the spectrum of the Extragalactic Background Light (EBL) which provides the E_T photons. Figure 2.1 shows a typical model for the EBL attenuation coefficients as a function of γ-ray energy. Please notice that above 1 TeV the effect is already very relevant for a redshift of $z = 0.1$.

Historically, the issue of EBL absorption became relevant after the detection at VHE of Mrk 421 in 1992 (Punch et al., 1992). In fact, right after the detection of that first extragalactic source, a systematic search for TeV emission from the most promising AGNs was performed by the Whipple Cherenkov telescope, initially with no success (Quinn et al., 1996). Theoretical speculation on the absence of TeV emission from other AGNs centered on the possibility of intergalactic absorption of the TeV photons. The observing program of Cherenkov telescopes has concentrated for a long time on the observation of relatively nearby ($z < 0.1$) objects. The recent detection of farther AGNs (e.g. Albert et al. (2008*c*), see also section 3.3) by the last generation of Cherenkov telescopes actually managed to enlarge the depth of the search, including as candidate targets also object with relatively large redshift ($z = 0.1$–0.6).

To correctly interpret the measured astrophysical spectra the knowledge of the EBL level is required because the measured flux has to be corrected by effect of γ-ray absorption (attenuation coefficients depends on the shape of the EBL). The intrinsic flux is always higher that the measured one. Unfortunately the level of the EBL is very difficult to determine by direct observations because of the overwhelming foreground light sources. Since the EBL is important by its own the information provided by the TeV absorption is potentially very useful once assumptions about the intrinsic spectra of the source can be done (Mazin and Raue, 2007). Notice that direct EBL measurements are representative only of the 'local' level of EBL whereas indirect measurements from γ-rays allow to probe the EBL all along the path traveled by the gammas[4].

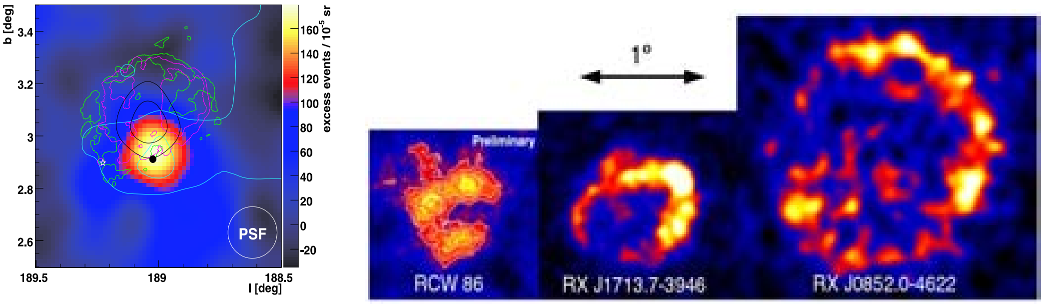

Figure 2.2: SNRs at TeV energies

---

[4] The 'evolution' of the EBL along the history of the universe has to be taken into account.

2.3 Cosmic gamma-ray sources

The nowadays established TeV-γ emitters (excluding the numerous unidentified sources that cannot be classified) are:

SuperNova Remnants (SNRs) A supernova is the explosion of a massive star at the end of its life. It can result in the formation of a Neutron Star (NS) or a Black Hole (BH), surrounded by a gas nebula. Here, non thermal processes accelerate particles up to TeV energies. In SNRs particle acceleration proceeds on the parsec distance scale in the shock formed in the interaction of the SN ejecta with the InterStellar Medium (ISM). Both leptonic and hadronic models have been proposed to explain the detected VHE radiation.

Pulsars and associated nebulae (PSRs and PWNs) As we just mentioned a supernova explosion always leads to the formation of a very compact object. The compact object might acquire rotational speed because of the inhomogeneities during the gravitational collapse which originates some angular moment. Its conservation during the shrink of the of object might lead to high rotational velocities. Pulsars are rotating neutron stars with an intense magnetic field. Strictly speaking they are also supernova remnant but they are classified differently. The models for these sources predict power law spectra with different cutoff locations in the 10-100 GeV region depending on the model (Polar-cap or Outer-gap for example).

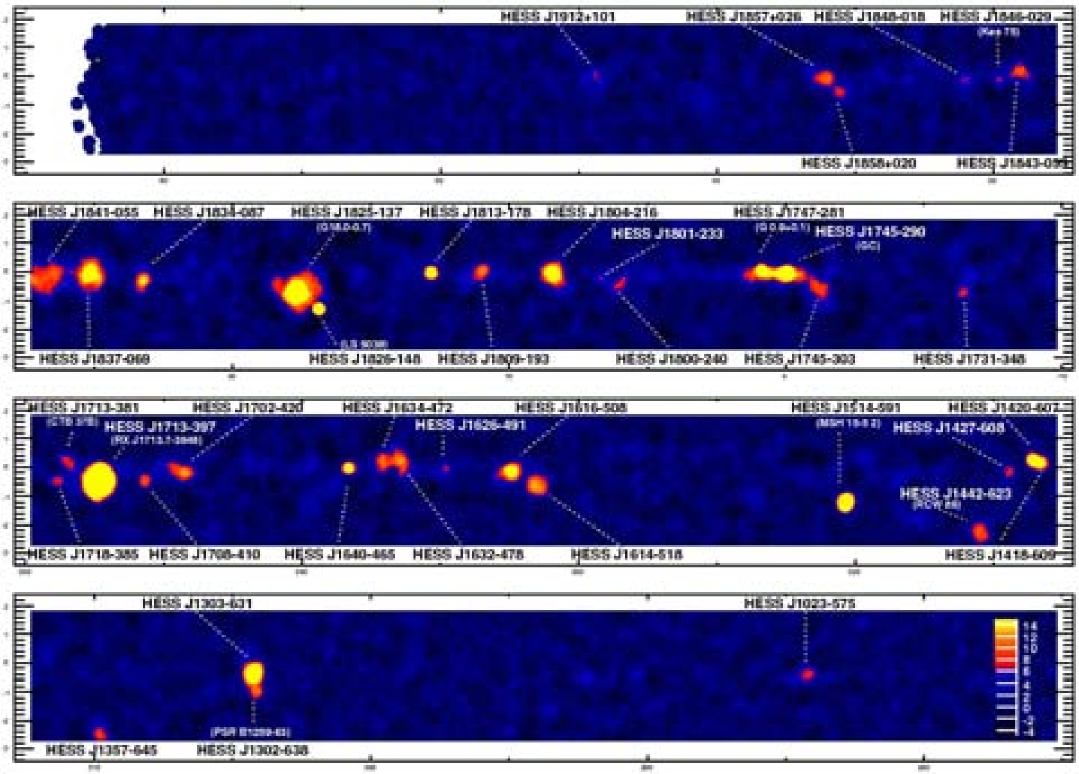

Figure 2.3: The result of the galactic scan performed by H.E.S.S. Cherenkov telescopes (Aharonian et al., 2006*b*).

Pulsar Wind Nebulae (PWNs), i.e. pulsars displaying a prominent nebular emission, currently constitute the most populated class of identified galactic VHE sources. The VHE emission from PWNs is likely of leptonic origin. Electrons are accelerated in the shock formed by the interaction of the pulsar wind with the supernova ejecta.

The most famous PWN is the Crab Nebula, a strong and steady emitter that is used as calibration candle in the VHE field. Its Spectral Energy Distribution (SED) shows two bumps, the first at low energy (roughly in the X-ray band region, attributed to synchrotron emission) and a second peaked at around 100 GeV. This second component likely results from inverse Compton scattering, by the synchrotron-emitting electrons, of softer photons in the shocked wind region.

Binary Systems (BS) These systems contain a compact object (a neutron star or a black hole) that accretes or interacts with matter outflows from a companion star. Compared to SNRs and PWNs, the Binary Systems (BS) are much more compact. The detection of this population of sources in the VHE band is very recent (Albert et al., 2006).

The Galactic Center (GC) The center of our galaxy (where the Sgr A* black hole is located) was established in the past years as a steady VHE photons emitter (with also a diffuse component). The GC is a very crowded sky region. There are three compelling candidates for the origin of the VHE emission: a SNR, a PWN and the black hole itself (even if the latter is disfavored due to absence of variability at VHE, despite the strong X-ray activity).

Active Galactic Nuclei (AGNs) An AGN is a galaxy with a supermassive black hole ($\gtrsim 10^6 M_\odot$) in its center. In general, it is characterized observationally by an extremely bright nucleus region although the phenomenology of AGN spectra is diverse and rather complex (see chapter 3). Nevertheless the so-called *unified model* has been invoked to explain all the different spectral categories of AGNs. This model includes a central engine (the black hole) surrounded by an accretion disk and by fast moving clouds, which emit Doppler-broadened lines. In around ten percent of all AGNs, the in-falling matter turns on powerful collimated relativistic jets orthogonal to the galaxy plane. If the relativistic jet is viewed at small angle to its axis, the observed jet emission is amplified by relativistic beaming. Such sources are called *blazars* and constitute the bulk of the AGNs detected at TeV energies.

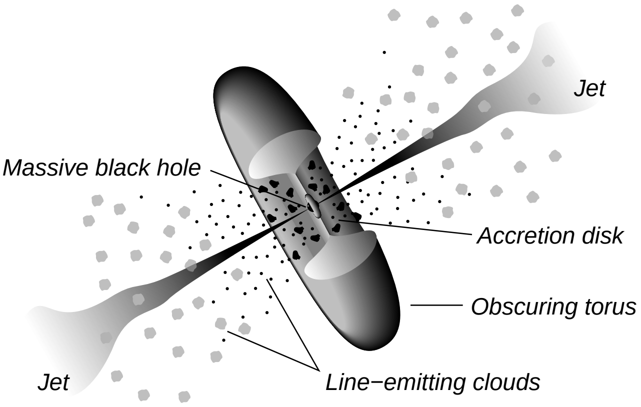

The emission is characterized by rapid variability (flares) that in certain cases reach several times the flux of the Crab Nebula. The mainstream interpretation is a synchrotron emission from a population of ultra-relativistic electrons and IC emission from soft photon scattering. Many hadronic models have also been proposed. One further aspect of TeV spectra of blazars is that they can be used as probes of the extragalactic background light (see the EBL section 2.2.1).

Gamma Ray Bursts (GRBs) A GRB is a sudden very short and intense emission of gamma rays. They are isotropically distributed in the sky, of extragalactic origin and classified by their main burst duration as *short* and *long* (the boundary being conventionally set at two seconds). An afterglow emission follows the gamma-ray burst in the X-ray band. Long GRBs seem to be related with supernova explosions. Up to now no GRBs have been detected in the VHE band. Nevertheless they are very interesting targets since in many models VHE radiation is predicted during the prompt or afterglow phase. Therefore VHE observations of GRBs could help constraining GRB models.

The number of sources is constantly growing in the last years, thanks mainly to the third generation of Cherenkov telescopes detectors (CANGAROO, H.E.S.S., MAGIC and VERITAS).

In figure 2.4 an updated sky map of the cited VHE gamma-ray sources is shown. On table 2.1 we present a summary of the currently known TeV emitters, classified by type (a large fraction is still without association). Please notice the large and increasing number of source populations which have turned out to be emitting VHE gamma-rays. In the so-called “Kifune” plot presented in figure 2.5, the number of established sources is plotted as function of the time. The discovery trend for TeV sources seems to follow the same evolution shown by the X-ray and γ-ray sources (at lower energies) in the past.

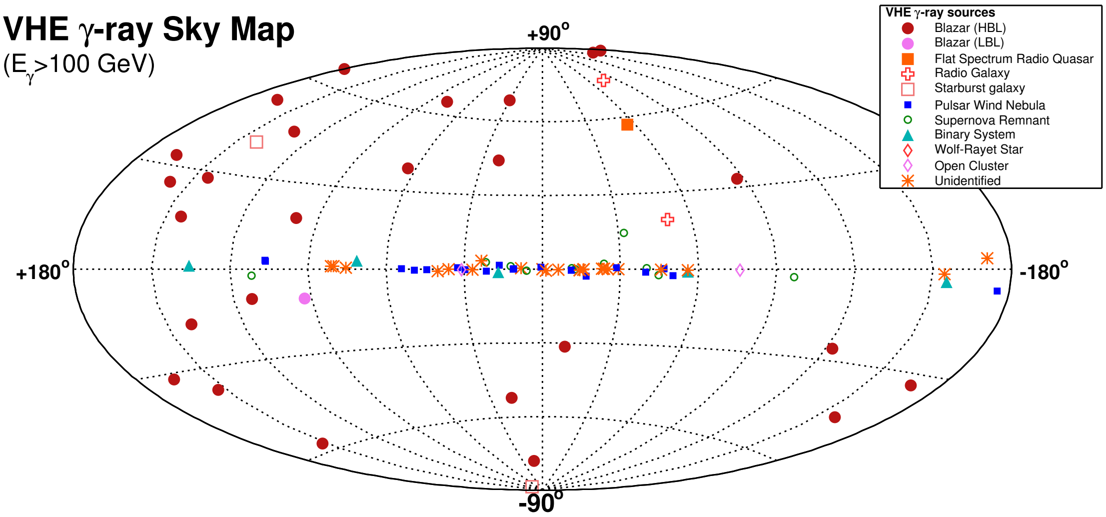

2009-11-18 - Up-to-date plot available at http://www.mppmu.mpg.de/~rwagner/sources/

Figure 2.4: The up-to-date sky map of the known TeV emitters (Wagner, 2009).

Class	2003	2005	2007	2009
Pulsar Wind Nebulae (PWNs)	1	6	18	19
Super Nova Remnants (SNRs)	2	3	7	9
Binary Systems (XRBs)	0	2	4	4
Wolf Rayet	0	0	1	1
Pulsar*	0	0	0	1
Diffuse Emissions	0	2	2	0
Active Galactic Nuclei (AGNs)	7	11	19	31
Starburst Galaxy	0	0	0	2
Unidentified	2	6	21	27
Total	12	30	71	94

Table 2.1: Established TeV sources classified by typology (from J.Hinton XXX ICRC summary talk, July 2007 and R.Wagner web page *http://www.mppmu.mpg.de/~rwagner/sources/*, December 2009). * Detected at 25 GeV.

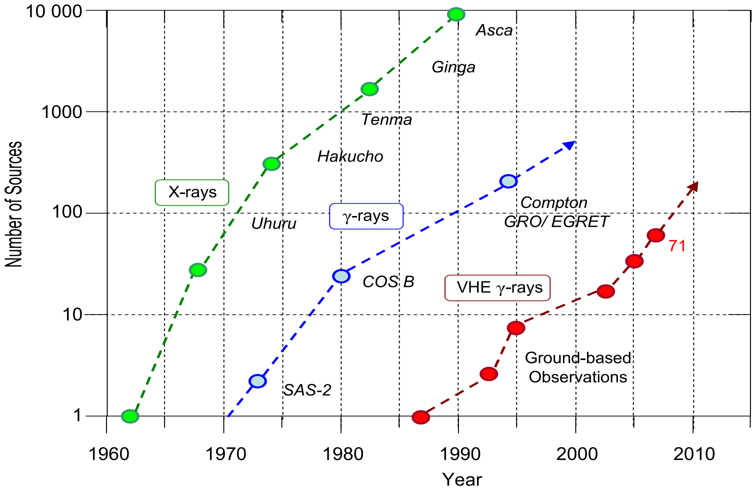

Figure 2.5: The “Kifune” plot updated to 2007.

2.4 The case of RX J1713.7-3946

The case of the shell-type supernova remnant RX J1713.7-3946 is the perfect example of how gamma-ray astronomy can shed light on the cosmic rays puzzle. This SNR was detected in VHE in 2004 by the H.E.S.S. Cherenkov array (Aharonian et al., 2004) . The source was spatially resolved (see figure 2.6) allowing for the first time to establish a direct connection between SNRs and CR acceleration sites. According to M. Longair these images will go straight into all the text-books.

The overall spectral index of the remnant turned out to be $\Gamma = 2.13 \pm 0.03$, value very close to the to spectral steepness expected from the Fermi acceleration at strong shocks. The morphology of the TeV γ-ray image agrees well with the emissions in the 1-3 keV

X-ray regime.

The results are compatible with a nonlinear kinetic theory of cosmic-ray acceleration in supernova remnants and imply that this supernova remnant is an effective source of nuclear cosmic rays, where about 10% of the mechanical explosion energy are converted into nuclear cosmic rays (Blümer et al., 2009). The previous statement is valid from a general point of view but there is a large variety in the characteristics of the specific astrophysical cases. For certain SNRs there are indication that the efficiency in the acceleration can be much higher than 10%, up to reach ∼50%.

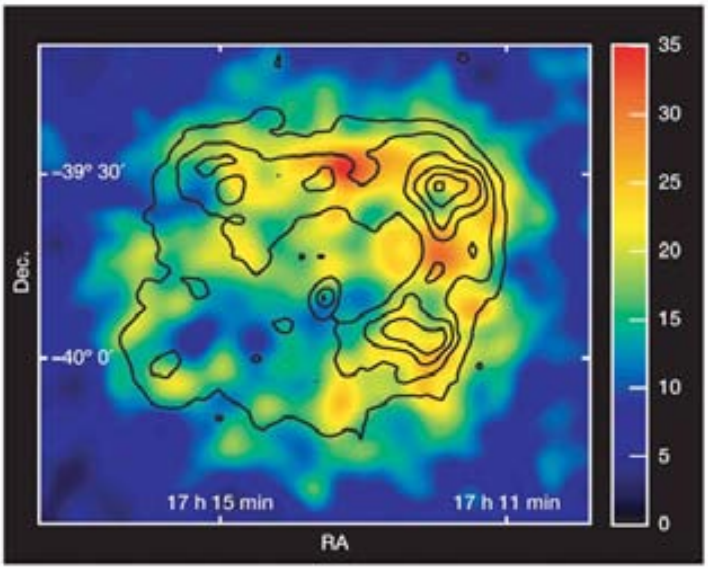

Figure 2.6: Spatially resolved γ-ray image of the SNR RX J1713.7-3946. From (Aharonian et al., 2004).

Chapter 3

Active Galactic Nuclei

What is an AGN?

3.1 AGNs

AGNs are special laboratories for extreme physics that we would like to understand. They are also our principal probes of the universe on large scales, so understanding them is essential to studying the formation and evolution of the universe (Urry and Padovani, 1995).

The acronym AGN stands for *Active Galactic Nucleus*. The visually most striking property of a galaxy hosting an AGN is the brightness of its nucleus region. In most of the cases the luminosity of the core competes, and often exceeds, the brightness of the rest of the host galaxy, in some cases apparently as much as 10^4 times the luminosity of a typical galaxy, in tiny volumes, probably $\ll 1$ pc (Krolik, 1999). This radiation can emerge over an extraordinarily broad range of frequencies.

The presence of a black hole at the center of an AGN was long suspected. Most experts in the field nowadays believe that the power for AGNs comes from *accretion* onto black holes. Namely a SuperMassive Black Hole (SMBH) with a mass from millions to billions of solar masses accretes matter and powers *jets* (collimated highly relativistic outflows) (Hinton and Hofmann, 2009). The accretion mechanism is widely studied and at the same time widely unknown. Many fundamental aspects of AGN jets and of particle acceleration in these jets are poorly understood, including the mechanisms that launch the jets, and their composition.

The ultimate goal is to discover which are the most relevant characteristics of AGNs (black hole mass and spin, accretion rate, etc.) and how they govern the production of radiation, the accretion of matter and the generation of jets. If one wants to summarize the whole puzzle in AGN studies in a single problem to be solved it would be to understand the mechanism(s) of their energy output.

3.1.1 What exactly are we talking about?

Although the black hole model has achieved widespread acceptance and an unified model exists (section 3.1.3), an AGN can be defined operationally i.e. through the list of the observable phenomena associated with them. It turns out that AGNs can be identified by several characteristics (not necessarily the same for all the objects). Following chapter 1 of J. Krolik's book "Active Galactic Nuclei: from the central black hole to the galactic

Popularity of the AGN characteristics	
Very small angular size	Many
High luminosity	Many
Broad band continuum	Most
Strong emission lines	Most
Variability	Most
Weakly polarized	Most
Radio emission	Minority
Strongly variable and polarized	Small minority

Table 3.1: List of the observational characteristics of an AGN and their popularity. Adapted from Krolik (1999).

environment" (Krolik, 1999) we will proceed now to list the principal characteristics which identify an AGN, keeping in mind that not all features are necessarily present in an a specific object (see also table 3.1). Each of these features is hardly ever seen in normal galaxies.

very small angular size When the AGN is close enough, such that a host galaxy of reasonable surface brightness can be seen, in optical images the nucleus often appears to be a bright point whose flux can often rival, or even exceed, the flux from the rest of the host galaxy. The picture we see depends strongly on wavelength. For example many AGNs have a much greater ratio of X-ray luminosity to optical than does any normal galaxy.

high luminosity The luminosity of an AGN can vary from $\sim 10^{42}$ to $\sim 10^{48}$ erg $\cdot$ s^{-1}. To put this in perspective, the characteristic luminosity of the field galaxy distribution (L_*) is 10^{44} erg $\cdot$ s^{-1}. In other words we see AGNs whose power output ranges from as little as 1% of a typical galaxy to $\sim 10^4$ times larger. A possible caveat that has to be taken into account is the possible intrinsic absorption. In many AGNs the active nucleus is obscured by extremely thick dust extinction which can grossly change its true luminosity estimation. It is important to distinguish between the luminosity inferred assuming isotropic radiation and the true luminosity.

broad-band continuum emission We can try do define "broad-band" continuum radiation in contrast to the standard galaxy spectrum. Since in first approximation galaxy are piles of stars we can expect a black body spectrum which is the sum of many black body spectra spanning through the typical surface temperatures of the stars. Since the temperature range is only a factor ten wide, a typical galaxy emits almost all its power within no more than one decade of frequency. An AGN has generally a spectrum which is flat from the mid-infrared to the hardest X-ray observed up to the point that it is inappropriate to speak of any frequency band dominating the output[1].

emission lines AGN emission lines are often very prominent and this makes AGN spectra stand in great contrast to the spectra of most stars and galaxies. There is an

---

[1] Exception to this general rules are the objects belonging to the 'blazar' sub-class (see section 3.2) which we will describe in detail later on, since they are very interesting sources for VHE astronomy.

interesting split in the line width distribution. In some objects, many of the lines have broad wings extending out from the line center, whereas in others the line are very sharp (a factor hundred sharper).

variability Most of the AGNs can be seen to vary in optical band by 10% only over a human life timescale but variability tends to increases at higher frequencies (shorter timescale). A small subset of AGNs, the blazars (section 3.2), vary much more strongly, and variability is also very much correlated with three other properties: polarization, compact radio structure and high-energy χ-ray emission.

polarization Most AGNs are generally weakly polarized, but just enough more strongly than standard galaxies as to be statistically distinguishable from them. The polarization level depends significantly on the frequency.

radio emission Some of the earliest radio astronomical observations discovered that many bright radio sources come in the form of double lobes with a galaxy located halfway between them. Many of the known AGNs are strong radio emitters and given the high resolution of radio instruments the phenomenology of that emission is widely studied. M 87 is a very interesting example of radio galaxy detected also at TeV energies (see chapter 8).

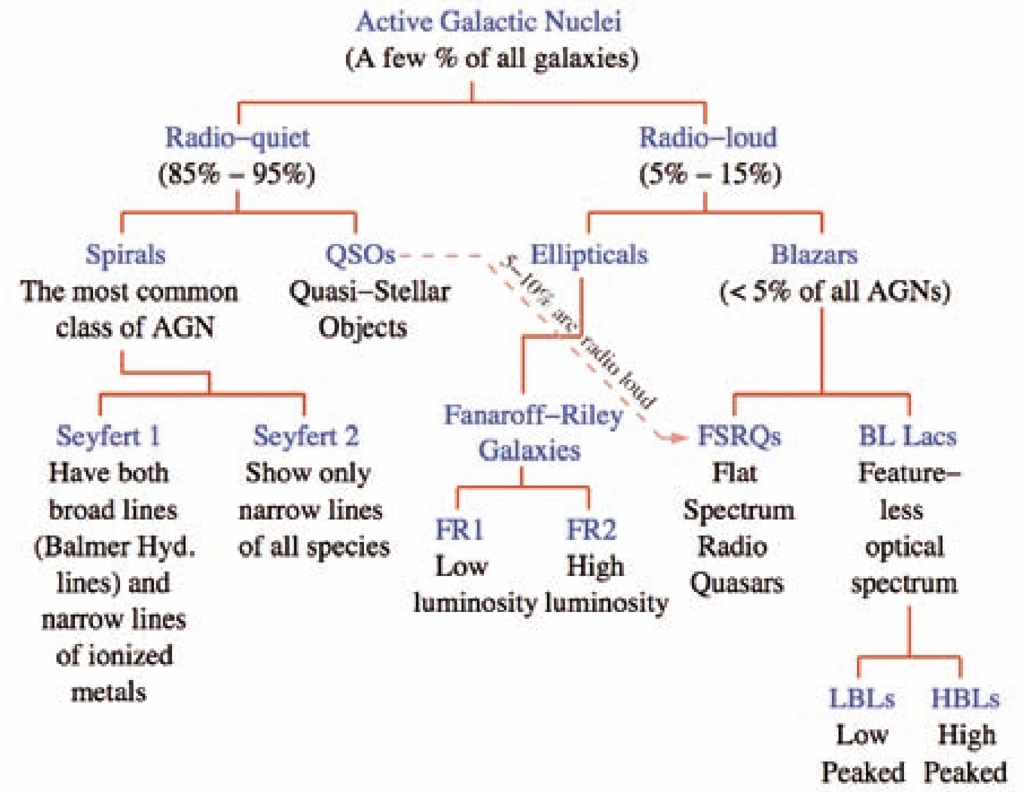

Figure 3.1: AGN classification scheme. Figure from Errando (2009), based on Urry and Padovani (1995).

3.1.2 Classification

Given the numerous different characteristics that an active galactic nucleus may have, the population of AGNs has been divided into several sub groups, each one collecting some of their possible features. The full complement of active galactic nuclei constitutes a zoo of different names, detection criteria, and spectral, polarization, and variability characteristics (Urry and Padovani, 1995).
Even if their spectra span basically over all the frequencies, the optical and radio observations of AGNs originate their classification (figure 3.1).

Roughly 5%–15% of AGNs are radio-loud. These behave exactly like radio-quiet quasars with the addition of emission from a jet. The characteristic of radio loudness itself may be related in some way to the host galaxy type or to BH spin which is thought to enable the formation of powerful relativistic jets. The radio-loud and radio-quiet features split AGNs on the radio side, whereas on the optical and UV front the bright (or weak) continuum emission together with the presence of broad (or narrow) emission lines is used as classification criteria. The AGNs with low optical flux are called *Seyfert galaxy* and *radio galaxy*, whereas the ones powerful in the optical band are classified as *quasars* or *BL Lacs* (grouped together with the name *blazars*). Please refer to figure 3.1 for a more detailed nomenclature.

BL Lac objects are characterized by very fast variability, unusually high and variable polarization, high brightness temperatures and superluminal motion of compact radio cores. This class of objects is particularly relevant for γ-ray astronomy (especially at the higher energies). In the VHE band, which is the domain of Cherenkov telescopes like MAGIC, they constitute the great majority of the detected extragalactic objects[2] (see chapter 2).

3.1.3 Unified scheme

The current picture of the physical structure of an AGN, known as the *unified model*, is illustrated in the two panels of figure 3.2. At the center is a SMBH whose gravitational potential is the ultimate source of the AGN luminosity. MHD (*Magnetic Hydro Dynamic*) processes govern the dissipation of energy from the accreting material which surrounds the BH in a flat accretion disk particularly bright at UV frequencies but also radiating from optical to X-ray. Strong optical and ultraviolet emission lines are produced in clouds of gas moving rapidly in the potential of the black hole. This region is know as BLR, acronym of *Broad Line Region*, given the widening of the emission lines because of the Doppler broadening. The optical and ultraviolet radiation is obscured along some lines of sight by a torus of dust well outside the accretion disk and broad-line region. Beyond the torus, slower-moving clouds of gas produce narrower emission lines, defining the so-called NLR (*Narrow Line Region*). Outflows of energetic particles occur along the poles of the disk or torus, escaping and forming collimated radio-emitting jets, and sometimes giant radio sources. The plasma in the jets streams outward at very high velocity, beaming radiation relativistically in the forward direction.

The unified model arose from the several evidences of anisotropy in the AGN emission, which suggested that a single type of object, viewed from different angles, might give rise to the observed variety of observational properties of AGNs. Being more specific we

---

[2] The most important and bright ones are Mrk 421, Mrk 501 on the boreal hemisphere and PKS 2155-304 on the austral hemisphere.

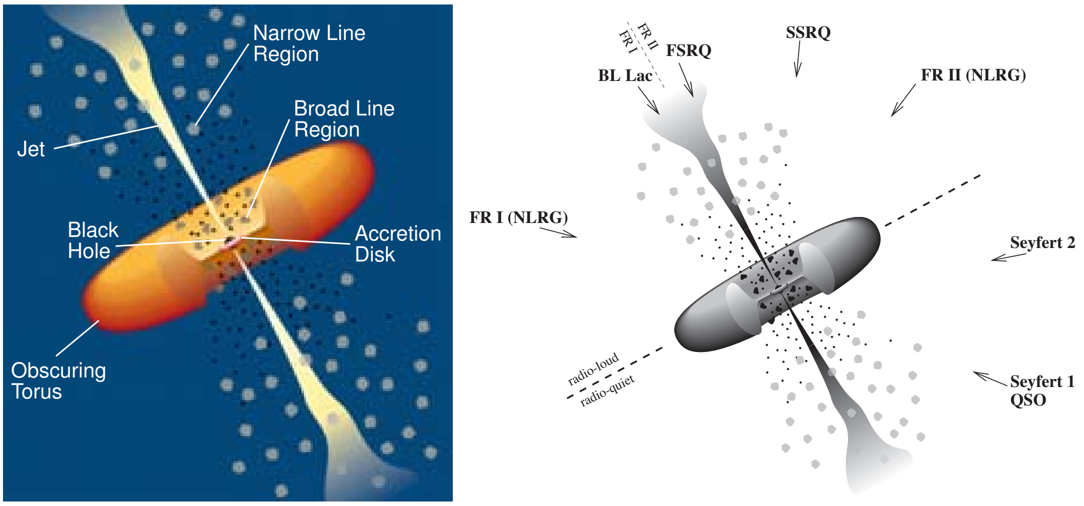

Figure 3.2: Schematic view of an AGN according to the unified model (adapted from Urry and Padovani (1995)). On the left panel the different elements and zones of the AGN and on the right panel the classification depending on the viewing angle with respect to the observer's line of sight.

recognize two kinds of anisotropy:

- Anisotropic radiation from obscuration (torus)
- Anisotropic radiation from relativistic beaming (jets)

The most direct evidence of circumnuclear obscuration comes from spectropolarimetry measurements, which shows linear polarization consistent with a thick wall of gas whose axis coincide with the radio jet axis. Moreover, spectroscopical studies reveal that deeper core observations are possible (Urry and Padovani, 1995) in the infrared band for AGNs showing broad emission lines in their spectra (obscured in optical frequencies). This is consistent with the smaller optical depth for long wavelengths.

Concerning the evidences of relativistic beaming, radio measurements plays an important role. Beside the apparent superluminal motion, which by itself reveals the existence of relativistically moving material, also the asymmetry of the giant radio lobes (symmetry of the two jets in the reference system is reasonable) supports the presence of relativistic jets.

Relativistic beaming is also supported by a very nice model independent argument which is the rapid variability at high energy (γ-rays). It sets in fact a maximum size for the emitting region and in order for gamma rays to escape the source, the optical depth for pair production $\tau_{\gamma\gamma}$ is incompatible with the observed luminosity (Urry and Padovani, 1995). The optical depth to pair production must be of the order of unity or less, which in term of *compactness*[3] translates in values of 40 or less. The experimental measurements reveals values within 5000–15,000 so that the true gamma ray luminosity in the rest frame of the emitting material must be much smaller than observed, and the true dimension much larger. Again, the relativistic beaming corrections elegantly solve the problem.

The asymmetry is compatible to be originated by a line of sight close to the jet axis of the AGN, leading to a relativistic boosting of the forward jet only. Now, different *orientations* of the AGN axis with respect to the observer would explain easily the observed

---

[3] A convenient dimensionless parameter that represents source luminosity divided by dimension.

“zoology” of AGNs which is also consistent with the evidences of anisotropy previously discussed. In other word it is not necessary to invoke different type of object to explain the various typology of phenomenological evidences. All this leads straightly to an *unified model*[4] (see figure 3.2, right panel).

A fundamental test of the unification model is whether the number statistics of the population agree with the relativistic beaming hypothesis (Urry and Padovani, 1995). The total number of beamed objects must be small compared to the number of parent objects (radio galaxies). Although the analysis of unbiased samples of AGNs is very complicated, the current measurements support this hypothesis (including the new Fermi results).

3.2 Blazars

After we introduced the unified model scheme we can characterized *blazars* using their observational characteristics (section 3.1.2: fast variability, none or dimmed emission lines, γ-ray emission, etc.) or define them as the AGNs with one of their jets pointing straight to the observer. In other words the ‘line of sight’ is very well aligned with the jets direction (or alternatively, is orthogonal to the accretion disk plane).
Blazars are divided in two subclasses: Flat Spectrum Radio Quasar (FSRQ) and BL Lac objects[5] BL Lac objects further are classified as HBL, IBL or LBL (where the first letter stands for *High-*, *Intermediate-* and *Low*-peaked) depending on the position of the lower energy hump in the SED spectra (see also section 3.2.1). These objects are in fact characterized by a two humped structure in their spectra, the lowest one typically located in the infrared to X-ray region.
It is widely believed that the relativistic jet is the key element of blazar emission. To explain the observed broad-band spectrum most model assumes that a relativistic population of particles (electrons, protons or both) is accelerated within the jet. The relativistic beaming plays a very important role in the emission properties of these objects.

3.2.1 The ‘blazar sequence’

In 1998 Fossati et al. (1998) published a study about the properties of the SED of a large sample of blazars. As we mentioned already the SED of a blazar (both FSRQ and BL Lac) is characterized by a double-humped shape. What they found about this structure is summarized in the three following points:

- The first peak occurs in different frequency ranges, depending on the sample and luminosity class of the blazar, with most luminous sources peaking at lower frequencies

- The peak frequency of the high-energy bump correlates with the peak frequency of the low-energy one

- The luminosity ratio between the high and the low energy components increases with bolometric luminosity

---

[4] The unification AGN types is discussed in Urry and Padovani (1995) (radio-loud part) and Antonucci (1993) (radio-quiet part).

[5] The prototype of the AGN variety now called BL Lac object was originally thought to be a variable star in the constellation Lacerta and was therefore given the name “BL Lac”.

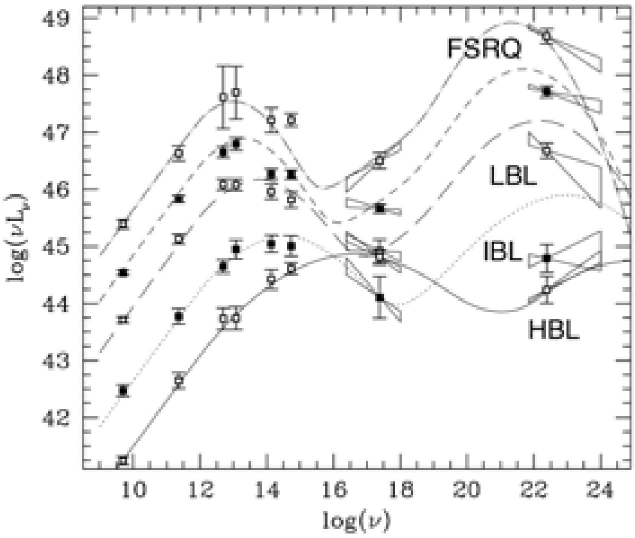

Figure 3.3: Average differential luminosity for a sample of 126 blazars, showing the transition from FSRQs to LBLs and HBLs (Fossati et al., 1998). The lines show a simple leptonic model proposed by Ghisellini et al. (1998).

This is what is known under the name of *blazar sequence* (in its simplest formulation) and that is visually described in figure 3.3. The classification LBL and HBL mentioned in the previous section is also introduced in Fossati et al. (1998), suggesting a continuous spectral sequence within the blazar family rather than separate spectral classes. LBLs are more luminous and have their first peak in the infrared–optical band and the second one at keV–MeV energies. IBLs lie in between the two. In LBLs the high energy component dominates over the low energy one. On the other hand, in HBLs the first peak is found at UV–X-ray frequencies and dominates over the high-energy component, which peaks at GeV–TeV energies.
The popularity of this scheme lies in the fact that a single parameter, related to the blazar luminosity, would govern the physical properties and radiation mechanisms in the relativistic jet present in BL Lac objects as well as in FSRQs.

Caveats of this scheme might reside on the very difficult task of obtaining unbiased samples of blazars and to consider all the possible hidden selection effects which might result in the observed properties and correlations. The blazar sequence was criticized by several authors in the last years. Survey and catalogs are unavoidably "frequency selected" and instrument-sensitivity dependent. For example, according to Padovani (2007), the luminosity to synchrotron peak frequency correlation does not hold after adding to the AGN sample new surveys previously not considered. Another example is given by Nieppola et al. (2008) who suggest that the synchrotron luminosities have to be corrected for the variable Doppler boosting across the peak frequency range. Using the Doppler-corrected values, the anti-correlation between luminosity and synchrotron peak frequency disappears.

The very recent γ-ray data collected by the Fermi telescope may shed more light on the blazar sequence issue since nearly hundred bright blazar have been already detected by Fermi in the first 3 months. In Ghisellini et al. (2009) and Ghisellini (2010) is discussed how this data can be used to investigate the blazar sequence. Given the γ-ray energy

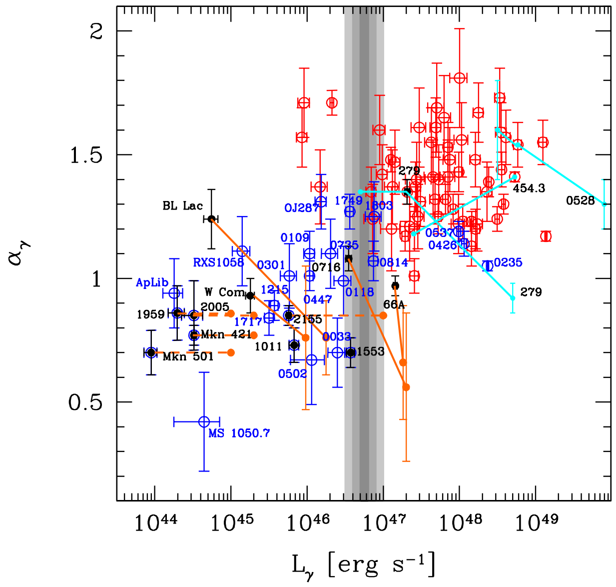

Figure 3.4: The γ-ray spectral index as function of the γ-ray luminosity of the blazars detected by Fermi during the first 3 months. Blue and red points are BL Lacs and FSRQs, respectively. Black symbols correspond to sources already detected in the TeV band (they are all BL Lacs but 3C 279). FSRQs are steeper and more luminous than BL Lacs (Ghisellini et al., 2009).

range where Fermi is sensitive, a simple consequence of the blazar sequence idea is that FSRQs should have a steeper γ-ray spectra slope. This turns out to be true using the new Fermi data (see figure 3.4).

3.3 TeV emitters AGNs

The first two extragalactic objects detected in the VHE γ-ray band were the two blazars Mrk 421 and Mrk 501 (described in section 7.1.3 and 7.1.4). As can be seen in table 2.1 the number of AGNs detected by Cherenkov telescopes increased very fast in the past six years, mainly thanks to the advent of the MAGIC, H.E.S.S. and (more recently) VERITAS detectors.

The large majority of the established TeV-emitting AGNs belongs to the blazar class, with the subclass of HBL (high peaked, BL Lacs) playing the most important role[6]. The IBL W Comae and the LBL BL Lac (the source itself, not the class) represent the remaining minority. The non-blazar objects are the distant flat spectrum radio quasar 3C 279, the radio-galaxies M 87 and Centaurus A and the starburst galaxies NGC 253 and M 82. On figure 3.5 an updated map of the extragalactic sources is provided.

This distribution in the type of AGNs is very likely (at least partially) biased by the observing criteria of the Cherenkov telescopes. The choice of the best AGN candidates was inspired during the first MAGIC observation cycles by their 'position' in the blazar

---

[6] Please see Hinton and Hofmann (2009) for a detailed compendium of the sources and http://www.mppmu.mpg.de/˜rwagner/sources/ or http://tevcat.uchicago.edu/ for updated detection references.

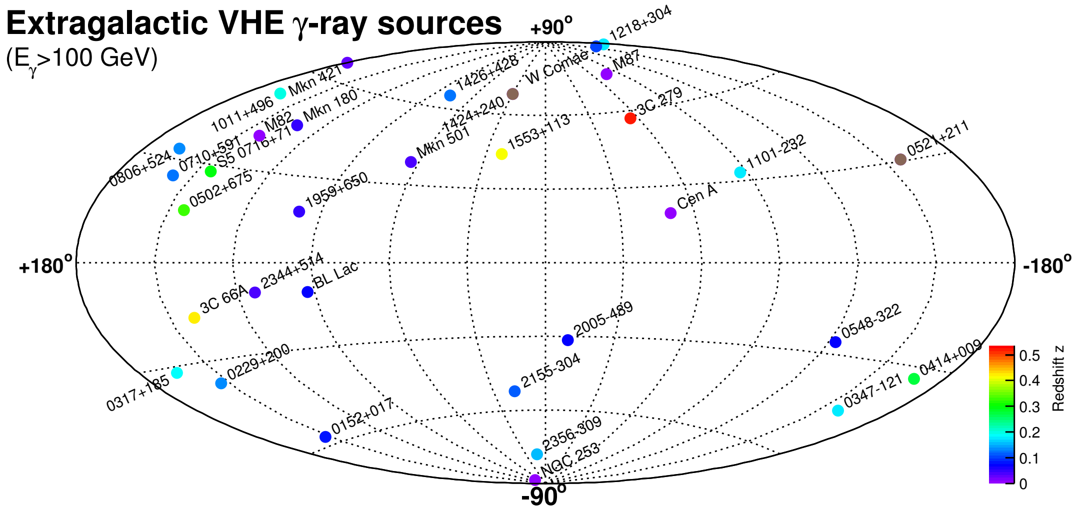

2009-11-18 - Up-to-date plot available at http://www.mppmu.mpg.de/~rwagner/sources/

Figure 3.5: Sky map of TeV emitters with extragalactic association. The color code refers to the redshift of the sources.

sequence Costamante and Ghisellini (2002), which clearly favor HBL as possible TeV emitters.

Despite the vastly larger distances, some AGNs, at the peak of their flares, outshine the strongest galactic gamma-ray sources by a factor of 10 or more. The redshift of the sources is very important in the TeV regime because of the intergalactic γ-ray absorption originated by the EBL (see section 2.2.1). The farthest object detected up to now is the FSRQ 3C 279 (Albert et al., 2008*c*) at a redshift of $z = 0.536$, which extended the transparency gamma-ray window to relatively high redshifts.
Observed spectral indices are in general rather steep (~ 2.5, power law fits), with few exceptions in case of strong flares of the sources when the high energy peak of the spectrum is supposed to move toward higher energies and thus leading to a flattening of the spectral slope (Γ up to ~ 2 and even less have been observed). Generally speaking the spectral indices tend to increase with the source distance, at least partially because of the mentioned EBL absorption, but perhaps also related to the fact that a distant AGN must be intrinsically brighter to be detectable (Hinton and Hofmann, 2009).

3.4 Emission models

The blazar emission models focus on how are produced the gamma rays that we detect, whereas the underlying mechanism that accelerate the primary particles are typically treated separately. Emission models generally divide in two big categories: *leptonic* and *hadronic*, depending on the nature of the particles that are accelerated (electrons and positrons or protons respectively[7]). At least four different channels have been proposed: IC scattering of electrons, interaction of protons with magnetic fields (synchrotron radiation), photon fields (photo-meson processes) and matter (inelastic $p - p$ collisions) (Aharonian, 2004). See sections 3.4.3 and 3.4.4.

---

[7] In the following, with the term ‘electrons’ we will generally refer to both e^+ and e^-. Hadronic models also involve electrons, and not exclusively hadrons.

Nevertheless, phenomenological models frequently leave open the question of how the particles are accelerated; possibilities include shock-wave acceleration in MHD turbulence in the jet, centrifugal acceleration of particles along rotating magnetic field lines near the base of the jet, or shear (Hinton and Hofmann, 2009).

Before going a little bit in detail about the leptonic and hadronic scenarios, let's clarify two short points which are important from the observational point of view. They represent the two main handles which allow us to test a theoretical model and in turn, to validate or discard a certain model (or to constrain its parameters).

3.4.1 Spectral Energy Distribution (SED)

In most fields of astronomy, the property of light that is measured is the specific flux (F_ν), the rate at which energy arrives per unit of area per unit of frequency ν. The standard unit per F_ν is the Jansky, 10^{-23} erg cm^{-2} s^{-1} Hz^{-1}. In the high energy (i.e. X-ray and γ-ray) astronomy, where photon counting devices prevail, the customary measured quantity is N_ϵ $(= F_\nu/(h\epsilon))$, the rate at which photons arrive per unit of area per unit of energy ϵ. However, when we speak of a "band" of the electromagnetic spectrum, whether it is radio, infrared, visible, or X-ray, we generally mean a span in the logarithmic of the wavelength. Therefore, for describing which band is most important in terms of energetics, the most convenient quantity is $\nu F_\nu = dF/d\,log(\nu)$, the energy flux per logarithmic bandwidth, a.k.a. SED.

3.4.2 Correlations

In order to understand the physical process at work in an AGN it is useful to observe the activity of TeV blazars simultaneously in different energy ranges. This is usually the case for the X-ray and the γ-ray range since several satellites provide full-sky monitoring data. Also the optical band is usually pretty well covered given the numerous optical telescopes operating around the world (often, also relatively small telescopes can provide valuable data for the study of blazars[8]). Alternatively, pointing observation can be scheduled in all the interesting energy bands (radio, UV, X-rays, etc.) but the time granted depends on the availability of the single instrument.

The activity of the source can be analyzed through a comparison of the different lightcurves. From study of the lightcurves one can extract the typical variability (for example through Vaughan et al. (2003)) at different energy ranges, or possible correlations in the flux variation within the different frequency bands (Edelson and Krolik, 1988). Tools for the study of the correlation are shortly describe in section 7.6.

Focusing on the X-ray/γ-ray bands sometimes a surprisingly precise correlation between the evolution of the two emissions is found. This provides an excellent opportunity to test theoretical models for very high energy emission of blazars (Katarzyński and Walczewska, 2010), since the different emission models provide different prediction regarding the relationship between the two bands.

---

[8] The finnish KVA optical telescope of 35 cm diameter has an ongoing long-term blazar monitoring program. The telescope is managed by the Tuorla University group whose many members are also part of the MAGIC collaboration. A ToO (Target of Opportunity) program based on optical trigger for γ-ray observation turned out to be particularly successful in the last years.

3.4.3 Leptonic models

The VHE γ-ray emission is thought to arise inside the jet being the relativistic beaming a key issue to explain the short timescale variability and the high luminosity at high energy.

In leptonic emission models, radio to X-ray emission is produced by synchrotron radiation from the population of non-thermal electrons, and VHE gamma rays can be produced if these electrons upscatter low energy photons through the inverse Compton process. Several models of different complexity are proposed in the literature for TeV blazars. The basic idea of all of them is a 'Synchrotron Self-Compton' (SSC) emission scenario. The simplest model (*one-zone SSC*) involves a single zone and a single population of relativistic electrons emitting synchrotron radiation from radio to X-rays and inverse Compton radiation from X-rays to γ-rays (Tavecchio et al., 1998). The seed photons for the inverse Compton process are the synchrotron photons themselves. The homogeneous SSC model assumes the radiation is produced in a single zone of the jet, a sphere of radius R (also called "blob"), relativistically moving at a small angle θ to the observer's line of sight. The observed radiation will be strongly affected by relativistic effects[9]. The key parameter is the Doppler factor $\delta = [\Gamma(1 - \beta \cdot \cos\theta)]^{-1}$, where Γ is the bulk Lorentz factor and $\beta = v/c$. Accordingly to this model, since are the same electrons to produce both low and high energy emission, the index of the two humps in the SED can be described by the same indexes α_1 and α_2.
The model can be completely specify by 7 parameters:

B	the magnetic field intensity
R	the radius of the emitting region
δ	the Doppler factor
n_1	the index of the relativistic electron spectrum (lower energy side)
n_1	the index of the relativistic electron spectrum (higher energy side)
γ_b	the lorentz factor of the electrons at the break
K	the electron density paramter

These models can be tested on the available data on the spectral energy distribution. The SED can be used to derive 6 + 1 "observable" quantities of particular relevance for the described model:

α_1	the index of rising part of the SED bumps
α_2	the index of falling part of the SED bumps
ν_s	the frequency of the synchrotron peak
ν_c	the frequency of the inverse Compton peak
$L_s(\nu_s)$	the luminosity of the synchrotron peak
$L_c(\nu_c)$	the luminosity of the inverse Compton peak
t_{var}	the minimum timescale of the variation (related to R by: $R \leq c t_{var} \delta$)

Moreover, one can obtain lower limit on the value of the Doppler factor from the required transparency of the source to γ rays[10] and from the radiative interpretation of

---

[9] When an emitting plasma has bulk relativistic motion relative to a fixed observer, its emission is beamed in the forward direction (in the fixed frame), a direct consequence of the transformations of angles in special relativity. An observer located in or near the path of this plasma sees much more intense emission (Urry and Padovani, 1995).

[10] Gamma rays can be internally absorbed because of the interaction (pair production) with the dense radiation field into (or in the vicinity) the compact γ-ray production regions (e.g. with the radiation field emitted in the narrow-band region: Aharonian et al. (2008*b*)). See also sections 2.2 and 2.2.1.

the time lags in the light-curves at different energies. If during a flare the soft photons lag behind the harder ones, the simplest explanation is through the hypothesis of the time necessary for freshly injected high-energy electrons to cool.

More evolved models include external populations of low energy photons that are upscattered through inverse Compton scattering. These are called 'External Compton' (EC) models. The populations of low energy photons considered in these models are photons emitted by the accretion disk, in the broad-line region, or even low energy photons escaping from the jet which are reflected by ambient dust and enter again into the jet with angles favoring their IC scattering (so-called *mirror* models). Other models foresee multiple emitting regions (*multiple-zone*) moving across the jet.

3.4.4 Hadronic models

Also in the case of hadronic models the VHE γ-ray emission is thought to arise inside the jet being the same arguments of short time variability and γ-ray high luminosity still valid.

Since the fact that particle acceleration is taking place in the relativistic jets of AGNs (synchrotron observation), it is a small speculative step to argue that this acceleration mechanism not only concerns electrons but protons (and nuclei) as well (Mannheim, 1993).

The protons with maximum Lorentz factor in the range 10^9–10^{11} GeV generate hard photons with energies from keV to TeV via pion and pair photoproduction and subsequent synchrotron cascade reprocessing. High energy radiation can also be obtained by protons through direct synchrotron radiation, but this process is know to be very inefficient. For proton energies larger than 10^8–10^{10} GeV photo-meson production:

$$p + \gamma \rightarrow p + k\pi$$

and nuclear collisions:

$$p + p \rightarrow \pi + X$$

are the processes invoked to explain gamma-ray production in blazars, by the so-called proton-induced cascade model (Mannheim, 1993). In that model, the target radiation for photomeson production is dominated by near/mid-infrared radiation. In blazars, such radiation can be emitted by hot dust at distances of $\sim$ 1–10 pc from the central source and/or by synchrotron radiation due to relativistic electrons in the jet. The main outputs of the photo-meson processes are pions. Pions take about 1/3 of the proton energy and convert it to photons, neutrinos, and, through muons, to electrons and positrons. The photons injected by neutral pions immediately interact with low energy photons producing electron-positron pairs. Most of this radiation is so energetic that it produces two more generations of photons and pairs.

The cascade emission ranges from X-rays to gamma rays competing with synchrotron-self-Compton emission, leading to the end to a more 'flat' IC peak with respect to leptonic models. TeV emission is expected to correlate with the with high state of the entire continuum flux. Further consequences are a diffuse flux of neutrinos maybe observable with the coming online of km^3 neutrino detectors. A neutrinos detection associated with a γ-ray flare would clearly favor hadronic models for blazars.

3.5 AGNs as UHECR accelerators

In chapter 1 we briefly discuss the problem of the cosmic-rays origin, in particular of the highest energy component. Active galaxies are one of the candidates for the acceleration of CRs of extreme energy ($> 10^{19}$ eV). The naïve argument 'if electrons are accelerated there at very high energies (as we conclude from observations), why shouldn't it be the case also for protons?' is somehow hard to weaken. In fact, although most of the detected VHE gamma ray emission from blazars can be explained by leptonic models, this does not mean that protons can not be accelerated as well. The universe is full of protons, if they are not accelerated together with electrons there should be a reason (even if the extremely high energies we are talking about have to be kept in mind).

The correlation of the arrival direction of UHE CRs with active galaxies closer than 100 Mpc reported by the PAO collaboration (Abraham et al. (2007), Abraham et al. (2009)) strengths this hypothesis and makes AGNs even more interesting than from the simple astrophysical point of view[11]. For example the radio galaxy Centaurus A is considered a promising UHECR source candidate (see also section 1.5).

The observation of variable, non-thermal emission form AGNs reveals that efficient particle acceleration somehow do occur since all the general processes which bring photons to γ-energies require accelerated charged particles. While efficient electron acceleration is in most cases strongly limited by radiative losses, this is much less the case for protons and heavier nuclei, suggesting that these particles could reach much higher energy via the same acceleration processes.

Particle acceleration might occur in the vicinity of the black hole, in the inner region of the jets or in the lobes of radio galaxies. In the vicinity of the BH rotating magnetic fields, either driven by the disk or the black hole itself, would accelerate the energetic charged particles, whereas in the turbulent jet environment and in the lobes the acceleration is thought to be originated by Fermi-type stochastic processes (Rieger (2009), Hardcastle (2010)). Possible mechanisms which could provide efficient UHECR acceleration are (Rieger, 2009):

direct electrostatic field acceleration If the central BH is rotating embedded in a magnetic field it will induce an electric field which behaves as an unipolar inductor. If a charged particle (with charge Z) can fully tap this potential, particle acceleration to ultra high energies might become possible. For the specific case of Cen A it would result in:

$$E = Z \cdot e \cdot \Phi \sim 3 \times 10^{19} Z\ eV$$

where $\Phi \propto (m_{BH}, B, a_{Kerr})$.

centrifugal acceleration Particle acceleration due to inertial effects in the vicinity of the BH, like centrifugal acceleration along rotating magnetic field are possible if the associated acceleration timescale remains larger than the inverse of the relativistic gyro-frequency.

diffuse shock acceleration (Fermi-I and Fermi-II) These mechanisms have been discussed in 1.3.1. They are based on stochastic processes in the turbulent AGN environment (e.g. in the jets or lobes). Particle acceleration occurs as a consequence of multiple scattering of moving magnetic structures, with a small energy gain in

---

[11] Firmly establish a correlation between AGNs and UHECRs would also leave the door open to hadronic models for the explanation of the blazar γ-ray emission.

each ‘scattering’ event. Fermi-II involve the presence of a ‘shock’ through which the particles could pass back and forth several times, with an average energy gain proportional to $(v/c)^2$. In the Fermi-I mechanism, the energy gain is instead $\propto v/c$ (see section 2.2).

shear acceleration This mechanism would work in the jet environment. The flow is supposed to have a smoothly changing velocity profile in the direction perpendicular to the jet axis, so that the scatterers embedded on it may be able to go through the flow difference dv and thereby get accelerated.

It should be noted that none of the above mechanisms are mutually exclusive. In fact is seems likely that, in a source like Cen A, hadronic CR can be accelerated in the nucleus and the kpc-scale jet as well as in the giant lobes.

Finally, as mentioned in section 3.4, we note that hadronic emission models for blazars foresee the emission of neutrinos together with γ-rays and charged particles. This means that neutrino telescopes might possibly have a handle to solve this puzzle.

Chapter 4

Detection of γ-rays

How do we detect γ-rays?

4.1 Detection of γ-rays

The techniques for the detection of gamma can be divided in two big branches: *direct* and *indirect*. The distinguish criterion is the containment or not of the primary γ-ray. Given the fact that the earth's atmosphere is not transparent to very energetic photons, direct detection is only possible through space-based experiments, i.e. using detectors on board of satellites. The biggest limitation of this direct approach is the size of the detector, which can not be very large due to the limitations on weight and size of the payloads

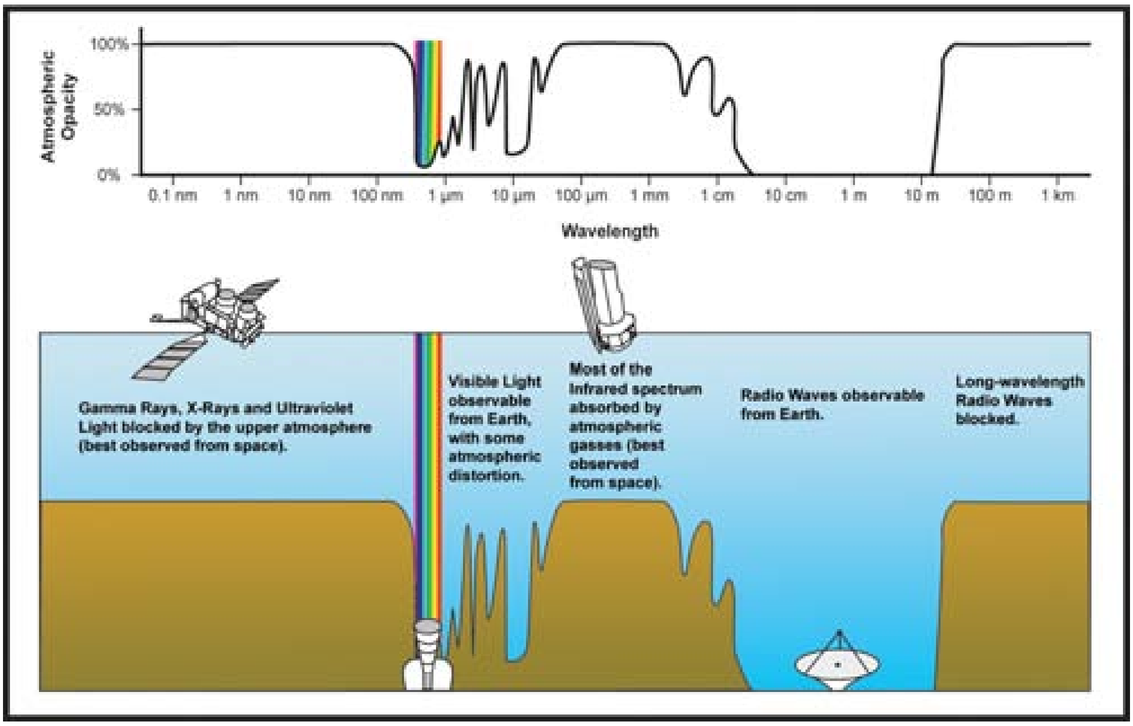

Figure 4.1: The atmospheric transparencies for all the frequencies of the electromagnetic spectrum.

that can be sent to space[1]. On the other hand, modern gamma-ray space telescopes have the advantage of a very good background rejection, spatial resolution and energy reconstruction. All these concepts will be more clear once discussed in chapter 6.

Indirect detection is instead performed through ground-based experiments. The atmosphere of the earth plays in this case a very important role. It can be almost considered as part of the detectors, since it is the medium where the primary cosmic particle (gamma ray or cosmic ray in general) interacts and develops a shower of secondary particles (section 4.2), which provide information about the primary. In the language of high energy particle physics, the earth's atmosphere can be considered a very deep electromagnetic calorimeter with approximately 30 radiation lengths of material. The actual detection of the secondary particles is not even needed for certain techniques, because in virtue of their ultra-relativistic speed, the secondary particles produce visible light through the Cherenkov effect (section 4.2.1), and these photons are free to propagate through the atmosphere and reach the photosensors located on the surface of the earth. In the last 40 years several detection techniques have been developed to detect CR at ground level, we just want to mention below the most relevant ones:

- Detection of secondary particles (used by experiments like AGASA, AUGER, HEGRA or KASKADE)
- Detection of the Cherenkov light produced by the secondary particles (used by experiments like Whipple, HEGRA, H.E.S.S., MAGIC and VERITAS)
- Detection of the fluorescence light produced by the secondary particles (used by experiments like AUGER or HiRes)

References to mentioned experiments are provided below[2]. On this thesis we will focus on the technique mentioned on the second point of the list. This detection technique is used by the so-called *Cherenkov telescopes*, and will be described in section 4.3. The MAGIC telescopes, the instruments used for the measurements reported in this work, will be discussed in chapter 5.

4.1.1 Satellite-borne γ-ray detectors

Space-based gamma-ray detectors opened in the past a new observation window in astrophysics (Longair, 1992), and the recent results from the Fermi satellite are focussing even more interest in this region of the electromagnetic spectrum (from MeV to few GeV photon energies) only accessible through satellite experiments.
From the physical point of view, depending on the energy of the primary gamma, three

---

[1] The new Fermi satellite, which represent the largest gamma-ray detector ever sent to space, has a collection area of only 1 square meter (http://www.nasa.gov/mission_pages/GLAST/main/index.html).

[2] Web page references of the experiment mentioned in the text:
AGASA: http://www-akeno.icrr.u-tokyo.ac.jp/AGASA/
AUGER: http://www.auger.org/
KASKADE: http://www-ik.fzk.de/KASCADE_home.html
Whipple: http://veritas.sao.arizona.edu/content/blogsection/6/40/
HEGRA: http://www.mpi-hd.mpg.de/hfm/CT/CT.html
H.E.S.S.: http://www.mpi-hd.mpg.de/hfm/HESS/
MAGIC: http://wwwmagic.mppmu.mpg.de/
VERITAS: http://veritas.sao.arizona.edu/
HiRes: http://www.cosmic-ray.org/

competing processes are relevant for the design of gamma-ray satellites: photo-electric absorption, Compton scattering and pair production. Depending on the target energy, different detection technique have been developed to retrieve information about the primary gamma ray. They are shortly described in the following.

0.1–0.3 MeV In this low energy range the photo-electric absorption is the dominant process. The detectors have characteristics similar to the X-ray telescopes, which use scintillator counters and solid state detectors.

0.5–10 MeV This is a transition region where the Compton scattering is the dominant process but pair production can not be excluded. Typical Compton instruments consist on two separated detector layers where one of the two acts as *converter* and the other as an *absorber*. The incoming direction of the primary gamma that Compton scatter with an electron of the converter, lies in a cone of fixed angle with respect to the coverter plane. If the allowed circular regions are projected simultaneously for all the events, sources can be identified by the clustering of the circles intersections. An example of this type of detector was the COMPTON satellite on board of the Compton Gamma-ray Observatory (CGO).

0.03–300 GeV In this high energy range the electron positron pair production is the dominant interaction. The primary γ-ray is first converted to a e^+e^- pair by a *converter* material. The two leptons are then detected by conventional means in the following layers of the detector. For example, the lucite (a synthetic polymer of methyl methacrylate) Cherenkov chambers were used in the early times, whereas more refined spark chamber arrays have been used later on. The key advantage of this second type of detector is its ability to measure the path of the electrons and positrons, which allows to precisely reconstruct the initial direction of the γ-ray. Examples of this kind of instruments were the OSO-III, SAS-II and COS-B satellites or the more recent EGRET satellite. All the mentioned detectors include all the important features of a successful γ-ray telescope: a "converter" region where the primary gamma interacts, a "tracker" capable to provide also the direction of the particle track and not only the dE/dx loss estimation and finally a "calorimeter" region which brings the electrons and positrons to rest in order to measure their remaining energy.

We know from chapter 1 that non-gamma particles largely dominate the CR flux. Even with instrument with a small FoV the ratio γ-particles/non-γ-particles is very small[3]. A common requirement for all γ-ray satellite detectors is a good *anti-coincidence* system, capable to suppress the cosmic-ray background composed by the non-gamma particles which isotropically hit the detector. Events produced by charged particles crossing the instrument are rejected by a veto in the trigger. The veto is enabled whenever a particle is detected in the two sided of the detector within a time interval compatible with the crossing time of the detector for a single particle. The shield may also unmask the fake track produced by an electron (or positron) entering the detector and mimicking the track produce by a γ-ray. In that case is in fact expected a time compatible signal from the scintillator due to the passage of the charge lepton through the shield of the satellite.

---

[3] In the case of the Fermi (see section 4.1.2) gamma-ray telescope, for every gamma ray that enters the detector it filters out 10^5 to 10^6 cosmic rays.

Finally, is interesting to notice that contrary to all other electromagnetic bands[4], no focusing is possible for γ-rays, which implies that the collection area is equal to the sensitive detector area.

4.1.2 The Fermi γ-ray telescope

Given the novelty and the relevance of this gamma-ray satellite for the astrophysics community a more detailed description of Fermi is provided in this section.

The Fermi gamma-ray space telescope (formerly called 'GLAST') is an international γ-ray space telescope that operates nominally in the photon energy range of 8 keV to greater than 300 GeV. Fermi carries two instruments: the Large Area Telescope (LAT, the primary instrument) and the GLAST Burst Monitor (GBM, the complementary instrument). The Fermi/LAT is an imaging, wide field-of-view, high-energy γ-ray telescope, covering the energy range from below 20 MeV to more than 300 GeV (Atwood et al., 2009). The four subsystems of the LAT instrument are:

tracker It consists of a four-by-four array of tower modules. Each tower module consists of layers of silicon-strip particle tracking detectors interleaved with thin tungsten converter foils. The silicon-strip detectors precisely measure the paths of the electron and positron produced from the initial gamma ray. The pair-conversion signature is also used to help reject the much larger background of cosmic rays. The aspect ratio of the tracker (height/width) is 0.4, allowing a large FoV (2.4 sr).

calorimeter It measures the energy of a particle when it is totally absorbed. The LAT calorimeter is made of a material called cesium iodide that produces flashes of light whose intensity is proportional to the energies of the incoming particle. The calorimeter also helps to reject cosmic rays, since their pattern of energy deposition is different from that of gamma rays.

anticoincidence detector (ACD) It is the first line of defense against cosmic rays. It consists of specially formulated plastic tiles that produce flashes of light when hit by charged-particle cosmic rays. The ACD forms a like a "hat" that fits over the tracker.

data acquisition system (DAQ) It collects information from the tracker, the calorimeter, and the anticoincidence detector and makes the initial distinction between unwanted signals from cosmic rays and real gamma-ray signals. This system also does an on-board search for gamma-ray bursts. The DAQ consists of specialized electronics and microprocessors.

The principal characteristics and performance parameters of LAT are listed in table 4.1.

The GBM consists of 12 detectors made of sodium iodide, for catching X-rays and low-energy gamma rays, and two detectors made of bismuth germanate, for high-energy gamma rays. Together, they cover the energy range between 8 keV to 30 MeV. The low-energy detectors are mounted in four banks consisting of three detectors each. The 12 detectors are oriented in various directions so they face different parts of the sky. The GBM uses the signals from the low-energy detectors to detect burst locations. The two high-energy detectors are positioned on opposite sides of the spacecraft, providing nearly full sky coverage.

---

[4] For X-rays it is possible to change the direction of the photons through the *grazing* reflection on specific materials.

Summary of the Fermi/LAT parameters	
Energy range	20 MeV to 300 GeV
Effective area	9500 cm^2
Energy resolution	from below 6% to 18%
Field of view	2.4 sr

Table 4.1: Summary of the Fermi/LAT parameters and performance (Atwood et al., 2009).

4.2 Air showers

When an energetic cosmic ray arrives on the top of the atmosphere, it starts a so-called Extensive Air Shower (EAS), a cascade of induced secondary particles propagating in the atmosphere. Since the primary ultra relativistic particle is very energetic (at least $\sim$ 100 GeV, well above its rest mass), also the secondary particles have a $\beta \simeq 1$, and they produce light through the Cherenkov effect (see section 4.2.1).

The development of the shower starts in the high atmosphere at around 20 km above the sea level. The primary, which can be a gamma ray, an electron or a cosmic-ray nucleus, interacts with an atmospheric nucleus and generates two or more secondary particles. Depending on the nature of the primary, different secondary particles are produced in a cascading process so that the total number of particles constituting the air shower rises rapidly. In the case of an electromagnetic shower the *Heitler model* (Gaisser, 1990) can be used to describe the development of the cascade. The model assumes that the number of particles goes like 2^n, where n is the number of "generations"7, up to reach the shower maximum. Each particle of the shower (above the Cherenkov threshold) produces light by the Cherenkov effect, since the particle speed is $\simeq c$ while light speed in the air medium is c/n (where n is the index of refraction of the air at the altitude considered). The shower dies when the energy loss of the secondary particles due to ionization is larger than their loss by bremsstrahlung (they start to be absorbed by the atmosphere). The value of the critical energy for the production of Cherenkov light is E$_{thr.}$ = 83 MeV for an $e^{\pm}$ (at sea level).

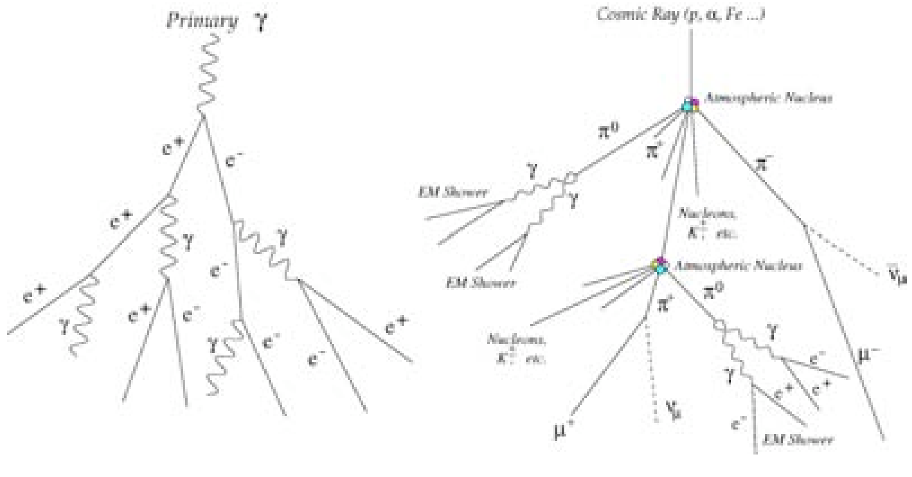

Figure 4.2: Electromagnetic (left) and hadronic (right) air shower development scheme.

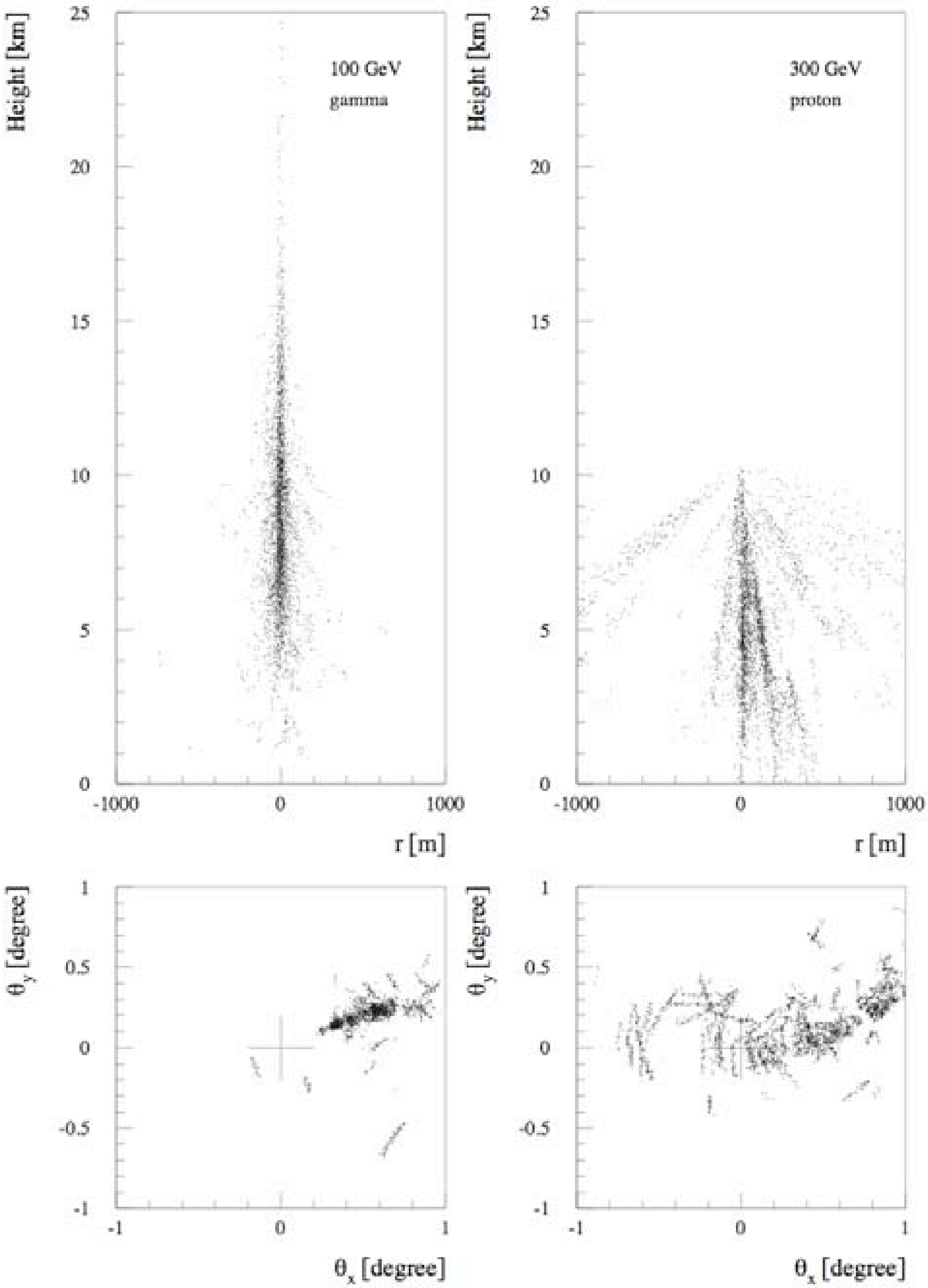

Figure 4.3: Simulations of shower development. For comparison, on the left an electromagnetic shower of E = 100 GeV and on the right a hadronic shower of E = 300 GeV.

Electromagnetic and hadronic air showers have different characteristics due to the different nature of the processes involved in their development. Roughly speaking electromagnetic showers have a more regular development since the main two physical process involved are the pair production and the radiation by bremsstrahlung. The multiple Coulomb scattering of the electrons and positrons determines the lateral shower spread of the shower. The characteristic scattering angle θ_0 is small, being a typical value $\sim 5^\circ$ (Aharonian et al., 2008*a*).

In the case of a hadron induced shower, the number of possible interactions and type of particles involved is larger (strong interactions) and they are dominated by the fluctuation in the initial nuclear interaction. The primary hadron (generally a proton) that collide with a nucleus of the high atmosphere can produce a great variety of secondary particles as pions, kaons, nuclei, etc.. Each secondary particle, if energetic enough, can produce other particles of hadronic nature by secondary collisions. The great majority of the secondary particles are π^+, π^- and π^0. The neutral pion decays 99%:

$$\pi^0 \rightarrow \gamma + \gamma$$

initiating a pure electromagnetic sub-shower, that means that roughly one third of the primary hadron energy goes in electromagnetic sub-shower components. The charged pion decays:

$$\pi^{\pm} \rightarrow \mu^{\pm} + \nu_\mu(\bar{\nu}_\mu)$$

and muons are produced. They have virtually no nuclear interaction and their radiation losses are small so that they can penetrate deep in the atmosphere. Their lifetime is also quite long ($\tau_\mu \sim 2.2 \cdot 10^{-6}$ s) and muons with Lorentz factors $\gamma \geq 20$ can actually survive intact up to the surface of the earth thanks to the relativistic dilation of their lifetime. This fact is relevant for Cherenkov telescopes (see 4.3): a single muon may produce enough Cherenkov light to trigger the data acquisition, resulting in a further, non negligible, source of background for the instrument.

In conclusion, in a electromagnetic shower the Cherenkov light is produced only by electrons quite well collimated with the shower axis. In a hadronic shower the Cherenkov light is produced by particles of different nature (hadronic and leptonic) with tracks much more sensitive to the results of the first nuclear interaction in the high atmosphere. This results in a wider spread of the shower particles with respect to the shower axis (see figure 4.3).

4.2.1 The Cherenkov effect

When a charged particle travels inside a transparent dielectric medium at a velocity $v = \beta \cdot c$ larger than the speed of light in the medium ($\beta > 1/n$, with n refraction index), light is emitted[5]. The radiation is originated by the reorientation of electric dipoles previously polarized by the charge passage. If a charged particle travels in a medium, it disrupts the local electromagnetic field in its boundary and the electrons of the atoms will be displaced and polarized. Upon returning to their original situation of equilibrium, the electrons emit photons. In normal circumstances no radiation is emitted (figure 4.4 a). In the case that the charged particle creating the disequilibrium travels faster than the emitted photons (figure 4.4 b), the wavefronts emitted in different points of the particle's trajectory can sum coherently (according with Huygens construction, fig. 4.4 c).

---

[5] This radiation was discovered by P.A. Cherenkov in 1934 and theoretically explained by Frank and Tamm in 1937.

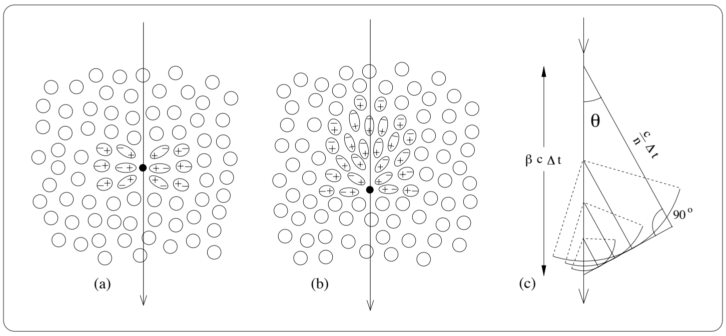

Figure 4.4: Polarization produced in a dielectric medium by a charged particle. (*a*) Small velocity. (*b*) High velocity. (*c*) Construction of the Cherenkov light wavefront.

If the dielectric is transparent, the produced light propagates in the medium. Photons are emitted with a fixed emitting angle θ with respect to the velocity vector $\vec{v}$ of the inducing particle. The Cherenkov emission angle can be expressed by:

$$cos\theta = 1/(\beta n) \tag{4.1}$$

which for the case of the atmosphere medium crossed by charged particles can be manipulated up to obtain the Cherenkov angle as a function of the altitude z:

$$\theta_c(z) = \cos^{-1}\left(\frac{1}{\beta n(z)}\right) \tag{4.2}$$

As already mentioned there is a threshold for the velocity of the particle for the production of Cherenkov light given by: $\beta_{min} = 1/n$. This results in an energy threshold for the involved particles:

$$E_{th} = \frac{m_0 c^2}{\sqrt{1-\beta_{min}^2}} = \frac{m_0 c^2}{\sqrt{1-n^{-2}}} \tag{4.3}$$

where m_0 is the rest mass of the particle. For detection purposes, it is also important to know the spectrum of the Cherenkov radiation produced in an EAS. The number of Cherenkov photons emitted per unit of path length and per unit of photon wavelength (λ) by a particle with charge Ze is given by (Yao et al., 2006):

$$\frac{\mathrm{d}^2 N}{\mathrm{d}x\,\mathrm{d}\lambda} = \frac{2\pi\alpha Z^2}{\lambda^2}\left(1 - \frac{1}{\beta^2\, n^2}\right) \tag{4.4}$$

where α is the fine structure constant[6]. The $1/\lambda^2$ dependency of the spectrum indicates that most of the Cherenkov photons are emitted at short wavelengths, in the ultraviolet range, and that it decreases along the visible region. However, due to the interactions of the Cherenkov photons with the air molecules in their path through the atmosphere, the spectrum observed at ground level is quite different from the emitted one (see Fig. 4.5), and it peaks at around 330 nm.

Cherenkov photons suffer the following attenuation processes in the atmosphere:

---

[6] $\alpha = \frac{e^2}{4\pi\epsilon_0\hbar c} = 7.297 \times 10^{-3}$

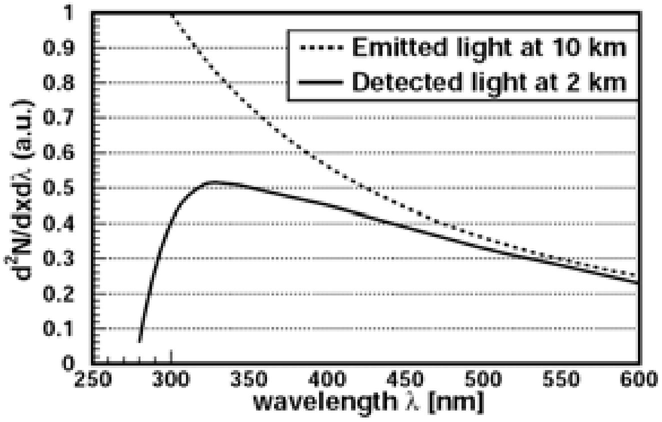

Figure 4.5: Spectrum of Cherenkov light at the shower maximum (dashed curve) and after traveling down to 2 km altitude (full curve).

Rayleigh scattering: Photons are scattered by polarizable molecules with size smaller than its wavelength, for example, by air molecules. The Rayleigh scattering cross section is proportional to ϕ^4, and if the atmosphere is in optimal conditions, it is the process responsible for most of the Cherenkov light attenuation from 15 to 2 km above sea level.

Mie scattering: Cherenkov photons also suffer Mie scattering through interaction with small dust particles suspended in the air (*aerosols*), whose size is comparable to the wavelength of the light. This effect is specially important when the atmosphere is polluted by dust, fog or clouds. The spectral dependence of the Mie cross section is proportional to ϕ^a with $1\ 0 \quad a \quad 1\ 5$.

ozone absorption: The absorption in the ozone layer takes place in the upper part of the atmosphere ($h \gg 10$ km) and affects mainly all the photons with wavelengths shorter than 290 nm, which are absorbed through the $O_3 + \chi \ll \quad O_2 + O$ process, which is the dominant one for absorption of ultraviolet light.

4.2.2 The light pool

The density of the Cherenkov photos at ground, also know as *light pool*, changes depending on the primary particle type and energy. Cherenkov photons emitted at different altitudes have different propagation angles with respect to the shower axis. This angle is mainly determined by two things: the multiple Coulomb scattering of the particles (5) and the Cherenkov emitting angle (0 7) that also varies during the shower development because of the change of the refraction index of the air[7]. Another minor factor is the scattering of the photons with the dust in the atmosphere. What turns out in the case of gamma-ray induced showers is that the light density is roughly constant up to around 120 m away from the shower axis (see figure 4.6), where a sudden drops occurs and the number of photons starts to fade away. The illuminated area on the ground is very extended (40,000 m^2). Since the Cherenkov angle and Coulomb angle are fairly large (on the order of the size of the field of view), the angular distribution of Cherenkov light in a subsample of the

---

[7] It is governed by: $cos \ _{ch} = 1 \ (\ n)$ and for example it decreases from 0 74 at 8 km to 0 66 at 10 km (Aharonian et al., 2008*a*).

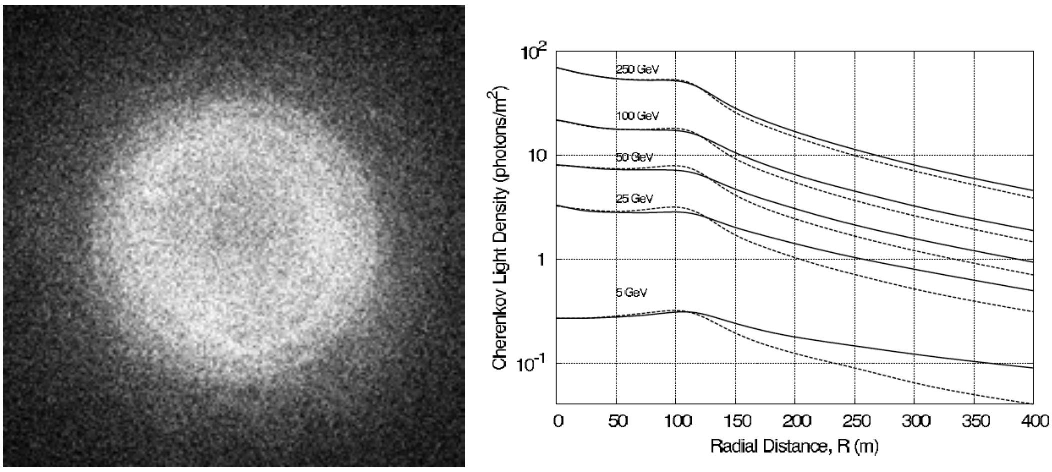

Figure 4.6: A χ-induced air shower produce a circular Cherenkov light pool at ground level. Starting from the core position, its density profile is roughly flat up to 120 m away, after which a steep drop occurs (separating the *core* from the *halo* region). On the left of this figure a plot of the Cherenkov photons produced by a χ-ray of 300 GeV on the ground. On the right a simulation of the Cherenkov light as a function of the impact distance (Aharonian et al., 2008*a*). The solid and dashed lines differentiate showers developing along to the earth magnetic field or 90 perpendicular to it.

light pool is close to what one would predict if the electromagnetic shower is emitted isotropically, giving a simple angular projection of the shower development (Aharonian et al., 2008*a*). Please note that curiously, the main dependency with the energy is in the density of Cherenkov photons in the light pool, and not on the size of the light pool itself.

4.2.3 Fluorescence

Charged particles traversing the atmosphere not only ionize, but also excite the atoms. Some of this appears in form of *fluorescence* from nitrogen molecules, with typically 5000 photons per km of track length, again in the blue wavelength region (300 450 nm, Perkins (2009)). This fluorescent light is emitted isotropically and is also used for the detection of air showers. For example, the Auger experiment uses fluorescence detectors in combination with direct particle detectors.

4.3 The Imaging Air Cherenkov Technique (IACT)

Up to date, the most efficient way to detect gamma rays above 100 GeV is with Cherenkov telescopes. We know from section 4.2 that energetic CR particles, as well as the VHE photons we are looking for, produce air showers when impinging on the atmosphere, and that the secondary particles of the shower emit visible light trough the Cherenkov effect.

A Cherenkov telescope is basically a collector of these Cherenkov photons (*mirror*), equipped also with a sensitive light detector (*camera*) in the telescope focal plane. The camera is usually composed of a matrix of phototubes, called *pixels*, which allow to measure not only the number of Cherenkov photons that hits the telescope mirror but also to detect a pixelized image[8] of the air shower. The main conceptual difference between ground-based gamma-ray telescopes and optical telescopes is that they not directly detect the photon flux that they observe (gamma rays), but the secondary photons (optical photons) produced in the particle shower. For this reason, contrary to standard telescopes, the focus of Cherenkov telescopes is not set to infinity but at roughly the height of the shower maximum (~ 10 km).

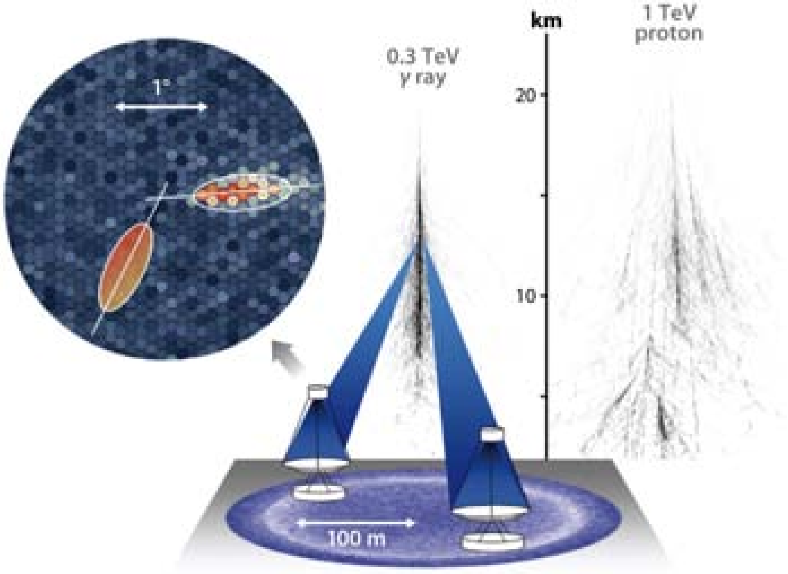

Figure 4.7: Imaging air Cherenkov technique cartoon. The Cherenkov light produce by an EAS is collected by two IACTs and the two images (see inlay) are combined to determined the direction of the primary (stereo technique). For comparison also an hadronic shower is shown on the right. Plot from Hinton and Hofmann (2009).

The core of the technique resides in the Cherenkov images of the showers. The Cherenkov photons, coming from different parts of the shower, will reach the pixels located in different regions of the camera depending on the angle between the telescope axis and the incoming photon direction (see section 4.3.2). The amount of detected Cherenkov light provides information about the density of the shower particles at different altitudes during the development of the shower in the atmosphere. Image properties (analyzed offline) give information about the nature, the energy and the incoming direction of the primary particle of the shower. For example images of EAS initiated by gamma rays have a compact elliptic shape, an the major axis of the ellipse indicate the shower axis projected onto the image plane. In contrast, the image of EAS produced by cosmic ray protons show a complex structure due to the initial hadronic interactions. Electromagnetic sub-showers due to π^0-mesons as well as penetrating μ-s from the decay of the charged pions contributes to the variety of the possible final image shape (Aharonian et al., 2008*a*).

The maximum angle between the telescope axis and the photon direction that allows the photon to reach the camera is the optical Field of View (FoV) of the instrument. The field of view of Cherenkov telescopes is generally quite small (few degrees), so that

---

[8] The IACT acronym stands for *Imaging* Atmospheric Cherenkov Technique but also for Imaging Air Cherenkov Telescope.

a *tracking* system is also required and observations are generally performed pointing at a particular source in the sky (see also 6.3).

The shape of the reflecting dish can be either spherical (as is the case for H.E.S.S.) or parabolic (like MAGIC). The second option has the advantage of preserving the timing structure of the Cherenkov light (useful at analysis level, see section 4.3.4) but has the drawback of more optical aberrations. This limits the possible FoV of the telescope (or alternatively requires a larger 'f/D'). Even in the case of a parabolic mirror shape the reflecting dish is generally tessellated by several small spherical mirrors, the only slight complication is the necessity of different curvature ratios depending on the distance of the mirror from the center.

4.3.1 Design and limits of a Cherenkov telescope

An IAC telescope is characterized by its sensitivity, the minimum detectable gamma-ray flux in a given observation time, by its energy threshold, the minimum energy of the primary gamma which the telescope is able to detect, and by its angular resolution, the accuracy in the reconstruction of the primary incoming direction.

Different choices can be made during the design phase of an IACT depending on the features that one want to optimize and the kind of physics whose the instrument is focussed. Generally speaking, galactic astrophysical sources have a 'harder' spectra, characterized by a strong flux of gamma even at high energies, whereas extragalactic AGNs have typically 'softer' spectra which might allow their detection only at relatively low energies (also because of the flux attenuation due to the EBL and to intrinsic high energy cut-offs foresee by some of the emission models).

The sensitivity can be boosted enhancing the background suppression, since it reduces the amount of time required to obtain a statistically significant signal. The most straightforward way to improve the background suppression is to observe the same air shower stereoscopically. This permits to reconstruct more precisely the shower features which disentangle a gamma shower from a background shower. Moreover, the stereo approach allows also a better reconstruction of the shower axis direction. This is worth not only to improve the telescope angular resolution, since the gamma direction is more precisely determined, but also to enhance the sensitivity for point-like sources, since a smaller "signal region" results automatically in less isotropic background. A stereo view is obtained by placing a whole array of Cherenkov telescopes instead that a single IACT. The distance between telescopes has to be optimized: they must be close enough to allow the light pool (section 4.2.2) of the same shower to reach at least two of telescopes of the array, but also far enough to guarantee a fairly different viewing angle of the shower. The collection area of the array is another parameter which has to be taken into account and optimized. All the modern Cherenkov telescopes experiments have moved in the stereo direction: H.E.S.S. is an array of four 12 meters diameter telescopes, as well as VERITAS, whereas MAGIC is now an array of two 17 meter telescopes.

Concerning the energy threshold, the dilution of the Cherenkov photons in the light pool for low energy showers makes its detection more difficult since less light from the shower is available, and it can be more easily confused with the fluctuation of the light of the night sky. The signal to noise ratio for a Cherenkov telescope is proportional to the square root of the mirror area times the reflectivity of the optics and quantum efficiency of the PMTs and inversely proportional to the square root of the signal-integration timescale and solid angle of the pixels (Aharonian et al., 2008*a*). The ratio grows only with a square root function because also the number of background photons is proportional to the mirror area and in general to the detection efficiency. Since the energy threshold is inversely proportional to the signal to noise ratio, it can be expressed by the following equation (Longair, 1992):

$$E_{th} \sim \sqrt{\frac{\phi\Omega\tau}{\varepsilon A}} \tag{4.5}$$

with A the mirror surface, ε the light detection efficiency (which includes the mirror reflectivity and the efficiency of the light detectors), τ the integration time of the Cherenkov signals, Ω the solid angle subtended by the collection mirror. The background flux from the night sky ϕ also enters in the formula as parameters since it vary from site to site.

Equation 4.5 suggests that an IACT design oriented to a lower energy threshold will include a large mirror surface (with high reflectivity), high efficiency light detectors, small FoV and fast readout electronics to minimize the background light integration time. A typical image for an event at the MAGIC energy threshold is originated by roughly 300 Cherenkov photons.

The main sources of unwanted background light, also know as Nigth Sky Background (NSB) are:

- stars
- airglow
- zodiacal light
- man-made artificial light
- moonlight[9]

Although the intensity of the NSB is much lower than that of the Cherenkov light produced in an EAS, typical NSB photoelectron rates are in the order of 0.2 phe/ns/pixel (Armada, 2005).
MAGIC is a low energy oriented Cherenkov telescope, with actually the lowest energy threshold of the current generation of IACTs.

4.3.2 Image formation

As already mentioned the mirror of a Cherenkov telescope can be parabolic or spherical. Photons coming parallel to the telescope axis will be concentrated in the focal point whereas photons coming with a certain angle θ with respect to telescope axis are focused in a certain point of the focal plane, distant ρ from the focal point (figure 4.9). Fixing a polar coordinate system in the focal plane, the focused position (ρ, ϕ) can be calculated from the incoming direction of the photon (θ, Φ) by the formulae:

$$\begin{aligned} \rho &= \sin(\theta) \cdot f \simeq \theta \cdot f & (4.6) \\ \phi &= \Phi & (4.7) \end{aligned}$$

Where f is the focal distance of the paraboloid. If the small angle approximation $\sin(\theta) \simeq \theta$ is applied[10], the distance from the focal point (the telescope camera center) goes linearly with the incident angle.

---

[9] IACTs might operate under moderate moonlight conditions as it was the case in the past for HEGRA and is currently the case for MAGIC.

[10] Since MAGIC camera acceptance is limited to $\simeq 3.5^\circ$, this approximation is well justified.

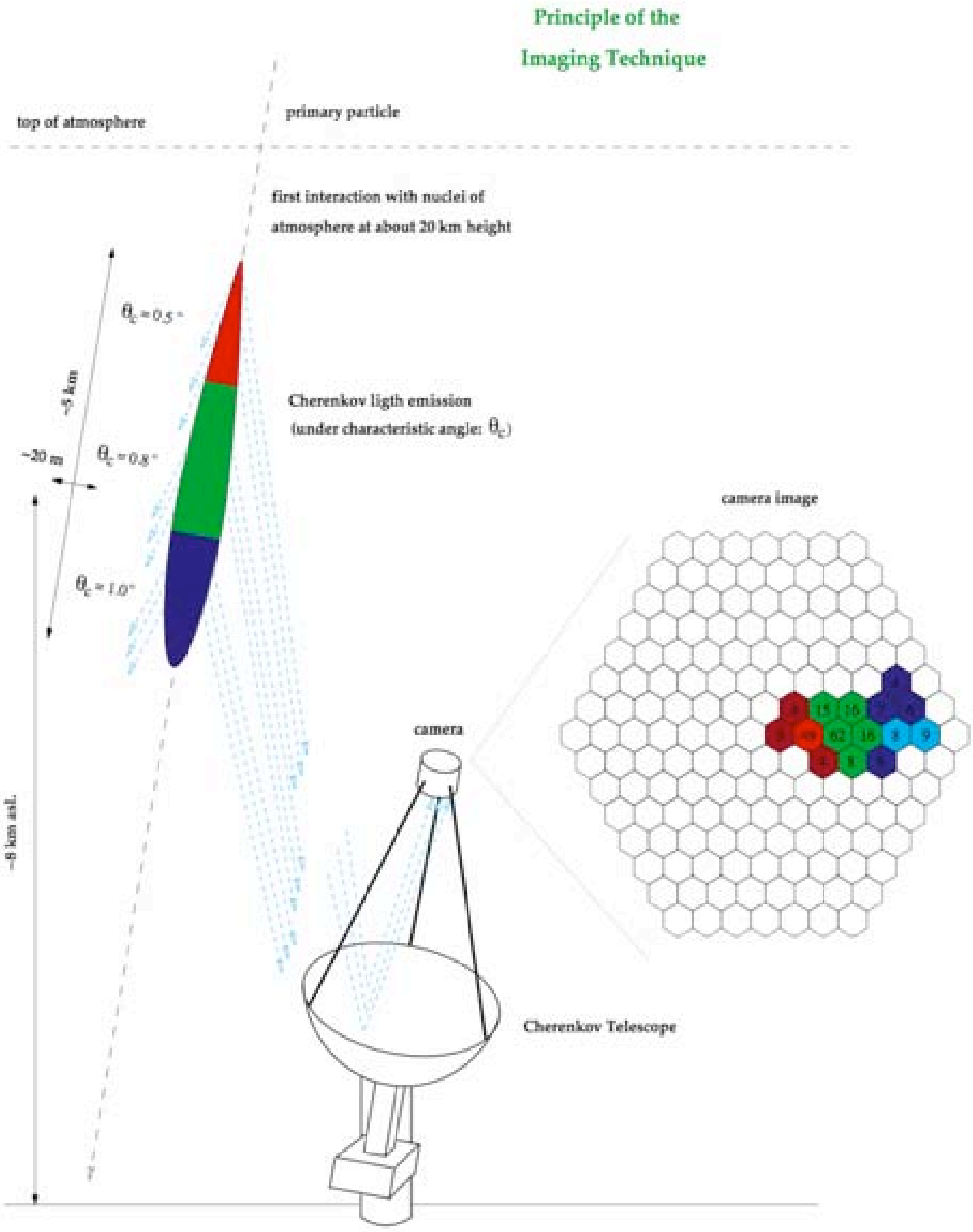

Figure 4.8: Image formation scheme in the camera of a Cherenkov telescope. The values are refereed to a 1 TeV γ-induced shower. The blue part is the image *head* whereas the red part is the image *tail*. The numbers written on the pixels are the number of Cherenkov photons impinging to the PMTs.

In other words: there is a univocal relation between illuminated pixels in the camera and (almost) parallel beams of Cherenkov photons with a certain incoming angle θ. Accordingly to figure 4.8, the red portion of the shower is focused near the camera center (tail), while the blue portion closer to the camera border (head). The different number

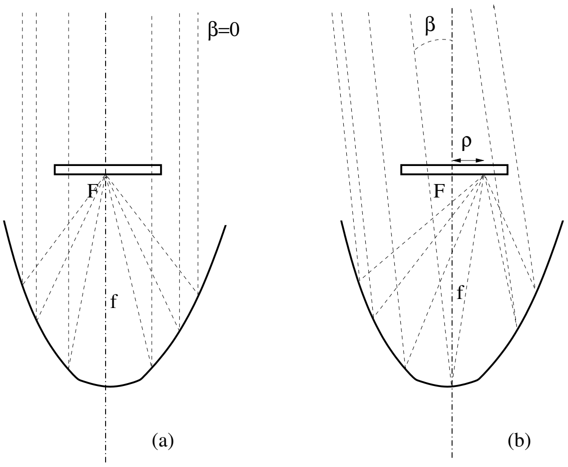

Figure 4.9: Image formation scheme. Vertical section. Projection of a photon beam parallel to the parabola axis (a). Projection of a photon beam slightly inclined (angle β) respect to the parabola axis (b).

of particles at different altitudes is reflected in the longitudinal structure of the recorded Cherenkov image. The Cherenkov images have also a transversal width that is correlated with the real width of the shower. The image width is actually one of the most powerful background rejection parameters when the data are analyzed (see section 4.3.4).

4.3.3 Image parameters

The imaging technique relies on the shower development information that is contained in the images formed in the telescope camera. Once the image is cleaned from the noise, some numerical parameters, useful to characterize the image, are computed. The image parameters are used in the data analysis to recognize the nature of the primary particle and its energy.

The fundamentals image parameters, at the base of the IACT technique, are the so-called *Hillas* parameters (Hillas, 1985). The parameters related to the image shape are obtained by computing the second order moments of the spatial charge distribution in the camera. In the following list the basic parameters are described[11]. For a graphical interpretation of some of the image parameters see figure 4.10.

- **SIZE**: Total number of phe in the image. Defined by:

$$Size = \sum_{i=1}^{k} N_i$$

  (N_i being the change in a given pixel). This value is roughly proportional to the primary particle energy for a fixed *impact parameter* (distance of the shower from the telescope axis, a.k.a. 'IP') of the shower.

---

[11] Other parameters commonly used in standard MAGIC analysis are also cited, even if they can not be considered as standard as the original Hillas parameters.

- **LENGTH**: Second moment of the light distribution along the major image axis.
- **WIDTH**: Second moment of the light distribution along the minor image axis.
- **DIST**: Distance between the image centroid and the source position in the camera (for standard observations the camera center and the source position in the camera coincide). This is correlated to the impact parameter of the shower.
- **ALPHA** or α: Angle between the direction of the major axis and the line joining the image centroid with the source position (see figure 4.10). Its absolute value is usually taken since the head tail orientation is normally not taken into account when 'Alpha-plots' are produced (see this and next chapters for more details).
- **CONC**[n]: Fraction of the total amount of photoelectrons contained in the n most luminous pixels. We will refer to Conc without any index for the case $n = 2$.
- **LEAKAGE**: Fraction of the light of the image contained in pixels that belong to the outermost ring of pixels of the camera. This parameter is useful to recognize images partially outside the camera (to be eventually excluded by quality cuts).
- **M3LONG**: Longitudinal third moment of the distribution of the charge along the major axis. This parameter is useful to resolve the head/tail degeneracy since it determine the side of the image with larger/lower charge.

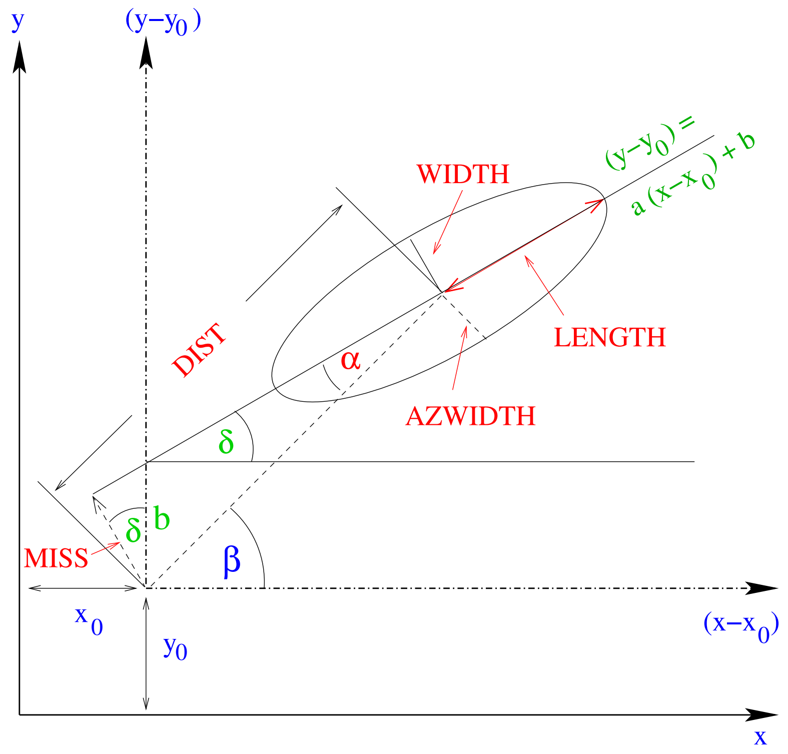

Figure 4.10: Graphical representation of some of the image parameter described in the text. The nominal position of the observed source is (x_0,y_0).

Please note that α represents the geometrical orientation of the image in the camera with respect to the source position. The final cut, before estimating the significance of a detection, is commonly done on this parameter[12]. Note that Alpha is not properly speaking a γ/hadron separation parameter, but rather a geometric information about the incoming direction of the primary particle.

4.3.4 The time information

If a Cherenkov telescope is equipped with a fast readout electronic for the PMTs, together with the image shape also an image "time profile" can be extracted from the data (see section A.2.3).

A novel technique which exploits this information is currently used by MAGIC analyzers for the reduction of MAGIC-I stand-alone data. In the thesis's chapters we will only resume some of the concepts when needed, further details are given in appendix A. The description of the MAGIC data analysis can be found in chapter 6.

4.3.5 Model analysis

An alternative approach for the analysis of Cherenkov telescopes data is the so-called *model analysis*. In this case the characteristics of the primary particle are determined comparing the recorded image with template images from a very large database of Montecarlo events. This analysis technique is also referred as a 'pixel wise' information approach. A likelihood-type test determines which one of the template events resembles better the real shower and then the corresponding simulation input parameter, as particle energy, impact parameter, etc. are assigned to the event. This type of analysis has a large potential with respect to the classical image analysis because there is no loss of information in the process. The real image is not forced to be approximated with an ellipse, as it is the case in the classical Hillas analysis. This approximation is in fact considered by many as pretty rough at this mature stage of the IAC technique.

The drawbacks of the model analysis are the handling of a more complicated analysis procedure and an increase of the computing time (or power) required to analyze the data. The data size also increases since the full image information is required to be available up to higher levels of the analysis.

Model analysis approaches have been studied both by the MAGIC (Mazin, 2007) and H.E.S.S. (de Naurois, 2003) collaborations and they resulted to lead to significantly better results either in terms of sensitivity, energy reconstruction, and angular resolution of the detectors.

---

[12] In the case of a point-like source. Different analysis approaches (like θ^2 analysis) are also possible. See section 6.2 for more information.

Chapter 5

The MAGIC telescopes

What are the characteristics of the MAGIC-I and MAGIC-II Cherenkov telescopes?

Figure 5.1: Picture of the two MAGIC telescopes (left: MAGIC-I; right: MAGIC-II).

The IACT technique allows modern Cherenkov telescopes to reach sensitivities of the order of one percent of the Crab Nebula flux in 50 hours of observation[1] (Hinton and Hofmann, 2009). In other words they can detect significantly the Crab Nebula in an observation time of few minutes while at the dawn of TeV astronomy many hours of observations were required.

The claimed sensitivity for the three major instruments operative in the field are 0.7 % for H.E.S.S., 1.6 % for MAGIC ($\simeq$ 1 % for stereo data, see also section 5.5) and 0.7 % for VERITAS. The energy resolution is roughly 20–30% and the angular resolution of the order of 0.1° or even less depending on the analysis method applied (see for instance

---

[1] See section A.3.3 for the definition of sensitivity.

Figure 5.2: Map showing the location of the current generation of Cherenkov telescopes.

Acero et al. (2010)).

As discussed in chapter 4, the major advantage of a Cherenkov telescope detector competing with other χ-ray astronomy instruments is the huge effective area, that compensates the extremely low flux of gamma rays at high energies. The main caveat is instead the large amount of background and its difficult rejection even at the analysis level, being the anti-coincidence trigger veto of the satellite detectors much more efficient (section 4.1.1).

On figure 5.2 the location of the most important Cherenkov telescopes is shown. The northern hemisphere is covered by the MAGIC and VERITAS detectors whereas the southern hemisphere is covered by the CANGAROO-III and H.E.S.S. arrays, with the latter playing the most relevant role.

The southern hemisphere is more suitable for the observation of galactic source because the central region of the galactic plane is visible under a smaller zenith angle and is apparently populated by a larger number of galactic TeV sources (see figure 5.3). On the other hand, the northern hemisphere is considered (probably just for historical reasons) more suitable for extragalactic observations, given the possibility to observe the most famous AGNs at TeV energies[2]. As mentioned, there are no deeper reasons to consider the northern hemisphere more suitable for AGN physics and actually the major blazar flare observed up to date was from PKS 2155-304, a southern hemisphere blazar.

The MAGIC collaboration comprises more than 150 physicists and astronomers coming from institutions from all over the world but mainly from Germany, Spain and Italy[3]. MAGIC stands for Major Atmospheric Gamma Imaging Cherenkov telescopes, where the term major underlines the fact that it is currently the array with the largest telescopes (17 m diameter mirror). The MAGIC telescope was designed as a detector capable to close the observational gap between space-borne χ-ray telescopes and the previous generation of Cherenkov instruments (The MAGIC collaboration, 1998). MAGIC-I (Cortina et al., 2005) was the first of the two telescopes which currently constitute the MAGIC

---

[2] On the norther hemisphere we have for example the two most stable&bright known TeV emitters: Mrk 421 and Mrk 501, the extensively studied quasar 3c 279 and the also very well studied radio galaxy M 87.

[3] http://wwwmagic.mppmu.mpg.de/gallery/pictures/People/

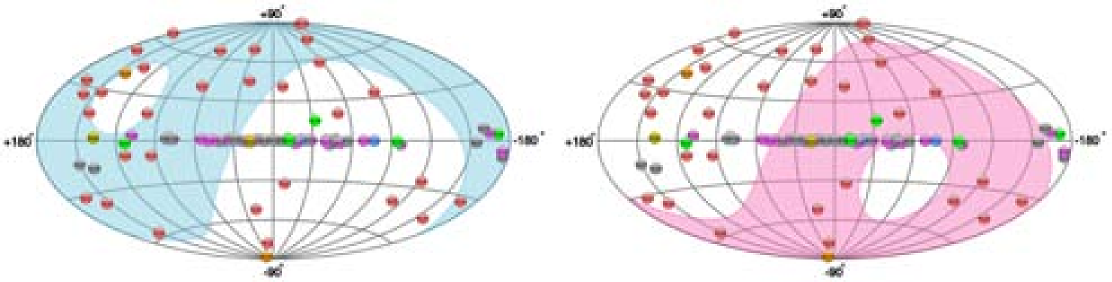

Figure 5.3: Sky maps of the known TeV sources (galactic coordinates). In the first panel the shaded area shows the portion of the sky visible (low zenith angle) from the MAGIC observation site (northern hemisphere). On the second panel the analogous plot for the H.E.S.S. observation site (southern hemisphere). Plots produced using the tools on *http://tevcat.uchicago.edu/*.

array. MAGIC-II is fundamentally a clone of MAGIC-I, but with a number of significant improvements (Cortina et al., 2009), as will be described in the following sections. The acronym MAGIC was meant at the beginning as the name of the stand alone MAGIC-I telescope. Now that a second telescope has been built, the term MAGIC generally refers to the stereoscopic system of two telescopes (MAGIC-I and MAGIC-II).

5.1 MAGIC-I

MAGIC-I is the first of the two MAGIC telescopes. Generally speaking it is a 'third generation' Cherenkov telescope, ideated after the success of the HEGRA experiment. MAGIC-I was specially designed to achieve high sensitivity at low energies (The MAGIC collaboration, 1998) and it started regular operations in 2004.

To achieve high performances at low energies (below 100 GeV) and to have the capability to measure fast transient events of the gamma-ray sky, several technological innovations were developed. The principal ones are:

- A lightweight frame structure, made of carbon fiber-epoxy material. The lightweight structure allows a quick pointing of the telescope which in 'fast movement' mode can point to any point in the sky in approximately 40 s.

- A parabolic high reflectivity mirror, with the largest size within the current generation of Cherenkov telescopes. The large size mirror permits to detect also the dim light of the low energy showers. In virtue of its parabolic shape the mirror is isochronous so that it preserves the time structure of the Cherenkov light front. The mirror is tessellated by small size (0.25 m^2) mirror tiles.

- An Active Mirror Control (AMC) system is also installed in order to allow the adjustment of the reflecting dish. The orientation of one square meter size mirror units can be adjusted via the AMC software.

- A very fast readout electronics in order to allow a precise sampling of the Cherenkov signals, which are very fast in time, and hence allow a smaller noise integration and a more precise measurement of the pulse arrival time.

- High quantum efficiency PMTs in order to increase the light collection efficiency.

5.2 MAGIC-II

MAGIC-II is the second telescope of the MAGIC array and is basically an improved version of MAGIC-I. In order to minimize the time and the resources required for design and production, the second MAGIC telescope is in most fundamental parameters a clone of the first telescope. The improvements reside in the camera (with a highly pixelized matrix of PMTs, a wider trigger area and an improved optical analog signal transmission) and in the readout (with a more flexible signal handling electronics and a cheaper and compact 2 GSample/s fast digitization system). A more detailed explanation of the MAGIC-II improvements are provided in section 5.4. The lightweight carbon fiber reinforced plastic telescope frame, the drive system (Bretz et al., 2009) and the active mirror control (AMC) are only marginally improved copies of the first telescope. MAGIC-II started regular operation in 2009.

5.3 MAGIC as a stereo system

The MAGIC experiment recently converted from a stand-alone telescope system to a *stereo* system. In stereo observation mode, i.e. simultaneously observing the same EAS with more than one Cherenkov telescope, the shower reconstruction and background rejection power are significantly improved. A better sensitivity is achieved as well as a better angular resolution and energy reconstruction. A reduced analysis energy threshold is also expected given the improvement in background suppression. In the case of MAGIC, with the installation of a second telescope, the overall sensitivity was expected to increase by a factor of 1.5–2 depending on the energy range (see also section 5.5). A picture of the two MAGIC telescopes is provided in figure 5.1.

A dedicated montecarlo study showed that there is only a moderate dependence of the sensitivity on the distance of the two telescopes (Moralejo et al., 2004*b*). The second MAGIC telescope has been installed 85 m away from the first telescope which resulted to be the optimal distance according to the study just mentioned.

The stereo system conserves the fast repositioning characteristic of the MAGIC-I telescope. Both telescopes will be able to reposition within 120 seconds to any sky position for fast reaction to GRB alerts.

The telescopes have been renamed officially “MAGIC Florian Goebel Telescopes” in memory of the project manager of MAGIC-II, great physicist and dear friend, who tragically died shortly before completing the telescope in 2008.

5.4 The telescopes components

We will describe in the next sections the key elements of the the two MAGIC telescopes[4]. In the case of MAGIC-II, newly developed components are employed whenever they allow cost reduction, improved reliability or most importantly increased physics potential of the new telescope with reasonable efforts.

---

[4] http://wwwmagic.mppmu.mpg.de/magic/factsheet/.

5.4.1 Frame

Lightness was one of the design goals for the MAGIC telescope in order to achieve a fast pointing system. For this reason an innovative choice was made for the realization of the telescope frame: the mirror dish is supported by a three-layer structure made of low-weight carbon fiber-epoxy tubes joined by aluminum knots. These materials combine light weight with high rigidity. According to the specifications the maximum deformation of the structure, for whatever position of the telescope, is below 3.5 mm. The total weight of the frame is $\sim$ 60 tons, the total moving components 72 tons (Bretz et al., 2009). The carbon fiber-epoxy is also specially resistant to the hard atmospheric condition of the site of observation in La Palma[5]. Tubes and knots are modular and the frame can be virtually unmounted and mounted again screwing its elements.

The telescope mount is of *altazimuth* type (see also section 5.4.8). It allows rotation of 400° on azimuth and -90° to +90° in zenith during normal observations. Nevertheless a $>$ +90° zenith distance can be set so that pointing the telescope slightly below the horizon is actually possible (potentially useful for very special studies).

The camera detector (see section 5.4.3) is kept in the focus location by a metallic arch stabilized by thin steel cables anchored to the main dish structure. In figure 5.4 a scheme of the MAGIC structure is provided.

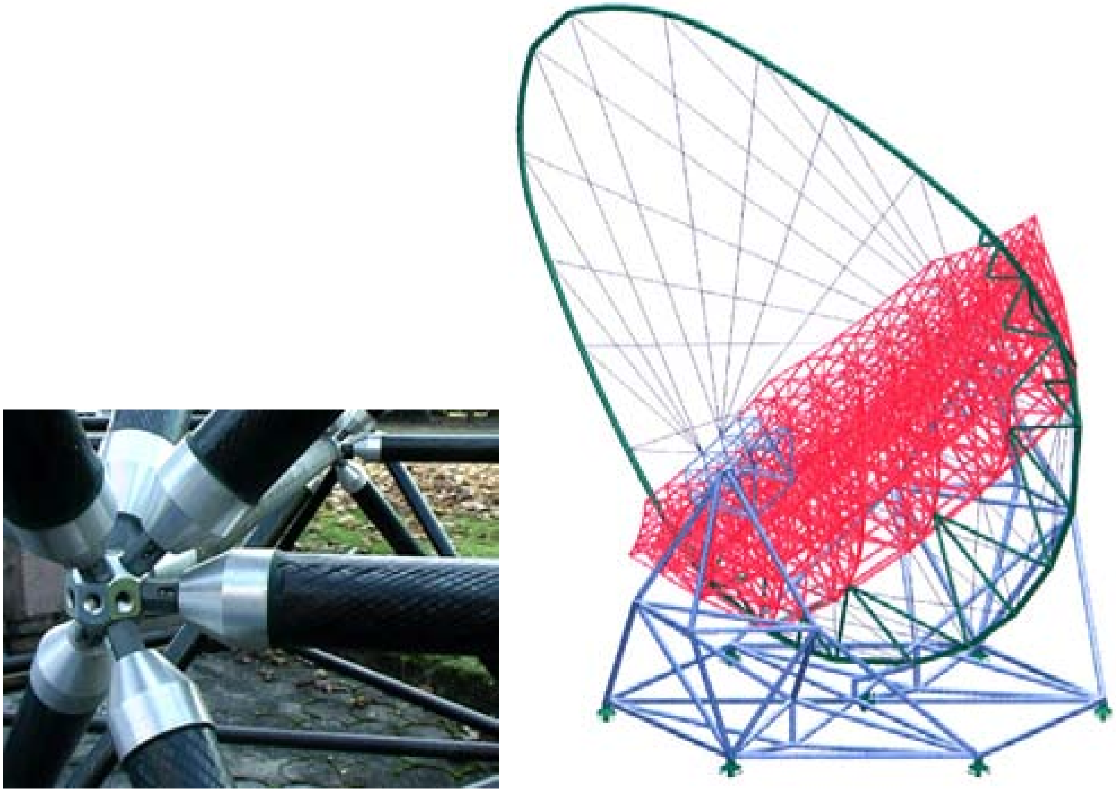

Figure 5.4: A picture of the aluminum knot junction between fiber-epoxy tubes used in the MAGIC telescope frame (left) and a general scheme of the MAGIC frame (right).

---

[5] Example are the strong solar irradiation during the day in summer or the very low temperatures which typically goes well below zero in winter.

5.4.2 Mirror

The Cherenkov pulses from γ-ray showers are sometimes very short (1-3 ns) but nevertheless they hide inside the flash a certain time development. The parabolic shape of the reflector of the MAGIC telescope preserves this time structure.

In MAGIC-II like in MAGIC-I the parabolic tessellated reflector consists of 247 individually movable 1 m^2 mirror units, which are adjusted by an *Active Mirror Control* (AMC) system depending on the orientation of the telescope. While in MAGIC-I each mirror unit consists of 4 individual spherical mirror tiles mounted on a panel, MAGIC-II is equipped with 1 m^2 spherical mirrors consisting of one piece. This reduces cost and manpower because it is no longer necessary to align all four mirrors individual tiles inside each panel before installing the panels on the telescope.

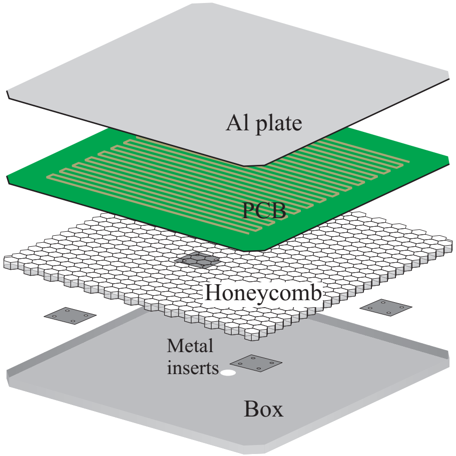

Figure 5.5: The aluminum mirror structure. The green layer is a simple resistive PCB where current can be circulated in order to heat to the whole mirror. This is meant to avoid the mirror to froze and the formation of condensation. The PCB is not installed in MAGIC-II mirrors.

Different technologies have been used for the production of the mirrors. There are actually three types of mirrors mounted on the MAGIC telescopes:

0.25 m^2 aluminum mirror These 'aluminum' mirror represent a remarkable innovation with respect to the conventional 'glass' mirrors historically used. They are composed by an aluminum box open on the upper side (a.k.a. "blanket") where an honeycomb aluminum structure is inserted in order to guarantee the necessary rigidity of the mirror. A thin aluminum plate is located on the top of the mirror and glued to the honeycomb (which is also glued to the box). The obtained object is called the "sandwich". See figure 5.5 for a sketch of the aluminum mirror structure. The upper side of the plate is finally polished using a special diamond milling machine which makes the surface reflective[6]. The polishing of the mirror surface is done by the LT-Ultra company in Germany. The reflecting surface is protected by a final layer of quartz-based material which coats the mirror and protects the surface from scratches and the aluminum from oxidation. The weight of a mirror of this type is of 3.5 kg.

MAGIC-I is composed almost entirely by these 0.25 m^2 aluminum mirrors, with the

---

[6] The achieved reflectivity is of the order of 80–90%, depending on the wavelength.

exception of a couples of 1 m^2 aluminum mirror (described in the next point) which were installed for testing purposes.

1 m^2 aluminum mirrors This is the second generation of the same type of mirror described in the previous point. As already mentioned the 0.25 m^2 mirrors are not mounted directly on the structure but in panels holding 4 mirrors each. The panel is mounted on the frame through the actuators of the AMC. The new one square meter mirrors are instead directly connected to the AMC actuators (i.e. directly linked to the frame). The structure of the 1 m^2 mirror is pretty similar to the 0.25 m^2 one, it is basically a scaled version of the same mirror. The main difference is the use of a mold to shape the whole mirror sandwich with a spherical curvature roughly similar to the final one before proceeding to polish of the surface. In such a way the thickness of the aluminum plate can be maintained small (3 mm = 0.012°) since there is no need to create the whole curvature milling the center of a flat plate, operation that would require a very thick (and heavy) aluminum plate.
The reflectivity and the radius of the circle containing 90% of the spot light have been measured to be around 87% and 3 mm respectively. Out of the 247 mirror tiles of MAGIC-II, 143 are of the type just described.

1 m^2 glass mirrors The remaining 104 mirror tiles of MAGIC-II are produced as a 26 mm thick sandwich of 2 mm glass plates around an aluminum honeycomb layer using a "cold slumping" technique. The frontal glass surface is coated with a reflecting aluminum layer and a protective quartz coating. The glass-Al mirrors show a point spread function which almost doubles ($\sim$ 6 mm) that of the all aluminum mirrors but the light spot is still well inside the size of a camera pixel. On the other hand the glass mirror has a somehow better reflectivity with respect to the aluminum mirror, and has a lower production cost.

5.4.3 Camera

The *camera* is one of the most important part of a Cherenkov telescope. The gamma/background separation power is highly dependent on the quality of the shower images, so it turns out to be very relevant for the sensitivity of the telescope. The main characteristic of a good camera are high quantum efficiency photosensors, a fine pixelization and a fast response.

The sensitive pixels in the cameras of the MAGIC telescopes are composed by PhotoMultiplier Tubes (PMTs). These are the devices actually appointed to convert the Cherenkov photons produced by the air shower into electrical signals. The PMTs of both cameras have a high Quantum Efficiency (QE) (of around 20–30% depending on the wavelength).

The MAGIC-I camera has an hexagonal shape, with two type of phototubes used: the small, of 0.1° diameter, which are located in the inner part, and the large ones, 0.2° diameter, which are used in the outer part of the camera (see first two panels of figure 5.6). The total number of channels is 577. The PMT photocathode is of spherical shape so that to guarantee a flat and complete coverage of the camera plane *winston cones* (light guides) of hexagonal shape are installed on the top of the PMTs. The winston cones are modular and are appointed to convey the light form the camera plane to the the PMT sensitive surface. The QE in the case of the MAGIC-I camera was enhanced through the

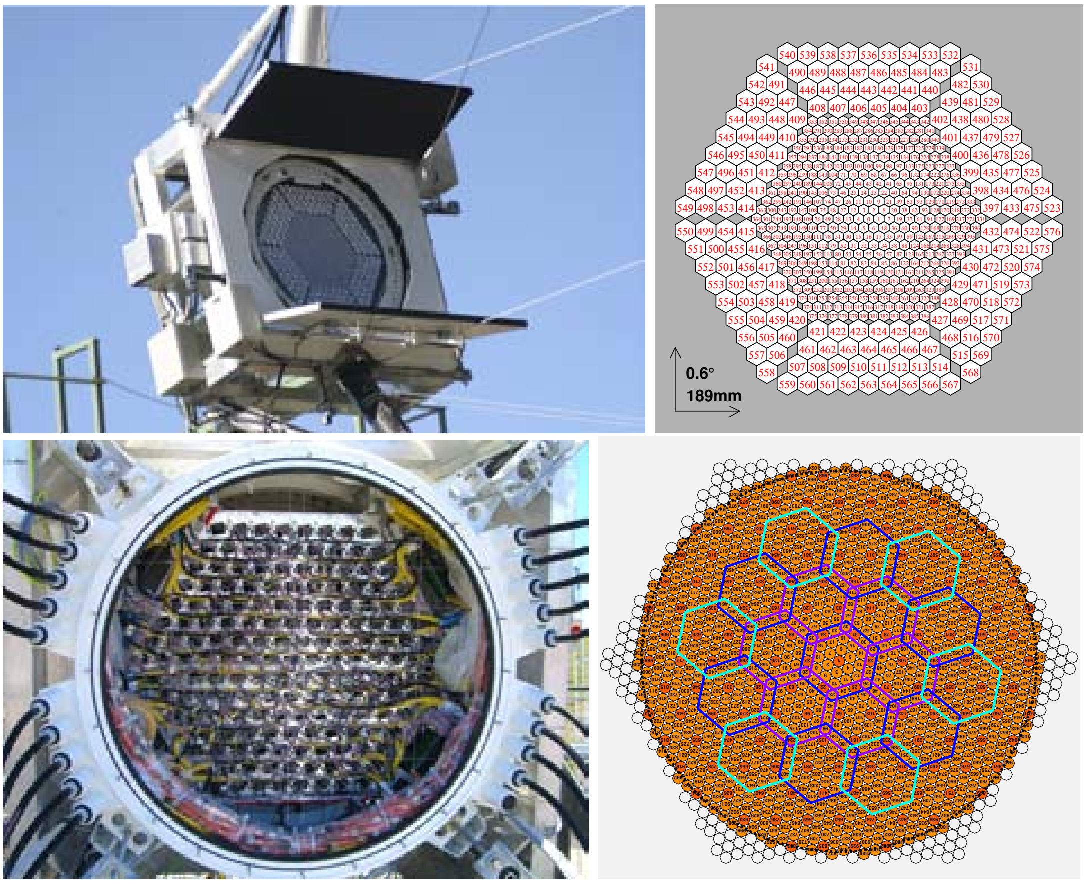

Figure 5.6: Pictures and schemes of the camera of MAGIC-I and MAGIC-II. Top left: MAGIC-I front picture; Top right: MAGIC-I camera layout; Bottom left: MAGIC-II back picture; Bottom right: MAGIC-II camera layout. Please notice the uniform pixelization of MAGIC-II in comparison to the two region of MAGIC-I camera.

use of a special coating of the cathode with a material called 'MAGIC lacquer' (Paneque, 2004). Thanks to the coating the efficiency at peak increased from $\simeq 25\%$ to $\simeq 30\%$.

The MAGIC-II camera has instead a circular shape with a single type of photosensor (of 0.1° diameter) so that it is more uniform and more finely pixelized (Borla Tridon et al., 2009). The 3.5° diameter FoV is similar to that of the MAGIC-I camera. To get an homogeneous 0.1° PMT camera of the same size of MAGIC-I, the number of channels has to be almost doubled (1039 pixels). In the first phase, the camera has been equipped with increased quantum efficiency (QE) photomultiplier tubes, while the modular camera design allows upgrades with high QE hybrid photo detectors (HPDs). A uniform camera (see figure 5.6, bottom panels) allows an increased trigger area compared to MAGIC-I.

Seven pixels in a hexagonal configuration are grouped to form one *cluster*, which can easily be removed and replaced. This allows easy exchange of faulty clusters. More importantly, it allows full or partial upgrade with improved photo detectors. The pixels currently mounted are the Hamamatsu R10408 6 stage phototubes with hemispherical photocathode, which typically reach a peak QE of 34%. The PMTs have been tested for low after-pulsing rates, fast signal response ($\sim$1 ns FWHM) and acceptable aging properties. Also in the case of MAGIC-II winston cones light-guides are used to minimize the dead area between the PMTs.

As mentioned already, the flexible cluster design allows field tests of this new technology within the MAGIC-II camera without major interference with the rest of the camera. For example 7-pixel modules in the outermost ring of MAGIC-II with HPDs have been equipped with HPD and read out by the acquisition electronics. These HPDs feature peak QE values of 50%.

5.4.4 Readout electronics

The gamma-ray signals are very short in time and therefore a very fast readout electronics is required. The pulses have to be first processed to generate the trigger signal and then digitized at ultra-fast speed. Afterwards they have to be stored for the subsequent analysis (see chapter 6).

Let's briefly review all the steps that from the Cherenkov light pulse leads to the final acquired data event. The Cherenkov photons produced by the air shower particles hit the winston cones and are conveyed to the PMT cathode and converted (with a certain efficiency) to photoelectrons. Consequently, the PMT produces an analog output signal whose amplitude is related to the intensity of the input light. A pre-amplifier, located right after the cathode, provides a first amplification of the signal. Right after, the pulse enters a transmitter board where it is transformed into a light pulse by means of a VCSEL (Vertical Cavity Surface Emitting Laser). The output of the VCSEL is coupled to an optical fiber, which transmits the signal from the camera to the control house. In the electronics room located in the control house the optical signal is converted back to optical through a photodiode and the signal is split in two branches. One branch is further amplified and transmitted to the digitizers while the other branch goes to a discriminator with a software adjustable threshold. The generated digital signal has a software controllable width and is sent to the trigger system of the second telescope with a software adjustable time delay. The sampled values are sent to the final data acquisition computer where they are organized in events and stored in raw data files.

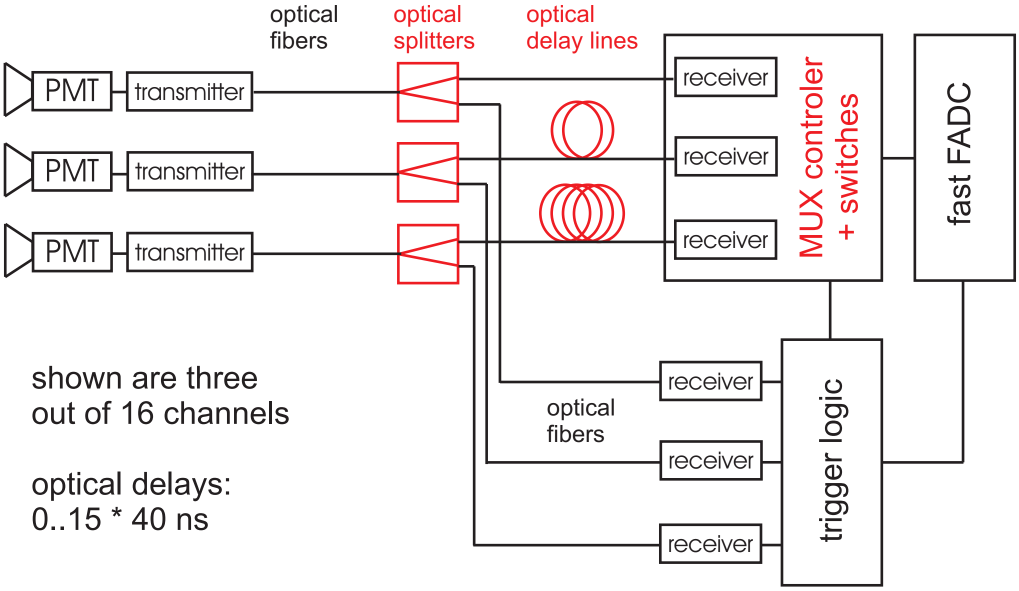

Figure 5.7: Readout system scheme for MAGIC-I (Goebel, 2007).

5.4.5 Trigger

The telescope *trigger* is a multiple level decisional system which determines the acquisition of an event (roughly speaking a camera shot, ∼ 40 ns long) in time coincidence with a cosmic shower. The photosensors are hit all the time by night sky background photons and only occasionally by the Cherenkov light produced by a cosmic shower. The light from an EAS is typically much more intense than the night sky background light and moreover involves several neighbor pixels at the same time. These two properties are used to discriminate the acquisition of an event. Low energy showers produce less Cherenkov light so that they can be more easily confused with fluctuations of the background light. The signals are processed by the receivers boards (see also section 5.4.4). For the pixels which lie within the *trigger region*, the receivers generate a digital trigger signal for each channel whenever the input signal is above a certain discriminator threshold. This is know as *level zero* (L0) trigger. These digital signals[7] are sent to the *level one* (L1) trigger unit whose task is to determine if the channels with signal above threshold have temporal and spatial correlation. Different topologies can be used for the spatial correlation, for example 3, 4 or 5 compact[8] "next neighbor" logic can be used. In case they are a global trigger signal is produce and sent to the *level two* trigger system, which at the moment has the only task of measuring the trigger rate and eventually imposing a scaling factor[9] to the rate of events which finally trigger the readout system.

The trigger system of the second telescope is basically a copy of the trigger of MAGIC-I. However, the uniform camera design allows an increased trigger area of 2.5° diameter FoV. This increases the potential to study extended sources and to perform sky scans.

When the two telescopes are operated in stereo mode a coincidence trigger (so-called *level 3* or L3 trigger) between the two telescopes rejects events which only triggered one telescope. In order to minimize the coincidence gate in the level 3 trigger, the triggers produced by the individual telescopes will be delayed by a time which depends on the pointing direction of the telescopes. This will reduce the overall trigger rate to a rate which is manageable by the data acquisition system.

Starting in 2007, an additional trigger system (*sumtrigger*) runs in parallel with the standard next neighbor trigger in the first telescope. The sumtrigger operates on the analog sum of groups of 18 pixels and has allowed to lower the trigger threshold of the MAGIC telescope by a factor of two, to 25 GeV (Aliu et al., 2008), with relevant consequences for the scientific program of MAGIC.

5.4.6 Digitization system

The *digitization* system is also referred as the '*FADCs*' (Fast Analog to Digital Converters) in virtue of the high speed of digitization. Pulses are sampled at the speed of 2 GSample/s. Both the MAGIC-I and MAGIC-II readouts digitize at the same sampling speed but with very different electronics. A custom made multiplexed system (*MUX*) which uses commercial FADC (*Aquiris*) for the final digitization is used in MAGIC-I (figure 5.7, Albert et al. (2008*a*)), whereas a completely new approach is used in MAGIC-II (see

---

[7] An adjustable delay allows to fine-tune the system to correct for the slightly different transit time in the electronics channels.

[8] This is the topological constraint.

[9] This is known in MAGIC as the *prescaler*, the observers can choose through the central control program to accept just a fraction of the global trigger signal coming from the L1 units. This is useful to reduce the trigger rate without increasing the trigger energy threshold.

appendix B). The new 2 GSamples/s digitization and acquisition system is based upon a low-power analog sampler called *Domino Ring Sampler* (DRS). The working principle of the chip is the following: the analog signals are stored in a multi capacitor bank (1024 cells in DRS version 2) that is organized as a ring buffer, in which the single capacitors are sequentially enabled by a shift register driven by an internally generated 2 GHz clock locked by a PLL to a common synchronization signal. Once an external trigger has been received, the sampled signals in the ring buffer are read out at a lower frequency of 40 MHz and digitized with a 12-bit resolution ADC.
For a 1 kHz trigger rate[10], 2 GHz sampling frequency and 40 ns wide digitization window, the data throughput is roughly 200 MBytes/s, thus being a challenge for modern data transmission and storage solutions. The MAGIC I telescope produces currently per year 100 TByte of raw data that is calibrated and reduced on-site.

5.4.7 Calibration

The calibration of the signals from each channel is done to translate the information recorded by the FADCs into incident light flux in the camera. This is accomplished by calculating a conversion factor between number of recorded FADC counts and number of photoelectrons in the PMT. The final calibration must be in terms of incident photons, so that also the different quantum efficiency of the PMTs is taken into account.

The MAGIC calibration system[11] provides fast light pulses at different wavelengths and variable intensity in order to calibrate the whole dynamic range of the camera photosensors and their readout chain. The system consists of a box located at the center of the telescope mirror dish which houses 64 LEDs emitting at three different wavelengths: 370 nm (UV LEDs), 460 nm (blue LEDs) and 520 nm (green LEDs). The light pulses have about 3-4 ns FWHM duration. Fastness is important for the calibration pulses in order to correctly resemble the real pulses of a real shower.

The calibration of the signals recorded by each pixel of the camera is done basically in two steps: first a relative calibration and then an absolute calibration. The relative calibration equalizes the response of different channels when exposed to the same input signal. An absolute calibration is needed in order to convert the signal recorded by a pixel in FADC counts into physical quantities more related to the flux of photons arriving at the camera.

The absolute calibration can be performed by several methods (Gaug, 2006). The one currently used is the *F-Factor* method also called 'Excess Noise Factor' method. It is based on the fact that a photomultiplier adds only a small excess noise to the intrinsic fluctuations of the photoelectron flux, excess noise which is linearly related to the initial number of photoelectrons that produce its output signal. The F-Factor of any electronic device is simply defined as:

$$F = \frac{(Signal/Noise)_{input}}{(Signal/Noise)_{output}} \tag{5.1}$$

being therefore a numerical value which accounts for the additional noise introduced by the readout and amplification chain, assuming it is independent of the signal intensity. From the knowledge of the F-Factor of the photomultipliers and the analysis of the output

---

[10] This is the maximum sustainable acquisition rate specified for the readout in the design phase. The typical (standard trigger) acquisition rate is ∼ 300–400 Hz.

[11] See Gaug (2006) for a detailed description of the MAGIC calibration system.

signal of each pixel, one can extract the average number of photoelectrons impinging on the first dynode of each photomultiplier. More details on the implementation of the F-Factor are given in the PhD thesis: Gaug (2006).

The calibration system of MAGIC-II is based on a frequency tripled passively Q-Switched Nd-YAG laser, operating at the third harmonic at 355 nm, which has been installed in the center of the mirror dish. The pulse width at 355nm is 700 ps. For providing a large dynamic range we are using two rotating filter wheels under computer control that allow to illuminate the camera with intensities within 100 steps from 1 to 1000 photoelectrons.

5.4.8 Drive

The *drive* system of the MAGIC Telescope (Bretz et al., 2009) has been another challenging issue due to the high pointing accuracy required, the large dimensions of the telescope and the fast repositioning goal. The drive system of the MAGIC telescope is quite similar to that of large, alt-azimuth-mounted optical telescopes. The azimuth axis of the telescope is equipped with two 11 kW motors, while the elevation axis has a single motor of the same power. The current maximum repositioning time is about 120 seconds[12], while the average is around 40 seconds.

The accuracy of the pointing is guaranteed by the *starguider* system. It is appointed to monitor the exact pointing position and to correct for a possible mispointing. This is done though a sensitive CCD camera mounted on the center of the mirror dish (see figure

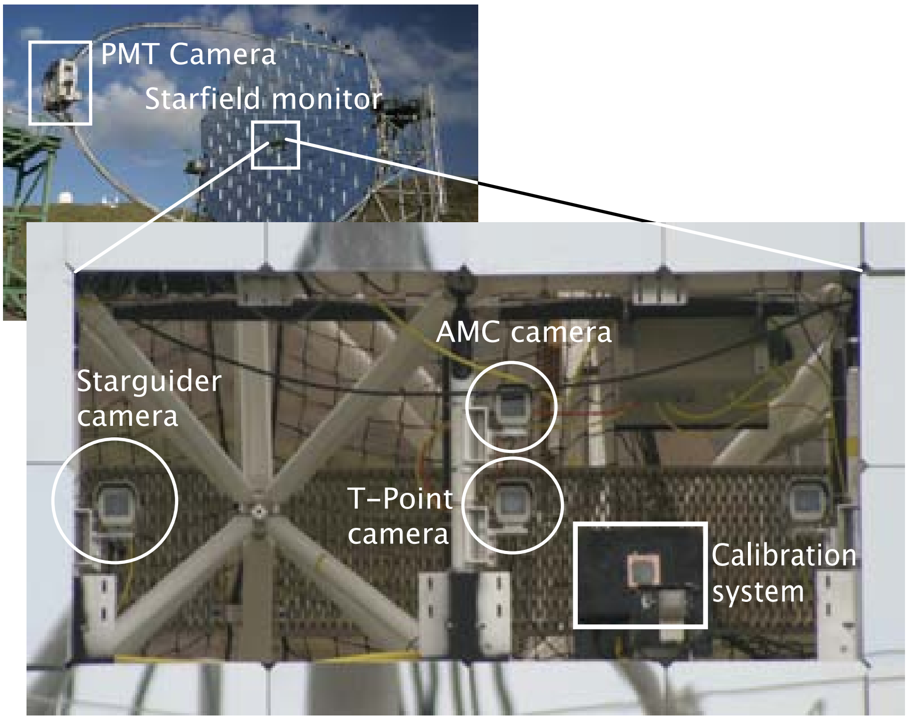

Figure 5.8: MAGIC-I central dish instrumentation. Similar devices are mounted also in MAGIC-II.

---

[12] This is the time spent to move the telescope 360° in azimuth. Generally the sky position where the telescope is pointing to and the position where it has to be pointed because of a prompt alert are not that separated.

5.8). The starguider camera points to the camera of MAGIC but its FoV is large enough (4.6°) to see also directly some of the stars in the FoV of the MAGIC camera. The actual pointing position can then be reconstructed by software and the actual pointing position recovered. The starguider information is actually used offline during the data analysis to correct for possible mispointings during the observtions. This is specially useful to precisely determine the position of a point source (Errando, 2009).

5.5 Performance of the stereo system

The stereoscopic view of the air showers improves dramatically the sensitivity of the MAGIC system. A factor $\simeq 1.5$–2 of improvement was expected and recent results form the MAGIC collaboration studies shows that the performances expected are actually achieved (see figure 5.9). The sensitivity at low energy actually results even slightly better than what expected from Montecarlo simulations.

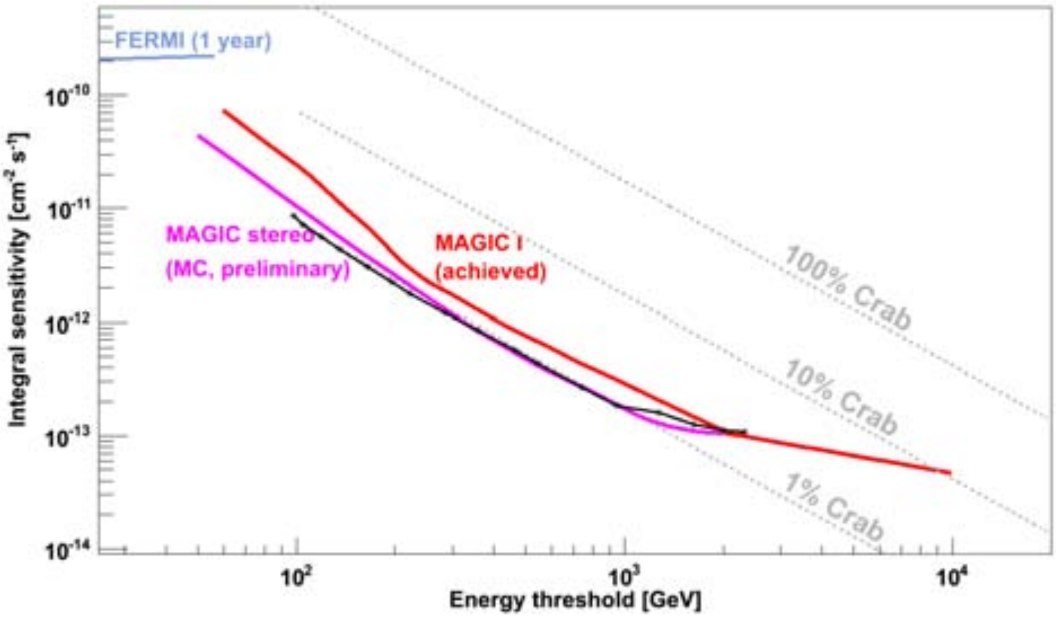

Figure 5.9: Preliminary MAGIC integral sensitivity. The red curve shows the sensitivity achieved with MAGIC-I stand alone. The pink and black curve represent respectively the expected (from Montecarlo) and achieved (from real data) sensitivity with stereo observations after the coming online of MAGIC-II.

5.5.1 Future plans

The smaller trigger area and somewhat lower light conversion efficiency of the first MAGIC telescope are know to limit the performance of the whole stereo system. This justifies a recent decision to upgrade the MAGIC-I telescope. The upgrade will affect the camera and readout and is planned in 2011.

The current MAGIC-I camera will be dismissed and a clone of the MAGIC-II camera (already in production) will be put in its place. The new MAGIC-I camera will be a clone of the camera of MAGIC-II, i.e., will have an increased trigger area and will be fully equipped with 0.1° FoV pixels. However its inner section (about 400 pixels) may be readily equipped with HPDs. In such a case the sensitivity of the new camera would significantly increase for low energy showers.

The readout will also be upgraded to a digitizing system similar to that of MAGIC-II and the current MUX readout electronics dismissed. The principal novelty of the readout will be the use of the DRS-4 chip instead of the DRS-2 chip currently used in MAGIC-I.

Chapter 6

Data analysis

How do we analyze the MAGIC data?

6.1 Data analysis

The final goal of a Cherenkov telescope experiment is to measure the flux of cosmic γ-rays from a given sky spot or region, generally associated with an astrophysical object. Possibly not only a single integral flux value is obtained but also a complete *energy spectrum* and a *lightcurve*, which is the gamma-ray flux as function of the time of the observation. We will describe in the following sections how it is possible to work out these final measurements in the case of the MAGIC telescope experiment described in chapter 5.

6.2 Analysis approaches

The data analysis strategy is typically chosen accordingly to the particular observation conditions and the intrinsic characteristics of the emitting source to be analyzed. The zenith angle range or the background light conditions (for example for observations during moon time) as well as the angular size (*point-like* or *extended*) or the expected characteristics of the spectrum (*soft* or *hard*[1]) are the key elements for the choice of the type of analysis. Often these characteristic are not well known, sometimes totally ignored, and in those cases the analyzer will try to make the most general and reasonable physical assumptions.

The analyzer can either decide to go for an *alpha*-type analysis or a *theta-square*-type analysis, being these two the final geometrical parameter space where to look for a gamma-rays excess signal. As explained in section 4.3.3, Alpha (in the following also simply: α) indicates the geometrical orientation of the image in the camera with respect to the source position. Since γ-rays coming from the pointed target will produce preferentially images oriented toward the position of the source in the camera, whereas the isotropic cosmic-ray background will produce randomly oriented images, an excess of events in the signal region (small α values) is expected. The other possible angular variable, θ, is defined as the angular distance in the sky between the expected emitting position and the reconstructed incoming direction of the recorded shower. The γ-rays coming from the

---

[1] TeV sources have typically power-law-like spectra $dN/dE \propto E^{-\Gamma}$. A 'soft' or 'steep' spectra is characterized by large Γ values (~ 3) whereas a 'hard' or 'flat' spectrum is characterized by smaller Γ values (~ 2).

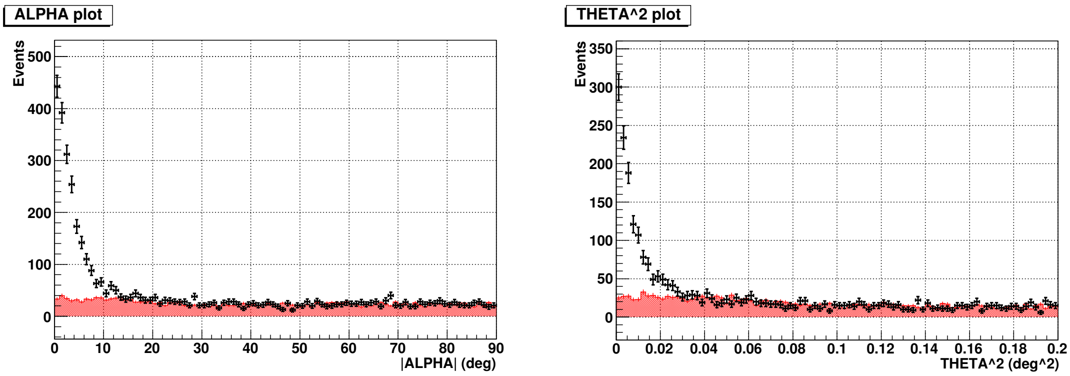

Figure 6.1: α-plot (left panel) and θ^2-plot (right panel) examples.

observed object will be reconstructed preferentially close to the source position in the sky, so that also in this case an excess is expected in the small θ^2 values region of the plot. The parameter is used squared in order to obtain a flat shape for an isotropic background[2].

The α-analysis approach is suitable when the emitting source can be considered as point-like. This depends of two factors: the extension of the source in the sky and the point spread function of the telescope. If the apparent size of the source (given its distance to the earth) is much smaller than the uncertainty in the reconstruction of the γ-ray arrival directions (typically $\sim 0.1°$) the source can be considered as point-like. Point-like sources are typically extragalactic objects, given their huge distance to the earth, but also galactic objects, when they are intrinsically small in size. In the case of a point-like source with very well known sky coordinates a so-called *source-dependent* analysis can be performed (a priori assumptions about the location of the source are done). A source dependent analysis has the advantage that some special image parameters can be used together with the standard image parameters. These extra parameters, like the third moment (with sign) of the light distribution along the major image axis, *M3long*, or the image time profile *Time Gradient* (see section A.2.3), allow a better background rejection and consequently an enhanced sensitivity in the analysis, but they require the knowledge of the source position to be properly computed.

The θ^2 analysis is instead more suitable when the source of gamma rays is extended or when the position of a point-like source is not well known. A 'source-independent' analysis allows the production of sky maps showing the excess of gamma rays in the observation field, but no assumptions about the source location can be done, resulting in a less sensitive analysis. In the case of a single dish telescope the reconstruction of the primary gamma direction is done through the so-called *Disp* method (see section 6.6.4), but the quality of the source position estimation degrades very fast lowering the energy of the primary gamma. For this reason when the analyzer aims to go at low energy in the analysis the α-approach is generally preferred, being easier to determine just the image axis orientation for small images. This is because of the limited number of pixel available: the image axis can still be reconstructed (even if poorly) whereas the Disp estimation become not reliable at all.

The θ^2 approach is always the standard analysis type for stereoscopic systems of

---

[2] The shape of the background is actually not totally flat because of the variation of the camera acceptance (it decreases going away from the camera center), resulting in a smooth peaking close to the 0 values (see figure 6.1).

IACTs because the incoming direction of the shower can be easily determined by the intersection of the axes of the multiple shower images.

6.3 Observation modes

Contrary to what one would expect from a common telescope, most of the MAGIC observations are not performed pointing directly to the expected emitting source, but 0.4° off-axis with respect to the source position. This observation mode is called *wobble*, or more properly *false-source tracking* mode (Fomin and et al., 1994). In the basic *tracking* mode (a.k.a. *on–off*), observations are two fold: part of the observation time is used to aim directly to the candidate γ-ray source and part is used to point to a "dark" (in the sense of free of gamma-ray sources) sky region. This second "off" observation is needed to estimate the background recorded together with the possible γ-ray signal. In other words, the number of events that after all the cuts still resemble gamma rays has to be properly estimated and subtracted from the "on" signal counts, in order to measure the real gamma excess[3]. In the case of wobble observations there is no need to spend time to perform off observations because the background estimation is done using the same observation field. In fact, if the real source is set far enough from the camera center, there is enough space in the field of view to define *off regions* in the sky area not affected by the γ-ray source. The number of off sources that can be fit is limited by the size of the camera (FoV) and by the constrain to not overlap one with the other (in order to remain statistically independent). This means that the maximum number of off regions increases moving away the source from the center of the camera. Unfortunately, the efficiency of the camera is not constant in the whole field of view, it decreases moving away from the center so that 0.4 degrees is actually the best compromise between efficiency and number of off position that fit in the camera. On figure 6.3 a sketch of the 3 off regions typically defined in this kind of analysis. Another advantage of the wobble mode respect to the tracking mode is the more accurate control of systematics. The off observations are in fact performed exactly at the same time of the on observations, leaving no room for eventual bias due to a different atmospheric conditions, different background light conditions and unforeseen changes of the ambient environment in general.

Drawbacks of the wobble mode are mainly two. The first is a loss in the gamma-ray detection efficiency, which is estimated to be of the order of 15–20% and is mainly caused by the smaller effective trigger region around the source position[4]. The second is the possible bias introduced by an off-center source position. There is for sure a small effect due to the zenith angle, which is slightly different for the source position and each one of the off positions. A worst bias effect is introduced by a non homogeneously efficient camera, since there might be regions of the field of view clearly favor or disfavored in term of efficiency (the only perfectly symmetric point is the camera center). In order to minimize this latter effects several precautions are taken when the data are analyzed,

---

[3] At the dawn of the IACT technique, the Whipple telescope was also observing in *discovery mode*. The source is tracked continuously without taking data off source on a control region. Events whose orientations are such that they are not from the direction of the source are used to determine the background level (Quinn et al., 1996). Technically, this is done extrapolating a fit function from the background region up to the signal region. Given the larger uncertainties involved this method is actually a deprecated, specially to establish new detections.

[4] The pixels connected to the trigger system resides in a circular region centered on the center of the camera, so that a source located 0.4° away from the center suffers by the loss of trigger efficiency in the outer part of the camera.

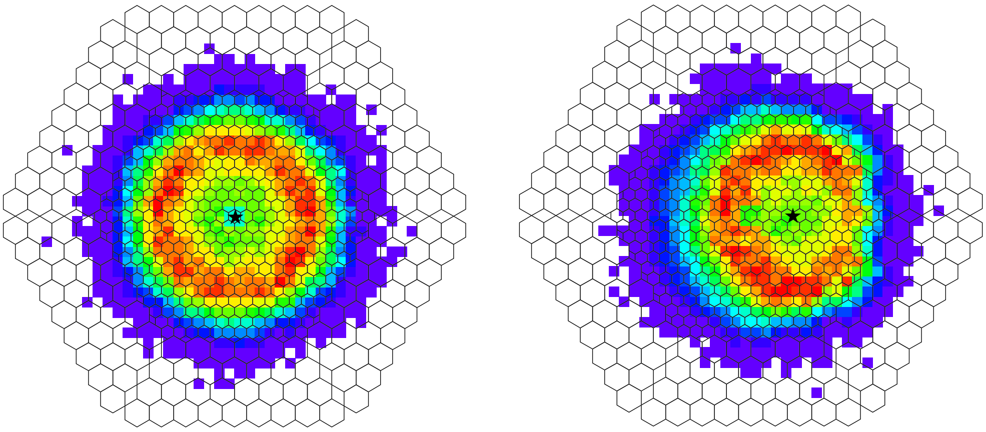

Figure 6.2: Center of gravity plots for tracking (left) and wobble (right) observation modes. Notice the loss in efficiency for the wobble mode due to the limited trigger area (loss on the edge of the camera). Plots from Errando (2009).

but the main action to counteract this problem is taken during the data-taking: two off-axis positions are defined, symmetrical one to the other, and the pointing position is swapped between the two every 20 minutes of observation time[5]. This guarantees that the same physical region of the camera is used both for the on and the off estimation. This compensates quite efficiently the effects of hardware inhomogeneities with the only condition that the observation time has to be long enough, namely at least 40 minutes, to guarantee the symmetry between the two wobble positions. A caveat of this procedure is the fact that the compensation due to the swap is fully guaranteed only for the *anti-source* (the off position located symmetrically to the source, see also figure 6.3). Bias effect from the “side” off regions are simply averaged by the swap, so that the safest analysis is obtained using only the anti-source off position.

6.4 Montecarlo production

The Montecarlo simulations of γ-ray events is of crucial importance in the analysis of the MAGIC data. Several studies have been performed inside the MAGIC collaboration in order to obtain a Montecarlo database as accurate as possible. Simulated gamma images have to resemble the true gamma to a very high degree of precision in order to obtain the correct image parameters to be compared with the real data. The agreement in the image parameter distributions for true and simulated γ-rays resulted to be good (Albert et al., 2008*d*). Although a single real gamma can never be identified with 100% confidence, the comparison real/simulated gamma is possible statistically. In fact, if the parameter distribution for real gammas is built as the difference of the on and off distribution for real events (when observing a strong γ-ray source!), the residual is the distribution for the real gammas.

Three types of events are produced in the simulation, γ, p and He^{++}, but the gammas are by far the most important. Since the background (protons and helium) features can

---

[5] This is actually the reason of the name “wobble”.

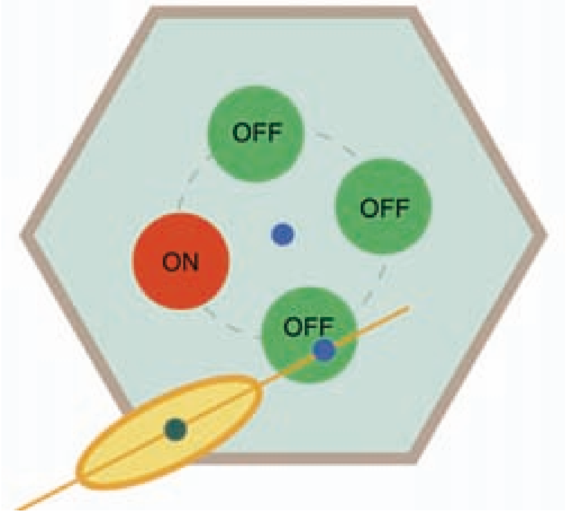

Figure 6.3: Sketch of the definition of the signal (on) and background (off) regions in wobble observations. The *anti-source* is the off position located symmetrically to the on position (the red circle) with respect to the center. Plot from Mazin (2007).

be also recovered from real cosmic events, which are the majority of the triggered events in a IACT, only gammas were massively produced. The production of simulated MAGIC events goes through three steps:

shower production The development of the electromagnetic air shower induced by the primary χ-ray is simulated using the CORSIKA 6.019 package (Heck et al., 1998) using the US standard atmosphere. The output files store the location and direction of the Cherenkov photons produced by the air shower when they reach the ground level, in the case of MAGIC at the altitude of 2200 m. Showers with different energy, zenith angle[6] and orientation with respect to the geomagnetic field are produced.

reflection of the Cherenkov photons The Cherenkov light pool information stored in the CORSIKA files are used by the `reflector` executable to simulate what happens when the light front hits the the mirror of the MAGIC telescope. The optical properties of the reflecting dish, like reflectivity and optical point spread function, are taken into account. Even if more related to the shower development, the absorption and scattering of the Cherenkov photons in the atmosphere is also included in this step of the simulation. The effects of the Rayleight scattering, due to the molecular atmosphere, and the losses because of the Mie scattering, due to the ozone and aereosol layers, are also taken into account. *Reflector* data files which store the positions and directions of the reflected photons in the camera plane are produced as output.

acquisition of the event The informations contained in the reflector files are used to simulate the final Cherenkov images. Notice that an optical smearing, tuned with the optical point spread function obtained from a star image, is applied to the direction of the Cherenkov photons. This is done at this late stage to enhance the flexibility, since the point spread function is subject to degradation and periodical

---

[6] MC files are actually grouped by *Zbins*. The Zbin is a parameter defined as the cosine function of the zenith angle, which is the physical quantity that actually affect the shower development in the atmosphere.

readjustment during the observation periods (see also figure 7.2). The program that takes care of this last step is called `camera` and its task is to simulate the response of the MAGIC camera (see 5.4.3), of the trigger and of the data acquisition electronics. The output files have the same format of a real MAGIC raw data file and can be interpreted by the MAGIC analysis software (see section 6.6).

Further details on the `reflector` and `camera` programs and on the MAGIC Montecarlo can be found in Majumdar et al. (2005), Moralejo et al. (2004*a*), Majumdar et al. (2006) and Commichau et al. (2008).

6.5 Data quality

As we know from chapter 4, imaging air Cherenkov telescopes are detectors which operate under not fully controlled conditions. Contrary to HEP accelerator experiments, where the laboratory environment is perfectly controlled, Cherenkov telescopes have to deal with the earth's atmosphere. Typically the observations are performed only under "good" weather conditions, but quantify it precisely is very hard.

The most important parameter used to evaluate the observation quality is the *trigger rate*. The *discriminator threshold* is the minimum signal required in a channel in order to discriminate the emission of a digital input signal for the trigger system (see also 5.4.5). These thresholds are optimized to have a negligible rate of random triggers. In other words, the thresholds are high enough not to run into random triggers generated by the NSB, but low enough to allow also the low energy showers to trigger the readout. Given the fact that the CR flux is dominated by the constant isotropic hadron background[7], the trigger rate is expected to be constant during an observation. Also within different nights if the discriminator thresholds are not changed the rate is expected to remain the same. A cut on the event trigger rate is an effective quality cut and is normally use by the analyzers to exclude problematic data from their data sample. For example a sudden worsening of the weather conditions due to clouds or fog immediately results in a drop in the trigger rate, whereas an increase of the rate is associated to an increase of the background light level.

A special device called *pyrometer* was installed at the observation site in La Palma. This tool allows to continuously measure the amount of clouds in the sky, and is particularly useful when the weather conditions are not very well defined (not a clear night but not an overcast sky either). This information, named *cloudiness*, is included in the data stream and is also used as a priori quality cut during the data selection phase.

Concerning the light conditions, the amount of background light during the observations can be estimated in several manners. For example, it can be directly measured by a CCD camera pointed at the sky or by the direct current intensity at the photocathode of the PMTs which is proportional to the number of photons hitting the phototube. Another parameter which is proportional to the luminosity of the sky, and that can be measured, is the average discriminator threshold value. These thresholds are initially set to some default values, for example the mean threshold in case of dark night observations, but can be increased by an automatic routine for those pixels which are detected to trigger more often. The main purpose of the mechanism is to "switch off" the pixels illuminated by the stars in the FoV but it also reveals an increase of the mean background light since in that case all the discriminator thresholds will be increased. For example, in case of observation

---

[7] Only $< 0.1\%$ of the triggering showers are due to gammas.

during a rising moon night, the mean discriminator threshold will progressively increase as the moonlight becomes brighter and brighter. This is another typical parameter that allow an a priori data selection depending on the required light conditions.

A typical MAGIC analysis normally includes also few hours of observation of the Crab Nebula source. These observations, if possible, are chosen within the same observation period and with a similar zenith angle of the observation of the analyzed source. Given the strong and steady signal from the Crab Nebula[8] these data are considered as a sort of test sample where to check the consistency and sensitivity of the current analysis.

6.6 The analysis pipeline

The software of the MAGIC collaboration is named MARS, acronym of Magic Analysis and Reconstruction Software (Moralejo et al., 2009). MARS is a collection of classes and executables written in C++ programming language and relies on the ROOT[9] software framework developed at CERN for the most basic functions. The program were constantly developed during the years by many of the MAGIC collaboration members, using a CVS (Concurrent Versions System) management framework. The author actively contributed to the development of the MAGIC software during his PhD.

The analysis of the MAGIC data is composed by several consecutive steps. The analysis chain starts from the huge raw data files stored by the data acquisition system of the telescope in La Palma and leads, in case of a positive detection, to the gamma-ray energy spectra and lightcurves which are eventually published in the relevant journals of the astrophysical community.

6.6.1 Raw data reduction

The first step of the analysis chain reduces the raw data files into ROOT files that have a format compatible with ROOT and with the MARS software. Also the relevant informations coming from the telescope subsystems (Drive, Camera Control, etc.) are in this phase merged with the event image data so that from now on they can be easily recovered in the data files. The executable in charge of this task is called `merpp`.

6.6.2 Calibration

When an atmospheric shower triggers the data acquisition of MAGIC, the information of all the camera pixels is stored by the Data AcQuisition (DAQ) system. The MAGIC telescope has a quite sophisticated readout system. The Cherenkov photons flashes, which we know to be very short in time, produce very short signal pulses at the cathode of the PMTs. The pulse is not simply electronically integrated and then measured but it is instead digitized with an ultra fast sampling frequency, namely 2 GSample/s. The sampled pulse is stored in the raw data, 50 samples are recorded by MAGIC-I whereas 80 samples are recorded by MAGIC-II. The reconstruction of these informations is called *signal extraction* and is performed by the `callisto` executable of the MARS package. The intensity of a signal is measured in *photo-electrons* (phe). On the figure 6.4 a typical

---

[8] The calibration of Cherenkov telescopes is very difficult because it is impossible to test the detector in laboratory conditions using for example a test beam. To bypass the problem, the Crab Nebula is used as "standard candle" source. It is a young PWN, extremely powerful in γ-rays.

[9] http://root.cern.ch/drupal/

Cherenkov pulse digitized by the MAGIC readout is shown. As mentioned the signal extraction procedure determine the intensity of the signal and its arrival time. Several extraction routines have been studied during the commissioning phase of MAGIC, from simple "fixed window" counts sum to more complicated "sliding window" algorithms. The current default procedure for the signal extraction is called *extract time and charge spline*. The routine first interpolates the pulse shape with a cubic spline curve and then scans a 7 samples wide integration window within the digitization area, maximizing the sum of the samples counts (Albert et al., 2008*a*). This number represent the intensity of the signal in terms of FADC counts. This maximum is associated with the peak position of the pulse. The *arrival time* is defined as the position of the rising edge of the pulse at 50% of the peak value.

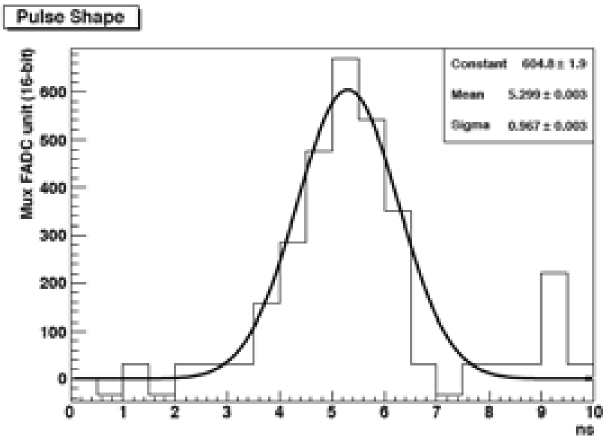

Figure 6.4: Example of Cherenkov pulse as digitized by the MAGIC readout (Goebel, 2007).

The `callisto` executable is also responsible for the *calibration* of the signal intensity. Once the number of counts is recovered by the signal extraction algorithm it has to be converted to the equivalent number of photoelectrons arriving to the first dynode of the PMT. To do so the so-called *F-Factor* method is used (Mirzoyan, 1997). Special data runs of pedestal and calibration events are taken for this purpose during the data taking. The pedestal events are obtained randomly triggering the telescope, so that no shower signal are recorded in the pixels and the data can be used to determine the baseline of the signals and its fluctuations. Calibration data events are generated by short ($\simeq 2$ ns) light pulses of intensity comparable to the real Cherenkov signals. The events are digitally triggered and stored in special data runs called *calibration runs* which are taken roughly every hour of observation. The number of phe generated during a calibration run is Poisson distributed with a mean N and a ROOT mean square $\sqrt{N}$. Now, the corresponding measured charge (after pedestal subtraction) in FADC counts also has a mean $\langle Q \rangle$ and a RMS σ but this latter RMS is wider than the pure poisson expectation. The relative widths of the distribution can be express as:

$$F \cdot \frac{1}{\sqrt{N}} = \frac{\sigma}{\langle Q \rangle}$$

where F is the characteristic F-Factor of the phototube. This factor takes into account the additional broadening of the measured distribution due to the multiplication process of the electrons in the dynodes. The F-Factors were measure in the lab previously to the installation of the photosensors in the camera and are known quantities. The calibration runs taken during the observation allow to compute the quantities $\langle Q \rangle$ and σ so that the *conversion factor* C can be computed by:

$$C = \frac{N}{\langle Q \rangle} = F^2 \frac{\langle Q \rangle}{\sigma^2}$$

and finally the number of phe by:

$$N = C \cdot Q$$

Calibration events are not only stored in the calibration runs but also in the normal data files, interleaved at a rate of 50 Hz with cosmic events, so that the conversion factor can be constantly updated[10]. See Gaug (2006) for all the details about the calibration of the MAGIC telescope.

6.6.3 Image cleaning

At this stage of the analysis the data are composed by the extracted signal and arrival time in all the pixel of the camera. Now, the shower information contained in the Cherenkov images have to be extracted from the full frame events. The calibrated pixel signals are first used to perform the *image cleaning* i.e. the pixels belonging to the shower image are selected from the whole camera picture (in figure 6.5 an example of an event before and after the cleaning is shown). This procedure is delicate since the Cherenkov light fade-away on the border of the images so that removing pixels depending on the intensity of the signal, which is the main handle available, inevitably results in cutting part of the image. In the next subsections the algorithms currently used in MAGIC are described in detail.

Standard image cleaning

In the MARS software different cleaning methods can be chosen by the user. The most commonly used is the *standard–absolute* method, used also for the production of the official data files provided by the MAGIC data center.

This standard procedure uses a threshold signal value (in terms of phe) to select the so-called *core pixels* (only clusters of at least two contiguous pixels above threshold are considered) and a second threshold to reject or select the neighbors as *boundary pixels.* A pixel of the camera is considered as part of the image if its charge is above the boundary threshold and at least one of its neighbors is a core pixel. The thresholds values often used in MAGIC analysis, before the MUX-FADC upgrade, were 10 phe for the core and 5 phe for the boundary pixels. The method is called *absolute* because the thresholds are set in terms of an absolute number of phe measured in the pixel. The alternative *relative* method, takes into account the fluctuation of the noise in the PMT considered: the absolute number of phe of the pixel is compared to the characteristic pedestal RMS of the pixel. A disadvantage of the relative method, is that the pixels illuminated by bright stars require a larger Cherenkov light density to survive the cleaning, since the

---

[10] Changes in the conversion factors can be due to variation in the transmission of the signal from the camera to the readout system during the night. For example the analog to optical converters are very sensitive to temperature changes.

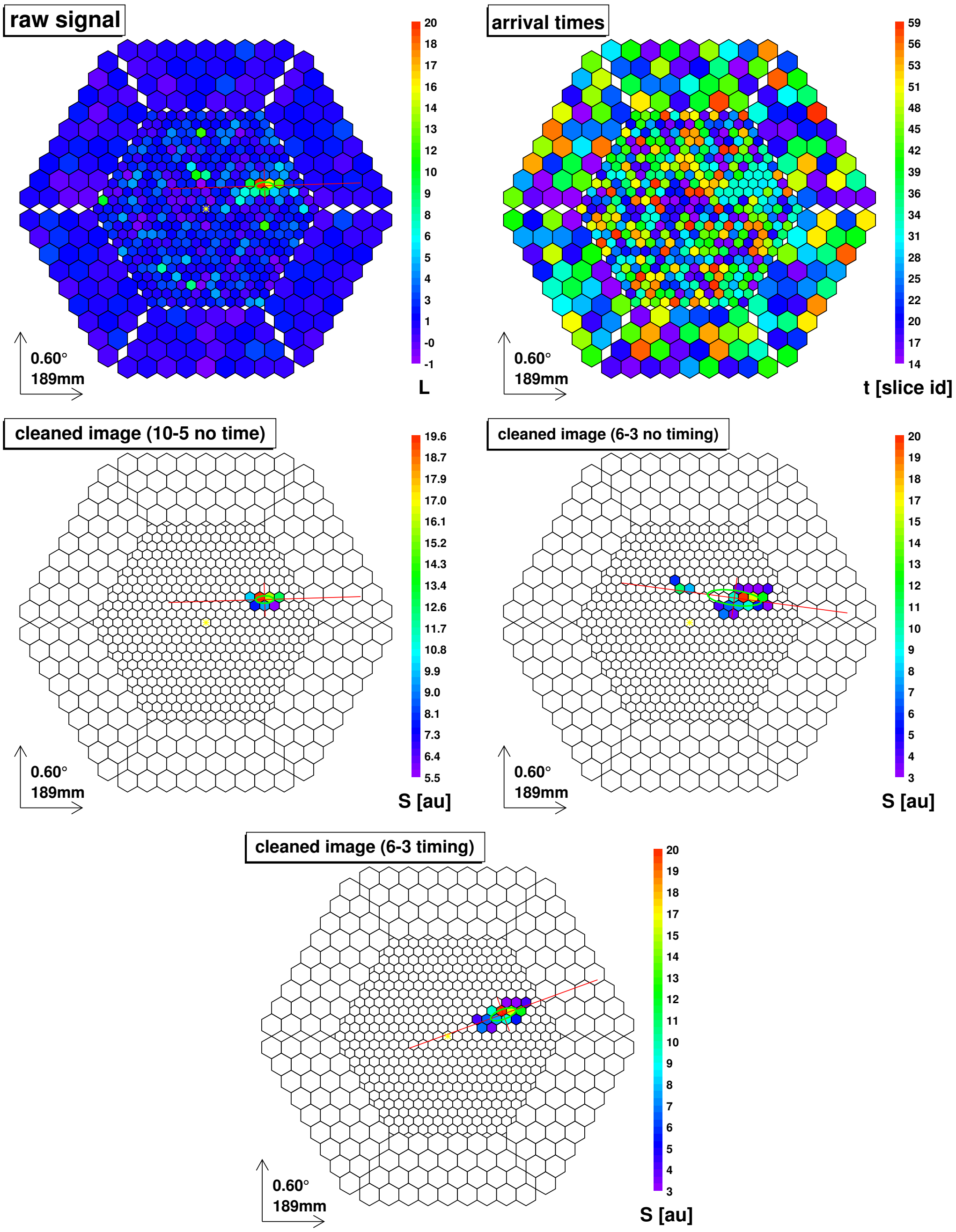

Figure 6.5: Illustrative γ-event images (Montecarlo data, energy = 71 GeV, impact parameter = 110 m). First row: display of raw recorded data (left) and arrival times information (right). Second row: comparison of standard cleaning with 10-5 phe minimum charge levels (left) and 6-3 minimum charge levels (right). Bottom: image obtained with the time image cleaning (6-3 phe minimum charge levels and 4.5 ns and 1.5 ns as time constrains). Notice the larger extension of the image cleaned with the 6-3 cleaning. The simulated gamma-ray source is located in the center of the camera (yellow star). From Aliu et al. (2009).

pedestal RMS is in this case very high. This makes the analysis more difficult since the same shower would appear rather different on different parts of the camera.

The choice of the cleaning method and the optimization of the threshold levels have been done quite empirically during the commissioning phase and the first observation cycles. Relaxing the cleaning levels results in a larger number of pixels per image and accordingly a lower analysis energy threshold, since a minimum number of pixels is needed to proceed with the analysis. On the other hand, a low threshold increases the probability to include in the cleaned image a pixel just due to noise (mainly due to NSB or other unwanted light pollution). The inclusion of pixels unrelated to the shower degrades the image parameters and worsens the performance of the subsequent analysis. The previously cited values of 10 and 5 phe were found to be a good compromise, but different choices can, in certain cases, produce better results.

Time image cleaning

Together with the signal intensity also an arrival time value is assigned by the signal extractor to each pixel. This arrival time is given in terms of time slices (t.s.), i.e. in terms of digitization samples units (1 t.s. = 3.3 ns for old FADCs data whereas 1 t.s. = 0.5 ns with the new MUX-FADCs).

Timing can be used to further constrain the selection of core and boundary pixels in the image cleaning algorithm. Since Cherenkov flashes are very short in time (of the order of few ns) NSB photons produce pulses statistically asynchronous with respect to the pulses of the shower image. A timing coincidence window between the mean arrival time and the single pixel arrival time can avoid to confuse NSB signals with real image tails. This further constrain allows to relax the standard cleaning levels, lowering in this way the energy threshold. This option can be easily enabled in the MAGIC software, in an analogous way as the thresholds values are set.
The resulting (standard with time constraint) procedure can be summarized in this way:

- During the first step of the image cleaning (that consists in finding out the core pixels scanning the whole camera looking for pixels above the core threshold) it requires that the arrival time of an isolated cluster of core pixels does not differ from the global arrival time (obtained averaging the arrival time of all the core pixels) by more than a fixed offset.
- In the second step, that consists in finding out the boundary pixels (a pixel is considered as boundary pixel if it is neighbor of at least one core pixel and its charge is above the boundary threshold), it requires that the time difference between the boundary pixel candidate and its neighbor pixels is less than a second fixed time constraint.

In other words: a pixel survives the image cleaning if its charge is above the boundary threshold, at least one of its neighbors is a core pixel and its arrival time is within ±Δt of that of the core pixel. The values for the two time constraint, called *TimeOffset* and *TimeDifference*, are set by the user in an analogous way as for the signal levels.

6.6.4 Image parameters calculation

The fourth step of the analysis consists in the calculation of the image parameters mentioned in section 4.3.3 and sketched in figure 4.10. Only the relevant information is kept at this high level of the analysis, for example the data about the single pixels signal is drop and only the image parameters values are kept. Consequently the size of the data files (*star files*) is reduced substantially. Both the image cleaning and the image parameter calculation tasks are performed by the `star` executable of MARS. In figure 6.6 the distribution of some of the image parameters are shown (please read the caption of the figure for further details).

A minimum cut in the image parameter Size is normally applied before proceed in the analysis chain. Roughly speaking, Size is the integrated light in the image image and related to the primary gamma-ray energy, so that a minimum Size cut immediately result in an increase of the analysis threshold. Nevertheless, a minimum Size cut is worth for several reasons. The image cleaning allows to survive shower images composed by at least 3 pixels, but it is clear that in many cases this is incompatible with a proper calculation of the Hillas image parameters. We also know that the background rejection power rapidly decrease at low energies. Small images are also much more sensitive to inefficiency of the camera as shown in figure 6.7.

A minimum Size cut removes at once the too small images, ensure a minimum background rejection power and reduce the extent of a possible inhomogeneities bias. The tuning of the cut value is a trade between minimum energy threshold and analysis performance. Typical minimum Size cuts lies within 80 and 200 phe. Another (weak) reason to apply a minimum Size cut is a considerably reduction of the analysis computing time.

In addition to the already mentioned classical Hillas parameters, further relevant image parameters have to be mentioned. In particular we will mention the time-related image parameters that the MAGIC experiment uses to enhance the analysis performance, and the parameter *Disp* which allows to produce θ^2 plots and sky-plots even with a stand alone Cherenkov telescope as it was MAGIC before the commissioning of the second telescope of the array. They are described in the following subsections.

Time-related parameters

One of the advantage of a fast readout is the possibility to digitize precisely the Cherenkov pulses. This allows to extract from the signals also a precise arrival time of the Cherenkov photons in the camera. The possibility to exploit the time information have been extensively studied in the past (Tescaro, 2007). From the results of those studies (Aliu et al., 2009) two time-related image parameters were introduced and added to the set of image parameters computed by `star`. They are shortly described in the following:

- **TIME GRADIENT**: This parameter measures the magnitude of the time profile of the event. To compute it, first the major axis of the image is found, then the pixel coordinates are projected along the axis so that the problem is reduced to one dimension. Finally, using only the space coordinate along the major axis, a graph of the arrival time is built and fitted with a linear function $y = m \cdot x + q$. The linear coefficient m represents the *Time Gradient* image parameter.
- **TIME RMS**: This parameter measures the arrival time spread of the Cherenkov photons in the pixels belonging the cleaned image. It is defined by:

$$TIME\ RMS = \sqrt{\sum_{i=1}^{k} (\ t_i - \bar{t}\ )^2} \tag{6.1}$$

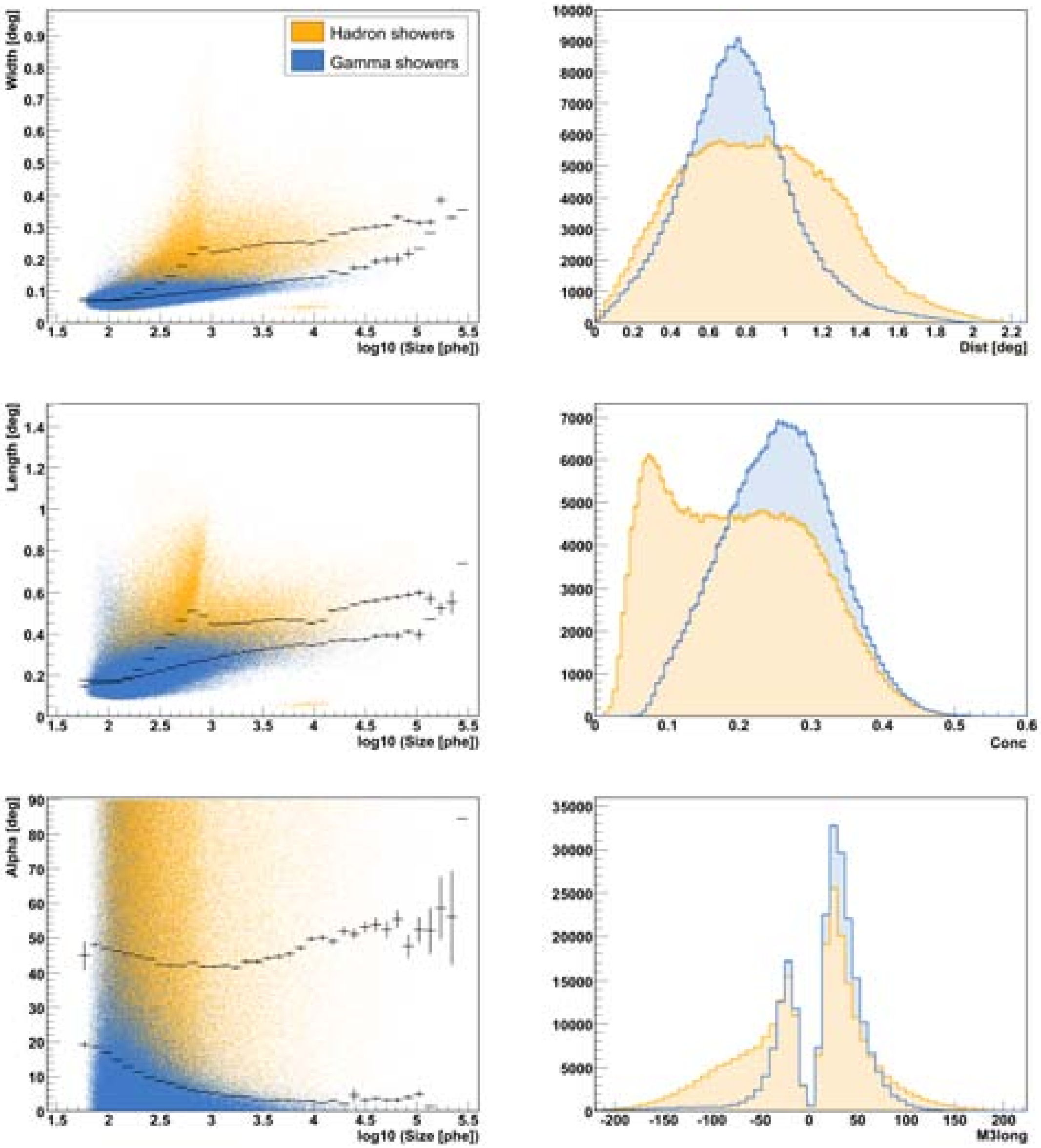

Figure 6.6: Distributions of different image parameters for simulated gammas and unselected data events (mostly hadronic showers). Width, Length and Alpha are shown as a function of the image Size. Black crosses show the position of the mean value of the parameter in each Size bin. Plots from Errando (2009).

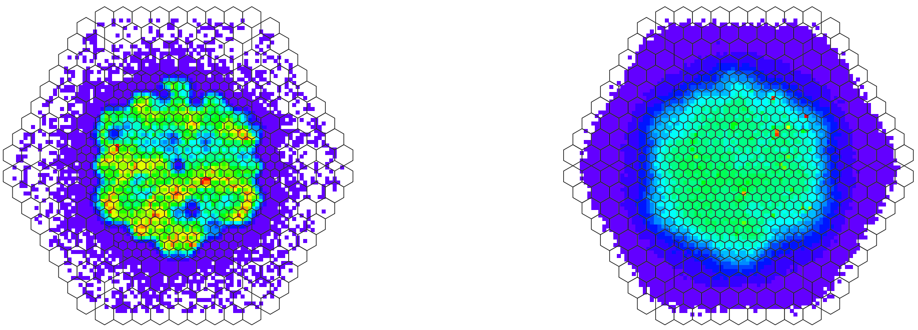

(a) *Size* < 150 phe (b) *Size* > 150 phe

Figure 6.7: Center of gravity distribution of MC simulated gamma-ray showers superimposed on the MAGIC camera layout. It is shown that showers with small *Size* are more sensitive to camera inhomogeneities, mainly caused by malfunctioning pixels and trigger inefficiencies while larger *Size* images show a uniform distribution throughout the trigger region. Plots from Errando (2009).

> Due to the time structure of the events, this parameter is also correlated with the Time Gradient. The RMS of the arrival times would be less correlated if computed respect a fit along the mean axis of the image.

Please see section A.2.3 for a more accurate description of these parameters and the full appendix A for a general explanation of the reasons of their background rejection power. Here, we just want to mention that previous studies determined that along the major axis of a gamma induced Cherenkov image is expected a time structure (time gradient). The magnitude of this gradient is related to the angle between the telescope and the shower axes, and for χ-initiated showers of a given direction, is well correlated with the Impact Parameter (IP) of the shower. In turns, Time Gradient is correlated with Dist for gamma-ray images from a point-like source, whereas no such correlation exists for hadron images (see fig. 6.8).

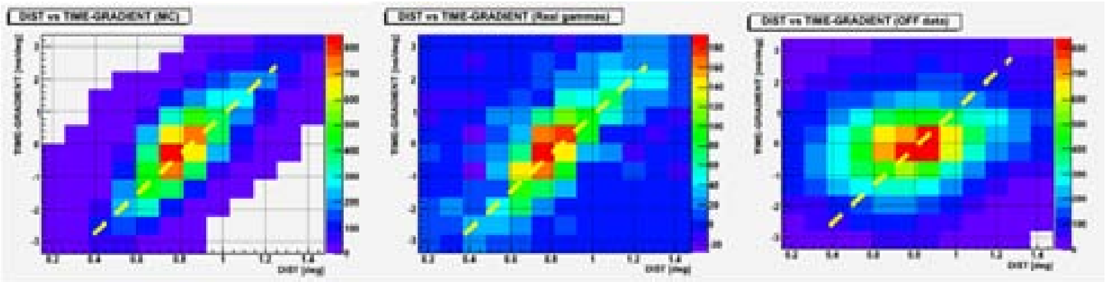

Figure 6.8: Time Gradient versus Dist parameter correlation for MC-χ-rays (left), real-χ-rays (center) and hadron (right) data. Notice the clear correlation in case of signal events and its absence in case of background events.

Regarding the Time RMS, it has been suggested in Mirzoyan et al. (2006) that it may be of help in identifying triggers produced by single, large impact parameter muons (whose images may otherwise be gamma-like), as well as other hadron-initiated showers (since their Time RMS distribution has, with respect to that of gamma rays, a longer tail towards large values). Unfortunately this parameter is not efficient as expected (see appendix A for a discussion).

Concluding, it is a proven fact that the analysis of MAGIC data that the inclusion of Time Gradient and Time RMS among the parameters already used in background discrimination, results in an enhancement of the telescope sensitivity (Aliu et al., 2009), with the major role played by the Time Gradient.

The ***Disp*** parameter

In section 6.2 we introduced the θ^2 analysis approach and mentioned that it is the standard for array systems of IACTs. The final plots where to compute the significance of the signal are made on the θ^2 parameter space with θ defined as the angular distance within the source position an the incoming direction of the γ-ray. In order to use this approach the incoming direction of each of the showers has to be reconstructed. In IACT arrays this arrival direction is given by the intersection of the multiple images axes on the camera plane, but it can be estimated also with a single Cherenkov telescope using the *disp* method (Lessard et al. (2001), Domingo-Santamaria et al. (2005)). The elongation of the shower image is correlated with the distance of the projection of the incoming direction of the shower in the camera with respect to the center of gravity of the image. This correlation can be parametrized and the coefficients optimized using MC data so that for each shower image the corresponding Disp can be computed[11]. Being the images symmetric there are actually two possible reconstructed positions. To break the degeneracy the M3long parameter (third moment of the charge distribution along the major axis) is used since it allows to chose the solution closer to the *head* of the shower (figure 4.8).

A new more performing method for the calculation of the Disp parameter have been recently introduced by the software developers of the MAGIC collaboration. The methos is described in the forthcoming MAGIC publication about 'AGN halos' which has not been released yet. The new method makes use of the Random Forest algorithm (see section 6.6.6) instead of the classical Width over Length parametrization. The improvement achieved mainly rely on the use of the Time Gradient parameter, which we know to be correlated with the impact parameter of the shower (see section 6.6.4), and the superior power of the RF method for the estimation of multivariate dependent parameters.

We have to mention that even if Disp can be considered an image parameter, it is not computed by `star` but in a further step of the analysis, namely by the `melibea` executable.

6.6.5 Background rejection

It is not possible to distinguish at trigger level the nature of an air shower. The fraction of recorded events due to gamma rays is of the order of 1 over 1000 even for strong gamma-ray sources like the Crab Nebula. Without a proper rejection of the background, the number

---

[11] The arrival direction position is assumed to lie along the major axis of the image, fact that is perfectly reasonable being the major axis the projection of the shower axis in the camera.

of gamma events in the signal region (low α for a point-like source) would be very small compared to the number of background events. As consequence, the observation time needed to have a statistically significant excess would be very long.

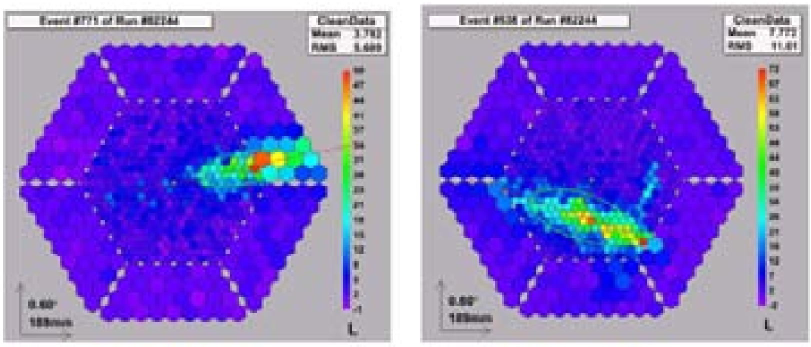

(a) γ-ray candidate (b) Hadron candidate

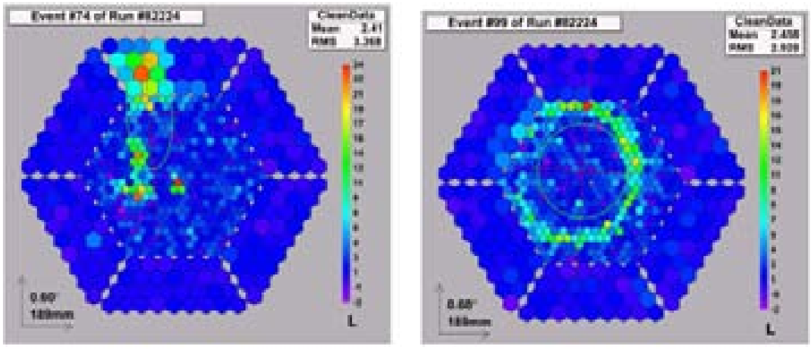

(c) Hadron candidate (d) Muon ring

Figure 6.9: Examples of MAGIC Cherenkov images.

The differences between electromagnetic and hadronic showers described in section 4.2 can be recognized in the recorded Cherenkov images (see figure 6.9 for some examples). The image parameters are supposed to characterize these differences in a quantitative manner.

Unfortunately, it is not possible to fully distinguish the nature of the shower that produces the image, for this reason it is more appropriate talk of γ-candidate and background-candidate events. The image parameters may be very similar between gammas and hadrons so that the accuracy of the background rejection separation is in this case very poor. Specially for low energy events, where the number of Cherenkov photons recovered is low and the size of the images is small, the separation is difficult up to becoming impossible below a certain energy threshold.

The next analysis step is the background rejection also known as gamma/hadron separation. This can be done with different algorithms. The most commonly used in the MAGIC collaboration is the so-called *random forest*, a classification method that makes use of the image parameters (described in the section 6.6.6). The strength of the γ/h separation can be defined by the analyzer (see section 6.6.6 for an explanation of the cut used for this purpose). A “hard” cut improves the separation quality but decreases the gamma efficiency ($\epsilon_\gamma = N\gamma_{survived}/N\gamma_{total}$). On the other hand, a “loose” cut increases the gamma efficiency but the probability that a given gamma candidate would actually be a γ-ray decreases.

6.6.6 The random forest

The Random Forest (RF) is a flexible multivariate classification method (Albert and et al., 2008). In the case of MAGIC the “objects” to be classified are the Cherenkov images generated by primary particles of unknown nature. Each event has a set of values (the image parameters) that we want to use to recognize the nature of the event.

The RF is first trained with events of known nature i.e. with gamma images (taken from MC simulation) and hadron images (taken from off data). In the separation training a quite large number of trees (default 100) are built by the RF. The creation of a tree proceeds in the following simplified manner: an initial data sample extracted at random from the training gamma and hadron samples is built. A cut in one of the separating variables[12] is applied and the initial sample is split in two accordingly (the first two branches of the three are formed). Very probably the two sub samples will still be a blend of γ and hadron events. The procedure is repeated iteratively (another random parameter and cut is chosen and the sub sample is split) so that the number of branches increases. The procedure stops when a sub sample composed only by gammas or by hadrons is found (a leaf of the tree is reached). The ending leaf is labeled as a 0 or 1 depending is made of gamma or hadron events respectively.

In the case of MAGIC the γ/h separation on the data sample to be analyzed is performed after the training, by a different executable (`melibea`), using the trees built in the training. Each event is passed through all of the separating trees. Depending on the characteristic parameter values of a given event, it will reach a particular leaf of each tree; the events scores a 1 or a 0 depending of the leaf label. A mean score is computed averaging over all the different separation tree results. This average is called *hadronness* (shortly: h) and represents a sort of probability for the event to be a hadron or a gamma. Gamma events well characterized will have a h value close to 0 whereas clear hadrons will score close to 1. Events of uncertain nature will fall in the middle of the range.

h groups in a single parameter the possible cut combination on the various image parameters, taking also into account the correlation between the parameters. On figure 6.10 the hadronness distribution for hadrons and gamma particles are shown. Please notice the low background rejection power at low energies whereas the separation is much more efficient at medium-high energies. The strength of the hadronness cut applied in the analysis determine the quality and the efficiency of the cut. The relative separation power of each variable introduced in the RF is measured by the so-called *Gini-index* plot (like the one provided in figure 7.3).

The RF turned out to be the easiest and most effective separation method accordingly to the study described in Bock and et al. (2004)).

---

[12] The cut value is optimized to separate the sample into its classes (in our case two: gammas and hadrons) whereas the choice of the variable is partially random. The *Gini-index* is used to optimize the cut and measure the classification power of the variable.

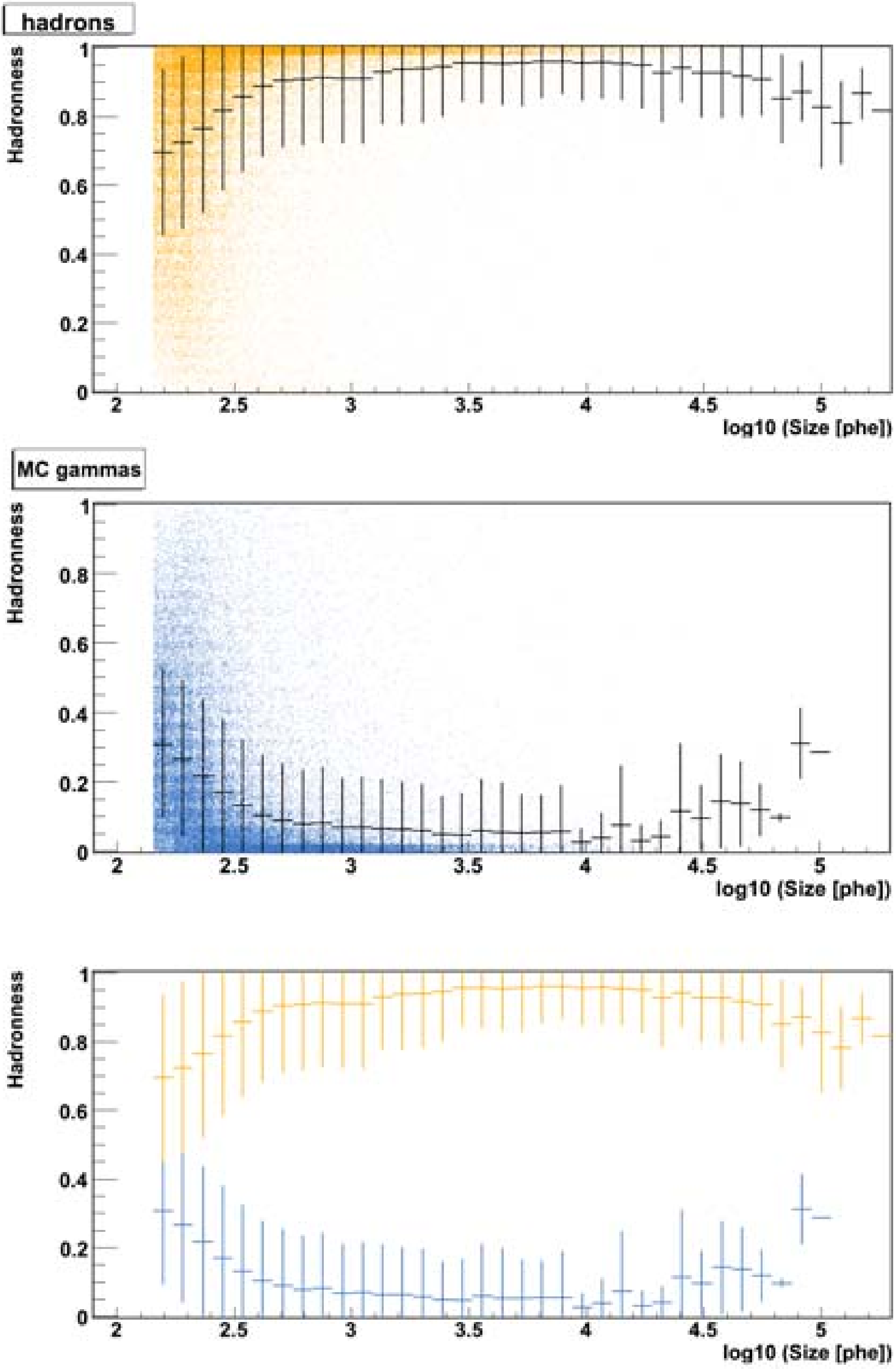

Figure 6.10: Hadronness distributions for hadron-like (upper panel) and gamma-like images (middle panel)as a function of *Size*. The black lines show the average h value for each Size bin and the error bar represents its RMS. These average profiles are compared in the lower panel.

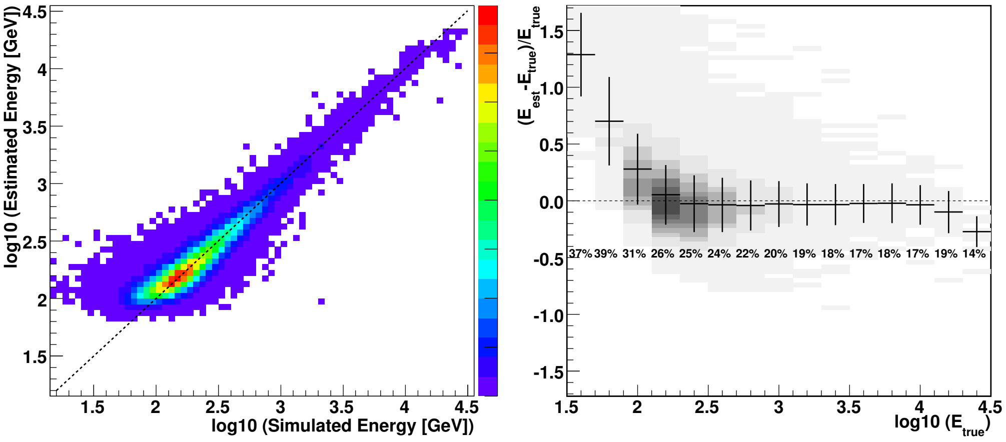

Figure 6.11: Migration matrix between estimated and simulated energy (left panel). Resolution of the energy reconstruction (right panel). Numbers indicate the energy resolution for each bin of simulated energy.

6.6.7 Energy estimation

The estimation of the energy of the γ-ray candidate events is performed with the Random Forest algorithm (see 6.6.6 for a general explanation of the method), which can also used for the estimation of a continuous variable. In an analogous way as for the background rejection, the random forest is trained with Montecarlo gammas, whose energy is known. The main difference stands in the way the RF-trees are built: the optimal cut in each node of the trees is chosen to minimize the variance of the true energies of the event samples resulting from the split, rather than their purity (Albert and et al., 2008). Like for background rejection, the RF energy trees are first built and after used to process the real data events in order to estimate the energy of the primary γ-rays. The set of image parameters typically used for the estimation of the energy is:

Size which is probably the most important parameter since it is directly correlated with the energy of the primary

Width the width of the image

Lenght the length of the image

Dist this is required to calibrate the amount of light of the shower reaching the telescope since this parameter correlates with the distance of the shower from the telescope.

Conc the concentration on the “highest” pixels

Leakage which provides information about the fraction of the Cherenkov image which lies outside the camera

Zenith angle the height of the source in the sky

The *energy resolution* is approximately 25% between 100 GeV and 1 TeV. At higher energies the resolution increases slightly up to ≈ 20% whereas below 100 GeV it worsens to rougly 30%. There are know bias in the energy reconstruction: the energy estimation tends to overestimate the energy of the primary γ-ray at low energies (below 100 GeV) and underestimate it at high energies (above 10 TeV). In the rest of the energy range the correlation between true and estimated energy is reasonably linear (see figure 6.11). The biases introduced by the energy estimation are later corrected by the unfolding procedure described in section 6.6.9.

6.6.8 Spectrum calculation

The spectrum calculation is one of the main goals of the analysis. The differential γ-ray energy spectrum is given by:

$$\frac{dF(E)}{dE} = \frac{N_\gamma}{dE dA_{eff} dt}$$

where N_γ is the number of detected γ-rays and t_{eff} the exposure time. In order to compute the real flux of γ-rays coming from the given source the number of excess events has to be divided also by the collection area of the instrument, the term dA_{eff} in the formula. The *effective collection area* A_{eff} is the area in which air showers can be observed by the telescope folded with the efficiency of all the cuts applied in the analysis (ϵ_γ). This efficiency can be estimated using Montecarlo gammas, being the efficiency defined as the number of produced gammas divided by the number of events surviving the analysis cuts.

The differential spectrum is computed dividing the sensitive energy range in equal bins (in logarithmic scale) and applying separate cuts for each energy bins.

Typically, loose background rejection cuts are applied in order to compute the spectrum. In fact, looser cuts reduce the effect of systematic uncertainties between data and Montecarlo events, which is important for the estimation of the effective collection areas. In such a way the spectrum is less affected by the residual discrepancy between data and Montecarlo. Loose cuts has also the advantage of a larger statistic of excess given the larger collection area.

An example of differential energy spectrum is given in figure 8.8, where a final M 87 spectrum published by MAGIC is provided.

6.6.9 Unfolding

In order to correct for the know biases in the energy reconstruction an *unfolding* procedure is applied to the raw differential energy spectra computed using the estimated energy of the gamma rays. The left panel of figure 6.11 shows the correspondence within the estimated energy and the true energy (*migration matrix*). The correction to be applied to the energy spectrum cannot be done through the simple inversion of the migration matrix because of the strong correlation within the adjacent energy bins and the fact that not always the matrix is invertible. Assumptions regard the true energy spectrum have to be done, for example a parametrization of the differential energy spectrum (in many cases a power law is a reasonable assumption for astrophysical γ-ray sources). Mathematically the distortion due to energy estimation biases and finite resolution can be written as follow:

$$Y(y) = \int M(x,y)\, S(x)\, \mathrm{d}x \tag{6.2}$$

where y is the estimated energy, x is the true energy. M is the migration matrix and Y and S are the measured and the true distribution.

At practical level the unfolding is performed by the `CombUnfold.C` ROOT macro included in the MARS software. Several unfolding methods can be chosen by the MAGIC analyzer, they differ on the algorithm for the calculation of the true distribution, as discussed in Albert et al. (2007*a*). Agreement within the different methods is required to be confident on the results. One of the method, named *forward* unfolding fixes the true distribution to a predefine function, like a power law. This can not be considered as reliable as the other unfolding method since a priori the source spectra can be whatever, but is indeed very useful in practice to obtain a "stable" result to compare with. Examples of the same spectrum unfolded using the different methods can be find in chapter 7 (e.g. figure 7.6, figure 7.9 or figure 7.13).

6.6.10 Lightcurve

The *lightcurves* are plots where the integral gamma-rays flux above a certain energy is shown as function of the epoch of the observation.

Typically, Cherenkov telescopes observations are not evenly performed. They are subjected to weather conditions and schedule constraints so that what one normally have is some few hours long observations spread within the whole observation period. These observation are normally divided in shorter time bins depending on the strength of the observed source. The choice of the time binning is normally a trade-off within the maximum number of points and reasonably small error bars for the flux values. The calculation of the flux is done as for the energy spectrum, but limited to a single integral flux point.

Flux values can be negative in the case of a negative statistical fluctuation of the number of excess events. In this cases *upper limits* are normally given instead of flux points. Also in the case of a positive, but non statistically significant γ-rays excess, upper limits can be given instead of flux points (this is specially true for non-firmly established sources). An example of lightcurve obtained with MAGIC is shown in figure 8.6.

The duration of the observation has to be taken into account as well as possible changes in the efficiency of the observation conditions. For example in case of observation during moon time, the efficiency decreases as function of the luminosity of the sky (see section 8.2.2 for a discussion of this issue).

Chapter 7

Markarian 421 and Markarian 501 multiwavelength observations

What is the MAGIC contribution to the knowledge of AGNs?

7.1 Why multiwavelength campaigns?

The evolution of the study of almost all kind of astrophysical sources led in the last years to the organization of *multiwavelength* observation campaigns (also simply 'MWL' in the following). They consist in performing simultaneous observation of the considered object using different instruments in order to cover a wide range of the electromagnetic spectrum. Nowadays, in many cases, the single observation by an isolated instrument can not provide new and interesting results for the study of a specific object. It has become clearer and clearer the necessity of a wider approach in the observation strategy.

Isolated observations on limited region of the spectrum have less chances to draw fundamental conclusion about the physics of the objects because of the intimate connection within energy ranges. There is no doubt that more informations can be extracted by an extended coverage of the spectrum. Moreover, the pronounced flux variability characteristic of some of the sources can easily void some of the conclusion one would draw about the emission mechanisms involved. For this reason also temporal coincidence is required (or at least a reasonable time overlap) when combined spectra are produced. Many theoretical models also predict correlation between the fluxes at different energies. Consequently they can be effectively tested only during truly simultaneous observations, which does not abound in the existing literature.

7.1.1 Motivations

The main target of this project was to collect an extensive multi-frequency data set that is simultaneous and representative of the average/typical SED from Mrk 421 and Mrk 501. The goals of the observations performed during a multiwavelength campaign can be multiple but they can be somehow summarized in two short points:

- Study the broad band spectrum of the source (SED)
- Study the flux variation of the source (variability and correlations)

As already stated several times, the SED of blazars is believed to be dominated by the synchrotron and IC peaks. The spectral changes in the spectrum, namely the hardening/softening in the rising and falling part of the two bumps, together with the (possible) displacement of the peak locations, would provide important inputs for the theoretical models. In particular these pieces of information can be useful for fixing model parameters. In fact, many models are afflicted by degeneracies in the choice of the parameter values i.e. different combinations of the model's parameters can reproduce a certain regions of the spectrum. They can instead be nailed down if a wide region of the SED (or many regions at different energies) has to be reproduced by the model.

Also from the study of the lightcurves a wealth of information can be extracted, in particular regarding the location and size of the emitting region in AGNs. We already know that constraints on the size of the emitting region can be provided by measurements of the minimum time variability. The typical time variability scale in the same time period at different energies is also interesting. Its correlation with the energy band can in fact reveal informations about an eventual common population or radiating particles.

This can be studied more deeply investigating the cross-correlations of the source activity between the different energy bands.

The activity of TeV blazars can be analyzed by the comparison of their lightcurves in the X-ray and γ-ray range. Such a comparison has shown in a few cases a surprisingly precise correlation between the evolution of the X-ray and and the gamma-ray emission (Katarzyński and Walczewska, 2010). These studies might lead us to a better understanding one of the fundamental (and still open) question on blazars: how flux variations are being produced.

Some of the still open and very fundamental questions regarding blazars sources are (i) the content of their jet (ii) the location and the structure of their dominant emission zone (iii) the origin of their variability, observed on timescales from minutes to tens of years (iv) the role of external photon fields (including, EBL) in shaping their observed γ-ray spectra, or, last but not least, (v) the energy distribution and the dominant acceleration mechanism for the underlying radiating particles.

7.1.2 MWL coverage

In order to improve our knowledge on blazar physics we performed long multiwavelength campaigns, namely from radio frequencies to VHE γ-rays, on the nearby blazars Mrk 421 (from January to May 2009) and Mrk 501 (from March to August 2009). Shortly, Mrk 421 and Mrk 501 are among the brightest TeV blazars known up to date an are probably the best candidates to be studied given their much larger flux compared to the other TeV blazar currently known. In the spectral energy distribution of these objects the two emission bumps are located at 1-100 keV and 1-500 GeV respectively. To fully constrains the emission models it is important to cover simultaneously both these energy bands and it is important to cover not only the peak but also the two rising and falling regions. Mrk 421 and Mrk 501 are particularly useful in separating the spectral characteristics intrinsic to the object from absorption effects in the intervening medium because they have almost the same redshift (Krennrich et al., 2001). Further details about the objects Mrk 421 and Mrk 501 are given in the next two sections: 7.1.3 and 7.1.4.

The two campaigns were organized by Dr. D. Paneque from SLAC/KIPAC and Dr. D. Kranick from ETH-Zurich. I contributed to the organization of the campaign during my stay at SLAC/KIPAC in spring and summer 2009 where I developed tools to collect the data provided by the analyzers of the several observations involved (see section 7.6).

From now on in the text we will also refer to the campaign with the 'MWL2009-Mrk 421' and 'MWL2009-Mrk 501' terms. Campaigns were also organized in 2008 and before but they could not exploit the novel valuable information from the new Fermi γ-ray satellite[1].

Instrument	Band/Frequency/Energy	Mrk 421-2009	Mrk 501-2009
Abastumani	optical, R band	yes	no
Effelsberg	radio, 2.6 to 32 GHz	yes	yes
Fermi-LAT	γ-rays, 10 MeV to 100 GeV	yes	yes
GASP	optical, R-bands	yes	yes
GRT	optical, V-R-B-I bands	yes	yes
KANATA	optical,	yes	yes
Lulin	optical, Rband	yes	no
MAGIC	γ-rays, 60 GeV to 10 TeV	yes	yes
Medicina	radio, 15 GHz	yes	yes
Metsähovi	radio, 37 GHz	yes	yes
MitSume	optical, g-Rc-Ic bands	yes	yes
Mew Mexico Skies	optic, R-V bands	yes	no
Noto	radio, 8 22 and 43 GHz	yes	yes
OAGH	radio, H-J-K bands	yes	yes
OVRO	radio, 15 GHz	yes	yes
ORM	optical, Rband	yes	no
ROVOR	optical, B-R-V bands	yes	yes
RXTE-PCA	X-rays, 3 to 31 keV	yes	yes
SMA	radio, 230 Gz	yes	yes
St. Petersburg	optical, R band	yes	no
Swift-UVOT	optical/UV, V-B-U-W1-M2-W2	yes	yes
Swift-XRT	X-rays 0.3 to 9.6 keV	yes	yes
Swift-BAT	X-rays 14 to 195 keV	yes	yes
Talmassons	optical, R band	yes	no
UMRAO	radio, 5, 8 and 14 GHz	yes	yes
Valle d'Aosta	optical, R band	yes	no
VLBA	radio, 15 and 43 GHz	yes	yes
VERITAS	γ-rays, 100 GeV to 10 TeV	no	yes
Whipple	γ-rays, 100 GeV to 10 TeV	yes	yes
Wiro	infrared, J-K bands	yes	yes

Table 7.1: Instruments involved (at least partially) in the Mrk 421-2009 and Mrk 501-2009 MWL campaigns (alphabetically ordered).

The remarkable spectral coverage of the two 2009 campaigns is summarized in figure 7.1 whereas on table 7.1 a list of the instruments involved, including their energy band range, is provided. The MAGIC telescope contributed to the campaign providing data

---

[1] The Fermi data was supposed to be available already for the 2008 campaigns but because of a delay in the launch the first data became available only in 2009.

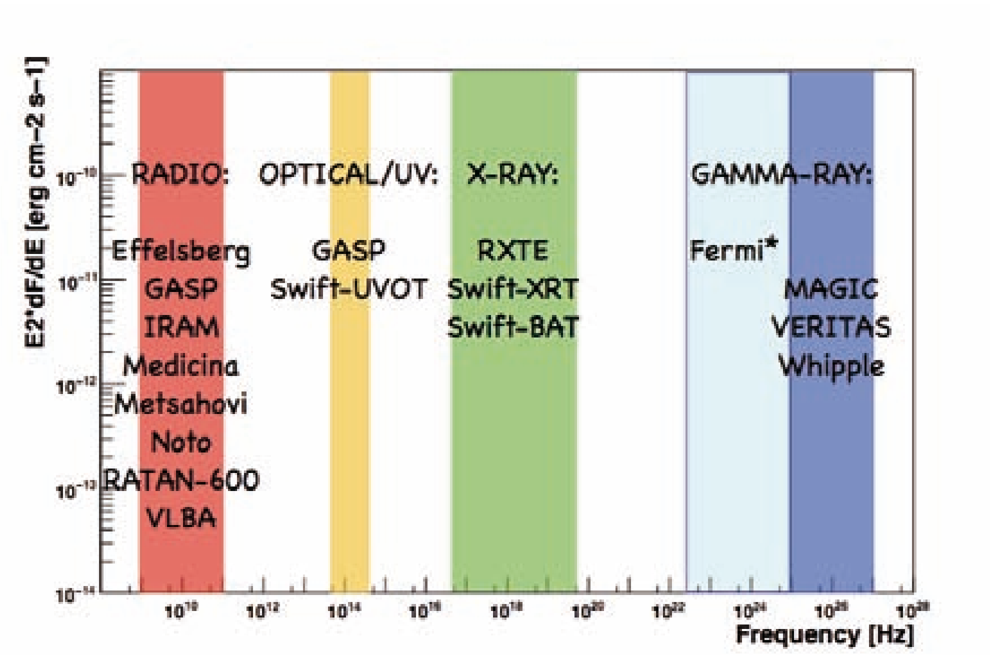

Figure 7.1: MWL campaigns coverage showing the frequencies covered by (some) of the instruments of the 2009 campaigns.

on the VHE band together with the US facilities VERITAS and Whipple.

7.1.3 Mrk 421

The blazar Mrk 421 was the first extragalactic object detected at VHE by the pioneer Whipple Cherenkov telescope (Punch et al., 1992), and the second source after the Crab Nebula. Few years later, the detection have been confirmed by the HEGRA collaboration (Petry et al., 1996). Mrk 421 is a northern hemisphere source (R.A. = 166.11 h, DEC. = 38 21) located at a redshift of 0.030. Since it guarantees a relatively high flux level even in quiescent state it is regularly detected by the current generation of Cherenkov telescopes. For this reason this object is specially suitable to study the quiescent state of blazars, which is typically more difficult to detect. Moreover, it is know as one of the fastest varying gamma-ray sources (Krennrich et al., 2001).

7.1.4 Mrk 501

The blazar Mrk 501 was the second extragalactic object detected at VHE (Quinn et al., 1996). It is a northern hemisphere source (R.A. = 253.87 h, DEC. = 39 76) located at a redshift of 0.034. This TeV source also guarantees a relatively high flux level even if not as high as its Mrk 421 cousin. On the other hand, the largest TeV flares are on the northern hemisphere was detected from this source in 1997. A variable TeV-flux on timescale of days could be established already in the detection paper by Whipple. It is also know as one of the fastest varying gamma-ray sources (Samuelson et al. (1998), Djannati-Atai et al. (1999)), time variability down to the scale of minutes was detected by MAGIC in 1995 (Albert et al., 2007*b*). It also led to several publication regarding more fundamental physics issues like constraints on the quantum gravity scale.

7.2 The MAGIC data and analysis

The goal of the MAGIC participation in the campaigns described above is to provide wide time coverage and high quality VHE γ-ray data. The low energy threshold of the MAGIC telescope has become specially important now that the Fermi satellite is operating since it is finally possible to close the gap between ground-based and space-born γ-ray detectors[2].

A dedicated observation proposal was redacted by the principal investigators and the MAGIC members involved in the campaigns to get scheduled the required observation time from the Time Allocation Committee (TAC) of the MAGIC experiment (Kranich et al., 2008). Observation time was granted by the TAC, fact that underlines the relevance of this project for the scientific output of the MAGIC telescope.

The MAGIC data considered in this chapter are the Mrk 421 and Mrk 501 observations during the campaign periods. Beside of those main data, a couple of hours of Crab Nebula data, chosen in the same period and zenith angle range (section 7.3), were analyzed. Given the strong and steady signal from the Crab Nebula, these data are analyzed here with the only purpose of guaranteeing the quality of the analysis, being the expected results very well known in this case. As mentioned in section 6.5 this is a standard procedure for MAGIC analyses.

The data were analyzed using MARS, the MAGIC standard analysis package. Please see chapter 6 for a general description of the MAGIC analysis procedure and software. Both possible analysis approaches, α and θ^2 (see section 6.2), were used here in order to compare the obtained results. Moreover, also different sets of analysis cuts were applied in order to check the stability of results (sections 7.3, 7.4 and 7.5). The estimation of the systematic errors that affect the measurements (yellow band in figures 7.10 and 7.14) can be also studied comparing the different results obtained.
The data samples considered and the details of the analyses are described in the following sections.

7.2.1 The Random Forest training

As described in section 6.6.6 about the MAGIC analysis, the rejection of the background events is perform using the Random Forest classification algorithm. The optimization of the gamma/hadron separation requires a gamma event sample and a hadron event sample to allow the algorithm to learn the characteristics of the two populations of events. The gamma events are taken from the MAGIC Montecarlo library available at the MAGIC data center whereas the background sample is taken directly from real data. Data runs with no gamma sources in the field of view are chosen for this purpose. Both these training samples are chosen such that they match the zenith angle of the observations, the light conditions, and for the real data also the same epoch of the blazars observations. This latter condition is not a real requirement of simultaneity, let's say that data taken in the same period are to be preferred because of the more similar hardware condition of the detector[3]. Two more Montecarlo gamma data samples are needed for the energy reconstruction optimization and for the Disp estimation optimization (see sections 6.6.7 and 6.6.4 respectively).

---

[2] The energy ranges covered by the two instruments are nominally 10 MeV to 100 GeV for Fermi and 60 GeV to 10 TeV for MAGIC.

[3] The telescope conditions may change because of required maintainance or hardware upgrade.

7.2.2 Montecarlo gamma sample

Since the gamma/hadron separation algorithm heavily relies on the characteristics of the simulated gamma events it very important to choose a MC sample which fits the conditions of the data that have to be analyzed. One of the key parameters is the optical PSF of the telescope in the considered period. The PSF of the telescope is automatically monitored daily using the muon ring images present in the data[4]. A plot (similar to the one on figure 7.2) and a table of the estimated optical PSF values from the muon ring analysis are available to the collaboration at the PIC data center web page.

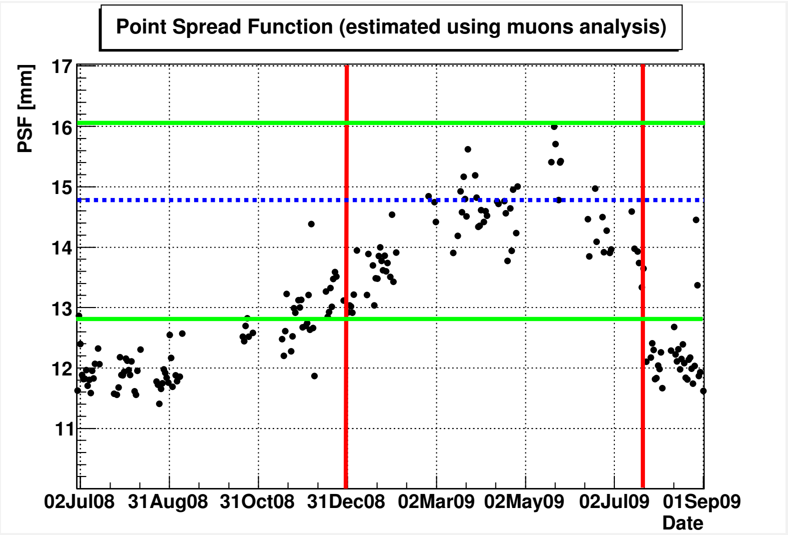

Figure 7.2: Optical PSF of the telescope monitoring plot. The red lines represent the start and the end of the MWL campaigns whereas the green lines mark the minimum and maximum PSF in that period. The blue dotted line indicates the PSF of the MC used in this analysis.

For the purpose of this analysis dark night condition MC was downloaded from the library, since most of the observation were performed during dark time. A good parameter for the estimation of the amount of background light is the mean Discriminator Threshold (DT, see also 6.5). The quality cut DT < 42 guarantees light conditions that can be safely treated in the context of a dark time analysis (Oña, 2006).

7.2.3 Hadrons sample

The same a priori quality cuts (see also 6.5) applied to the data from the source observations are applied also to the off training sample. These cuts are applied on the averages of each sub-run, which means on time period of ≈ 2 minutes. The quality cuts for this analysis are summarized in table 7.2

The sources and dates used to build the background sample are listed in table 7.3. Mrk 421 was also included in the off sample in order to cover a zenith angle gaps which could not be covered by completely "off" observations with no gamma signal on it. This should be avoided since it implies that some (real) gammas are used as background sample events and a slight worsen of the sensitivity may occur. In this particular case it is still

---

[4] This monitoring system was partially developed and maintained by the author.

Cut	Value
Zenith angle	within 6° and 35°
Cloudiness	less than 40 %
Discr. thresholds	less than 42
Event rate	above 200 Hz

Table 7.2: A priori quality cuts applied. Concerning the zenith angle range: it has been chosen such that the range is as wide as possible. The size of the range is limited because at a certain point the image parameters become so different at large zenith angle that they can not be treated together. The range chosen here still allows a safe single training of the Random Forest for the background rejection. 6° is the minimum zenith angle during the observation considered here. It is determined by the culmination position of the two sources (very similar for both Markarians).

acceptable since Mrk 421 data represents just a small fraction of the whole background sample, the gamma-ray flux was not particularly high. Moreover, the only alternative would have been using data from a very different time period, which would have led to worse effects from the point of view of the analysis because of the possibly different conditions of the detector.

Source	Days†
2MASX032+34	January 15^{th}
Mrk 421	January 22^{nd}, 24^{th}, 28^{th}
Mrk 421	March 1^{st}
MS1050.7+494	March 17^{th}, 19^{th}, 20^{th}, 23^{rd}
MS1050.7+494	April 1^{st}
1H1722+119	March 30^{th}, 31^{st}
1H1722+119	April 2^{nd}
PKS-1424+240	April 17^{th}, 19^{th}
PKS-1222+216	April 18^{th}

Table 7.3: Hadrons sample used for the training of the Random Forest algorithm.
† The “day after” convention is adopted i.e. the name of the day refers to the second of the days which compose the observing night.

7.2.4 Gini-index

The gini-index plot obtained for the alpha analysis gamma/hadron separation optimization is reported in figure 7.3. As mentioned in section 6.6.6 this plots shows the relative power of the separation variables in the classification of the events. The Gini indexes obtained for this analysis are quite typical. As expected the better separating parameter is the width of the Cherenkov images Width, that once correlated with the Size parameter is a very powerful gamma/hadron separator. Other parameters, like Size or Zenith Angle score less because they are mainly used to take into account of the correlations of the image parameters (for all type of showers).

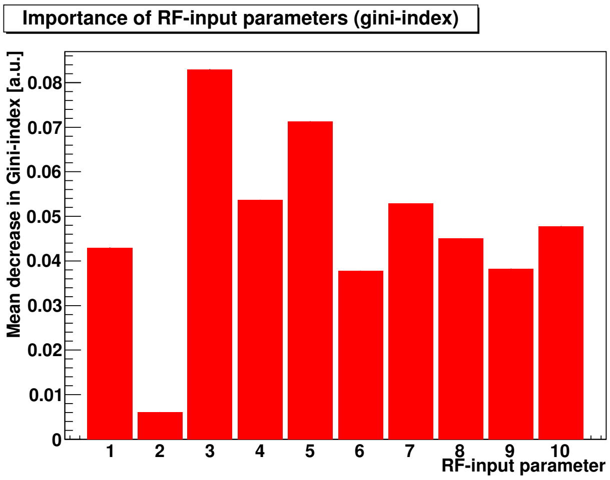

Figure 7.3: Gini-index plot for the Mrk 421 and Mrk 501 analysis. The plot is produce by the osteria executable during the Random Forest background rejection training. The parameters shown are: 1-size; 2-zenith distance; 3-width; 4-length; 5-size/width*length; 6-conc; 7-dist; 8-m3long; 9-timeRMS; 10-time gradient.

7.2.5 Analysis threshold

The energy threshold of the analysis is estimated using a Montecarlo test sample (statistically independent from the sample used for the training). The very same gamma/hadron separation procedure and energy estimation that would be applied to the real data is applied to the simulated gammas so that both true and estimated energy values are accessible for this test sample events. This allows us to know the energy threshold after the analysis cuts (but also to estimate the efficiency of all the possible cuts). The energy threshold is defined as the peak of the reconstructed energy distribution for a given size cut. In figure 7.4 the energy thresholds obtained using different minimum Size cuts are shown.

7.3 MAGIC results: Crab Nebula

As analysis test sample we used four days of Crab Nebula observations (table 7.4), for a total observation time of 6.3 hours taken very close in time with respect to the two MWL campaign periods. The same quality cuts described in table 7.2 were applied to these data.

The goodness of an analysis depends on several factors, also related to the specific target of the analysis. High sensitivity, low energy threshold, high gamma efficiency and good angular resolution are just some of the parameters that determine the quality of an analysis. Anyway, the sensitivity is probably the most important of the list, and it is typically checked on Crab Nebula data once the analysis pipeline is ready. The significance (per observation hour) of the excess from a steady known source is also a good checking parameter but the *sensitivity* is generally preferred. The easiest and more common way to compute it is in terms of Crab Nebula flux units. It is given by the formula:

$$S = \frac{5}{\sqrt{50h/T_{obs}} \cdot (N_{exc}/\sqrt{N_{bckg}})} \tag{7.1}$$

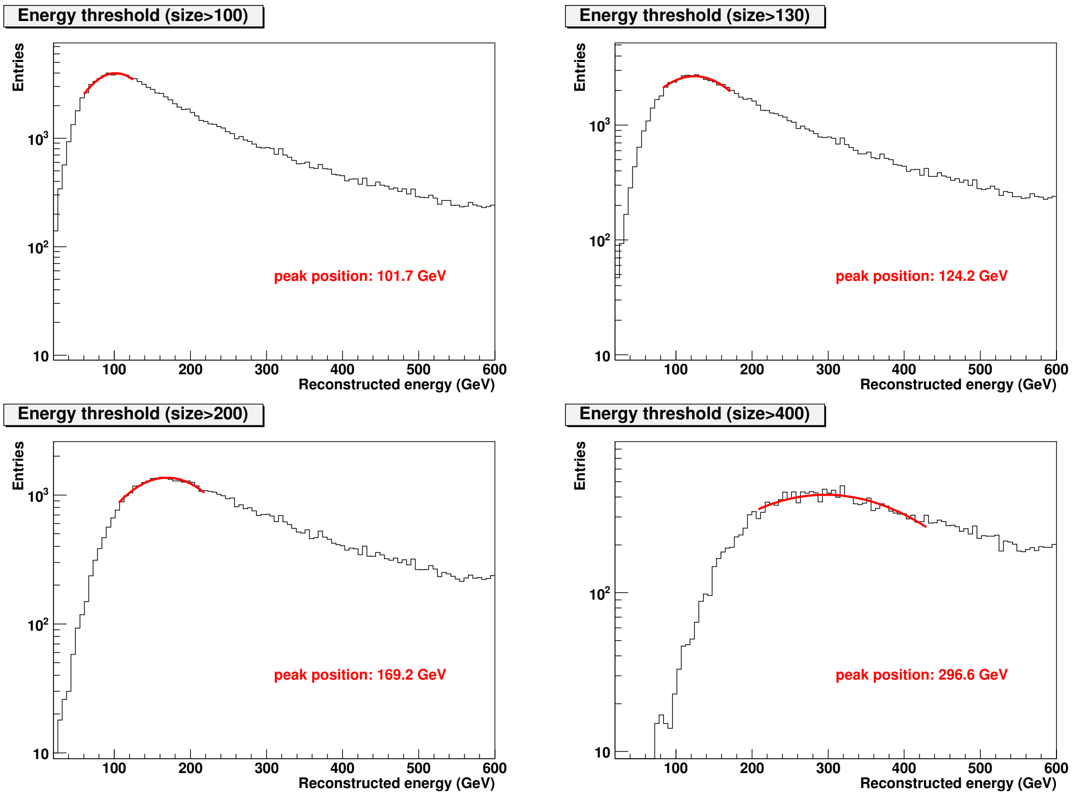

Figure 7.4: Analysis energy threshold for different Size cuts. The E_{th} is determined by the position of the peak in the distribution of the reconstructed energy in the MC gamma test sample.

where $N_{exc.}$ is the number of excess events obtained from the Crab Nebula observations. The sensitivity is the minimum γ-ray flux detectable in 50 hours, at a signal to noise ratio ($N_{exc}/\sqrt{N_{bckg}}$) of five. The expression 7.1 is the sensitivity formula commonly use in the field, but please notice that the simplified significance formula: $N_{exc}/\sqrt{N_{bckg}}$ is used instead of the more accurate *Li&Ma* formula[5] (Li and Ma, 1983). Anyway it is safe to apply this approximation because the simplified significance differs substantially from the true significance only when the number of background events is huge compared to the background, which is never the case when the minimum flux is computed.

Month	Days
January	22^{nd}, 23^{rd}, 24^{th}
March	14^{th}

Table 7.4: Crab Nebula data sample used to check the analysis.

The integral sensitivity heavily depend on the minimum Size cut applied. For the MAGIC telescope the optimal sensitivity is obtained at an energy threshold of $\simeq$ 280 GeV (corresponding to roughly 400 phe minimum Size cut), where we are able to detect 1.6% of the Crab Nebula flux in 50 h of wobble observations (Aliu et al. (2009), Tescaro (2007)).

---

[5] The approximation reside on the fact that $N_{exc}/\sqrt{N_{bckg}}$ assumes a perfect knowledge of the background, whereas the *Li&Ma* takes its erron into account.

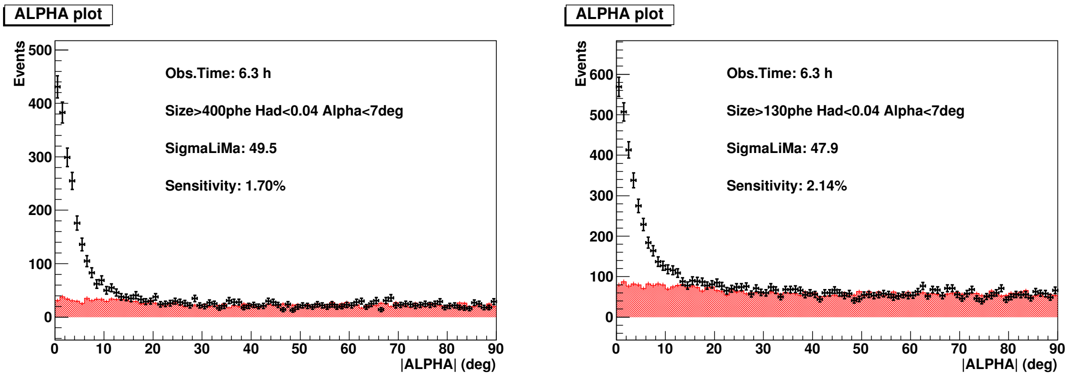

Figure 7.5: Apha plots for the test sample of CrabNebula. The sensitivity with a Size cut larger than 400 phe resulted to be 1.7% of the CrabNebula flux which is comparable with the reference value of 1.6%. On the right panel the sensitivity for a Size cut larger that 130 phe is also reported, since this would be the minimum Size cut used for the calculation of the energy spectra of the analyzed blazars.

For this analysis we found a sensitivity of 1.7% of the Crab Nebula flux, which is in agreement with the expected sensitivity (see figure 8.2). The sensitivity improves slightly with a harder minimum size cut of 450 phe, where it increases up to 1.66% (not shown in the figure). Again, in order to check the quality of the analysis here performed, the Crab Nebula spectrum has been computed using the test data.

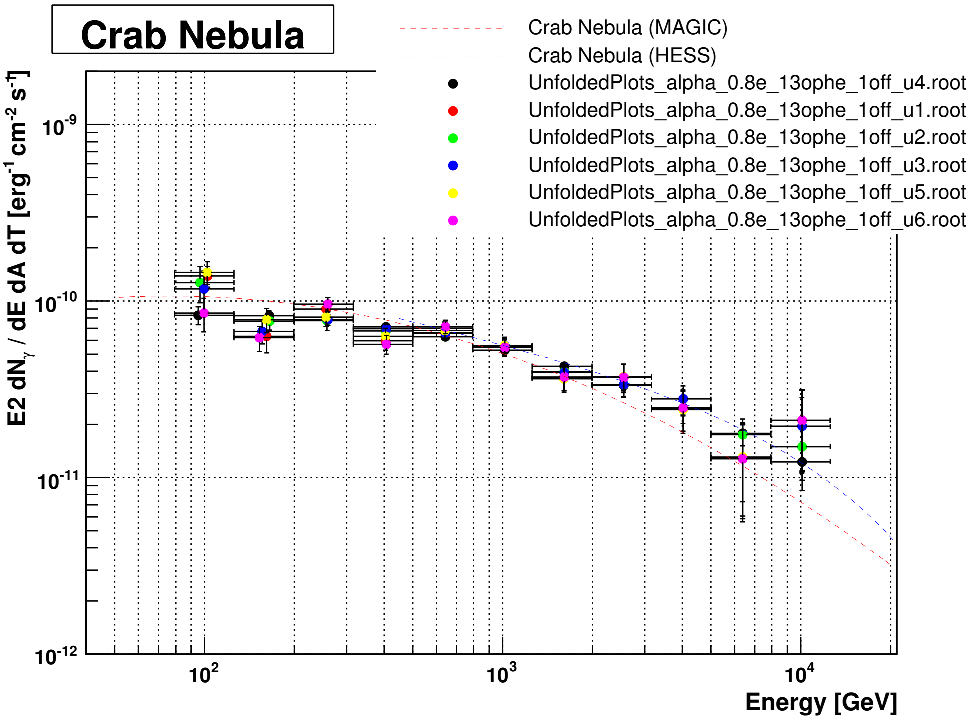

Figure 7.6: Crab Nebula spectra obtained from the test data sample. spectra obtained with different unfolding methods.

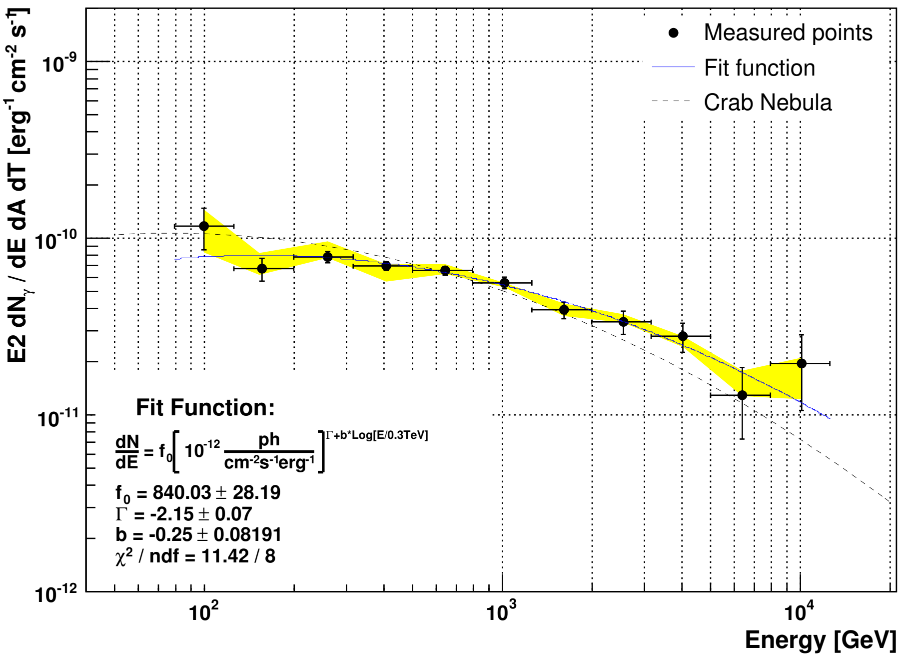

Figure 7.7: Crab Nebula spectrum obtained using the Bertero unfolding method (u3). The yellow band is represents the spread of the fluctuation obtained from figure 7.6.

The spectra is plotted in the 'E^2' representation (or SED), and results to be compatible with the Crab Nebula results from other observations from MAGIC and other instruments. These results are shown in figures 7.6 and 7.7.

7.4 MAGIC results: Mrk 421

Mrk 421 is in average the strongest and most variable[6] source between the two considered blazars. It is maybe the most appealing because it has a higher flux in its low state. The observations for the MWL campaign were planned in such a way to have one hour of observation every two days for a three-month period.

These were not the only data available, since also the observations coming from a different proposal involving Mrk 421 were included in the data set. The only requirements were that the data was taken within the campaign period, and that they fulfilled the data quality requirements. To be more specific, a 'bright AGNs monitoring' proposal was also approved for observation in cycle IV and it involves the Mrk 421, Mrk 501, 1ES 1959 and M 87 sources.

One of the main drawbacks of ground based experiments as IACTs as compared to satellites is that the observations can not be performed in case of bad weather. Technical problems is another source of observation time loss. For this two reasons, and because of the quality cuts imposed, the effective observation time is always smaller respect to the

---

[6] Although is Mrk 501 which detains the record regarding the intensity of a flare, Mrk 421 is in average more prone to change its flux level.

original scheduled time.
For Mrk 421 the observation days which passed the quality cuts are listed in table 7.5, and amount to a total of 28.2 h.

Month	Days
January	22^{nd}, 24^{th}, 26^{th}, 28^{th}, 30^{th}
February	1^{st}, 3^{rd}, 25^{th}
March	1^{st}, 17^{th}, 19^{th}, 21^{th}, 23^{th}, 29^{th}, 31^{st}
April	15^{th}, 17^{th}, 19^{th}, 21^{th}, 22^{th}, 23^{th}, 24^{th}

Table 7.5: Mrk 421 data sample after quality cut selection.

The overall Alpha plot for the selected data sample is presented in figure 7.8. The Size cut applied is Size $>$ 400 phe, corresponding to an energy threshold of $E_{th} \simeq 300$ GeV accordingly to the last panel of figure 7.4. A very solid 70.2 σ signal is found. The final cuts applied to obtain this value are optimized using the Crab Nebula data sample (choosing the cuts that result in the optimal sensitivity): Hadronness < 0.04 and Alpha $< 7°$.

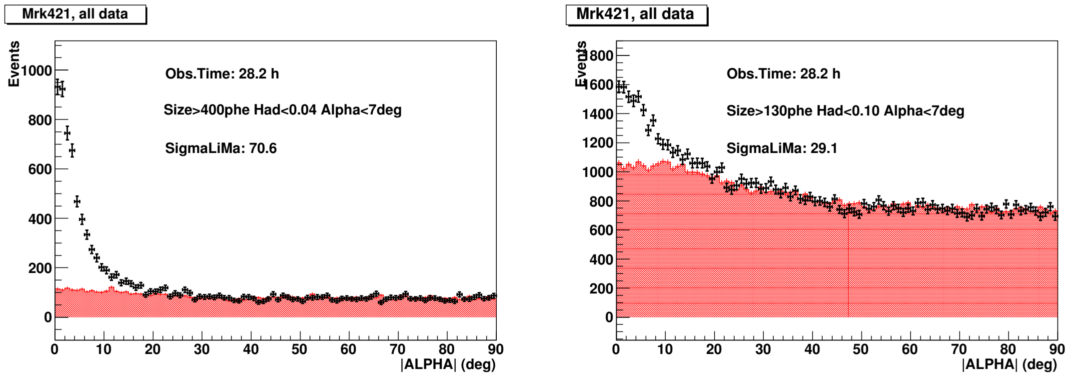

Figure 7.8: Mrk 421 alpha plots (whole data sample). On the left an integral Size bin (Size>400 phe). On the right a differential size bin with 100<Size<400 phe.

The most important output from this analysis is probably the SED spectrum during the whole campaign. The VHE data points are very important to allow a correct modeling of the source. The high photon statistics in these data allows a remarkably precise estimation of the spectrum, namely $\sim$ 10 data points spread in a range of almost two decades of energy. As any physics measurement the computed spectrum is affected by statistical and systematic errors. Concerning the statistical part, the errors of the flux values are determined by the significance of the signal in the considered energy bin an by the uncertainty in the estimation of the collection area (obtained from the MC). The estimation of the systematic error is more difficult (Albert et al., 2008*d*), but at least part of it can be also estimated from the data. The robustness of the analysis is in fact estimated performing different analysis approaches and cuts. In this way the component of the systematic error due to the non perfect agreement of the Montecarlo with the data will show up (a perfect Montecarlo would reproduce the data equally good with any kind of cuts). Also, changing the approach for the background estimation between 1 and 3 off zones permits us to evaluate the level of inhomogeneity of the camera. Very different results would indicate a severe non-uniformity problem.

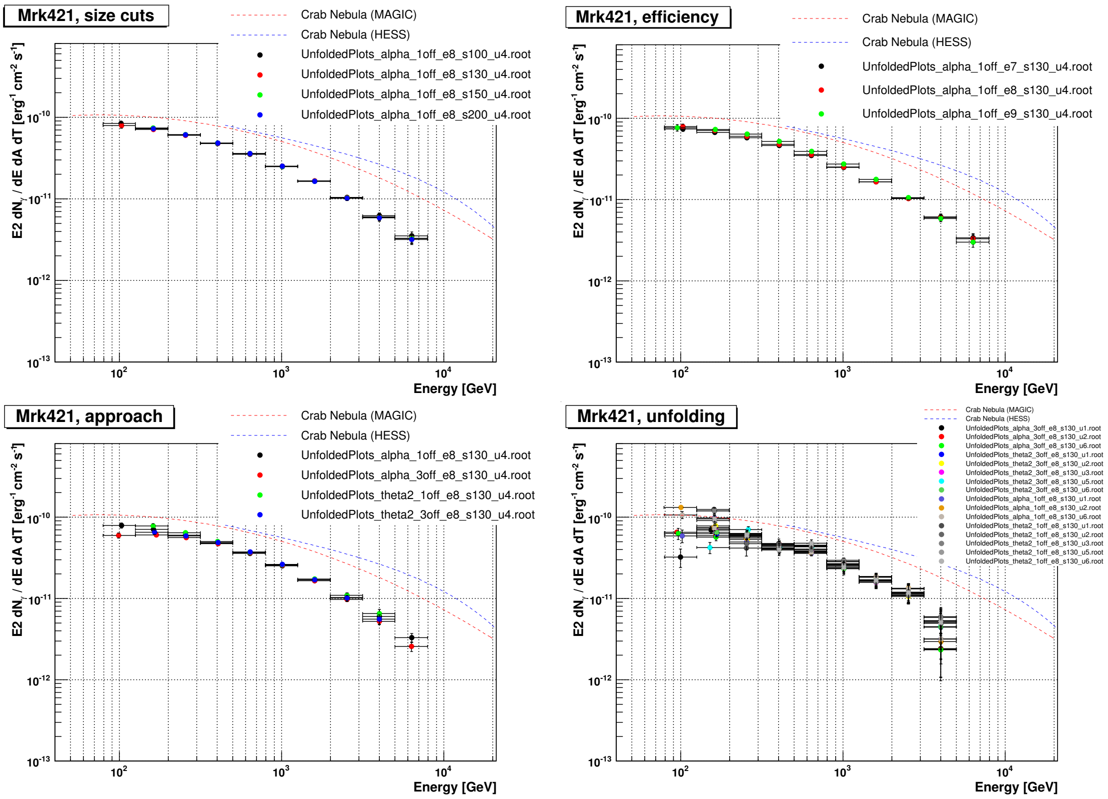

Figure 7.9: Mrk 421 spectra obtained using different analysis approaches and settings. The last tag in the legend names identifies the unfolding method applied to unfold the spectra: u1-Schmelling, u2-Tikhonov, u3-Bertero, u4-forward, u5-Schmelling2 and u6-Bertero2. In the top left panel a different minimum Size cut was applied, whereas in the top right panel what was changed is the final cut efficiency. In the third panel different approaches for the analysis are applied: alpha/theta2 and 1off/3off. In the last panel the different "real" unfolding methods are finally compared.

As described in section 6.6.9, the last step of the analysis chain that leads to the spectrum is the unfolding. Given the several methods available, in some of the plot only the forward method is shown, so that the comparison is more significative and understandable. We remind that the forward unfolding method fixes the unfolded spectra exactly on the wanted fitting function shape, letting free only the function parameters. This is very useful when we want to consider only the effect of the different analysis settings/approaches, reducing the uncertain coming from the unfolding procedure itself, which is studied separately.

In figure 7.9 we present some of these spectra obtained with different configuration of the analysis software. Let's have a closer look to this figure. The top left panel shows the energy spectra for different minimum Size cuts. This is useful to understand the effect of different analysis thresholds. The top right panel shows the energy spectra for different hadronness and α cut efficiencies. This is useful to understand the stability of the results depending on the strength of the cuts applied. The bottom left panel shows the energy spectra for different analysis approaches (α and θ^2) and number of off regions. This is also useful to evaluate the stability of the results. Finally the bottom right panel shows the energy spectra for a fixed cut configuration but different unfolding methods. This plot is meant to evaluate the effect of the unfolding procedure by itself which is the largest source of systematic uncertainly.

We can see that the systematic error is larger at the edges of the spectrum. The systematics on the background estimation can easily affect the measure of the the smaller excess signal on the low energy bins. When the relative number of excess events, even if large in absolute terms, is just few percent of the background, it might happen that a small deviation in the shape of the background distribution can change significantly the number of excess events, actually by much more than the pure statistical fluctuations. When we use the distribution of α (or θ^2) with respect to the off regions as estimation of the residual background, we are implicitly assuming that the camera behaves exactly the same as for the on and the off regions. Given all the analysis precautions which are taken this is indeed quite true, but up to a certain degree. Discrepancies of the order of 1% or less can not be eliminated completely. Moreover, at low energy the estimation of the effective area from Montecarlo is more sensitive to the cut chosen since it rises steeply with the energy. On the upper edge the reduced statistics leads to larger statistical errors and as a consequence the spread of the points increases. Also the effect of the unfolding procedure leads to larger spreads on the edges of the spectrum since it has a larger degree of freedom in applying correction to the original data points[7].

A representative spectrum for Mrk 421 is given in figure 7.10, where the data points have been fit with a curved power law function (see the inlay on the bottom left of the figure). The yellow band, which is meant to represent the systematic error in the spectra measurements, is obtained from the last panel of figure 7.9 as the maximum spread of the points there found.

The lightcurve of Mrk 421 during the whole campaign has also be computed and is shown in figure 7.11. The χ^2 test with a constant fit function results incompatible with the constant flux hypothesis. Even if it is clear that the source flux is not constant the lightcurve also reveal the absence of large flares during the considered observation period. The average flux of the source during the entire campaign above 300 GeV was of $7.52 \cdot 10^{-9} gammas \cdot cm^{-2} \cdot s^{-1}$ equivalent to 60.5% of the Crab Nebula flux.

---

[7] Being the points of the spectrum very much correlated, a point in the middle of the spectrum is ‘stabilized’ by the neighbor points.

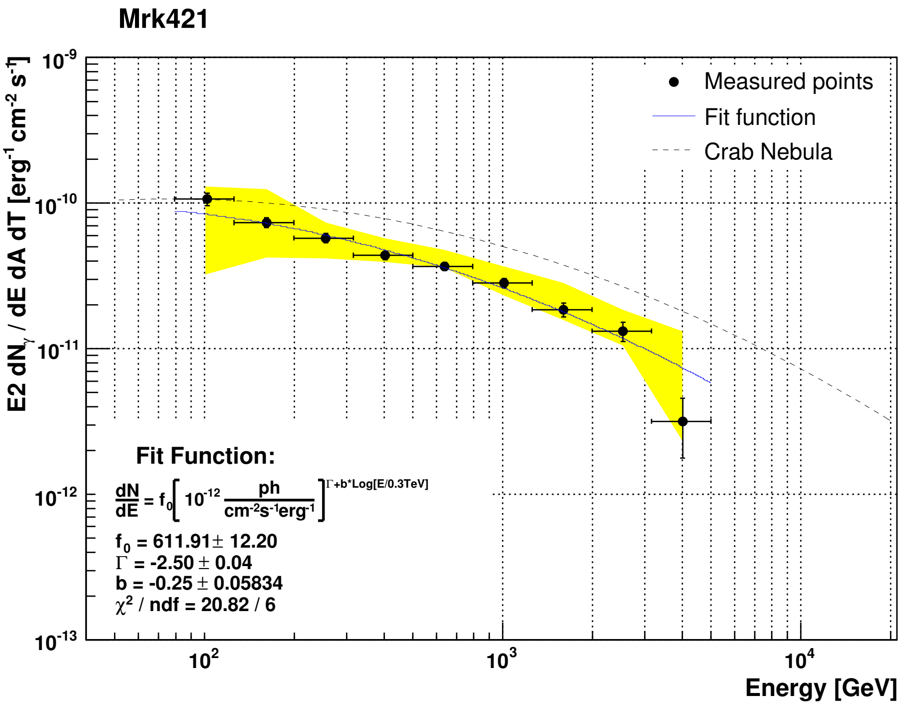

Figure 7.10: Mrk 421 representative spectrum. The analysis configuration is: α analysis approach, 1off region for the background estimation and method 6 (Bertero2) for the unfolding correction.

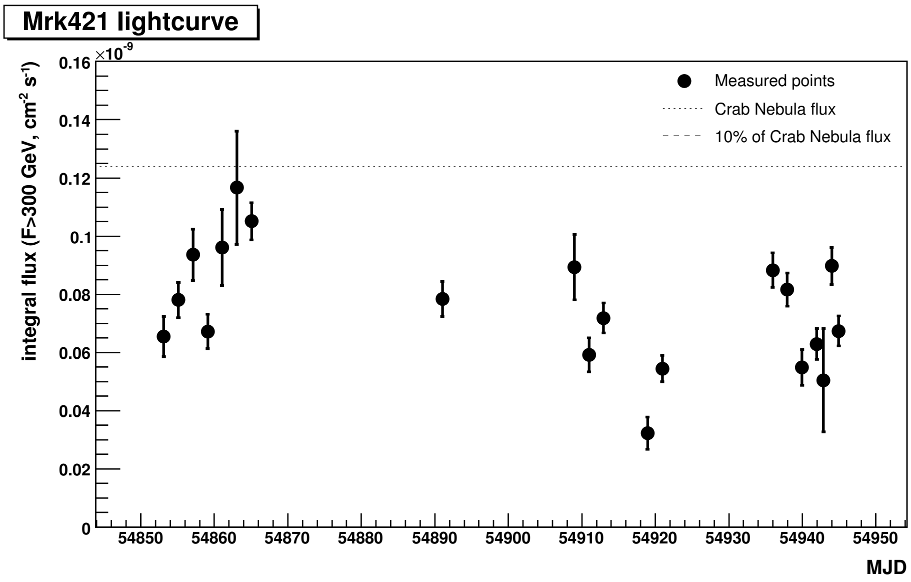

Figure 7.11: Mrk 421 lightcurve for the whole campaign. The analysis configuration is: alpha analysis approach, 1off region for the background estimation. The dashed line represent the flux level of the Crab Nebula for this minimum energy cut.

7.5 MAGIC results: Mrk 501

In the case of Mrk 501 a different observation policy was adopted with respect to Mrk 421. Mrk 501 is also 'strong' and relatively easy to detect although not that much as Mrk 421. The low state flux is much lower than for Mrk 421, fact that can hinder the detection in short observation periods. For this reason the sampling rate for this source was decreased to once every five nights, but with an observation time of 2 h, instead of just 1 h, during an overall observation period of two months.
For Mrk 501 the observation days which passed the quality cuts are listed in table 7.6, and amount to a total of 16.2 h. Also in this case the reduced effective observation time is due to the time loss due to bad weather, technical problems and quality cuts.

Month	Days
March	1^{st}, 23^{th}, 29^{th}, 31^{th}
April	1^{st}, 2^{nd}, 3^{rd} 4^{th}, 5^{th}, 17^{th}, 18^{th}, 19^{th}, 25^{th}, 27^{th}
May	26^{st}, 27^{th}
June	14^{st}, 29^{th}
July	14^{st}

Table 7.6: Mrk 501 data sample after quality cut selection.

The overall Alpha plot for the selected data sample is presented in figure 7.12. The Size cut applied is Size $>$ 400 phe, corresponding to an energy threshold of $E_{th} \simeq 300$ GeV accordingly to the last panel of figure 7.4. A solid 31 σ signal is found. The final cuts applied to obtain this value are optimized using the Crab Nebula data sample (the same cut that results in the optimal sensitivity): hadronness < 0.04 and alpha $< 7°$.

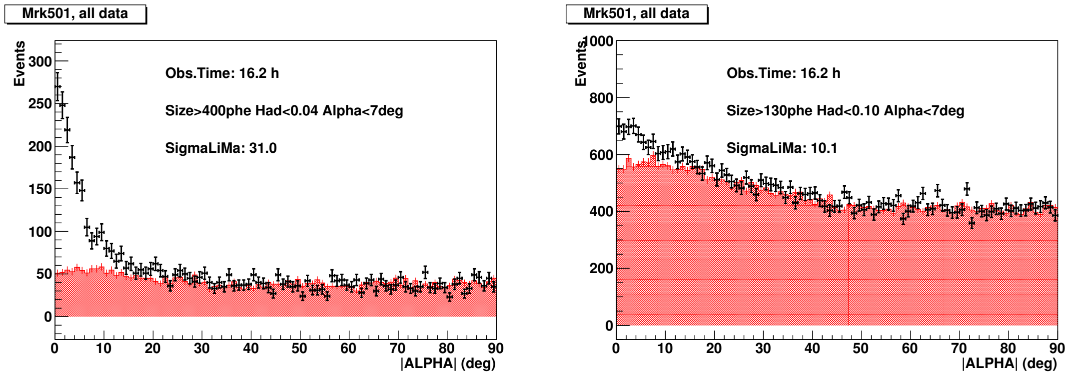

Figure 7.12: Mrk 501 Alpha plots (whole data sample). On the left an integral Size bin (Size>400 phe). On the right a differential Size bin with 100<Size<400 phe.

As for Mrk 421, we compare now several SED of Mrk 501 obtained with different approaches and parameters of the analysis (see figure 7.13). The figure has the same format of the figure 7.9 described in the previous section.

A representative spectrum for Mrk 501 is given in figure 7.14, where the data points have been fit with a simple power law function (see the inlay on the bottom left of the figure). The yellow band, which is meant to represent the systematic error in the spectral measurements, is obtained from the last panel of figure 7.13.

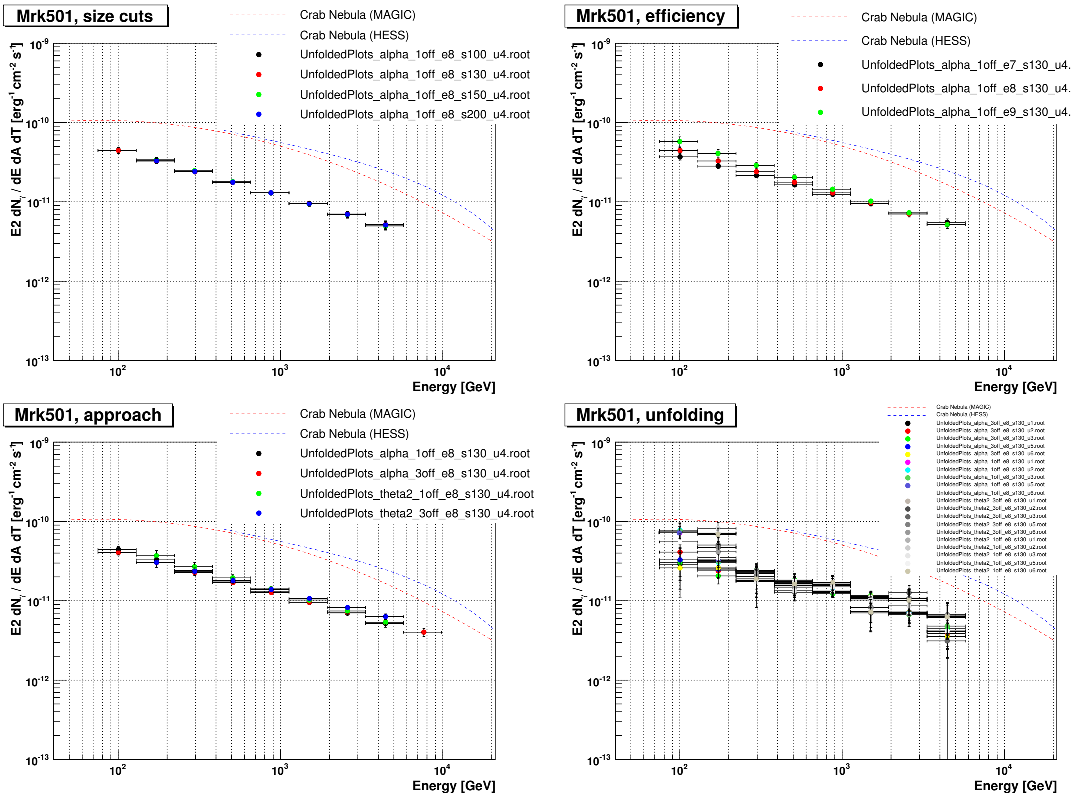

Figure 7.13: Mrk 501 spectra obtained using different analysis approaches and settings. The last tag in the legend names identifies the unfolding method applied to unfold the spectra: u1-Schmelling, u2-Tikhonov, u3-Bertero, u4-forward, u5-Schmelling2 and u6-Bertero2. In the top left panel different minimum Size cut were applied, whereas in the top right panel what was changed is the final cut efficiency. In the third panel different approaches for the analysis are applied: alpha/theta2 and 1off/3off. In the last panel the different "real" unfolding method are finally compared.

The lightcurve of Mrk 501 during the whole campaign has also be computed and is shown in figure 7.15. The χ^2 test with a constant fit function leads to a constant fit probability of $\simeq 6{\times}10^{-11}$. The average flux of the source during the entire campaign above 300 GeV was of $3.38 \times 10^{-9} gammas \cdot cm^{-2} \cdot s^{-1}$ equivalent to 29.8% of the Crab Nebula flux.

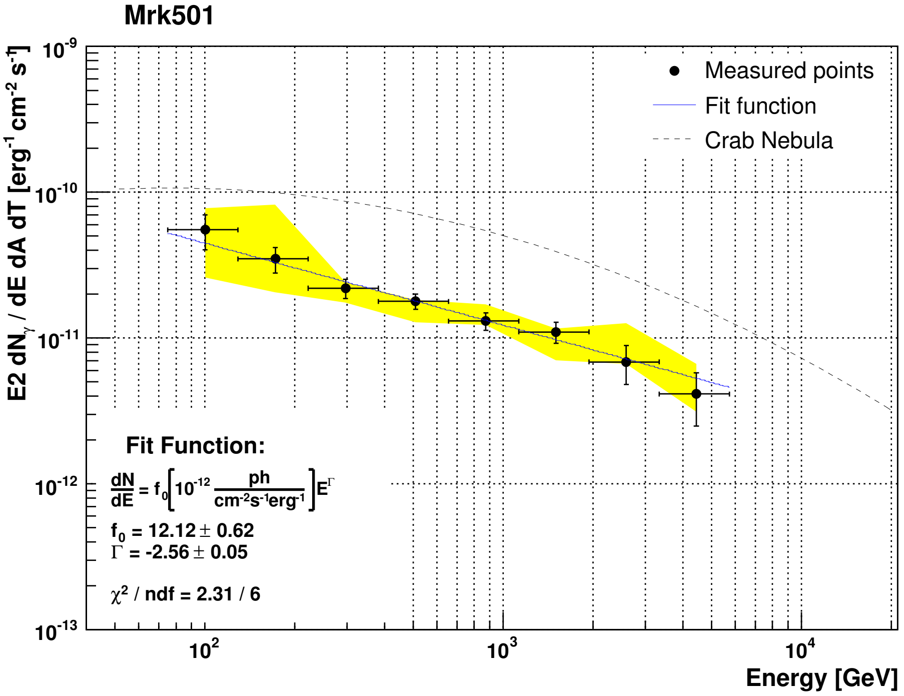

Figure 7.14: Mrk 501 representative spectrum. The analysis configuration is the same as for figure 7.10.

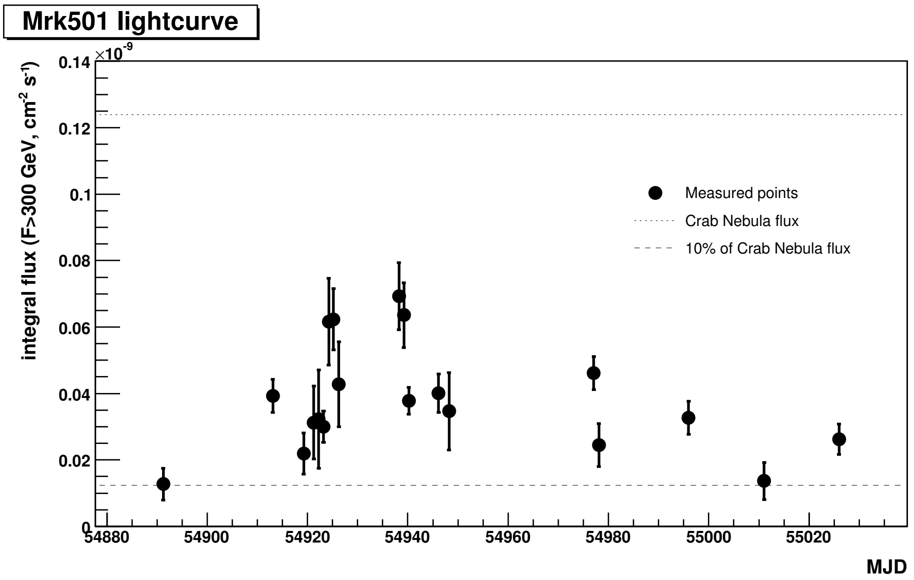

Figure 7.15: Mrk 501 lightcurve for the whole campaign. The analysis configuration is the same as for figure 7.11. The two dashed line (see inlay legend) represent the flux level of the Crab Nebula (10% and 100%) for the same minimum energy cut.

7.6 MWL handling tools

For the management of the data of the campaigns several software tools were developed. The final results were provided to the principal investigators (and to the all working team) by the various analyzers in a predefined text format, with a quite strict protocol. This was required in order to allow us to automatize the merging of the data.

A collection of Python[8] scripts and ROOT macros were developed. Some are dedicated to handle the lightcurves the others to handle the spectra. What they do is to read in the relevant information from the standard text file, relying on the location of the predefined keyword that have to be included together with the data, an to produce output files (typically text or ROOT files) containing the complete information. These tools allow to store and plot all together the data coming from the various instruments involved in the campaigns. This is very useful for the further steps of the study: the modellization and interpretation of the results. These tools also allow the automatic selection of the data on the basis of time period and data quality criteria.

The main tools are:

`LIGHTCURVE.py` This Python script reads in all the lightcurves file provided in the working directory and creates `TGraphErrors` type objects where the lightcurves are stored and can also very easily be plotted in a nice graphical format. A special ROOT macro called `AnalyzeLightcurves.C` allows to produce overlapped lightcurves reading the information stored in the `LIGHTCURVE.py` output file.

`SED_average.py` This script is appointed to construct a single spectral energy distribution from all the provided data input files. It allows as argument a start and a finish dates which are used to cut the data outside the time range of interest. In case that more than one spectral point is available at the same energy within the considered period the two values are averaged and a single final data point is provided. The macro also convert the data points to the final $erg \cdot cm^{-2}s^{-1}$ units, since different standards are used for different energy bands.

`ReformatGalaxy.py` This is a script to correct for the contribution of the host galaxy to the total measured flux. This is required in certain energy bands, like for example the optical frquencies.

`ReformatLightcurves.py` A service Python script which converts the text file from the 'lightcurve' standard data format to the 'spectrum' standard data format. A lightcurve can in fact be seen as a point in a spectrum for several time periods. This is specially useful for measurements from instruments which do not make spectroscopy as for example optical measurements in a certain band.

Moreover, a tool for the study of the correlation between the different lightcurves was developed. The `dcf.C` ROOT macro follows the prescription of Edelson and Krolik (1988) to compute the *Discrete Correlation Function* (DCF) of two time series. The method permits to compute the correlation coefficient between the variations of two lightcurves also for unevenly sampled data series[9] also scanning a predefined set of time lags.

---

[8] *Python* is a very powerful script programming language, which on the contrary of more basic scripting tools as *Bash* also allow to very easily use libraries from external packages.

[9] This is the case for many of our measurements since the lightcurves have different time scales and bins and regular observations can not be guaranteed by ground based experiment because of the often suboptimal weather conditions.

7.7 Multiwavelength results

In figures 7.16 and 7.17 the final coverage actually achieved by the campaigns is reported, whereas in figures 7.18 and 7.19 we present the remarkably complete SED measurements.

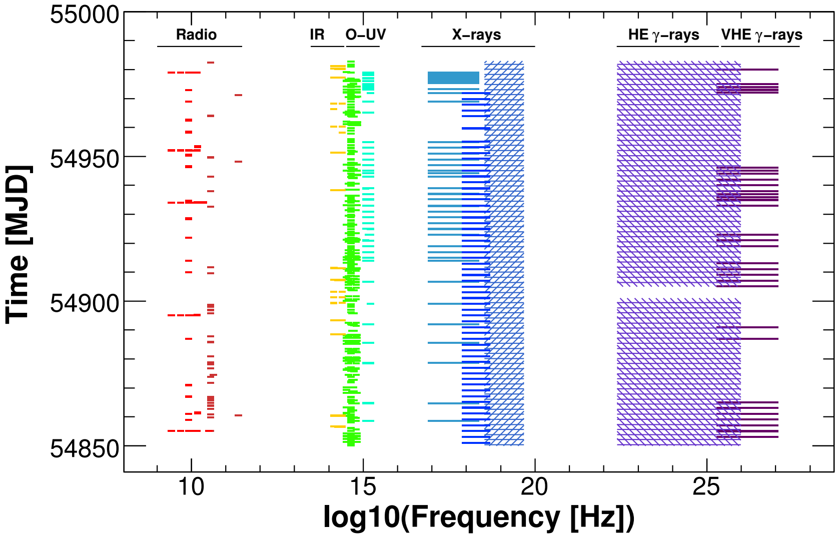

Figure 7.16: Mrk 421 MWL observation coverage. Plot provided by D. Paneque.

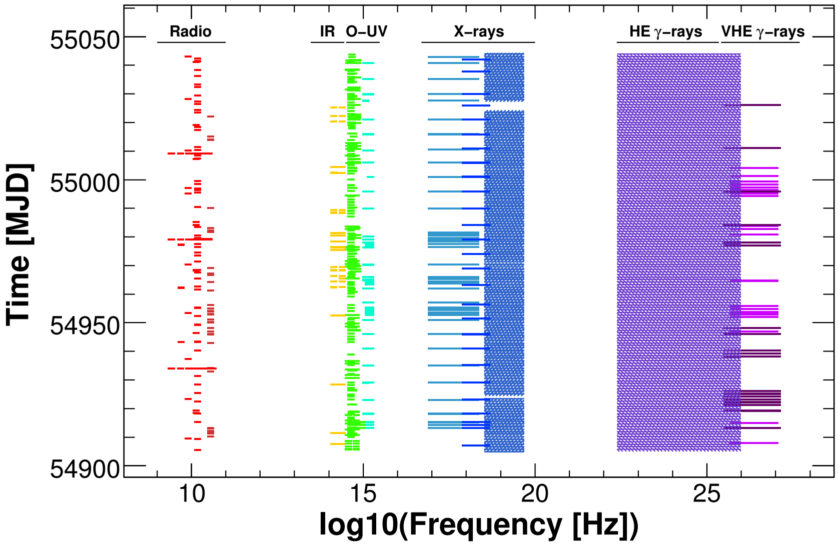

Figure 7.17: Mrk 501 MWL observation coverage. Plot provided by D. Paneque.

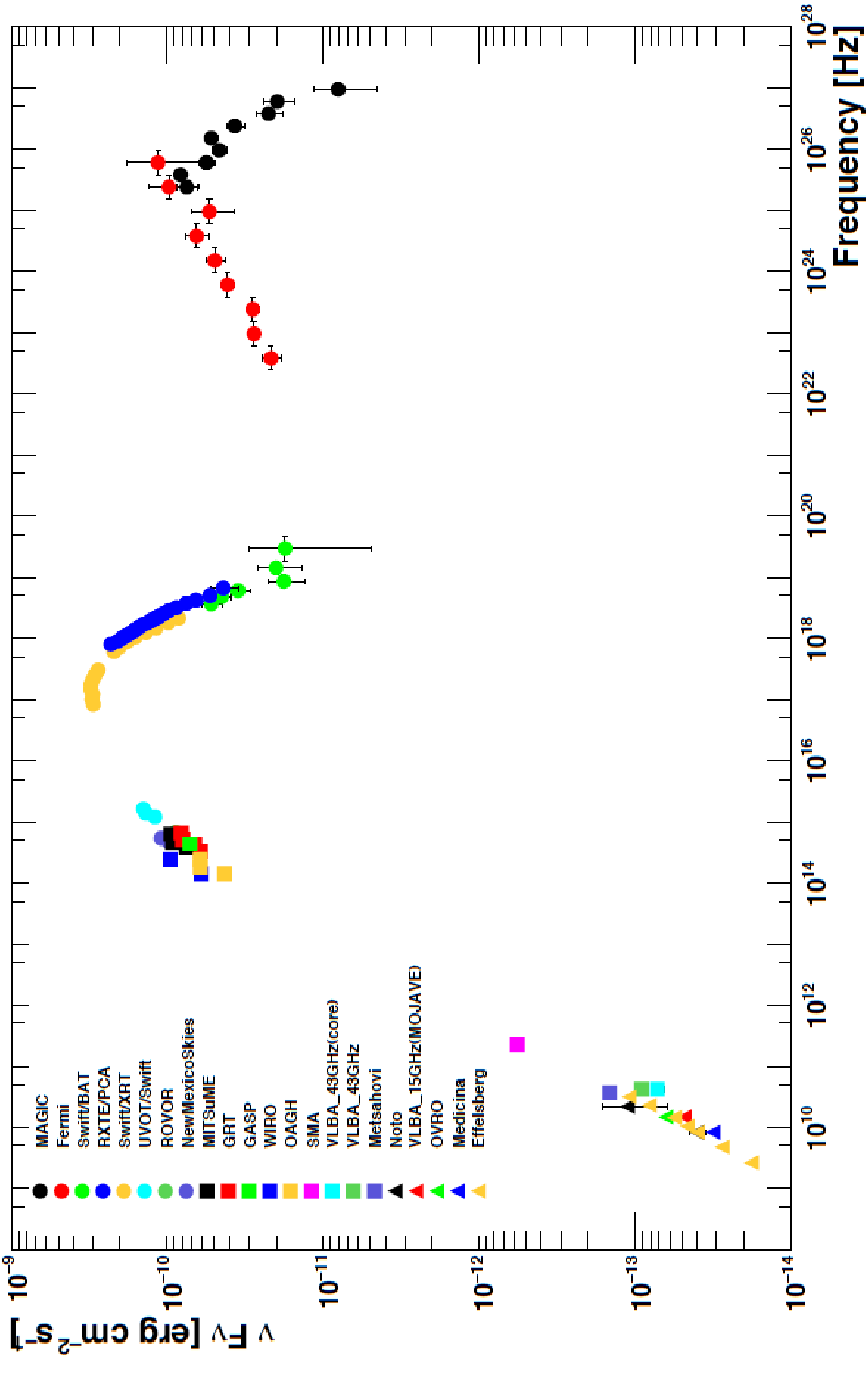

Figure 7.18: Mrk 421 MWL overall SED.

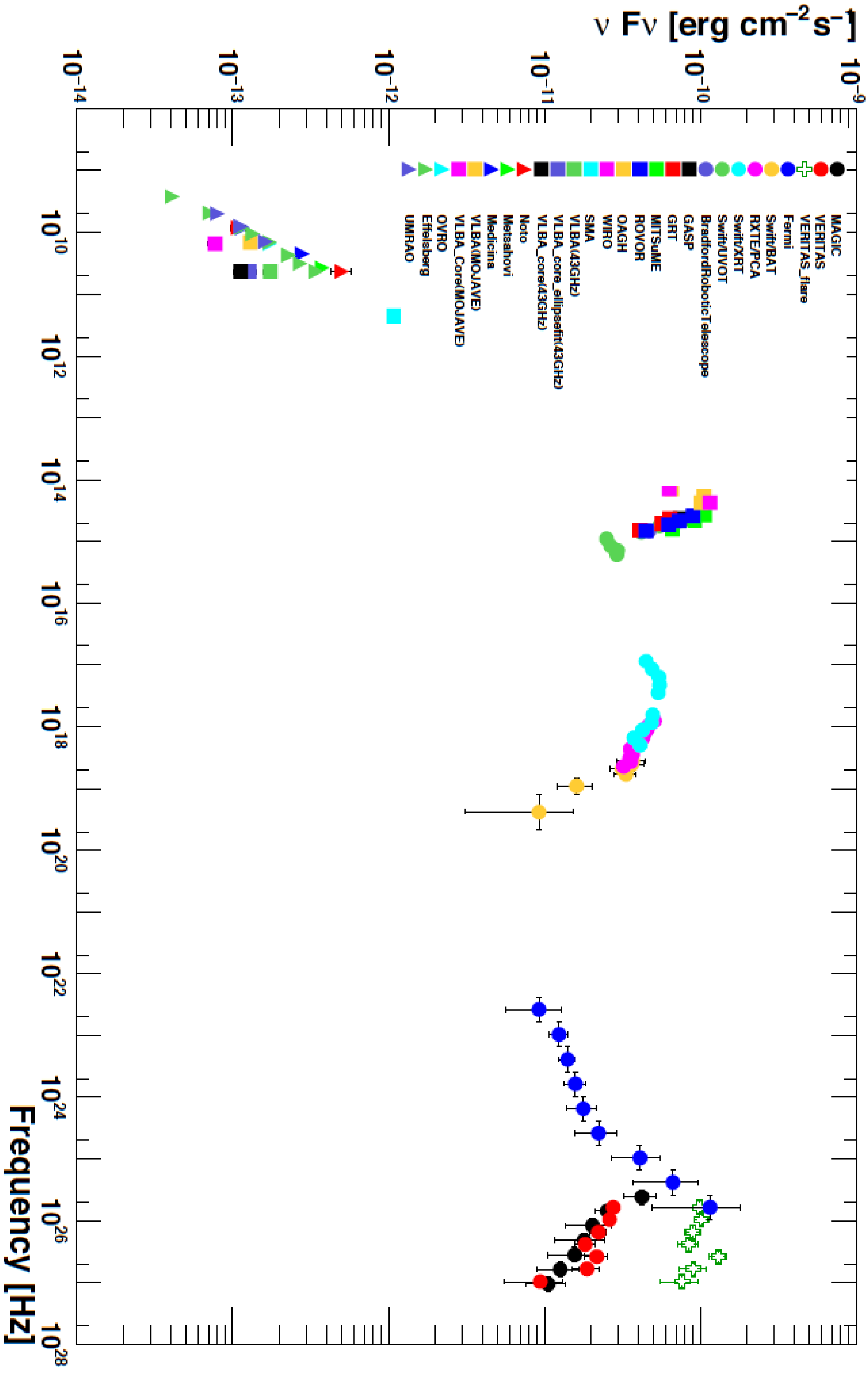

Figure 7.19: Mrk 501 MWL overall SED.

7.8 Discussion

Both the MWL2009-Mrk 421 and MWL2009-Mrk 501 campaigns provided us with an unprecedented high quality data set for the study of blazars. The wide coverage, across the whole energy spectrum (see figures 7.16 and 7.17), and the 'simultaneity' of the observations are the strongest points of the data sets.

We already know that the SED of TeV blazars is typically characterized by two humps at X-ray and γ-ray energy respectively. The importance of a wide coverage is easily explained by the fact that theoretical emission models predict the blazar emission in the whole spectrum and therefore they are better constrained by data points located all across the energy range of the SED. Simultaneity is important because of the characteristic variability of the observed objects. The conclusions we draw form a certain SED makes sense only if the data point in the spectrum refers to the same "event" in the source. The fact that blazars may vary with timescales as short as minutes[10] makes it impossible to ensure the strict simultaneity needed to achieve a significant signal in the region of overlap between ground-based and space-born telescopes, but during periods of low activity of the source when it remain in a certain characteristic state (low, high or intermediate) the long-term data can be used to constrain that particular state of the source. Obtain truly simultaneous data is also complicated by the different nature of the observing instruments. Ground based instruments, which are a significant part of the instruments involved in the campaign, can typically observe only during the night, so that the time observation windows have strong constrains, and simultaneity can be technically impossible depending on the geographic location of the detectors. The observation modes are also different from instrument to instrument. Some of the satellite telescopes observe in survey mode (24 h coverage) whereas many of the ground based telescope perform point observations during precise time slots.

7.8.1 The IC peak region

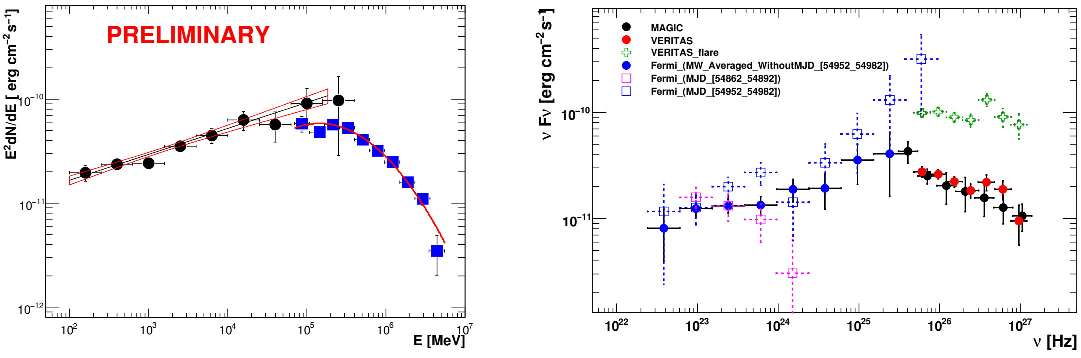

Figure 7.20: Inverse Compton peak region of the SED for Mrk 421 (left) and Mrk 501 (right). On the Mrk 501 plot, the Fermi/LAT data from the multi-frequency campaign is split in 2 data sets: MJD 54952-54982 (blue open squares) and the rest (blue filled circles).

For the first time the IC bump region could be effectively sampled, both in the rising

---

[10] At TeV energies there are several examples of flaring activity with significant flux variation in time scale of minutes. The variability timescale is also very different depending on the considered energy band.

and falling edges with a significant overlap within the Fermi and MAGIC measurements. The gap between ground-based and satellite-born γ-ray telescope has been finally closed.

Please notice that the low energy spectral component is also very well characterized with Swift/UVOT, Swift/XRT and RXTE/PCA and Swift/BAT data, covering nicely the peak of the synchrotron continuum. The only large region of the SED with no available data corresponds to the photon energy range 200 keV–100 MeV, where the sensitivity of the current instruments is still too low.

7.8.2 The EBL correction

Although both blazars are at low redshift ($z \simeq 0.03$), the attenuation of its VHE MAGIC spectrum by the extragalactic background light (see section 2.2.1) is non-negligible. The EBL absorption varies significantly between models. For example at high energy (4 TeV) the expected absorption varies from the $e^{-\tau_{\gamma\gamma}} = 0.29$ of the "Fast Evolution" model (Stecker et al., 2006) to the $e^{-\tau_{\gamma\gamma}} = 0.58$ of the Franceschini et al. (2008) or Gilmore et al. (2009) models. Nevertheless, most of the models agree on values $e^{-\tau_{\gamma\gamma}} \sim 0.5$–$0.6$ (including Kneiske et al. (2004) and Finke et al. (2010)).
The spectra presented here were corrected by the EBL absorption using the model from Franceschini et al. (2008).

7.8.3 The complete SED

We turn now to modeling the multi-frequency data set collected during the campaigns in the context of homogeneous hadronic and leptonic models. The complete Mrk 421 and Mrk 501 SEDs reported in figures 7.18 and 7.19 were considered.

The simplest model typically used to describe the emission of BL Lac objects is 'leptonic', namely the one-zone Synchrotron Self-Compton model (SSC, see also section 3.4). This kind of model is attractive due to its simplicity as well as a moderate success in accounting for the spectral and temporal properties of the TeV-emitting BL Lac blazars studied so far. We adopted the 1-zone SSC code described in Finke et al. (2008). Within this framework, the radio through X-ray emission is produced by synchrotron radiation from electrons in a homogeneous, randomly-oriented magnetic field (B) and the the γ-rays are produced by inverse Compton scattering of the synchrotron photons by the same population of electrons which produce them (see also section 3.4.3). This model was applied to both, Mrk 421 and Mrk 501, spectral energy distributions.

In the case of Mrk 421, the spectra was also attempted to be modeled in the context of an 'hadronic' scenario, adopting the Synchrotron-Proton Blazar (SPB) model from (Mücke and Protheroe, 2001*a*). Here, the relativistic electrons (e) injected instantaneously in the strongly magnetized (with constant magnetic field strength B) blob loose their energy predominantly through the synchrotron channel. The resulting synchrotron radiation of the primary e component dominates the low energy hump of the blazar SED, and serves as target photon field for interactions with the instantaneously injected relativistic protons (with index $\alpha_p = \alpha_e$) and pair (synchrotron) cascading.

Given the different characteristic of the two blazars Mrk 421 and Mrk 501, we will discuss the two modeling separately.

7.8.4 Modeling of the Mrk 421 SED

The electron distribution from the 1-zone SSC models is typically parametrized with one or two power law (PL) functions (that is, zero or one break) within an electron Lorentz factor range defined by γ_{min} and γ_{max}. In the attempt to model the SED of Mrk 421 with the Finke et al. (2008) model, we found that a single or even double power law spectra for the electrons distributions is not sufficient. In order to properly describe the shape of the measured broad-band SED during the 4.5 months long campaign, the model requires an electron distribution parameterized with three PL functions (and hence two breaks). In other words, we must add 2 extra free parameters to the model: the second break at $\gamma_{brk,2}$ and the index of the third PL function $p3$. We note here that, an alternative possibility might be to use an electron distribution parametrized with a curved function such as that resulting from episodic particle acceleration Perlman et al. (2005) or the log-parabolic function used in Tramacere et al. (2009).

Even though the very complete SED constrains the shape of the electron distribution quite well, there is still some degeneracy in the range of allowed values for the general source parameters R_b (comoving blob radius), B and δ (Doppler factor). In order to minimize the range of possible parameters, we note that the emitting region radius is constrained by the variability time, t_v. We fixed this parameter to two possible values $t_{v,min}$ = 1 day and $t_{v,min}$ = 1 h. The resulting SED models obtained with these two variability timescales are shown in figure 7.21.

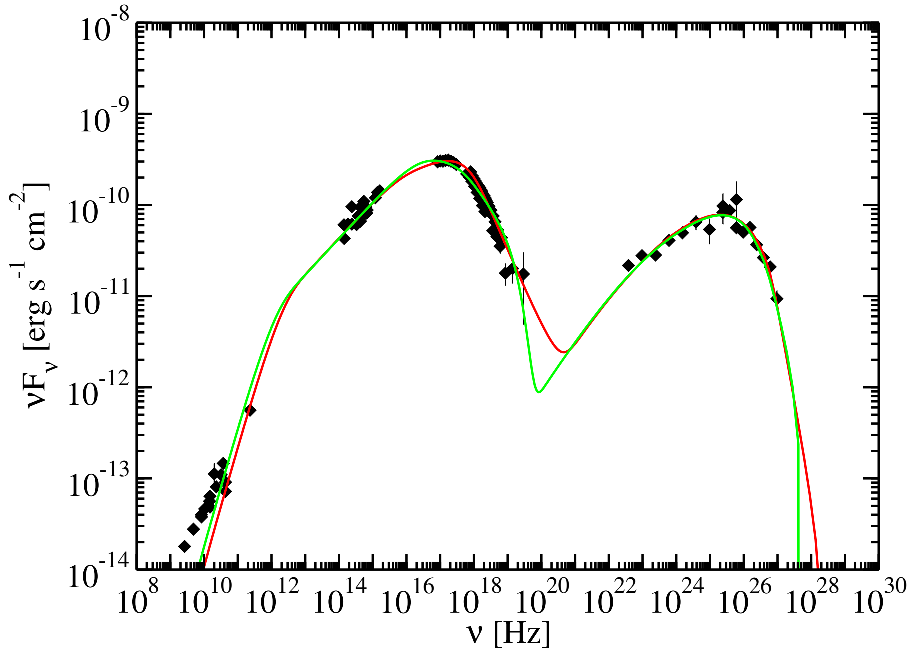

Figure 7.21: Mrk 421 leptonic SED modeling with two 1-zone SSC model fits obtained with different minimum variability timescales: t_{var} = 1 day (red curve) and t_{var} = 1 h (green curve) .

Another difference of our 1-zone SSC model with respect to previous works relate to the parameter γ_{min}. This parameter has typically not been well constrained because the radio data can only be used as upper limits for the radio flux from the blazar emission. In our modeling we use simultaneous Fermi/LAT data, which adds an additional constraint to the model[11]: if χ_{min} is arbitrarily increased, then the predicted flux by the model will under-predict the measured Fermi/LAT flux below 1 GeV.

It is important to note that the resulting parameters differ from the most popular values found in the literature, but the agreement between the data and the model turns out to be very satisfactory in the entire measured broad-band SED.

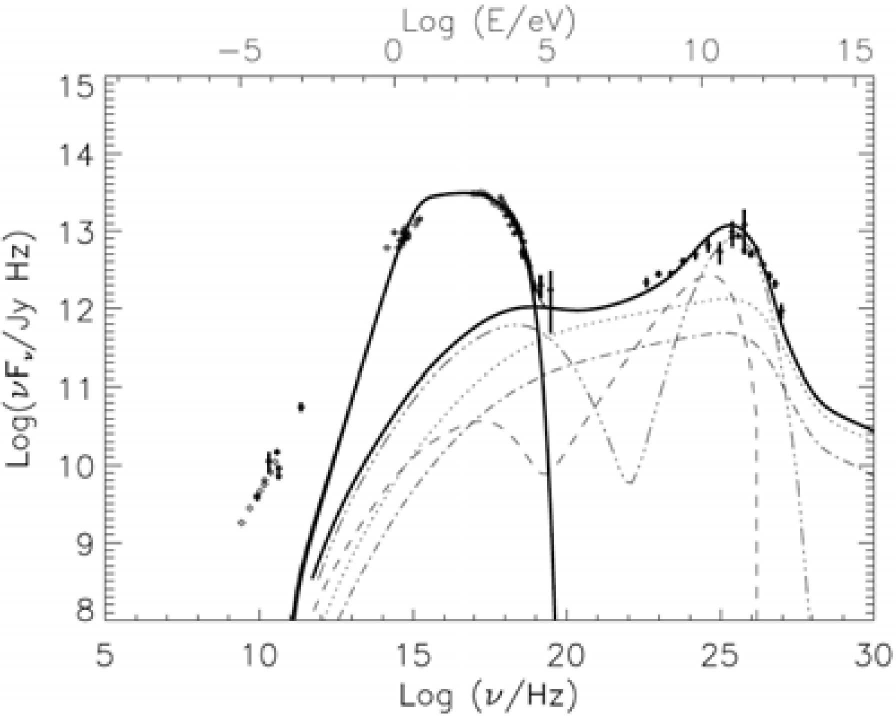

Figure 7.22: Mrk 421 hadronic SED modeling. Hadronic model fit components: ^{0}-cascade (dotted line), cascade (dasheddottedline), -synchrotron and cascade (dashed-triple-dotted line), proton synchrotron and cascade (dashed line). The solid line is the sum of all emission components. The model parameters used are: $\tau = 12 =$, $B = 50$ G, $R = 4 \quad 10^{14}$ cm, $\sigma_e = \sigma_p = 1.9$, $\chi_{p\,max} = 2\,3 \quad 10^9$, $_p = 510$ erg/cm^3, $e\ p \quad 0\,125$, $\chi_{e\,min} = 600$, $\chi_{e\,max} = 4 \quad 10^4$, $P_{jet} = 4\,4 \quad 10^{44}$ erg s ^{1}.

Let s move for Mrk 421 also to the case of an hadronic emission scenario. Figure 7.22 shows the result of the attempt to model the spectra with the hadronic model from (Mucke and Protheroe, 2001*a*) (synchrotron-proton blazar). The agreement, even if not perfect, also in this case turns out to be reasonable. In the context of this hadronic model, the measured spectra in the χ-ray band is dominated by synchrotron radiation of muons (produced during photomeson production, prior to their decay) as well as proton synchrotron radiation, with significant overall reprocessing. The interplay between muon and proton synchrotron radiation together with appreciable cascade synchrotron radiation initiated by the pairs and high energy photons from photomeson production is responsible for the observed MeV-GeV flux while the TeV emission is dominated by the high energy

---

[11] We remind that in SSC leptonic modeling the electrons which produce the synchrotron and -ray radiation are the same, so that the slope of the rising part of the two humps in the SED are strictly related.

photons from the muon synchrotron component. The source intrinsic model SED predicts > 10 TeV emission on a level of 2 to 3 orders of magnitude below the sub-TeV flux, which, will be further weakened by the EBL-caused gamma-ray opacity.

7.8.5 Modeling of the Mrk 501 SED

Although the source did not show large flux variations like the ones recorded by EGRET in 1996 or the ones measured by X-ray and χ-ray instruments in 1997, significant flux and spectral variations at χ-ray energies are present, and therefore the averaged SED constructed for the whole period has to be interpreted with caveats. A relevant TeV flare (4 times larger flux level) was detected by VERITAS during the time interval (MJD54952.9 54955.9). Unfortunately, no measurements during the same time period were possible with the MAGIC telescope since the detector was in a shut-down for a technical upgrade. The difference in the high energy part of the spectrum is clearly visible in figure 7.20 (right panel).

To model the emission of the archetype TeV blazar Mrk 501 we used again the 1-zone SSC model by Finke et al. (2008). For this, we assume a general power-law form between the minimum and maximum electron energies, χ_{min} and χ_{max}, allowing for multiple spectral breaks in between, as well as for an exponential cut-off above χ_{max}. The broad-band data set for Mrk 501 requires in fact two different electron break energies. The measured SED is hardly compatible with a simpler form of the electron distribution with only one break and an exponential cutoff. However, some smoothly curved spectral shape might be perhaps an alternative representation of the electron spectrum (Tramacere et al., 2009).

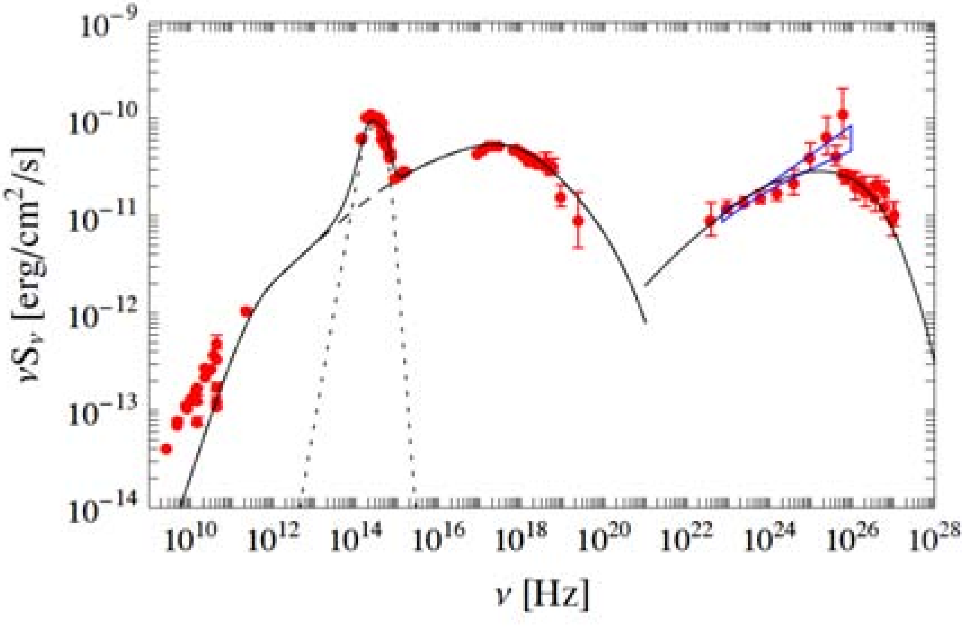

Figure 7.23: Mrk 501 leptonic SED modeling averaged over all the observations taken during the multi-frequency campaign on 2009 (March 15^{th} - August 1^{st}). Blue bow-tie in the figure corresponds to the power-law fit to the average Fermi/LAT spectrum (photon index 1.74 0.05). Dotted black curve denotes the fit to the starlight emission of the host galaxy assuming a template of a luminous elliptical as given in Silva et al. (1998).

7.8.6 Conclusions

In short, the data collected during these campaigns measure the spectra of two of the most important blazars with unprecedented coverage and with nearly the best simultaneity achievable for months-long campaigns.

The broadband SED of Mrk 421 was modeled with two different scenarios: leptonic (one zone synchrotron self-Compton) and an hadronic model (Synchrotron Proton Blazar). Both frameworks are able to describe reasonably well the average SED, implying comparable powers for the jet emission, which constitute only a small fraction ($\sim 10^{-2}$–10^{-3}) of the Eddington luminosity. The leptonic scenario suggests that the acceleration of the radiating particles (electrons) is through diffuse shock acceleration in relativistic shocks mediated by cold protons. On the other hand, in the hadronic scenario, the particle acceleration could be through extraction of electromagnetic energy from the vicinity of the supermassive black hole.

It is important to stress that the modeling results from the previous works related almost exclusively to the high activity of Mrk 421 and Mrk 501. In our case we study instead a relatively low activity state, and the modeling is applied (within the already mentioned caveats) to a truly broadband simultaneous SED.

The conclusions from this study could perhaps be extended to all high synchrotron peaked BL Lacs, being the spectrum of these two objects widely believed to be an archetype of the radio-to-γ-ray emission of the BL Lac class of AGN.

The results presented here, together with a dedicated report and discussion about the Fermi results will be documented in two forthcoming papers. Many of the threads of discussion reported in this thesis are taken from the drafts of the mentioned forthcoming papers which are currently under internal revision and will be hopefully submitted to the journals within few months.

Chapter 8

Observations of Messier 87 during an intense flare activity

What is the MAGIC contribution to the knowledge of AGNs?

8.1 Motivations

The MAGIC collaboration performed monitoring observations of the radio-galaxy M 87 starting from January 2008, sharing the task with the VERITAS and H.E.S.S. experiments. In early 2008 a rapid flare in VHE gamma rays was detected by the online automatic analysis of the MAGIC telescope. Several substantial changes of the flux level during a 13-day long period were already evident from the results of the online analysis and from the output of a fast preliminary analysis.

M 87 has been one of the targets for the MAGIC telescope since the beginning of operations. Many hours of observation have been spent on this source since it is particularly interesting for the study of the AGN physics. Messier 87 is in fact a powerful nearby Radio Galaxy located only 16 Mpc away ($z = 0.00436$) from us. On the light of the latest results it is also considered a *misaligned blazar*, i.e. with one of its jets not pointing straight along the line of sight as for a blazar, but with a fairly small angular opening. The hint of VHE γ-ray emission reported by HEGRA (Aharonian et al., 2003) in 2003 contributed to make this source particularly appealing for observation by Cherenkov telescopes. Some of the reasons of the interest for this source are the following:

non-blazar type TeV-AGN As described in section 8.1.1, M 87 was the first known non-blazar active galaxy found to emit very high energy gamma rays. Together with the very recent discovery (at VHE) of the source Centaurus A , M 87 belongs to this interesting new class (TeV radio galaxies) of VHE γ-ray emitters.

variability timescale According to Aharonian et al. (2006*a*), the typical γ-ray emission variability for M 87 is on a timescale of years, with some exceptional activity which allowed the H.E.S.S. collaboration to claim flux variation above 730 GeV on timescales of days. This reported short term variability narrows down the size of the emission region to the order of the light-crossing time of the central black hole. The results reported here, published in Albert et al. (2008*b*), further push down the variability to timescales of one day.

location of the emitting region On the jet of M 87 several hot-spots are know at different frequencies. The question about the site of acceleration of VHE photons is still open even if there are indications that point to the innermost region of the AGN as most probable emission site.

Doppler factor The misalignment of the jet is very relevant to study the effect of the relativistic boosting factor to the accelerated photons. As described in chapter 3, this Doppler factor plays a very important role in the blazar emission models and the fact that M 87 can be seen as a blazar viewed from a slightly different point of view may lead to some insights about the AGN physics. M 87 is a very suitable object where to test the leptonic and hadronic emitting scenarios currently "on the market".

The MAGIC observations of M 87 described in this thesis are one of the most interesting result to which the author contributed during his PhD work, namely as main analyzer of these data. The scientific output from this specific observation is reported in the papers Albert et al. (2008*b*), Tescaro et al. (2009*b*) and on the *Science* paper Acciari et al. (2009*b*), where the MAGIC data are combined with data from other IACT experiments and other wavebands instruments.

Although probably the most appealing candidate, M 87 is not the only radio galaxy detected in γ-rays. Cen A is another object, rather similar to M 87, detected by the H.E.S.S. experiment at TeV energies (Aharonian et al., 2009). The FERMI satellite detected γ-ray emission (at lower energy with respect to Cherenkov telescopes) not only from M 87 and Cen A but also from the radio galaxy Per A, which actually has a factor 200 larger luminosity with respect to M 87 (Abdo et al., 2009). While the extragalactic γ-ray sky is dominated by blazars, this optimistically indicates an emerging population of γ-ray radio galaxies.

In this section we have first described why M 87 is considered so interesting whereas a general review of the object is given in the next section (8.1.1). In the further two sections we will describe the details of the analysis here performed (section 8.2) and then proceed to report about the results obtained: on section 8.3 and its subsections the energy spectrum and lightcurves are discussed. Finally on section 8.4 some of the implication of the results and an outlook to the relevant questions still open are mentioned.

8.1.1 Messier 87

M 87 is a giant elliptical radio galaxy (RG, Virgo A) of Fanaroff-Riley-I-type (FR I, Fanaroff and Riley, 1974) in the Virgo Cluster at a distance of 16 Mpc (Macri et al., 1999). Its optical size is 8.3 arcmin major diameter and 6.6 arcmin minor diameter[1]. It is powered by a supermassive black hole (BH) of $(3.2 \pm 0.9) \times 10^9 \mathrm{M}_\odot$ (Macchetto et al., 1997).

The M 87 jet was the first-ever observed (Curtis, 1918), and due to the proximity of M 87, its morphological substructures can be resolved and a unique view of its innermost regions is possible. The jet, originating from the RG core, extends to 20" (Marshall et al. 2002; equivalent to a 2 kpc projected linear distance).

Several compact regions ("knots") along its axis are resolved in the radio, optical, and X-ray regimes (see figure 8.1). These knots have similar morphologies in all wavebands, although the X-ray knots appear to be tens of pc closer to the core than the optical and radio knots (Wilson and Yang, 2002). The variable brightness of the knots may be due to

---

[1] http://nedwww.ipac.caltech.edu/

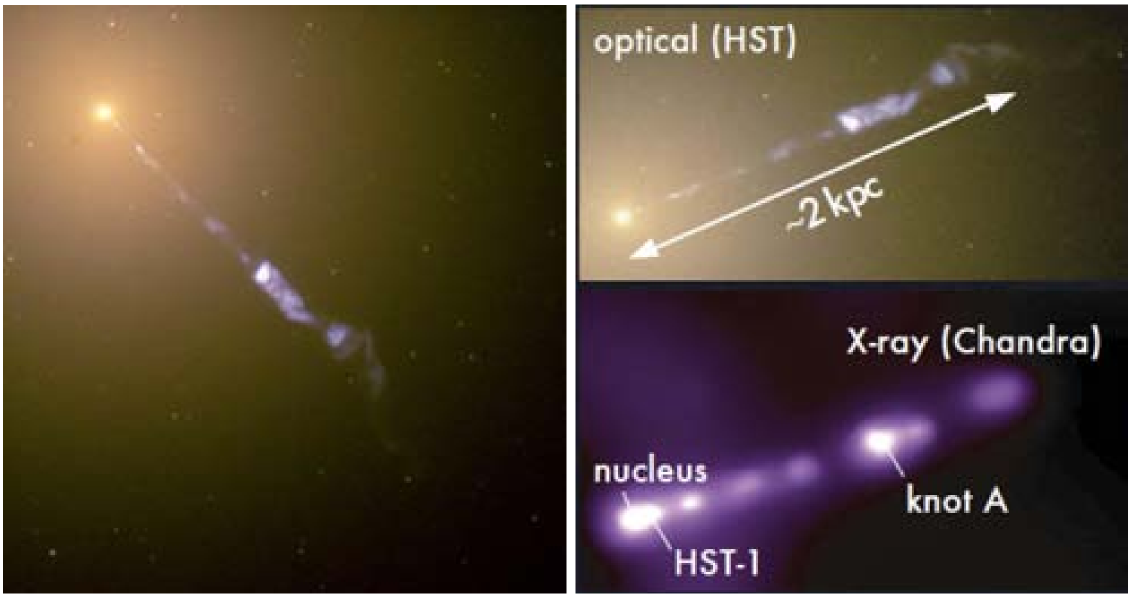

Figure 8.1: Images of M 87 at different wavelengths. Left panel: optical image of the relativistic jet and part of galaxy (HST); right panel: Comparison of the optical image of the jet with the X-ray image from the Chandra satellite. Notice the brightness of the core/nucleus region and the several resolved knots along the jet. Please refer to figure 8.12 for more details about the inner region.

several shock fronts in the jet, being responsible for particle acceleration and non-thermal emission. Superluminal motion of the knots has been observed in the optical (Biretta, 1996) and radio (Forman et al., 2007) wave bands, constraining the viewing angle of the jet to < 43 4 .

HST-1, which is the most prominent feature of the jet, has shown many flares exceeding the luminosity of the M 87 core emission. Its X-ray brightness has increased by a factor > 50 from 2000 to 2005 (Harris et al., 2006). A correlation between radio, optical, and X-ray luminosity points to a common origin of the emission. The measured superluminal motion in HST-1 is higher than in other knots, suggesting a viewing angle of < 19 for this part of the jet. The core itself is variable, too, and also shows a correlation between the emission levels from radio frequencies through X-rays (Perlman et al., 2003).

The first hint of very high energy ($E > 250$ GeV) χ-ray emission was reported by Aharonian et al. (2003) (HEGRA), and later confirmed by Aharonian et al. (2006*a*) (H.E.S.S.) and Acciari et al. (2008) (VERITAS). Also MAGIC reported the detection of M 87 in Albert et al. (2008*b*).

8.2 The MAGIC data and analysis

The data set comprises observations from 2008 January 30 to 2008 February 11 (see table 8.1). These were performed in the wobble mode for 26.7 hours. The zenith angle of the observations ranges from 16 to 35 .

The data were analyzed using MARS, the MAGIC standard analysis package. See section 7.2 for a general description of the analysis procedure and software, and chapter 7 for an example of a full analysis complete with all the technical details. In this chapter we

Month	Days†
January	30^{th}
February	1^{st}, 2^{nd}, 4^{th}, 5^{th}, 6^{th}, 7^{th}, 8^{th}, 11^{th}

Table 8.1: M 87 data sample after quality cut selection.† Same convention as in table 7.3.

will skip some of the technical plots not relevant for the discussion, mentioning directly the results when opportune. The treatment of the partial moon data will be instead described in detail in section 8.2.2, since it is not explained in any of the previous chapters.

In an analogous way as for the Markarian's analysis (see section 7.2), the data sample has been cleaned of the data which do not fulfill the requirements of the a priori quality cuts (similar to the ones described in section 7.2.3). After removing these runs with unusually low trigger rates, mostly caused by bad weather conditions, the effective observing time amounts to 22.8 h.

The choice for the optical PSF of the Montecarlo gamma sample was done according to the telescope PSF on January-February 2008: ≈ 12 mm. The hadron sample used for the training of the Random Forest was built from observation of AGNs which resulted in no detection of gamma rays (so that an 'extragalactic', 'empty', field of view was guaranteed).

The energy threshold of the analysis is estimated using a Montecarlo test sample (statistically independent from the sample used for the training). The energy threshold is defined as the peak of the reconstructed energy distribution for a given size cut. For this analysis, the cut Size > 400 phe results in an energy threshold of $\simeq 300$ GeV whereas the minimum Size cut Size > 100 phe leads to $E_{th.} \simeq 100$ GeV.

8.2.1 Check of the analysis

Besides the M 87 data, a couple of hours of Crab Nebula observations, chosen in the same period and zenith angle range were analyzed. Namely 1.7 h of wobble data from the observation performed in 2008 on February 1^{st} and February 2^{nd}. As in the case of the analysis of Mrk 421 and Mrk 501, described in chapter 7, these Crab Nebula data were analyzed with the only purpose of checking the M 87 analysis.

We will report here the α-plots which show that the sensitivity of the analysis is also in this case in agreement with the expectations. Actually, the sensitivity obtained with this particular Crab Nebula data sample is slightly better than the expected 1.6% Crab Nebula flux units. This should not surprise too much since this estimation is done using a relatively small Crab Nebula data sample (1.7 h only), which is therefore more prone to statistical fluctuations. An energy spectrum was also computed which was, within statistical errors, compatible with the published spectra of the Crab Nebula (Albert et al., 2008*d*).

8.2.2 Moon data

The capability of the MAGIC telescope to observe under moderate moonlight has been studied in Albert and et al. (2007) and Britzger (2009). In both cases a pragmatic approach was taken, i.e. using real observation of the Crab Nebula instead of Montecarlo simulation. TeV γ-ray signals from the Crab Nebula were detected with the MAGIC telescope during periods when the moon was above the horizon and during twilight.

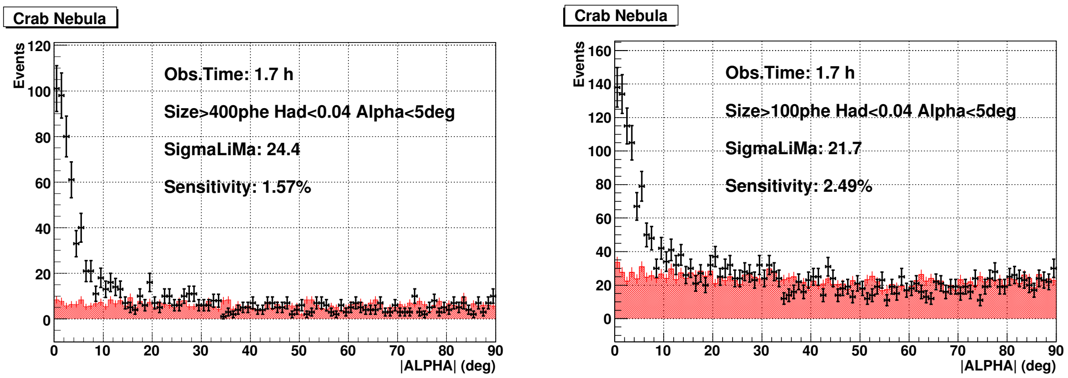

Figure 8.2: Apha plots for the test sample of Crab Nebula. The sensitivity with a Size cut larger than 400 phe resulted to be 1.57% of the Crab Nebula flux, which is very close to the reference value of 1.6%. On the right panel the sensitivity for a Size cut larger that 100 phe is also reported, since this would be the minimum Size cut used for the calculation of the energy spectra.

These observation required an increase of the trigger Discriminator Thresholds[2] (DT, see also 5.4.5). The setting of the DTs can be done manually by the observers, loading a table of values suitable for the particular light conditions, or automatically by the Central Control. This latter adjustment is performed by a routine which checks the trigger rate of each pixel in the trigger area, and increases the threshold for that pixel if the rate is higher than expected. As a consequence the average DT will have a higher value for observations with high background light. This automatic procedure is slower than the manual option if the light conditions are very different from those assumed by the pre-loaded table, but is very efficient when the light conditions are changing smoothly and reasonably slowly (for example in the transition from ‘dark time’ to ‘twilight’).

The checks performed during the moon observations showed that the image parameters for Cherenkov images with Size above 200 phe are not altered by the increased diffuse background light. This means that the analysis based on the Hillas parameters does not have to be adapted for data acquired under moonlight, and in particular the γ/hadron separation power is not reduced for this kind of observations. This is actually the reason why we use absolute thresholds values to perform the cleaning of the events (section 6.6.3). For large enough pulses, no dependency of the image parameters on the level of background light is expected.

Now about how to quanitify the loss of performance during moon observations. The main effect is due to a less efficient trigger given the increased discriminator thresholds. This results in a smaller collection area with respect to what simulated in the Montecarlo (which is used to compute the final γ-ray flux). Observations of the Crab Nebula were divided into different samples according to the observation date and the DT value. For each of the samples the γ-ray rate (R) was computed and for a given Size range, the dependence of R with the DT is found to be described by the following linear function:

$$R = R_0(1 - S_0(DT - DT_0))$$

where R_0 is a normalization factor, S_0 is the *efficiency loss rate*, and DT_0 is a reference

---

[2] During moon time observations there is no need to change also the high voltage settings since the camera PMTs were especially designed to avoid high currents and therefore there is no risk to damaging them.

DT value that, for convenience, is chosen as the one used in dark observations. The knowledge of this functional dependence allows to correct the data flux obtained using a standard "dark" analysis depending on the characteristic DT value of the data (see section 8.3.4).

Observations during moderate moon conditions allow to increase the duty cycle of MAGIC from 12% to 18% (Albert and et al., 2007). Useful indications on how select the data depending on the light conditions and which type of analysis is worth to adopt can be found in Britzger (2009).

8.3 Results

8.3.1 Preliminary results

In figure 8.3 we report the preliminary lightcurve which was computed in Crab Nebula flux units few days after the flare (1^{st} of February). The lightcurve was obtained comparing the number of excess events obtained in the day by day α-plots with the number of excess events obtained from the Crab Nebula applying the same cuts.

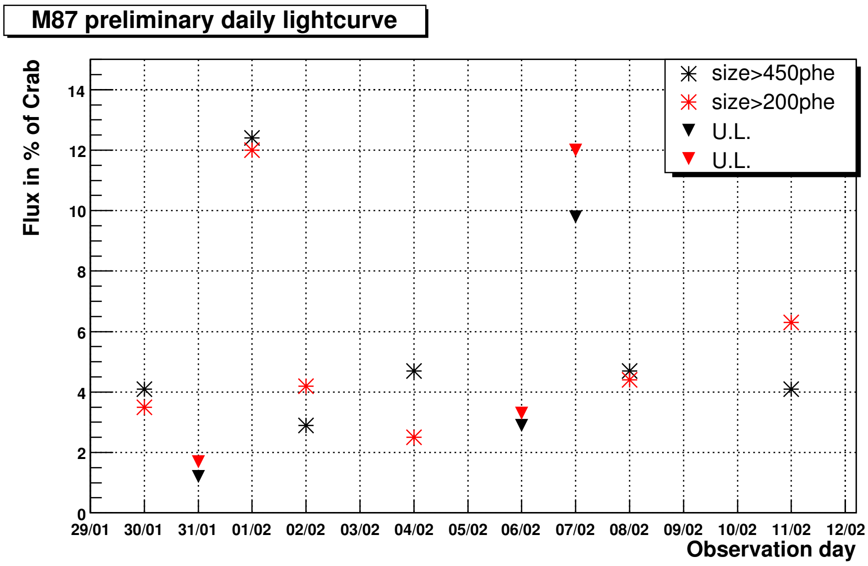

Figure 8.3: Preliminary lightcurve for M 87, obtained from a fast analysis few day after the "flare" (1^{st} of February). Reverse triangle markers are flux upper limits.

In figure 8.4 the α-plots for each one of the days of the M 87 flare complex are reported. The day whose the plot refers to is indicated on the title.

The cut in Hadronness for γ/hadron separation was optimized on a the contemporaneous data set of the Crab Nebula mentioned in section 8.2.1. The final cut $\alpha < 5°$ (figure 8.5) was also optimized on the Crab Nebula data to determine the number of excess events and the significance of the signal. After the final Alpha cut (resulting in an overall cut efficiency of 37% for MC γ-rays), the total signal of 241 events over 349 normalized background events corresponds to an excess with a significance of 9.9 σ. The highest flux was observed on 2008 February 1 at a significance of 8.0 σ. For the background estimation

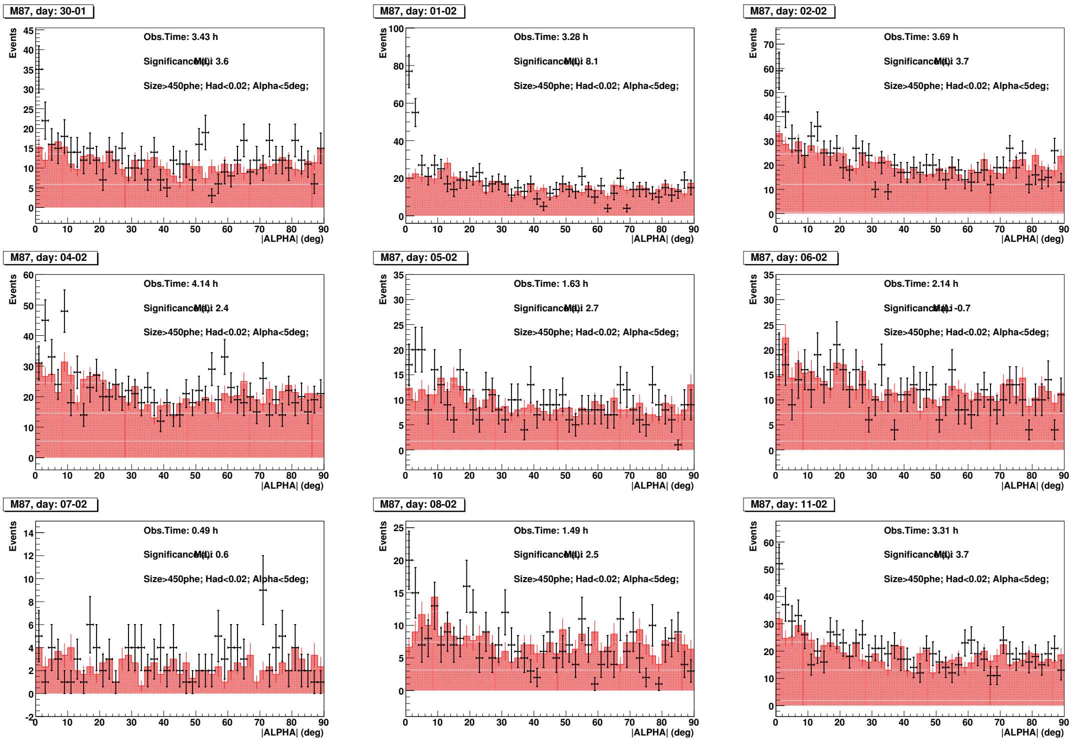

Figure 8.4: Day-by-day α-plots. The background is estimated using three off regions.

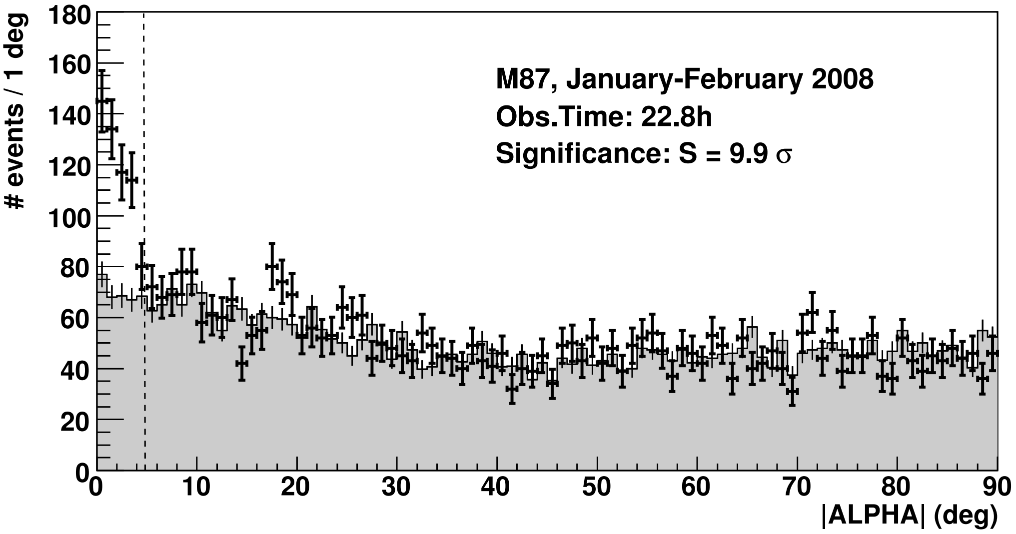

Figure 8.5: α distribution for the overall data sample. The background (gray histogram) is estimated using three OFF regions arranged symmetrically to the ON-source region with respect to the camera center. A γ-ray excess with a significance of 9.9 standard deviations is obtained. (Albert et al., 2008*b*)

three off sky regions are chosen symmetrically to the on (source) region with respect to the camera center.

8.3.2 Results: Lightcurve

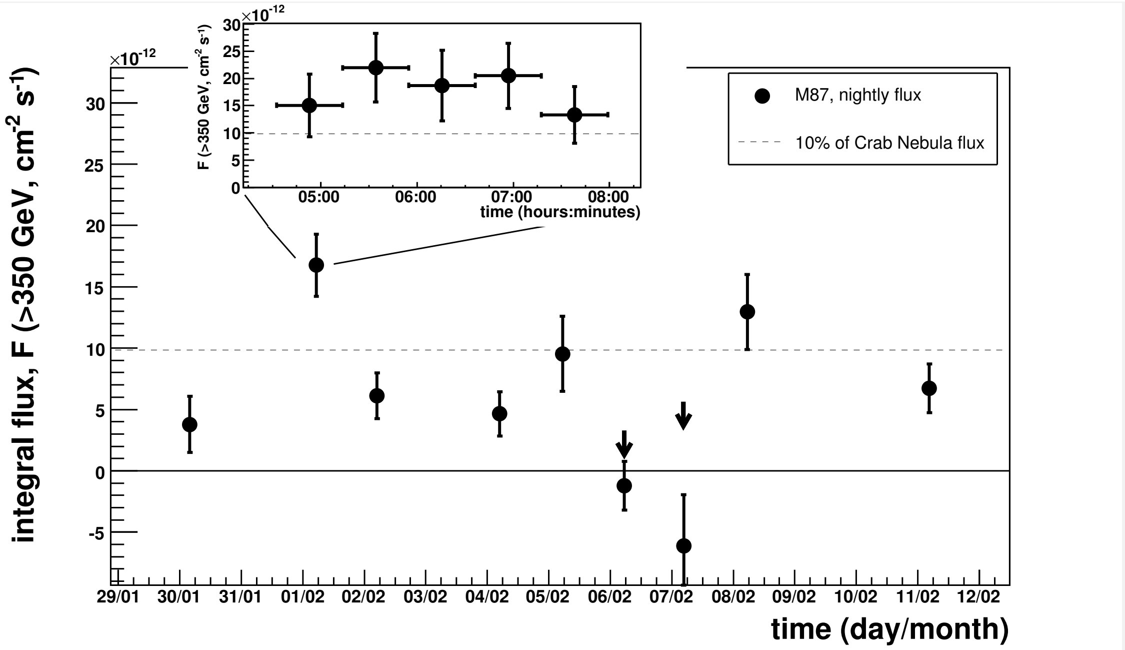

Figure 8.6: The night-by-night light curve for M 87 as measured from 2008 January 30th (MJD 54495) to 2008 February 11th (MJD 54507). The lightcurve refers to the integral flux above 350 GeV; flux variations are apparent on variability timescales down to 1 day. The inlay shows the light curve above 350 GeV in a 40 min time binning for the night with the highest flux (February 1st). The vertical arrows represent flux upper limits (95% c.l.) for the nights with negative excesses.

In searching for time variability, the data set was divided into nine subsets, one per observing night. In figures 8.6 and 8.7 we show both the light curve above the analysis threshold (150–350 GeV) and in the energy range at which MAGIC has the highest sensitivity (> 350 GeV). The low-energy range shows no significant variability with a χ^2 of 12.6/8 (probability of $P = 0.13$) for a fit to a constant flux. Instead, in the energy range above 350 GeV clear variability is found. A fit by a constant has a χ^2 of 47.8/8 corresponding to $P = 1.1 \cdot 10^{-7}$. The correlation coefficient between the two energy bins is $r = -0.25^{+0.40}_{-0.33}$ (1-σ errors), suggesting that there is no significant correlation, but we note the rather large error bars in the low energy range. We also investigated a night-by-night variability. There are five pairs of observations on consecutive nights in the total data set. We calculated individual probabilities P_i for these pairs to correspond to the same flux level and the corresponding significances. We then computed a combined significance $P_{\rm comb}$ following the prescription given by Bityukov et al. (2006): $P_{\rm comb} = \left(\sum P_i\right)/\sqrt{n}$, with $n = 5$. We interpret the resulting $P_{\rm comb} = 5.6\,\sigma$ as a proof that the flux varies on timescales of 1 day or below. Note that the 1 day variability is claimed from this combined analysis rather than from the 2008 February 1 flare alone. We find our statistics not

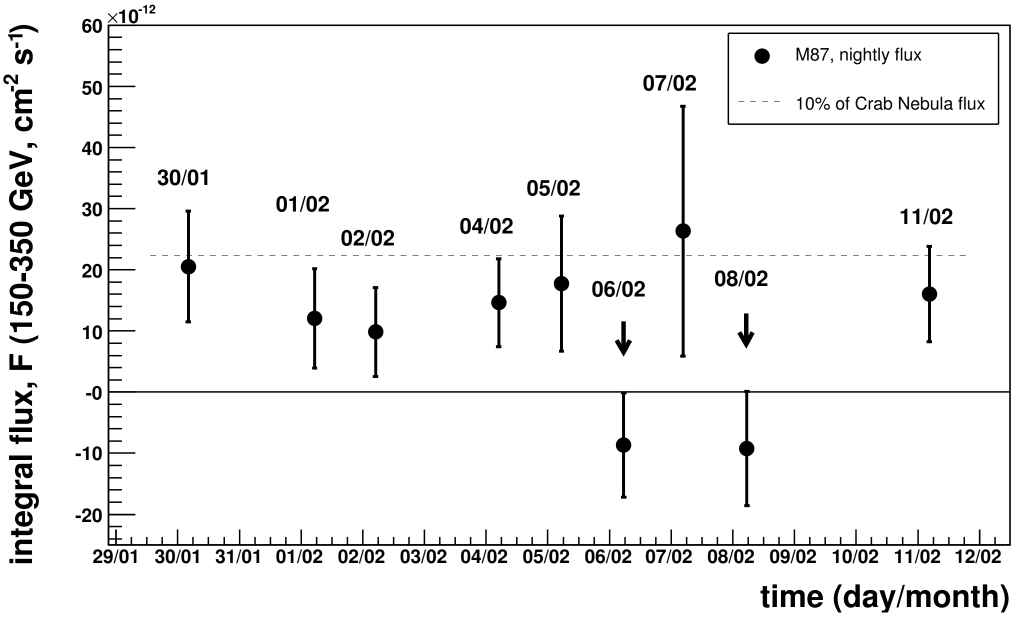

Figure 8.7: The night-by-night light curve for M 87 as measured from 2008 January 30^{th} (MJD 54495) to 2008 February 11^{th} (MJD 54507) in the energy bin 150–350 GeV. The flux is consistent with a constant emission. The vertical arrows represent flux upper limits (95% c.l.) for the nights with negative excesses.

sufficient enough to determine the flare shape. Given the number of the observed changes in the flux level, the data might belong to a complex of two sub-flares.

We also looked for shorter time variability, but in none of the observation nights there is a significant flux variation in the two energy bands. A typical example in a 40 minute binning is shown in the inset in figure 8.6 for February 1^{st}.

8.3.3 Results: Spectrum

To derive a differential energy spectrum, we applied looser cuts than those in figure 8.5 in order to get a spectrum less sensitive to the residual discrepancies between data and Montecarlo (section 6.6.8). Looser cuts reduce the effect of systematic uncertainties between data and Montecarlo events, which is important for the estimation of the effective collection areas. As side effect a higher number of γ-ray candidates events are retained. This lowers the effective analysis threshold down to 150 GeV. The derived spectrum was unfolded to correct for the effects of the limited energy resolution of the detector (Albert et al., 2007*a*).

The averaged differential energy spectrum of M 87 (figure 8.8) extends from ~ 100 GeV to ~ 10 TeV and can be well approximated by a power law:

$$\frac{\mathrm{d}F}{\mathrm{d}E} = (2.89 \pm 0.37) \times 10^{-12} \left(\frac{E}{1\,\mathrm{TeV}}\right)^{-2.30\pm0.11} \frac{1}{\mathrm{TeV\,cm^2\,s}}.$$

The errors are statistical only. We estimate an 11% systematic uncertainty in the normalization and 0.20 for the spectral index (Albert et al., 2008*d*). The measured values are

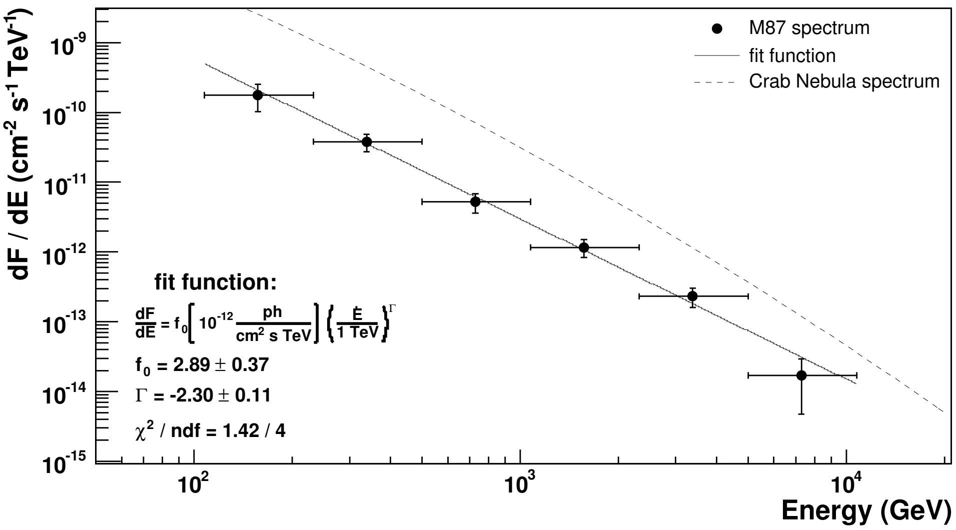

Figure 8.8: The differential energy spectrum of M 87 for the total data sample. The horizontal error bars represent width of the energy bins. The best-fit function, assuming a power law, is given by the solid line. The Crab Nebula spectrum (Albert et al., 2008*d*) is given by the dashed curve for reference.

in good agreement with the H.E.S.S. (spectral index $\Gamma = -2.2 \pm 0.15$, Aharonian et al. 2006*a*) and VERITAS ($\Gamma = -2.31 \pm 0.17$, Acciari et al. 2008) results. The observed spectrum is not significantly affected by the evolving extragalactic background light (EBL) due to the proximity of M 87 (section 2.2.1).

To investigate a possible dependence of the spectral index on the absolute flux level, we divided the data sample into 'high' and 'low' state subsamples. The high sample comprises the two nights with the highest flux above 350 GeV (February 1 and 8), while the low state comprises the nights of lower-flux data (January 30^{th}, February 2^{nd}, 4^{th}, and 11^{th}).

Both the high and low state spectra (figure 8.9) can be well described by a power law:

$$\frac{\mathrm{d}F}{\mathrm{d}E} = f_0 \left(\frac{E}{1\,\mathrm{TeV}}\right)^{\Gamma} \left[\frac{10^{-12}}{\mathrm{cm}^2\,\mathrm{s}\,\mathrm{TeV}}\right]$$

with $f_0^{\mathrm{high}} = (4.81 \pm 0.82)$, $\Gamma^{\mathrm{high}} = (-2.21 \pm 0.18)$ and $f_0^{\mathrm{low}} = (2.58 \pm 0.92)$, $\Gamma^{\mathrm{low}} = (-2.60 \pm 0.30)$ for the high and low states, respectively.

There is a marginally significant hardening of the spectral index with the higher flux on the level of 1–2 standard deviations, depending on the way the significance is calculated. Although no spectral hardening can be a priori expected that turned out to be the case for certain data sets of blazars. The hardening reported here is not significant, so that no conclusion can be drawn. Even under the hypothesis of an actual spectral index dependence, the spectral hardening could be hidden by the large errors or simply not be present at all since the proximity of the two flux levels (less than a factor of 2 difference).

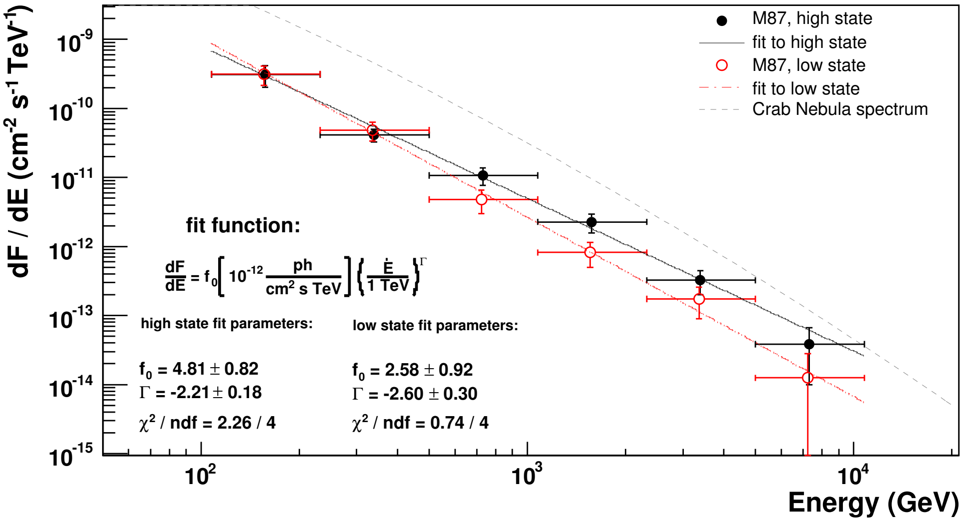

Figure 8.9: The differential energy spectra of M 87 divided into ‘high’ (filled circles) and ‘low’ (open circles) states. See text for the details. The best-fit functions, assuming power laws, are given by the black solid and red dashed-dotted curves, respectively.

8.3.4 Efficiency loss correction

As we described in section 8.2.2, in case of observations performed under moderate moon light observations the γ-ray flux obtained by a standard dark-time analysis has to be corrected for the loss of efficiency. In the specific case of these data, the first two days of observation are affected by partial moon light conditions. Moreover, in the subsequent days the final part of the observation time was under twilight conditions (being M 87 the last source in the schedule for those nights).

The spectrum and the light curves were corrected for trigger inefficiencies due to higher discriminator thresholds during partial moon light and twilight conditions (Albert and et al., 2007). These corrections are always smaller than 20% (with no corrections required for most of the data points). Please find in figure 8.10 a plot where the lightcurve is shown before and after applying these corrections (on the left panel also the average DT for each day[3]).

The variability of the source is the most relevant astrophysical result obtained from these data. It has been checked with special care. We report in figure 8.11 a comparison of lightcurves obtained by applying different analysis settings. The very first result obtained with the default `fluxlc` cuts is plotted together with the final lightcurve with optimized cuts. Also the lightcurves obtained changing the Alpha cut from 5 to 10 degrees and the miniumum Size cut from 100 to 250 phe are plotted. Finally also the lightcurve obtained removing all the runs marked as ‘twilight’ was added to the plot. Notice that no efficiency corrections are yet applied for any of the lightcurves shown in this plot.
The different settings affect only marginally the lightcurve points, proving the robustness of the result.

---

[3] Please notice that only the first two days have a significantly different DT with respect to the rest of the days.

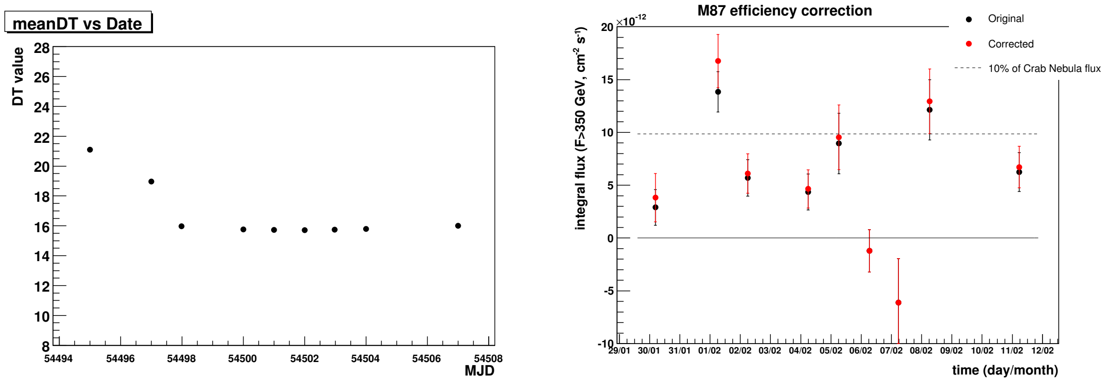

Figure 8.10: On the left panel: average DTs for the M 87 observation days. On the right panel: comparison of the main lightcurve before and after the efficiency loss correction (see text). The correction affects only marginally the results.

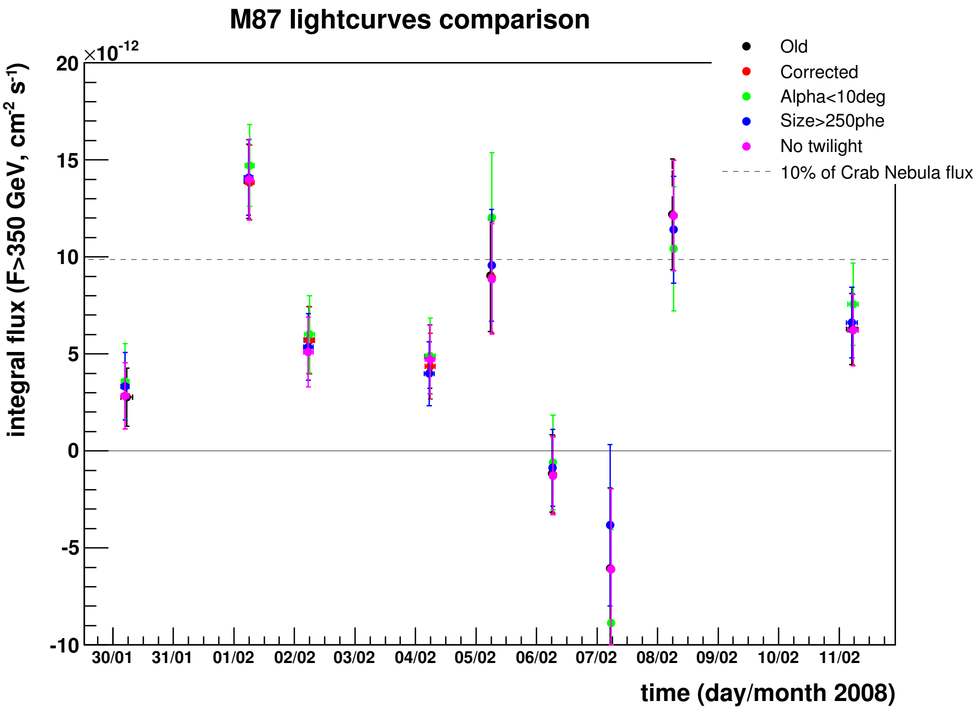

Figure 8.11: Comparison of different lightcurves obtained with different analysis settings. This plot is meant to check that the different analysis choices affects the results within statistical errors. On the legend the 'Old' refers to a non optimized analysis. 'No twilight' refers to a data set were all the twilight runs were removed. A cut in estimated energy > 350 GeV was applied.

8.4 Discussion

We summarize in this section the conclusions which can be drawn from the M 87 results reported in this chapter (referenced in Albert et al. (2008*b*)) together with the other recent H.E.S.S., VERITAS and Fermi results on M 87 (Aharonian et al. (2006*a*), Acciari et al. (2008), Acciari et al. (2009*b*) and Abdo et al. (2009)).

Messier 87 is one of the closest detected extragalactic TeV γ-ray source. In virtue of its closeness and contrary to most of the AGNs it is detected as non point-like in many frequencies. Actually, it is in many cases very well spatially resolved, also in the inner region of its nucleus. This fact is very important because the key to identifying the location of the VHE γ-ray emission lies in connecting it to measurements at other wave bands. In fact, in case that correlated variability is detected, we might shed light on the location of the emitting gamma-ray region and about the mechanism of acceleration of the primary particles.

The γ-ray flux level of M 87 during the reported flare period was unprecedentedly high. While hundreds of hours of observation during the previous MAGIC observation cycles could not lead to any firm detection of the source, the 3.3 h of data taken in the night between January 31^{st} and February 1^{st} 2008 allowed, stand-alone, a solid detection of M 87 (more than 8 σ, which increases to $\approx$ 10 standard deviations if one considers the whole flare complex). The merit of the bare detection is to reinforce the previous detections from the H.E.S.S. and VERITAS experiments and to once more confirm that TeV gamma-rays are emitted by extragalactic sources other than blazars.

The TeV measurements might shed light over several issues like the location and size of the γ-ray emitting region or the radiation processes therein at work. The clearly non thermal nature of the studied radiation suggests an extreme environment as the location of the emitting region. For this reason, either the relativistic jet or the area in the close vicinity of the central SMBH turn out to be the most natural candidates. The 2 kpc scale plasma jet (Curtis, 1918) originating from the center of M 87 is resolved at different wavelengths (radio, optical, and X-ray, see figure 8.12). Along the jet, previous monitoring observations show two near-stationary components (parsec scale) and features that move at apparent superluminal speed (100 pc scale). The angle between this plasma jet and the line of sight is estimated to lie between 15° and 25° (Acciari et al., 2009*b*)[4].

The brightest part of the jet is indeed located at its *base*, the region of the jet located closer to the central black hole. For example, radio observations (VLBI) of the M 87 inner jet show a well-resolved, edge-brightened structure extending to within 0.5 milli-arc sec (0.04 pc or 70 R_S) of the central part. Generally, the core can be offset from the actual location of the black hole by an unknown amount, in which case it could mark the location of a shock structure or the region were the jet becomes optically thin. Please notice that the term *core* might be ambiguous. It might refer to the central region of the galaxy in general, to the base of the jet or to the region in the very close vicinity of the black hole, where the jet is not collimated yet. Below with the term 'core' we refer to the inner part region in general, but excluding all the knot features.

---

[4] The inclination angle of the jet is not very clear. Typical models assume a M 87 jet misalignment around 30°–35°, but this refers to the large scale structures (farther from the core). The superluminal motion requires instead a tighter jet orientation (within 19°) which in this case very likely refers to emitting blobs located in the inner part of the jet, where the orientation is not necessarily the same as the large scale jet. SSC models applied to the measured SED proposes even tighter angles ($\theta = 10°$, Abdo et al. (2009)). As final remark, the observed inclination of the jet relative to the observer's line of sight, is what demonstrates that M 87 is not a blazar and qualify it as a different class of TeV AGN emitter.

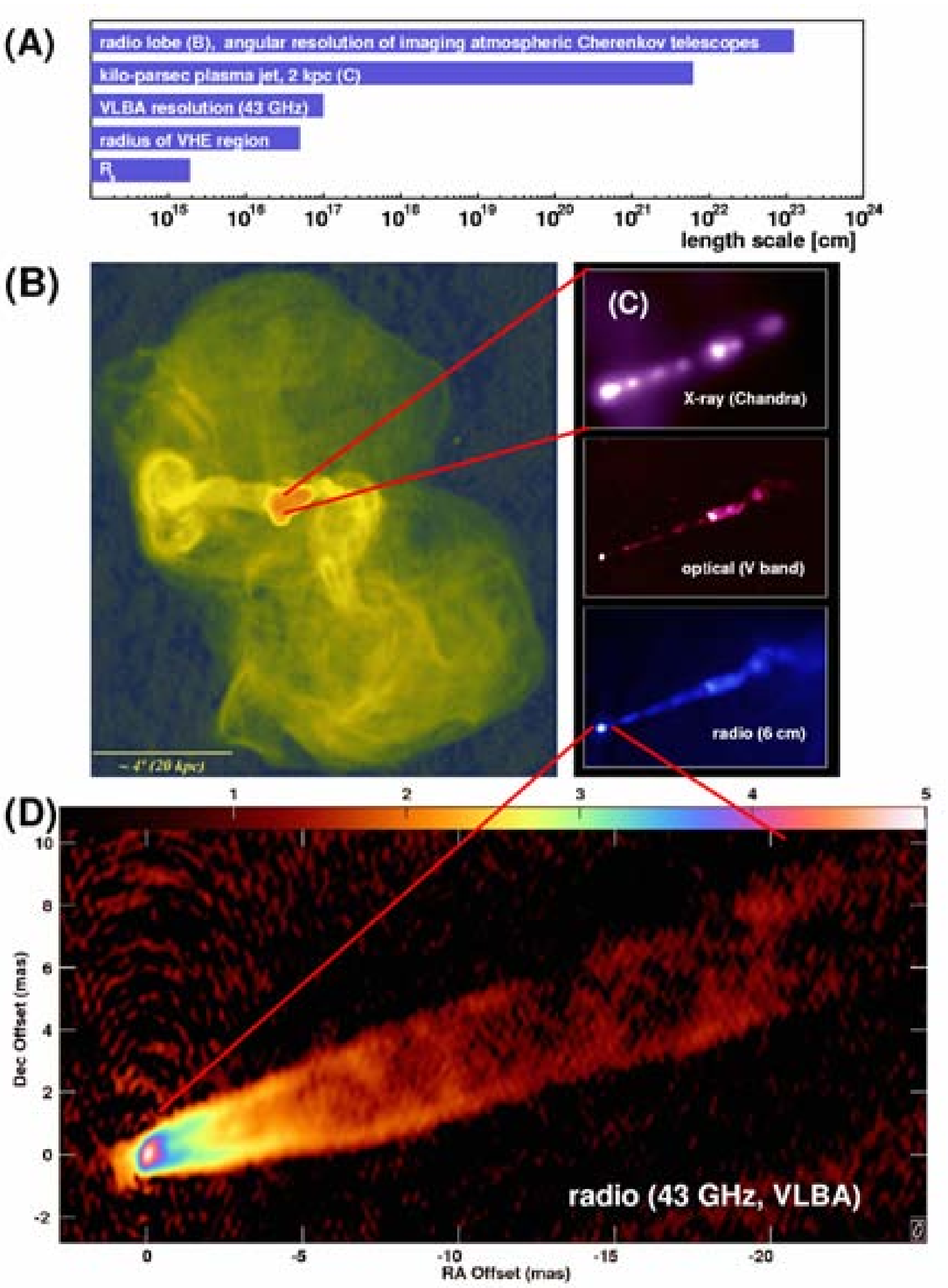

Figure 8.12: M 87 at different photon frequencies and length scales. (A): Comparison of the different length scales. (B): 90 cm radio emission measured with the VLA. The jet outflows terminate in a halo which has a diameter of roughly 80 kpc. (C): Zoomed image of the plasma jet with an extension of 2 kpc (2000), seen in different frequency bands: X-rays (Chandra, upper panel) optical (V band, middle) and radio (6 cm, lower panel). Individual knots in the jet and the nucleus can be seen in all three frequency bands. The innermost knot HST-1 is located at a projected distance of 0.86 arcseconds (60 pc, 105 R_s) from the nucleus. (D): An averaged radio image based on 23 images from the VLBA monitoring project at 43 GHz. The color scale gives the logarithm of the flux density in units of 0.01 mJy per beam. Image from Acciari et al. (2009*b*).

Several bright spots or *knots* were resolved and identified along the jet at radio, optical and X-ray frequencies. The brightest are 'knot A', with a size of 80 pc, and 'HST-1', with no robust lower limit on its size yet. The size of these spots is very important to identify the location of the γ-ray emitting region especially because no spatial exclusion can be provided because of the insufficient angular resolution of the γ-ray detectors. The size of the VHE γ-ray emission region is in fact constrained by the timescale of the observed flux variability. The typical $\approx 0.1^\circ$ angular resolution of the Cherenkov telescope does not allow to resolve any structure in M 87. Although the γ-ray point-like spot is centered on the M 87 nucleus, its angular size of ~ 3 arcmin is in fact compatible with any of the considered emission region, like HST-1 or knot A (Aharonian et al., 2006*a*).

Nevertheless, the angular resolution of Cherenkov telescopes is sufficient to exclude the core of the Virgo cluster and radio outer regions (radio lobes) of M 87 as the source of the VHE γ-rays. This is not the case for the γ-ray detection from the FERMI space telescope, where the poorer angular resolution ($\theta_{68} \simeq 0.8^\circ$, depending on the energy) does not allow to disentangle a possible contribution from the extended radio features to the total gamma-ray flux. The Cherenkov telescopes angular resolution allows also to exclude another hypothesis related to dark matter. It is thought that dark matter might be constituted by a new weakly interacting particle which could possibly annihilate and produce γ-rays. Dark matter is expected to accumulate in galaxies forming a wide halo all around the "visible" galaxy, so that in the case of the near-by M 87 the eventual γ-ray radiation is expected to be extended and not point-like as detected. Even more important, the emission due to dark matter is expected to be steady and not variable as observed.

The data analyzed in this thesis allowed to firmly nail down the time-scale variability to $\leq$ 1-day (improving the previous few-days time-scale variability reported by H.E.S.S. in Aharonian et al. (2006*a*)). The detected day-scale time variability, for any reasonable values of δ (1–50), implies a constraint on the size of the TeV γ-ray source to a size similar to the Schwarzchild radius of the BH, which for M 87 corresponds to $R_S \approx 0.001$ pc (Acciari et al., 2008). The constraint depends on the Doppler factor δ because the light travel-time, which is what actually constrains the size of the emitting region, has to be computed in the rest frame of the emitting region to be valid. The time-scale variability argument excludes knot A as possible origin site of the TeV emission but cannot be used to discard HST-1 because of its unknown size.

Another intensively debated topic is the physics process responsible for gamma-ray emission in M 87. In the modeling of the γ-ray radiation one of the main issues which has to be taken into account is the absorption of the gammas by optical-IR photons. If the radiation field in the accelerating region is too high, it might result opaque to γ-ray propagation. With its expected low accretion rate, and consequent low bolometric luminosity, the nucleus of M 87 is thought to be effectively transparent for γ-rays up to an energy of 10 TeV. The core radiation at optical-IR frequencies is not strong enough to attenuate significantly TeV γ-rays even at 5 Schwarzschild radii away from the BH (Neronov and Aharonian, 2007). This allows a γ-ray production region in the immediate vicinity of the M 87 core. In blazars without prominent disk or broad-line features, the VHE emission is explained by inverse Compton processes involving the synchrotron photons and their parent electron population (Maraschi et al., 1992). Alternatively, in hadronic models, interactions of a highly relativistic jet outflow with ambient matter (Dar and Laor, 1997), (Beall and Bednarek, 1999), proton-induced cascades (Mannheim, 1993), or synchrotron proton radiation (Mücke and Protheroe, 2001*b*) (Aharonian, 2000) may produce VHE

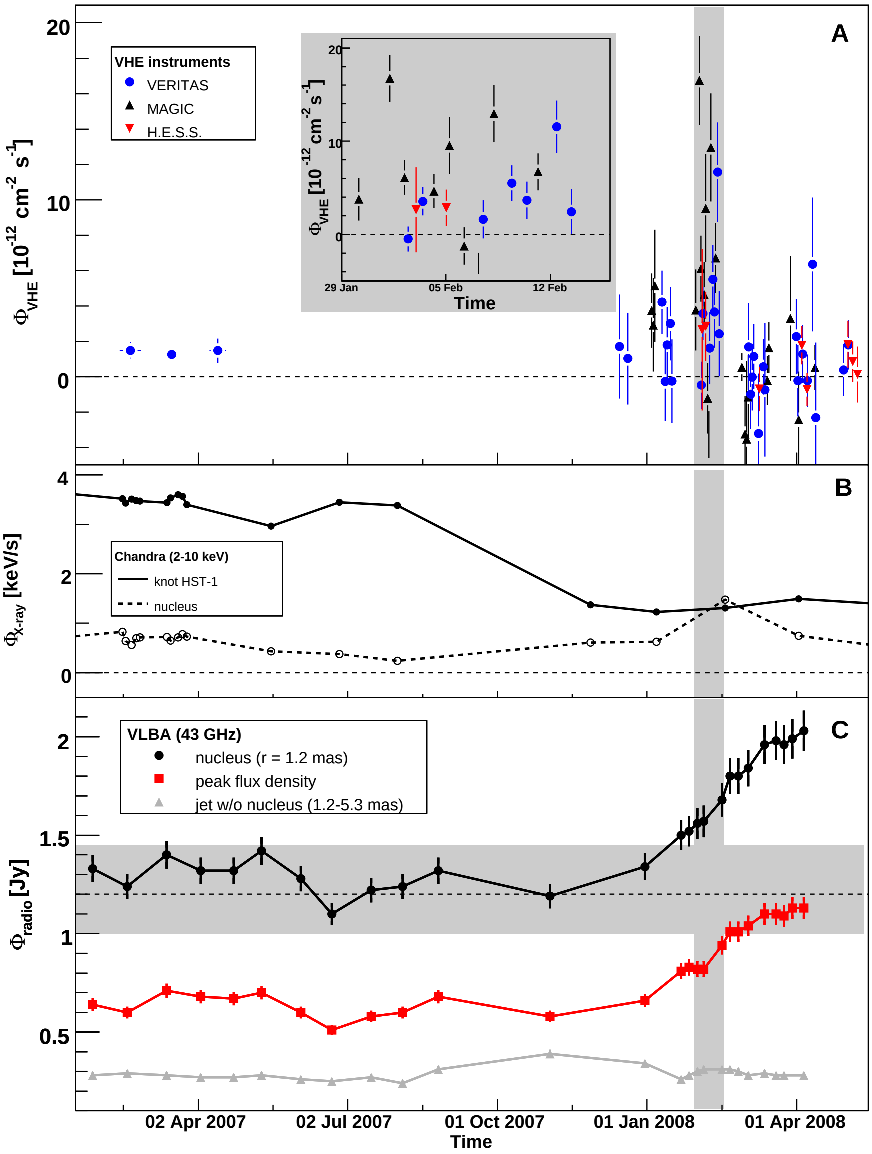

Figure 8.13: Combined M 87 light curves from 2007 to 2008. (A): VHE γ-ray fluxes (E >0.35 TeV, nightly average), showing the H.E.S.S., MAGIC and VERITAS data. Monthly-binned archival VERITAS data taken in 2007 are also shown. The systematic uncertainty in the flux calibration between the experiments was estimated to be on the order of 20% based on Crab Nebula data. The inlay shows a zoomed version of the flaring activity in February 2008; the time span is indicated by the grey vertical box in all panels. The lightcurves reported in section 8.3.2 refer also to the grey vertical box time period. (B): Chandra X-ray measurements (2–10 keV) of the core and the knot HST-1. (C): Flux densities from the 43 GHz VLBA observations are shown for (i) the core (circular region with radius r = 1.2 mas = 170 R_s centered on the peak flux), (ii) the peak flux (VLBA resolution element), and (iii) the flux integrated along the jet between distances of r = 1.2–5.3 mas. The error bars correspond to 5% of the flux. The shaded horizontal area indicates the range of fluxes from the nucleus before the 2008 flare. Whereas the flux of the outer regions of the jet does not change substantially, most of the flux increase results from the region around the nucleus. Figure from Acciari et al. (2009*b*).

γ-rays[5].

As mentioned at the beginning, the key for the understanding of the VHE γ-ray emission from this source lies in connecting the measurements at other wave bands (with considerably higher spatial resolutions) with the γ-rays. In most TeV γ-ray emission models, a correlation between γ-ray and X-ray fluxes is expected and the relationship can be used to distinguish between models.

The VERITAS collaboration reported strong evidence for a year-scale correlation between the γ-ray flux reported by TeV experiments and the X-ray emission (2-10 keV measured by ASM/RXTE, (Acciari et al., 2008)) with both linear and quadratic functions fitting pretty well the measured correlation. Since the variable component of the ASM/RXTE flux is likely dominated by X-ray emission from the core, and there is a strong correlation between the TeV and ASM/RXTE fluxes, they conclude that the core is the most likely candidate for the source of the TeV γ-ray emission.

In the period covered by the MAGIC data, at X-ray frequencies the innermost knot in the jet (HST-1) is found in a low state, whereas in mid-February 2008, the nucleus was found in its highest X-ray flux state since 2000. This is in contrast to the 2005 VHE gamma-ray flares, which happened after an increase of the X-ray flux of HST-1 over several years, allowing speculations that HST-1 might be the source of the VHE γ-ray emission (Cheung et al., 2007). The fact that VHE and X-ray flares from the nucleus happen simultaneously is a good evidence that they are connected[6] (see figure 8.13 and its caption).

Another way to disentangle between different emission models is to look for correlations between the photon index in the TeV location and the TeV flux state. Such correlation has been observed in the past in BL-Lac objects such as Mrk 501 and Mrk 421, but the case of M 87 is different. Unfortunately the γ-ray flux from M 87 is generally very low and close to the sensitivity of the present generation of Cherenkov telescopes. The uncertainties on the spectral index makes very hard to draw any statement on a possible similar behavior as it is indeed the case for the spectra reported in section 8.3.3.

The MAGIC data alone cannot put strong constraints on VHE γ-ray emission models. The relatively hard VHE spectrum found for M 87 ($\Gamma \approx -2.3$) is not unique among the extragalactic VHE γ-ray sources if one considers intrinsic spectra, i.e. EBL corrected. Also, we did not measure a high-energy spectral cut-off. Because no signature for an absorption can be identified in the energy spectrum up to 10 TeV (Aharonian et al., 2006*a*), one can derive an upper limit on the luminosity of the infrared radiation field at 0.1 eV. Such a low central IR radiation luminosity supports the hypothesis of an accretion disk with low radiative efficiency.

From the FERMI side the faint point-like γ-ray source ($>$ 100 MeV) has a spectral index of 2.26 ± 0.13. The SED reconstructed by the FERMI collaboration, using data also from Chandra (X-ray) and VLBA (radio, core only) can be fit by a one zone SSC jet model assuming a slightly smaller angle with respect to the line of sight ($\theta = 10°$) and Doppler factor $\delta = 3.9$ (Abdo et al., 2009).

---

[5] Interestingly, in such a scenario M 87 might also account for part of the observed UHECR. See also section 3.5.

[6] The observed pattern can be explained by an event in the central region causing the VHE flare. The plasma travels down the jet, and the effects of synchrotron self-absorption causes a delay of the observed peak in radio emission because the region is not transparent at radio energies at the beginning of the injection (Acciari et al., 2009*b*).

Concluding: during the MAGIC observations, a strong signal of 8 σ significance was found on 2008 February 1^{st}, triggering the other IACTs as well as *Swift* observations. For the first time, we assessed the energy spectrum below 250 GeV, where our observations can be well described by a power law that shows no hint of any flattening.
A variable (significance: 5.6 σ) night-to-night γ-ray flux above 350 GeV was found, confirming the short-time variability of M 87 reported by Aharonian et al. (2006a). The variability timescale, on the order of or even below 1-day, restricts the emission region to a size of $R \leq \Delta t\, c\, \delta = 2.6 \times 10^{15}\,\mathrm{cm} = 2.6\, \delta R_S$.

Summary and Conclusions

The first chapters of this thesis were dedicated to provide an overview of the physics framework in which my PhD was embedded. In the second part I described my personal contribution to γ-ray astronomy from the observational point of view whereas the appendixes were dedicated to my technical developments.

From the technical point of view, the most relevant result which was achieved is the demonstration of the effectiveness of the“timing” in the analysis of the data recorded by a single-dish Cherenkov telescope. The idea that the arrival time of the Cherenkov signals could provide a handle to reject the unwanted background was proposed early in the development of Cherenkov astronomy. Its practical realization resulted to be not so simple for several reasons. First of all, special choices in the Cherenkov telescope design have to be made, as the parabolic shape of the reflecting dish instead of the more classical spherical shape. Secondary, it requires a fast digitization electronics, which is expensive and technically challenging, and which was not part of the equipment of the first Cherenkov telescopes. Moreover, a very fine sampling increases significantly the data volume, which results in a more complex data readout (computing/storage/transfer/reduction). Finally, provided the ‘time information’ is recorded, it had to be determined how to actually exploit it. One of the ideas was to reject small size muon showers using their characteristic very short time spread. Unfortunately, the results in this thesis revealed that this approach is still not technically feasible analyzing the MAGIC telescope data, although it is at the moment the most suitable instrument to exploit the time information. The approach that was actually successful was instead the determination of the longitudinal time profile of the Cherenkov images. Images posses a precise ‘time gradient’ structure along their major axis, and the sign and magnitude of this quantity provide important information about the impact parameter of the shower, which in the case of a non-stereoscopic view by a single telescope is a poorly determined parameter. The improvement achieved by the use of the timing information in the analysis of the MAGIC-I standalone data is as large as a doubling of the observation time (halve of the residual background).

The second technical result achieved was the successful realization and installation of the MAGIC-II readout software. The readout program allows the data acquisition of the over a thousand pixels installed in the MAGIC-II camera (roughly twice as many channels as MAGIC-I). The readout of the MAGIC-II events in coincidence with MAGIC-I results in up to a factor two (energy-dependent) increase in sensitivity, increase, in virtue of the stereoscopic view of the γ-ray showers.

From the astrophysical point of view, we discussed in this thesis the analyses and results from three interesting data sets recorded by the MAGIC Cherenkov telescope during the observations of three AGNs: the bright blazars Markarian 421 and Markarian 501, and the radio-galaxy Messier 87. All these three sources can be considered a the 'best candidates' for the class of object they belong to, since they are prototype object for their class, they are relatively bright in γ-rays, they are located close-by (compared to other AGNs) and they are very well studied objects in many other wavebands (from radio to X-rays). All the three observations were performed during special time periods: two big multiwavelength campaigns in the case of the two blazars and an exceptional flaring activity in the case of M 87.

The Mrk 421 and Mrk 501 MAGIC data have a relevant role for the depiction of the broad-band spectrum of blazars. Moreover, the fact that they were observed in the context of two multiwavelenght campaigns, allows the interpretation of the TeV measurements with a deeper focus. MAGIC was not the only Cherenkov telescope involved in the two campaigns but it has the advantage of a lower energy threshold with respect to the competitors. The combination of the data from the Fermi γ-ray space telescope and MAGIC allowed, for the first time, to cover with a significant overlap the observational gap between ground-based and space-borne instruments. Even more important, the combination of the Fermi and MAGIC data allowed to precisely determine the shape and position of the inverse Compton hump of the SEDs. This is important for the modeling of the gamma emission. The obtained SEDs were modeled both with a classical leptonic scenario: a 1-zone Synchrotron Self-Compton model. What was found is that for both Mrk 421 and Mrk 501 blazars, the SED is pretty well reproduced. One important point of the discussion is that to achieve a nice agreement between model and data, is necessary to introduce multiple breaks in the electron injected spectrum (at least two breaks instead of the more classical none or single break).

Although the interpretation of these results looks promising, they have to be considered just as a first attempt to interpret the data. This precious data set (simultaneous and wide coverage) will lead for sure to new attempts of interpretation and modeling from the blazar community. In my opinion, the major result obtained from this campaign is the achievement of the complete SED from the data reduction of the multiwavelength data set.

Let us summarize now the January-February 2008 flare from the misaligned blazar M 87. The detected variability timescale in the VHE γ-ray flux allowed to establish new limits on the size of the gamma-rays emitting region. The analysis described in this thesis allowed to decrease the previous 'few'-days time scale variability to 1-day only (with clear statistical significance). This is relevant for the ongoing discussion about the location of the gamma-rays acceleration site because it favors the core of the galaxy as possible emitting location. M 87 is specially interesting also in virtue of its morphology, which is spatially resolved at many wavelengths. Thanks again to a 'multiwavelength approach', we could associate the detected γ-ray emission (which a poor spatial resolution) with some of the bright spots which are detected at other frequencies, in case that time correlation between lightcurves is found. The MAGIC data here discussed, together with the data of the two other major Cherenkov telescopes (H.E.S.S. and VERITAS), used in combination with other wavelength measurements (from radio, optical and X-rays), leaded to the first H.E.S.S., MAGIC and VERITAS joint publication. The interpretation of the multi-band lightcurves resulted to strength even more the core of the galaxy as the more probable emitting site.

The γ-ray astronomy field is evolving very fast. Month after month new exciting discoveries and developments twist our view of the most violent phenomena which occur in the universe. In my opinion, this is very good news, because it is a clear sign of the health of the field of 'astroparticle physics'. This is even more exciting in the perspective of a new generation of Cherenkov telescope facilities for the detection of VHE gammas, (like CTA and AGIS) which will have much better sensitivity and lower energy threshold than the current generation of ground-based TeV telescopes. This, combined with the hopefully long life of the Fermi γ-ray telescope mission could provide in the next years important insights for the understanding of the most energetic astrophysical processes.

Hopefully, in ten or twenty years from now, we will have the luck to see clear answers to many of the questions that at the moment look so interesting and at the same time so unclear. And again we will be asking ourself: 'What's next?'

Short list of the references associated to this thesis:

Messier 87: Albert et al. (2008*b*), Acciari et al. (2009*b*) and Tescaro et al. (2009*b*).

Blazars Mrk 421 and Mrk 501: Papers not released yet.

Timing analysis: Tescaro et al. (2007), Tescaro (2007) and Aliu et al. (2009).

MAGIC-II readout: Tescaro et al. (2009*a*).

Appendix A

Timing analysis

A.1 Introduction

As described in chapter 4, Imaging Atmospheric Cherenkov Telescopes (IACTs) collect the Cherenkov light from Extensive Air Showers (EAS) to form an image of them. The morphology of the shower image (see chapter 6) is used to recognize the few γ-ray initiated showers among the much more numerous hadronic showers initiated by cosmic ray nuclei. This standard approach only exploits the knowledge of the spatial distribution of the Cherenkov photons in the camera plane, but further informations regarding the shower distance and orientation are in principle available in the photon arrival times (Hillas, 1982).

The possibility of using effectively the timing information to improve the performance of IACTs has been explored in earlier works. The HEGRA collaboration measured on their data a time gradient along the major axis in the Cherenkov images (HEGRA Collaboration et al., 1999). They suggested that this information may be useful to estimate the distance to the shower core and the shower direction in the case of a single Cherenkov telescope, but of limited use in an array of IACTs, where a stereoscopic view of the shower is available. A recent MC study (de La Calle Pérez and Biller, 2006) suggests that the use of the time profile of Cherenkov images may lead to important background rejection improvements in future Cherenkov instruments (even if, according to Holder (2005) by the VERITAS collaboration, pioneering tests on real data led only to marginal improvements). A different approach to exploit the time information is proposed by the authors of Mirzoyan et al. (2006), capitalizing on the different characteristic time spread of the images of gamma-initiated air showers as compared to hadronic showers or images from distant single muons.

In the first years of operation of MAGIC[1], the PMT signals were digitized with 300 MSamples/s FADCs (see also section 5.4.6). In February 2007 the data acquisition of the MAGIC telescope was upgraded with ultra-fast FADCs capable to digitize at 2 GSamples/s (Mirzoyan and et al. (2002) Goebel (2007)). The implementation of a faster readout facilitates an improvement in the telescope performance for two reasons: a reduction in the amount of night sky background light integrated with the real signal, and an improvement in the reconstruction of the timing characteristics of the recorded images.

In this appendix we will present an analysis method which makes use of signal timing,

---

[1] The MAGIC-I Cherenkov telescope is described in detail in chapter 5.

and compare its performance to that of the standard MAGIC analysis used before the first half of 2007. This method was developed before the installation of the second telescope (MAGIC-II) of the current MAGIC telescopes stereo system and is therefore meant for the analysis of MAGIC-I stand-alone data.

The timing analysis is composed of two different parts. The first is the use of the time information to enhance the efficiency and to lower the threshold of the image cleaning procedure, thanks to the introduction of time constraints. The second is the use of additional time-related image parameters in the algorithms for the suppression of the isotropic background of hadron-initiated showers. Although the possibility of using timing to improve the IACT technique was suggested a long time ago, this method (Aliu et al. (2009), Tescaro et al. (2007), Tescaro (2007)) is, to our knowledge, the first time in which it has been successfully applied to real data.

A.2 Analysis method

When an atmospheric shower triggers the MAGIC telescope, the information of all camera pixels is stored by the DAQ system (see also section 5.4.4). This information consists mainly of the digitized pulse of the PMT corresponding to each pixel in time slices of 0.5 nanoseconds. From the digital information of the pulse it is possible, through the so-called signal extractor routine, to reconstruct the number of photons that arrived at the pixel and their mean arrival time. This can be done in several manners. For the current MAGIC data (with 2 GS/s sampling), a simple cubic spline is built from the FADC readout, and its integral in a range around the highest peak provides a measure of the charge recorded by the pixel. The arrival time is defined as the position of the rising edge of the pulse at 50% of the peak value. Before the upgrade of the FADC system, the pulse shape and duration was dictated by the artificial stretching introduced in the electronic chain to ensure that the pulse spanned over several FADC samples (then taken every 3.3 ns). For those older data, the *digital filter* algorithm Bartko et al. (2005), which makes use of the known pulse shape Albert et al. (2008*a*), was used. After calibration, the charge (Q) is converted to photo-electrons units (phe, see also section 6.6.2).

A.2.1 Image Cleaning

As we know from chapter 6, the information from the pixels is first used to perform the *image cleaning*, that aims at identifying which pixels belong to the shower image. Please refer to figure 6.5 for an example of an event before and after the cleaning.

In the MAGIC Analysis and Reconstruction Software (MARS, see also section 6.6), different cleaning methods can be chosen by the user. The most commonly used is the *standard - absolute* method. The choice may depend on the sky around the source (galactic or extra-galactic) or the prevailing background light conditions. This procedure uses a threshold signal value q_1 (a fixed value in terms of phe) to select the *core pixels*, namely all those with charge above q_1 and which have at least one neighbor fulfilling the same condition[2]. In a second stage, all pixels which have at least one *core* neighbor, and whose charge is above q_2 (with $q_2 < q_1$), are included in the image (these are called *boundary pixels*).

---

[2] This additional requirement avoids the selection of pixels unrelated to the image whose large charge results from an afterpulse in the PMT.

Relaxing the cleaning levels q_1 and q_2 results in a larger number of pixels per image, and accordingly a lower analysis energy threshold, since a minimum number of pixels is needed to proceed with the analysis. On the other hand, a low cleaning level increases the probability to include in the cleaned image a noise pixel (mainly due to NSB or other unwanted light pollution). The inclusion of pixels unrelated to the shower degrades the image parameters and worsens the performance of the subsequent analysis.

Together with the signal intensity also an arrival time value is assigned by the signal extractor to each pixel. These times can be used to further constrain the selection of core and boundary pixels in the image cleaning algorithm: Cherenkov flashes are very brief (of the order of few ns), and NSB photons produce pulses asynchronous with respect to the pulses of the shower image. A timing coincidence window between the mean arrival time and the single pixel arrival time can avoid to confuse NSB signals with real image tails. This further constraint allows to relax the cleaning levels q_1 and q_2, lowering in this way the energy threshold. The time information has already been used for the image cleaning in the analysis of the observations of the Crab Nebula with MAGIC (Albert et al., 2008*d*). However, the algorithm used in that analysis differs from the one currently used by MAGIC (described here) and can be found in detail in Otte (2007).
The current procedure can be summarized in this way:

- After selecting the core pixels in the same way as in the standard procedure, we reject those whose arrival time is not within a time Δt_1 of the mean arrival time of all core pixels.

- In the selection of the boundary pixels we add the constraint that the time difference between the boundary pixel candidate and its neighbor core pixels is smaller than a second fixed time constraint Δt_2.

The charge levels of the standard cleaning commonly used in the past in the analysis of MAGIC data are $q_1 = 10$ phe for the core pixels and $q_2 = 5$ phe for the boundary pixels. For the time-cleaning approach, the charge threshold levels were decreased to 6 and 3 phe respectively. Concerning the time constraints, the values $\Delta t_1 = 4.5$ ns and $\Delta t_2 = 1.5$ ns were selected. The choice of these values is supported by a study based on Montecarlo data (see Tescaro et al. (2007) and Tescaro (2007) for more details), in which we have assumed "dark night" conditions (and hence the used criteria would not be optimal during moon light or twilight observations when the number of noise photons is higher). The setting of these time constrains resulted also not very critical for choices within $\simeq 1$ ns respect the values used here.

In figure 6.5 an example event is shown. The image footprint is visible in the arrival time display (upper right plot) because of the short duration of the Cherenkov flash, illustrating the validity of the time image cleaning approach. The arrival times of the signal pixels are distributed within few ns. The other pixels have, as expected, a random arrival time distribution. In the second and third rows of figure 6.5 the same event is plotted after applying different cleaning methods.

A.2.2 Timing characteristics of the shower images

As previously introduced, Cherenkov images present some timing features, the most important of which is a dependency between the timing profile along the major axis of the image and the Impact Parameter (IP) of the shower. The model proposed by the

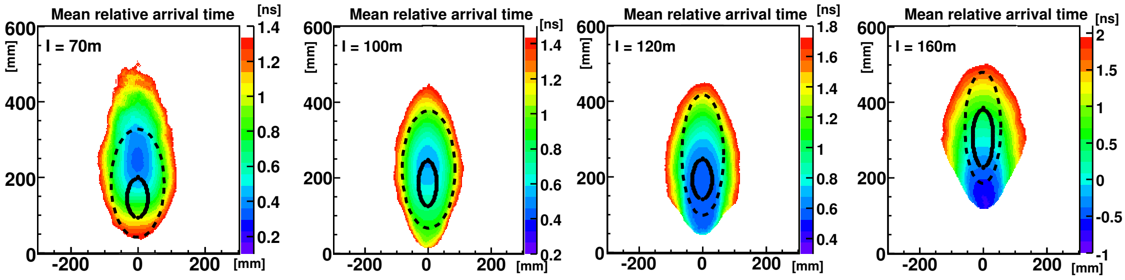

Figure A.1: Relative arrival time distributions of photons, averaged over a large sample of Montecarlo γ-events (Energy=100 GeV) for several values of the impact parameter. The black solid line marks the 50% of the maximum photon density whereas the dashed line (≈10% of the maximum) represents qualitatively the border of the image after the cleaning procedure. The time profile of the recorded images changes clearly depending on the IP of the primary shower. The source is located in the (0,0) position. Plots from Mazin et al. (2008).

HEGRA Collaboration et al. (1999) explains well this relationship. In case of a small impact parameter (IP $\leq$ 60 m), the light emitted in the higher part of the shower (the *shower head*) will arrive delayed with respect to the light emitted in the lower part of the shower (the *tail*), since the photons emitted first travel slower (at a speed c/n) than the ultra relativistic particles of the shower that produce the photons at lower altitudes. In case of a larger impact parameter (IP $\geq$ 120 m), the effect just described is reduced or even inverted, as the arrival time from the tail becomes the sum of the times spent in the paths of particles and photons, respectively. In this latter situation, the photons emitted in the lower part of the shower will arrive later than the photons emitted in the upper part. Events with an intermediate impact parameter show a flat time profile. These features are well visible in the templates of average Montecarlo gamma-ray images on the MAGIC camera (figure A.1), created by the superposition of many events at fixed values of energy and impact parameter. These are part of a dedicated MC sample produced for a different study Mazin et al. (2008) on the applicability of the 'model analysis' to the MAGIC data (see also section 4.3.5). In these templates, it is possible to recognize the dependency of the timing structure with the IP: the arrival time increases from shower head (bottom part of the images) to shower tail at large impact parameter, and from tail to head for small impact parameters.

A.2.3 Definitions of time-parameters

In order to exploit the timing characteristics of the showers in the analysis stage, some time-related image parameters have to be introduced. A linear fit of the arrival time versus the distance along the major image axis provides an easy way to characterize the time profile of a shower image. Another useful quantity may be the overall spread of the arrival times of all pixels surviving the cleaning. Based on these considerations, two new time-related image parameters have been introduced:

- ***Time Gradient***: this parameter measures how fast the arrival time changes along the major image axis. The pixel coordinates are projected onto this axis, reducing the problem to one dimension. Then the arrival time versus the space coordinate along the major axis is fitted to a linear function $t = m \cdot x + q$. The slope m is called in the following *Time Gradient* of the image. The sign of this parameter is positive if the arrival time increases as we move away from the location of the source on the camera, negative otherwise. It is therefore a parameter which depends on the position of the candidate gamma-ray source.

- ***Time RMS***: the root mean square of the arrival times of all pixels belonging to the image after cleaning. It measures the spread of the arrival times irrespective of the pixel position in the camera. This parameter has been suggested as a possible background discriminator in Mirzoyan et al. (2006). It must be noted that due to the time structure of the events, this parameter is correlated with the *Time Gradient*.

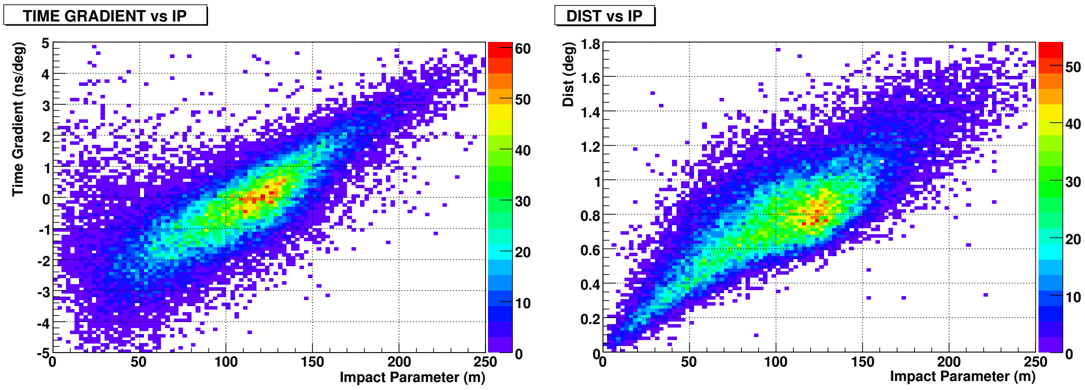

Figure A.2: Scatter plot of *Time Gradient* vs IP (left) and scatter plot of *Dist* vs IP (right) for Montecarlo γ-events. A cut *Size* $>$ 200 phe has been applied. Note that the impact parameter correlates better with *Time Gradient* for distant showers, whereas the correlation is better with *Dist* for nearby showers. The information provided by the two image parameters is hence complementary.

For the geometrical reasons explained in the previous section, the *Time Gradient* is well correlated with the impact parameter, as can be seen in the left panel of figure A.2. On the other hand, the classical *Dist* parameter, which is the angular distance from the image center of gravity to the source location on the camera, is also correlated to the impact parameter for gamma rays coming from a point-like source: as we increase the impact parameter, the image gets longer and moves away from the source, as we observe it at an increasingly larger angle[3]. A consequence of this is that *Time Gradient* is correlated with *Dist* for gamma-ray images from a point-like source (see fig. 6.8), whereas no such correlation exists for hadron images, since hadron showers are distributed isotropically, and therefore no strong correlation of *Dist* and the impact parameter is expected for them. Already from this, one can expect some improvement in the background discrimination through the use of the *Time Gradient* in the analysis.

Another way of looking at this is the following: the shower direction is not well determined by a single IACT. When observing a point-like source, all gamma-ray images will be pointing (within $\simeq 10^\circ$) towards the source location on the camera, but so will many background cosmic-ray showers whose axes are coplanar with the line pointing from the mirror dish center toward the source. The bare shower shapes allow to eliminate some of those, but the timing profile provides additional independent information to recognize the gamma-rays (the images with “consistent” values of *Dist* and the *Time Gradient*)

---

[3] Fluctuations in the shower development make that, even for a fixed energy, the altitude at which it develops changes from event to event, which blurs the correlation of *Dist* and the impact parameter.

and reject the background, and is therefore expected to improve the performance of the analysis.

Note that in stereoscopic IACT systems the determination of the shower direction and the impact parameter is obtained by the intersection of the multiple shower images, and thus the information that could be provided by the timing is redundant[4]. Therefore, the results obtained in this study can not be extrapolated to the case of stereo observations.

The papers Mirzoyan et al. (2006) and Sobczynska (2007*a*) characterize quantitatively the gamma, hadron and muon characteristic time spread. In particular muons are expected to have a typical time spread below 0.7 ns whereas for the majority of the gamma events it is above this value. The authors state that a readout $\geq$ 2 GSample and hardware features similar to the ones of MAGIC could permit to tag the muon events in order to reject them at analysis level. However, in Mirzoyan et al. (2006) an idealized reflector (more isochronous than the real MAGIC dish) and possibly some other idealizations, were used, making the conclusion, in our opinion, too optimistic regarding the rejection of single muons.

A.2.4 Role of the Montecarlo simulation

Making sure that the Montecarlo reproduces the features of the real data is very important to perform a good background rejection and energy estimation. In the MAGIC analysis, both tasks rely heavily on the MC simulated events. The MC is also crucial when the gamma-ray flux of a source is computed, since the estimation of the collection area is done using a Montecarlo 'test' sample. Therefore, the detector simulation was updated to reproduce the digitization features of the new 2 GSample/s digitization system: beyond the higher digitization speed, also the level of electronic noise and the overall precision of the time determination have been adjusted, taking into account the entire electronics chain. The time resolution can be estimated from the calibration events (light pulses of few ns duration), looking at the distribution of the arrival time difference between any two camera pixels (Goebel, 2007). The RMS of the distribution is 550 ps. This correspond to a time resolution for a single pixel of $550/\sqrt{2} = 390$ ps. Actually, Cherenkov pulses are generally faster than the calibration pulses, and hence, for a pulse of comparable amplitude, showers signals have a better resolution.

A demonstration of the *Time Gradient - Dist* correlation described in section A.2.3 can be seen is given in figure 6.8. The left plot of the figure is made with pure γ-MC events while the central panel displays the difference between *on*-source and *off*-source distributions (from a Crab Nebula sample described later), and therefore shows the distribution of the gamma-ray excess. A correlation *Time Gradient - Dist* is present in both cases. Such correlation is almost completely suppressed for hadron images (even after a cut in the α parameter), as shown in the plot on the right of figure 6.8.

A.3 Experimental results

The data sample chosen for this study consist of 5.7 h of Crab Nebula observations performed in wobble mode during the nights of the 7^{th}, 9^{th}, 15^{th} and 17^{th} of February 2007 (soon after the installation of the new MUX FADCs readout) at a zenith angles

---

[4] In the special case of a two telescopes stereo system, the impact parameter can still be poorly determined, for example for events in which both telescopes view the shower from the same direction. In such a case the two image axis directions are very similar and the intersection point is close to degenerate.

smaller than 30°. As described in section 6.3, the wobble mode eliminates the need for taking dedicated 'off' runs. The main disadvantage of the wobble method is a small reduction of the trigger efficiency leading to a reduction of $\simeq$ 15–20% in the nominal flux sensitivity, since the trigger area is limited to $\simeq 1^\circ$ around the camera center. Weather conditions were good during all the nights considered.

A.3.1 Analysis comparison strategy

In order to compare the sensitivity with and without the help of the timing information, three different analyses of the above mentioned Crab Nebula data sample were performed:

1. The standard analysis commonly performed on the MAGIC data before the upgrade of the DAQ. The image cleaning levels were 10 and 5 phe (see section A.2.1), and no time information was used. The standard image parameters (Size, Width, Length, Dist, Conc and the third moment along the major axis, dubbed M3long[5], see section 4.3.3) were used to perform the γ/h separation. This is the reference analysis for the comparison.

2. An analysis using 6-3 phe as cleaning levels, with the time constraints described in section A.2.1. The same standard parameters of analysis 1 were used for γ/h separation. This analysis is meant to evaluate the effect of the time cleaning.

3. The same 6-3 phe time cleaning of analysis 2 is used. In this analysis, in addition to the standard image parameters, the *Time RMS* and the *Time Gradient* image parameters (see section A.2.3) were used as input for the background rejection. This analysis is meant to evaluate the analysis improvement due to the timing parameters (used together with the time cleaning).

In all cases the image parameters were the input to the Random Forest event classification algorithm (see section 6.6.6), which was used to perform the γ/h separation task. As we know from section 6.6.6, the RF tags each event with a single value called Hadronness (ranging from 0 to 1) which is a measure, based on the image parameters, of the likelihood that the event is a background event.

The sum of the signals (in phe) of the two pixels with highest signal (in the following *Size-2*) was used as parameter to select event samples of different energies. Like the classical event Size, Size-2 is correlated with energy, but unlike Size, it is very weakly dependent on the cleaning levels[6]. If we had chosen the total Size to define the samples, we would have faced the problem that they would correspond to different energies in analysis number 1, therefore making the interpretation of the results more difficult.
Three different bins of Size-2 are considered in this work: the first one (Size-2 $>$ 100 phe) corresponds to the energy range where the integral flux sensitivity of MAGIC is best (resulting in a peak gamma energy of around 280 GeV); the second bin (40 phe $<$ Size-2 $<$ 100 phe) is intended to study the performance at intermediate energies (peak energy

---

[5] This measures the image asymmetry along its major axis. It is a source-dependent parameter, since its sign is referred to the source position on the camera. The sign is defined such that it is positive when the shower head is closer to the source than the shower tail, as is the case for properly reconstructed gamma rays.

[6] Considering two different image cleanings and applying the same Size-2 cut, the two data samples obtained will contain essentially the same events, differing only in the events that survive just one of the cleanings.

$\simeq$ 150 GeV). Finally, the performance for gamma rays below 100 GeV, which will be discussed in a separate section, has been evaluated in the Size-2 range from 20 to 40 phe. The estimated energy distributions for the *excess* events in each of the three Size-2 bins just mentioned (obtained from the real data sample) are shown in figure A.3.

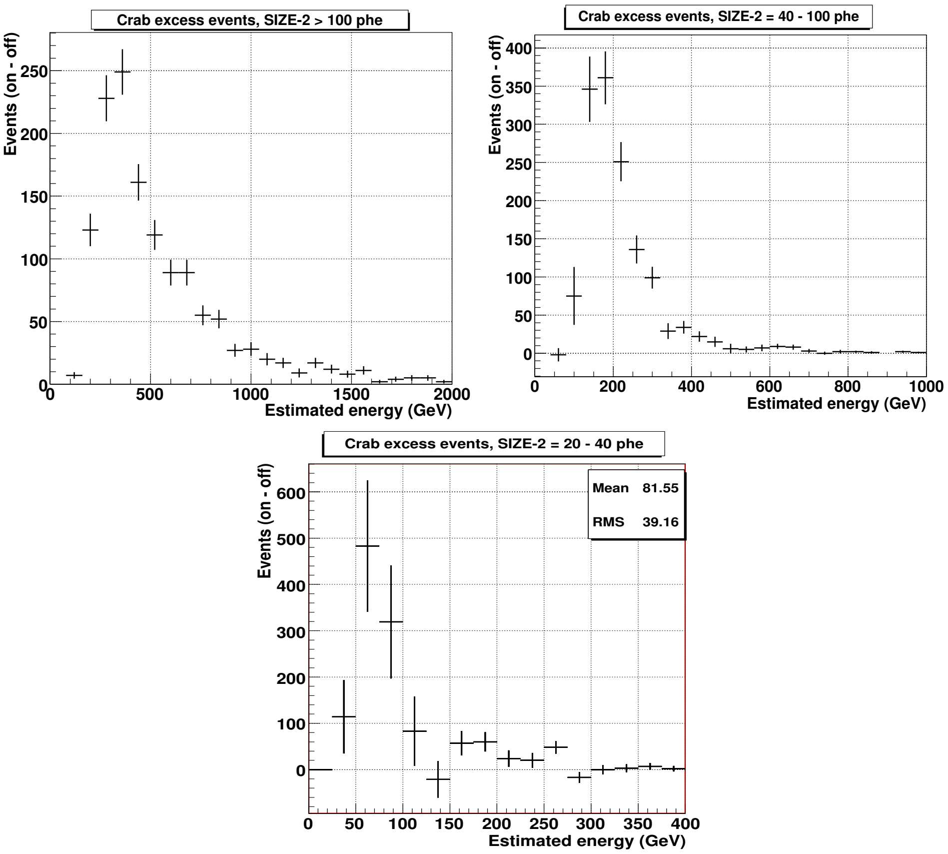

Figure A.3: Distribution of estimated energy for the Crab Nebula excess events (analysis 3) in the three ranges of Size-2 considered: above 100 phe, from 40 to 100 phe and from 20 to 40 phe.

A.3.2 Background rejection

For the two higher Size-2 bins considered, a series of three α-plots are shown in figures A.4 and A.5. The first α-plot is relative to the standard analysis (1), the second to the time cleaning analysis (2) and the third to the time cleaning and time parameters (3). In the case of analysis 1, the α and Hadronness cuts are optimized to obtain the best statistical significance of the excess. For the analyses 2 and 3, the Hadronness cut was chosen so that we got the same number of excess events as in analysis 1 (after applying the same α cut). In this way we can easily compare the background supression provided by each analysis procedure. Note that the histograms with error bars represent the α distribution of the excess events, instead of the usual plot showing the *on*-source data before the background subtraction. In this way we can immediately see that the gamma excess is similar in all three analyses, regardless of the background level.

The main result from this comparison is that the use of the time cleaning and the

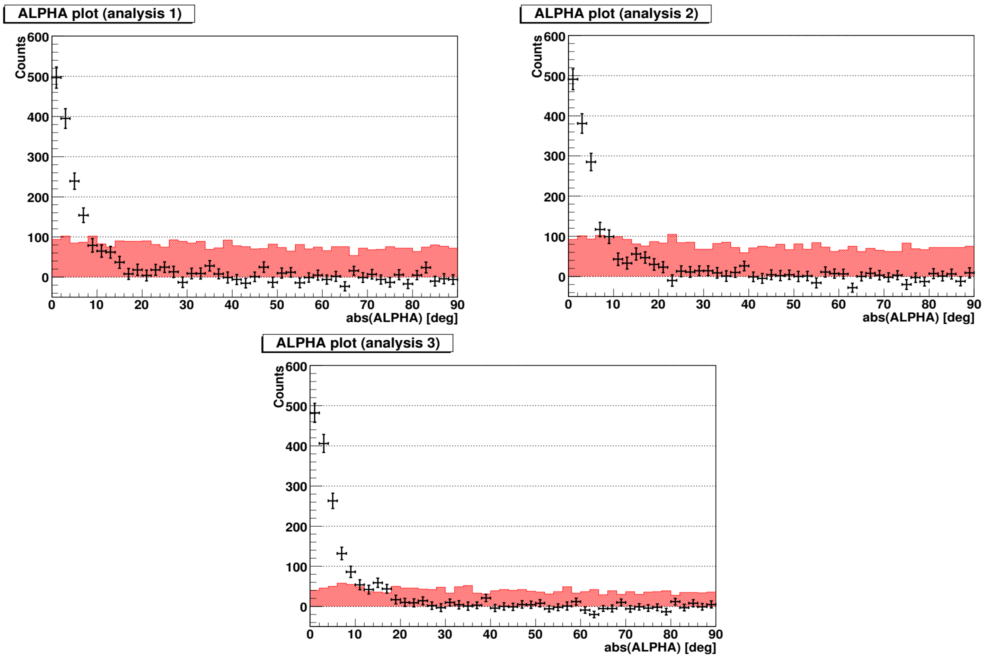

Figure A.4: Crab Nebula α-plots (excess and residual background) obtained with the three tested analysis methods. The Size-2 parameter is above 100 phe, corresponding to an energy distribution peak of $\simeq$ 280 GeV. Fixed the optimal cut for analysis 1, the other cuts are chosen in order to have roughly the same number of excess events in all three analyses.

time parameters allows to halve the residual background while keeping the same number of excess events, with respect to the analysis using no time information. This can clearly be seen in figures A.4 and A.5 and the corresponding tables. Note that the quoted significance values are calculated using only one false-source position for the background estimation, so the ratio of *on*-source to *off*-source exposure is one. The results for the lowest Size-2 bin will be discussed in section A.3.4.

Analysis	HADR. cut	α cut (deg)	Excess (γ/min)	Background (events/min)	$\sigma_{Li\&Ma}/\sqrt{h}$
1	0.09	8	3.78±0.13	1.08±0.06	12.5
2	0.10	8	3.75±0.13	1.14±0.06	12.3
3	0.07	8	3.78±0.12	0.57±0.04	14.0

Table A.1: Statistics of the plots in figure A.4 (Size-2 > 100 phe; $E_{peak} \simeq$ 280 GeV), obtained with 5.7 h of observation.

A.3.3 Flux sensitivity to point sources

From the results of the Crab Nebula observations we can estimate the flux sensitivity to point sources achievable with the different analyses. We define the flux sensitivity as the minimum gamma ray flux detectable in 50 hours, where "detectable" means that the excess of gamma rays corresponds to a signal to noise ratio of five ($N_{exc}/\sqrt{N_{bg}} = 5$, see also section 7.3). This is the standard definition commonly used in the field, but note that

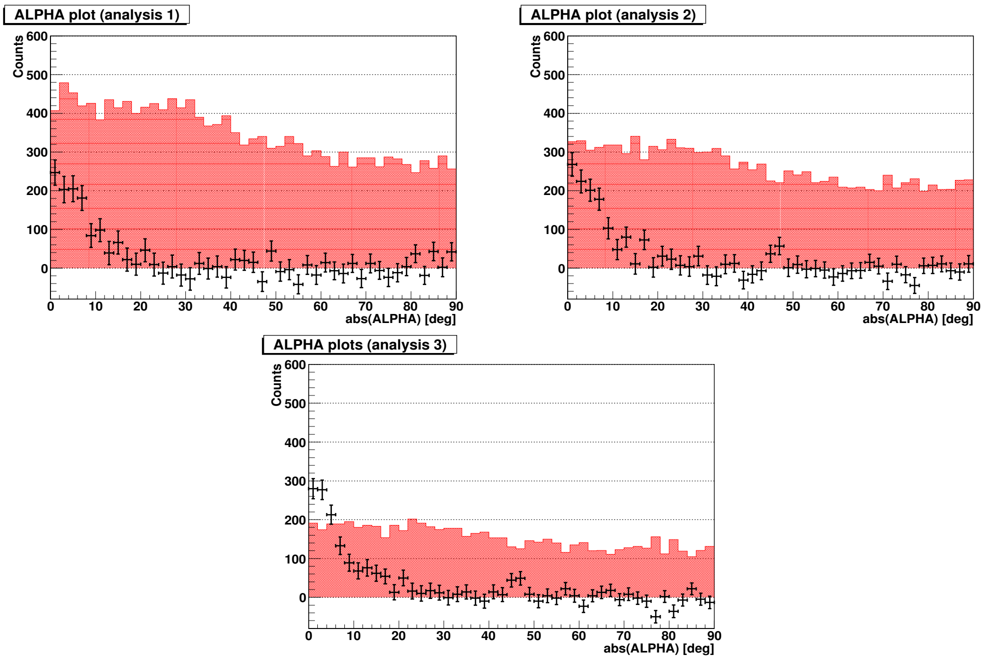

Figure A.5: Crab Nebula α-plots (excess and residual background) from analysis 1, 2 and 3, in the Size-2 range from 40 to 100 phe, corresponding to an energy distribution peak of $\simeq$150 GeV.

Analysis	HADR. cut	α cut (deg)	Excess (γ/min)	Background (events/min)	$\sigma_{Li\&Ma}/\sqrt{h}$
1	0.10	12	3.00±0.23	7.58±0.15	5.5
2	0.09	12	3.01±0.21	5.62±0.13	6.2
3	0.07	12	3.12±0.17	3.29±0.10	7.8

Table A.2: Statistics of the plots in figure A.5 (40 phe $<$ Size-2 $<$ 100 phe; $E_{peak} \simeq 150$ GeV), obtained with 5.7 h of observation.

it does not correspond exactly to a "5σ detection", because the real significance is usually computed with a more complex formula Li and Ma (1983) which takes into account the uncertainty in the determination of the background.

The flux sensitivity depends on the strength of the background discrimination cut (Hadronness $< h_{max}$). Actually, the cuts which maximize the statistical significance of the excess from a strong source like the Crab Nebula, as used in the previous section, are not the ones resulting in the best flux sensitivity: weak sources require tighter cuts. In this section we present the results of a scan of the Hadronness cut values, shown in figure A.6: the flux sensitivity (in percentage of the flux of the Crab Nebula) is plotted as a function of the rate of excess events. Each Hadronness cut of the scan leads to a different rate of excess and background events and thus to a different flux sensitivity. The figures correspond to the two Size-2 bins considered in the previous section. The black triangles represent the standard analysis 1, whereas the blue squares and red circles refer to the analysis 2 (with the time cleaning) and 3 (time cleaning and time-related parameters). Note that, since the values are derived from real Crab Nebula observations, the flux percentage is relative to the true Crab flux, and not to the simple power-law

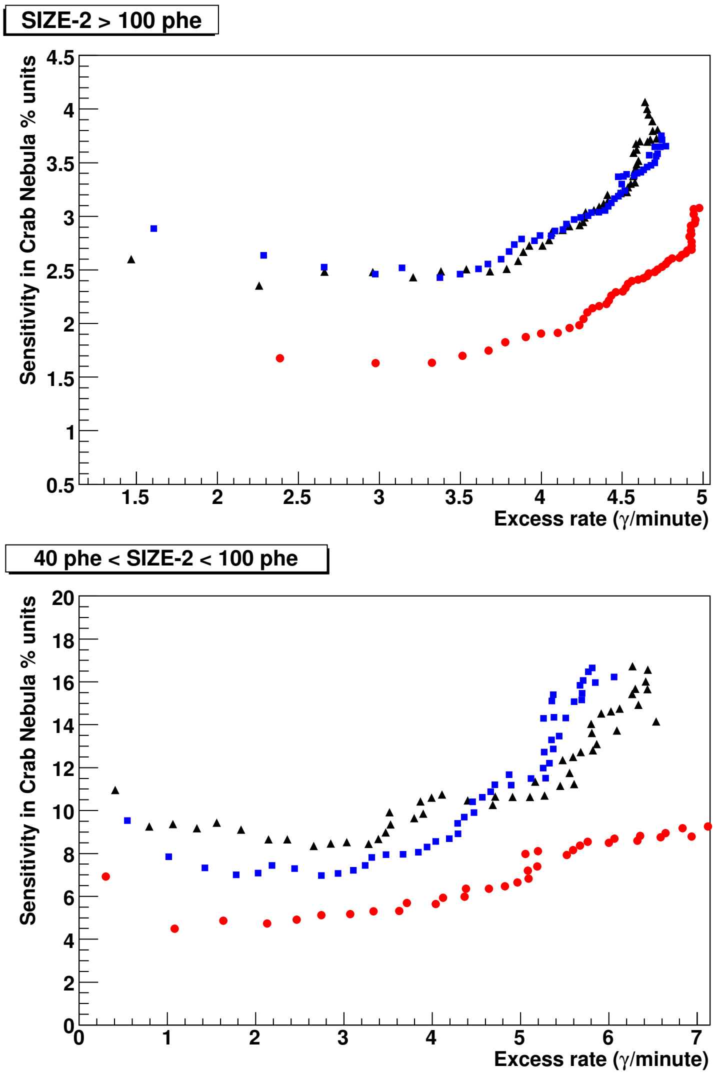

Figure A.6: Sensitivity (for 50 h) curves as function of the rate of gamma-rays after cuts. The black triangles, blue squares and red circles correspond to analysis 1, 2, and 3, respectively. Upper panel: Size-2 > 100 phe, corresponding to an energy distribution peak of ≃ 280 GeV. Lower panel: 40 < Size-2 < 100 phe, corresponding to an energy distribution peak of ≃ 150 GeV. The curves are obtained by a scan of the cut in the Hadronness parameter.

spectrum that is often assumed in sensitivity estimates based on MC. For each choice of Hadronness, a fixed α cut (of 7° and 10° respectively) was applied in order to compute the sensitivity. The improvement coming from the use of timing in the analysis is clear in both cases. It must be noted that in the higher energy bin, all of the improvement comes from the use of the timing parameters, whereas in the lower one the introduction of the time cleaning already results in some improvement in sensitivity. The best integral sensitivity that can be reached is around 1.6% of the Crab flux for a peak energy of 280 GeV (left panel of figure A.6).

We have computed also the flux sensitivities in differential bins of estimated energy for analysis 3, shown in table A.3.

E_{est} range (GeV)	H. cut	α cut (deg)	Excess (γ/min)	Backg. (events/min)	Sensitivity (% Crab)
$100 < E < 200$	0.02	12	0.70±0.06	0.23±0.03	6.3
$200 < E < 300$	0.02	8	0.80±0.06	0.11±0.02	3.7
$300 < E < 500$	0.02	8	1.00±0.06	0.09±0.02	2.8
$500 < E < 1000$	0.04	4	0.79±0.05	0.03±0.01	2.1
$E > 1000$	0.06	4	0.28±0.03	0.005±0.003	2.1

Table A.3: Sensitivity (% Crab in 50 h) and statistics for some differential energy bins using the time cleaning and the timing parameters in the analysis 3 of section A.3.1. Cuts are optimized separately in each bin with the best sensitivity criteria. Observation time: 5.7 h.

A.3.4 Use of timing at lower energies

The background suppression capabilities degrade as we move towards lower energies. This trend can be clearly seen by comparing figures A.4 and A.5 and their corresponding tables: if we focus on analysis 3, we notice that we move from having a signal nearly seven times larger than the residual background, to having a signal (integrated below the α cut) slightly smaller than the background. This is mainly a result of the worsening of the gamma/hadron discrimination and of the fact that the spectrum of the Crab Nebula is harder than that of the background, although this latter contribution is smaller.

In figure A.7 we show the results for analyses 2 and 3 in the Size-2 range from 20 to 40 phe, where most of the excess comes from sub-100 GeV gamma rays (see right pad of figure A.3). Given the modest signal (a mere 5.7 σ significance in analysis 3), we have in this case adjusted the cuts to obtain the same background rate ($\simeq$ 80 events/min) in both analyses, and then compared the gamma-ray excess. Once more, the improvement in performance due to the introduction of the timing is clear, though less significant due to the large residual background. With roughly the same background rate the excess rate for analysis 2 is 2.5±0.7 γ/min whereas for analysis 3 it is 4.0±0.7 γ/min. In this energy range, analysis 1 even fails to produce a significant signal, due to the high cleaning levels.

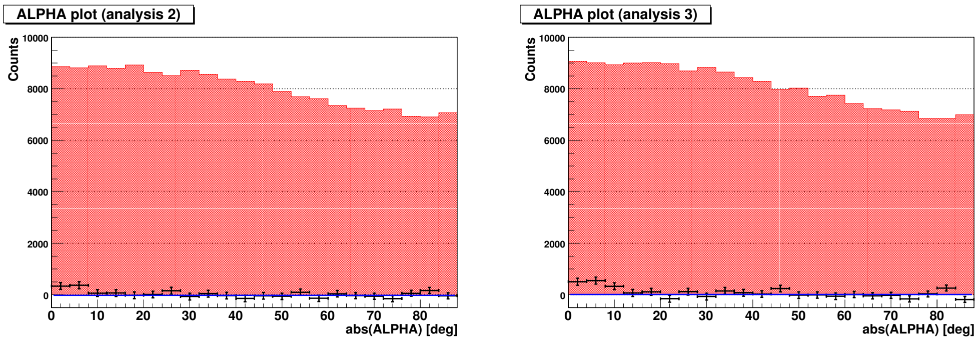

Figure A.7: Crab Nebula α-plots (excess and residual background) from analysis 2 and 3 in the bin of Size-2 from 20 to 40 phe (estimated energy of the gammas mostly below 100 GeV). Note that in this case we have adjusted the background rate instead of the excess rate to be the same in both cases. The α cut applied is of 12°.

For even lower energies than those of our third bin of Size-2 = 20 to 40 photoelectrons, the background overwhelms the signal even of a strong source like Crab, and is actually setting a further limitation for the observation of weak sources. The signal must not only be statistically significant, but also well above the systematic uncertainty in the determination of the background, which is at least of a few percent and, unlike statistical significance, it does not get better with longer observation times.

It has to be noted that, even after strong background rejection cuts, a certain amount of "irreducible" background survives. The background rejection power of the imaging technique degrades fast with the lowering of the energy of the primary gamma-ray. The reason of this degradation can be attributed both to the physics of the air showers and to the technical limitations of the IACT instruments. The irreducible background is made up by shower images which are similar to gamma induced images in all of the image parameters used for the event discrimination. This may reflect the shortcomings of the instrument in recording the small and faint images of low energy showers, resulting from its limited light collection efficiency and camera pixelization. A larger reflecting surface or an increased quantum efficiency camera, together with a finer pixelization, would obviously improve the accuracy of the reconstructed image parameters. On the other hand, even assuming a perfect IACT detector, there is no guarantee that the intrinsic characteristics of the cascades are different enough to permit to distinguish the nature of the primary particles. The study of the characteristics of the gamma-like background (see for example Maier and Knapp (2007) or Sobczynska (2007*b*)) heavily rely on the MC simulation packages. The nature of this irreducible background is attributed to π^0-s, primary electrons and long flying relativistic particles (like μ-s). Proton-induced air showers typically produce pions in the first interaction stage. The charged pions decay into muons, whereas the π^0-s (most often decaying into two gammas) originate electromagnetic sub-showers. If the energy of the primary particle is above a few hundred GeV, the superposition of the sub-showers from different π^0-s with diverging trajectories make hadronic showers to appear wider and more "patchy" than gamma-initiated ones. As is well known, this is the feature of hadron-initiated cascades which allows best to suppress them in the analysis of IACT data. However, as the energy of the hadronic primary goes down, the pion multiplicity drops, and the chances that the light of a single electromagnetic sub-shower dominates the image recorded by an IACT get larger. This means that, regardless of the characteristics of the telescope, the amount of irreducible hadronic background will necessarily increase as we go down in energy.

Also the background images due to distant muons can easily get confused, by a single-dish IACT, with low energy gammas. Those images have generally a small size which make it difficult to recover information from the shower shape. The time spread of pixel signals has been proposed in Mirzoyan et al. (2006) as a parameter which may be used to suppress such background, but as we will discuss in section A.4, the method does not seem to work efficiently for MAGIC. The improvement in sensitivity in the < 100 GeV energy range is due to the contribution of the *Time Gradient* parameter.

In summary, even though the overall background discrimination worsens very fast with decreasing energy, the use of the timing parameters (mainly the *Time Gradient*) has been shown to improve background suppression efficiently in the whole energy range of MAGIC, even below 100 GeV.

A.3.5 Energy estimation

The Random Forest method can also be used for the estimation of a continuous variable. It is the standard method used in the analysis of MAGIC data (see section 6.6.7) for estimating the energy of the showers (under the assumption that they are gamma rays). In an analogous way as for the background rejection, the RF is trained with MC gammas, whose true energy is known. No background event sample is needed for this kind of training.

In order to evaluate the improvement in the energy reconstruction due to the use of the signal timing, the energy of a test sample of Montecarlo γ events (different from the sample used for the training) was evaluated and compared to the true known energy of the primary gamma rays. An improvement in the energy reconstruction is expected if the image parameter *Time Gradient* is added to the default set of parameters since it provides information about the distance of the shower. This should help to avoid the degeneracy between small, nearby showers and the large, distant ones. As introduced in section A.2.3, both *Dist* and *Time Gradient* parameters are well correlated with the IP and can be used for its estimation. Notice that the correlation of *Dist* is rather good for small IP event whereas for larger IP the estimation with *Dist* becomes poorer (figure A.2). In case of *Time Gradient* the correlation is better for higher IP values, very likely because for distant showers the time structure of the images is more pronounced and as a consequence more precisely measured.

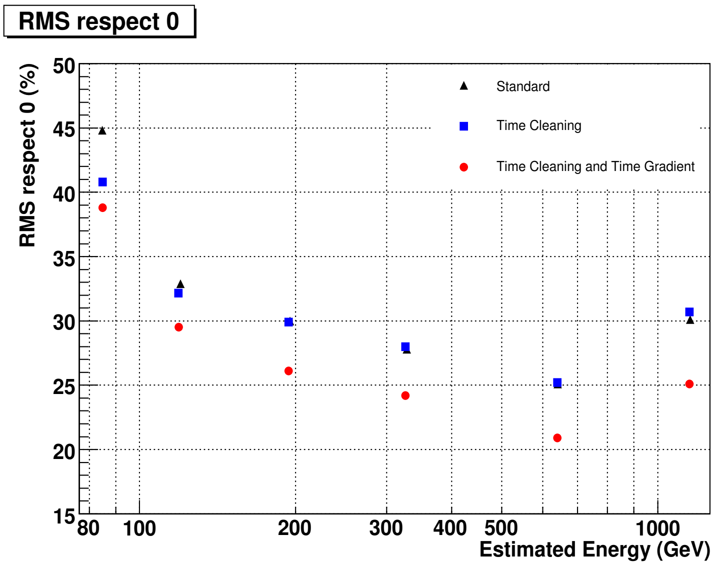

Figure A.8: Graph of the value of the RMS with respect to zero of the quantity $(E_{est} - E_{true})/E_{est}$ for different energy bins. This value is an overall estimator of the energy resolution. The black triangle and the blue square show data processed with the standard set of energy estimation parameters (image cleaning 10-5 phe and time image cleaning 6-3 phe respectively). The red circles correspond to data processed with time image cleaning and also *Time Gradient* used as energy estimation parameter (time image cleaning 6-3 phe).

The distributions of the quantity $(E_{rec} - E_{true})/E_{rec}$ for different energy bins were used to estimate the quality of the energy reconstruction. In fig. A.8 the black triangles refer to the energy estimation with the standard parameter set, that is, data processed with the 10-5 phe image cleaning without time constraints. The blue squares correspond to an energy reconstruction performed with the standard parameter set and the time image cleaning 6-3 phe (see section A.2.1), while the red circles are obtained from the time-constrained image cleaning and the *Time Gradient* image parameter being added to the standard set for the energy estimation. The graph represents the value of the RMS of $(E_{est}-E_{true})/E_{est}$ with respect to zero instead of the mean value. This quantity is preferred to the simple RMS as an overall estimator of the quality of the energy reconstruction, since it takes into account not only the spread of the distribution, but also a possible bias with respect to zero (see Tescaro (2007) for more details). "Leakage" effects for images located close to the edge of the camera could be important when the energy reconstruction is performed since the number of photons in the part of the image outside the camera is actually not measured. A standard selection cut *Leakage* $<$ 10% is applied in this analysis and tests with tighter *Leakage* cuts revealed no significant changes with respect to the shown results. The use of the *Time Gradient* image parameter in the energy estimation yields a relative improvement in energy reconstruction of around 15%.

A.4 Summary

A significant improvement of performance of the MAGIC Cherenkov telescope, both in terms of flux sensitivity and energy resolution, can be achieved by using the timing of signals in the reconstruction of shower images. The reason for the improvement is twofold: on one hand, the time-constrained image cleaning allows to reduce the cleaning charge levels without adding noise coming mainly from the night sky background light, which results in a lower analysis energy threshold. On the other hand, the timing profile of the images, represented by the *Time Gradient*, provides information about the shower impact parameter, a relevant quantity which is otherwise poorly determined by a single-dish IACT. This analysis method is now established as the new standard for the analysis of MAGIC-I stand-alone data.

From the sensitivity graphs of section A.3.2, it is possible to conclude that the time cleaning alone results in a significant sensitivity improvement in the low energy regime (40 $<$ Size-2 $<$ 100 phe), coming from the increased event statistics. At higher energies it does neither improve nor worsen the telescope performance significantly although the lower cleaning results in more pixels per image. In contrast, the *Time Gradient* seems to be helpful in the entire energy range accessible to MAGIC. This parameter allows to reject hadron showers whose images are gamma-like in shape and oriented towards the gamma-ray source location on the camera, but whose *Dist* and *Time Gradient* parameters are not consistent with what is expected for a gamma shower coming from a point source.

The background rejection power shown by the *Time RMS* in this study is much lower than foreseen in Mirzoyan et al. (2006). This is most likely due to the too optimistic assumptions regarding the telescope features made by the authors of that work with respect to the actual characteristics of MAGIC, in particular regarding the reflecting dish. In the final mounting the panels of the MAGIC mirror are staggered in a chessboard pattern to facilitate their movement and to ensure a proper focusing, and this causes the parabolic dish not to be perfectly synchronous. The mirrors staggering together with the other sources of time spread in the acquisition chain, like the jitter in the transit time of the electrons in the PMTs, lead to a time-RMS response larger than expected from the authors of Mirzoyan et al. (2006). The value that results from almost synchronous input signals, for example muon events, is ≈ 0.7 ns, a value comparable with the time spread of the low-energy γ-events (see figure A.9). Therefore, the tagging of single distant muons

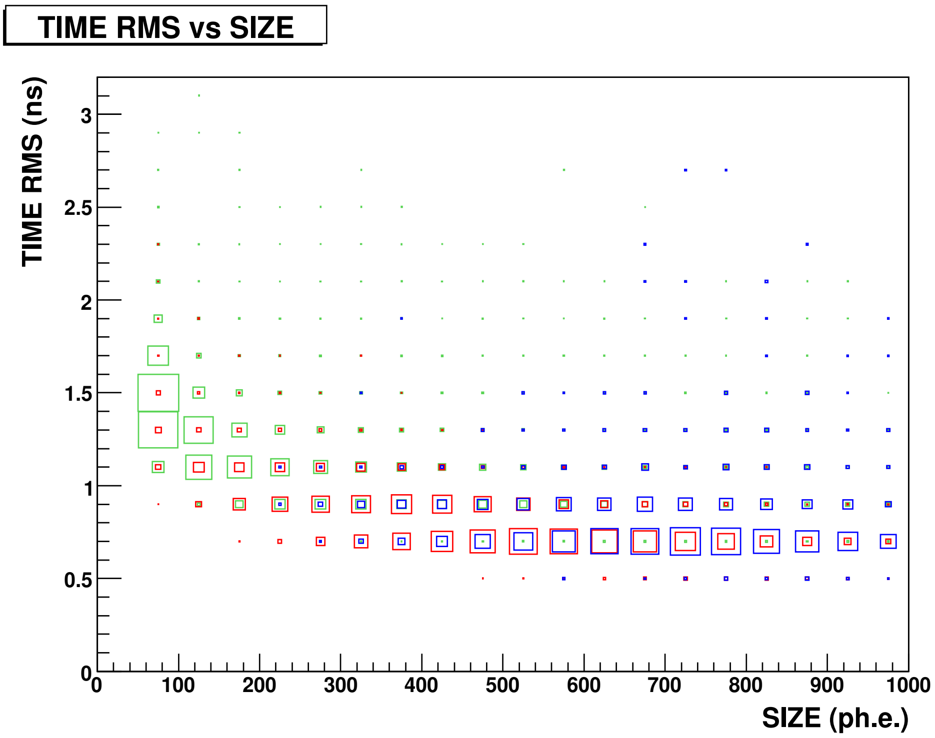

Figure A.9: Time RMS versus Size of the event. The green color refers to simulated gammas, red to simulated muons and blue to clear real muon events (an image arc of at least 180° is required). Gammas and muons extensively overlapped in the considered parameters space. Notice the absence of events below 500 ps, evidence of our blindness to time features below this threshold, and the increase of the time RMS values at very low sizes likely due to the worsening of the time resolution for very small signals.

from just their time spread is at the moment not possible.

In conclusion the use of timing information in the analysis of MAGIC data provides a considerably better background suppression and results in an enhancement of about a factor 1.4 of the flux sensitivity to point-like sources, as tested on real observations of the Crab Nebula. This gain is equivalent to doubling the available observation time.
Improvements of the order of 15% have been found in the event energy reconstruction. In fact the time gradient gives information about the real impact parameter of the shower and therefore it helps to distinguish distant high energy showers from closer, low energy ones.

The *Time Gradient* is most likely not very useful for stereo IACT systems, but test on real data about the opportunity of use it for the reduction of the MAGIC stereo system data are currently ongoing. The time image cleaning algorithm would be instead worth for either stereo and single IACT systems.

Appendix B

The MAGIC-II data acquisition system

B.1 Introduction

As we know from chapter 4 the Cherenkov flashes from atmospheric showers are very short in time and therefore a very fast readout electronics is required. The analog signals coming from the camera of MAGIC-II are very fast (the PMTs provide 2.5 ns width pulses, as described in: Borla Tridon (2009)). The pulses have to be first processed to generate the trigger signal and then digitized. Afterwards they have to be stored for the subsequent analysis (Moralejo, 2009). A fast readout allows one to minimize the integration time and thus to reduce the influence of the background from the light of the night sky. Moreover, with a fast sampling also the arrival time information can be obtained and exploited to improve the background discrimination (Aliu et al., 2009).

In this chapter the most important features of the MAGIC-II readout are described, with particular attention to the readout software. In section B.2 a general description of the data acquisition system is given whereas on section B.3 detailed informations about the software architecture are provided. References for this chapter are: Tescaro et al. (2009*a*), the theses Bitossi (2009) and Aleksić (2009) and the chapter about the DAQ of MAGIC-II of the TOM (Telescope Operation Manual).

During my PhD studies I worked actively in the development and installation of the readout system of the MAGIC-II, and have been responsible of the readout software for the past 3 years. The system have been developed mainly at the IFAE institute in Barcelona (Spain) and at the department of physics of the Pisa University (Italy) by a team of physicists and engineers from both institutions. I worked mainly at my home institution in Barcelona (IFAE) but I also spent several weeks in Pisa (INFN-Pisa) working with the Italian team whenever required for the development of the system. I also spent a three-month long period at the site of the MAGIC experiment in La Palma (in summer 2008), where I could finalize my previous development work, contributing to the actual on-site installation of the hardware and the software described in the following.

The first light ceremony of the MAGIC-II telescope took place on April 24-25th of 2009. After few months of standalone operations, necessary for the final commissioning, the array system is now fully operational and is taking data regularly in *stereo* mode i.e. with a trigger policy which requires coincidence between the two MAGIC telescopes.

B.2 The MAGIC-II readout

The readout of the data of a Cherenkov telescope as MAGIC-II can be divided in few different parts: reception of the analog pulses and eventual generation of an input trigger signal (by the *receivers*), digitization of the Cherenkov pulses (by the *digitization electronics*) and storage on disk of the data (by the *DAQ program*).
The readout is a pretty complex system which has to operate very fast but at the same time guarantee reliability during the operation. The number of channels to be read out is over one thousand[1], almost a factor two larger with respect to MAGIC-I. The single telescope acquisition rate is of the order of few hundred events per second, which requires to handle and store in the disk a data flow of the order of 100 MByte/s. The amount of data delivered by the MAGIC telescopes is by far the largest among all the telescopes installed at the observatory of the Roque de los Muchachos.

The readout system of the second MAGIC telescope differs significantly from the readout of MAGIC-I (see Goebel (2007)). New receivers boards have been designed (section B.2.1). The digitization of the analog signals is now performed through the so-called DRS2 chip[2]. A dedicated set of electronic boards have been developed to carry and operate this new chip (section B.2.2). The slow control software, which guarantees the correct and stable functioning of the readout electronics, has been newly developed as well (section B.2.3). The final data acquisition software is a multi-thread C++ program based on the MAGIC-I DAQ and adapted to the new hardware features (sections B.2.4 and B.3). The whole system is finally controlled at higher level by the central control software (section B.2.5).

B.2.1 Receiver board

The receiver board interfaces the analog signals from the telescope camera with the level ONE trigger system and the digitization electronics. A photo of the MONSTER (Magic Optical NanoSecond Trigger and Event Receiver) board is provided in figure B.1. The board layout can be schematized in three parts: *analog*, *trigger* and *control*.
The optical fibers from the camera are connected to the analog channels of the receiver through LX5 connectors located on the back side of the board. A pigtail routes the signal to a photodiode where it is converted back from optical to electrical analog signal. The signal is then split in two branches, one which drives the signal to the digitization input and the second where the signal is shaped for the *level one* trigger. An analog switch allows to inject in the analog channel an adjustable amplitude DC signal instead of the camera pulses. This is a useful tool for the calibration of the system. The following tables summarize the specifications of the new receiver board.

Total gain	18.5 dB
Jitter	<100 ps
Bandwidth	750 MHz (>1 GHz capable)
Working range:	$0.25 \div 1150$ mV (differential output)
Inter-channel delay	<1 ns
Crosstalk	1:1000
Noise (receiver only)	<200 μV RMS
Gain dispersion	30%

---

[1] 1039 with PMTs only.

[2] http://drs.web.psi.ch

Figure B.1: Picture of the MONSTER receiver board. On the top left part of the board you can see the L0 trigger components. On the top right the components dedicated to power the board and the VME backplane connector. On the bottom right part you can see the orange pigtails and the LX5 connectors for the optical fibers. On the bottom left you can see the connectors for the sumtrigger mezzanine and the domino mezzanine.

Minimum input pulse	800 ps
Work frequency (pulse width 2.7ns)	>150 MHz
Digital programmable pulse width	2.7-12.7 ns (10ps resolution)
Digital programmable channel delay	0-20 ns (10ps resolution)
Signal transition time	9.9 ns
Jitter	<100 ps

The trigger part represents the *level zero* of the trigger system chain. If an analog pulse is above a certain threshold, a signal is generated that is sent in LVDS standard to the level one trigger. This discriminator threshold is easily programmable for the individual channels so that a stable trigger rate can be guaranteed even under variable light conditions (moonlight observations, stars in the field of view, etc.). Thanks to dedicated channel rate counters the IPR (Individual Pixel Rate) information is available online. The board also permits to inject test patterns in the trigger output for testing purposes.

The firmware installed in the control part of the board is developed in VHDL code. It allows to monitor the board temperature, count the rate of the level zero trigger pulses up to the frequency of 50 MHz and manage all the control signals (trigger pattern, DC levels etc.).

The MONSTER is a highly integrated board: a single receiver includes 24 channels. Maximum power consumption is of 75 W per board. The MONSTER board is fully compatible with the MAGIC-I telescope electronics.

B.2.2 Digitization electronics

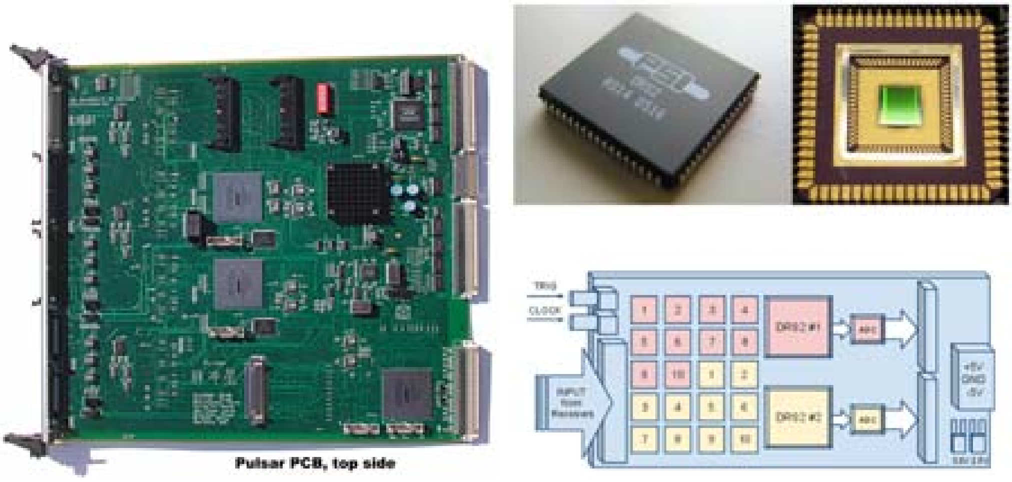

Figure B.2: Pictures of the Pulsar board, of the DRS2 chip. On the bottom right the layout of the Domino mezzanine board.

The digitization system for the MAGIC-II telescope (Bitossi, 2009) has been designed to fulfill the following requirements:

- Ultra-fast sampling (2 GSample/s) of a large number of channels based on the DRS2 chip (domino)
- Synchronous sampling of all channels to measure the timing structure of the camera images
- Modularity to allow for variations in the number of input channels
- Possibility to easily upgrade the sampling electronics from the DRS2 to the DRS4 chip
- Flexibility and re-configurability to meet future changes on the operation of the experiment

Backbone of the readout is the PULSAR[3] (PULSer And Recorder), a general purpose 9U VME interface board for HEP applications developed by the University of Chicago. The general design philosophy of PULSAR is to use one type of motherboard (with a few powerful modern FPGAs and SRAMs) to interface any user data with any industrial standard link through the use of custom mezzanine cards. The design is such that users can choose which standard link to interface with via simple custom transition module or mezzanine card. The picture B.2 shows a PULSAR board with the main FPGAs: from top DATAIO-1, DATAIO-2 and CONTROL. The DATAIO FPGAs handle the dominos readout sequence and store the data into local SRAM memories. The CONTROL FPGA builds a formatted data packet to be transmitted to the DAQ computer. The PULSAR board is used as a motherboard that hosts the mezzanines carrying the DRS.

The mezzanine holding the Domino chips is a PMC card. Four of these mezzanines are plugged on the rear side of the PULSAR board for a total of 80 channels each. On the front panel are located the trigger and clock inputs, coming from the trigger and clock fan-out boards, located over the PULSAR crates. These signals come via coaxial

---

[3] http://hep.uchicago.edu/˜thliu/projects/Pulsar/

cables equipped with SMA connectors. The clock input is a 2 MHz signal that is used to synchronize the domino PLL, ensuring in this way the same frequency and phase for all the samplers in the readout system. On the bottom right of figure B.2 a sketch of the mezzanine is shown, showing the two trigger and clock signals and the layout of the input signals on the mezzanine. A mezzanine is equipped with two DRS2 chips capable to simultaneously digitize 10 input channels each. With DRS2 ten channels are routed to the top domino and the other ten channels are routed to the bottom domino. The domino mezzanine has a ± 5 V independent power supply. Secondary 3.3 V and 2.5 V are generated on each mezzanine with linear regulators. The ADC has a nominal 12-bit resolution, the bandwidth of the DRS2 is 200 MHz, noise is of the order of 1 mV.

A special PULSAR board, named *digital*, is specially programmed to sample the trigger signal and to measure its arrival time. This information is transmitted to the rest of the PULSAR boards, named *analog*, for reading out the region of interest only. External digital information, like time stamp or trigger information, can be introduced in the dataflow via two front panel connectors. Each connector carries 32 bits of digital information for a total of 64 bits per PULSAR. Another dedicated PULSAR (*busy*) provides the busy signal that stops triggers when the readout system is busy processing one event.

The full readout system is made by using 14 analog PULSAR plus 2 special PULSAR boards, hosted in two 9U VME crates. The currently installed system is capable to readout a maximum of 1132 channels.

B.2.3 Slow control program

The slow control of the MAGIC-II readout system is called *Magic Integrated Readout* (MIR). It is a multithread C-program, using which the following subsystems can be configured and monitored:

- Trigger system (level ONE, level TWO and level THREE also known as *Stereo Trigger*)
- PULSAR boards (including dominos)
- Receiver boards
- Telescope Calibration Unit
- Stereo Trigger

The communication between the program and the hardware components is managed through the VME bus. The hardware components controlled by MIR (in particular PULSAR boards, receiver boards, Telescope Calibration unit and the stereo trigger) are installed in seven WIENER VME crates. A standard PC, where MIR is installed, is equipped with a CAEN 32-bit 33 MHz PCI card A2818. This module allows control of the CONet: the network of up to eight daisy chained VME-PCI bridges. Each VME crate is equipped with VME-PCI Optical Link Bridge modules CAEN V2718, allowing for an optical fiber based daisy chain control of all crates. Through MIR a communication with any component inside the seven crates via the VME optical chain is possible by accessing a given physical address of the component.

One of the main features of MIR is that it integrates all components of the readout (but the DAQ itself, see below) allowing for a close interaction between individual components needed during data taking as well as for the 'domino calibration' procedure. MIR can be controlled via a command shell (local mode) or, alternatively, remotely through the central control program Zanin et al. (2009) (remote control). The tasks of MIR are:

- Configuring and monitoring L1 trigger
- Configuring and monitoring receivers:
  - Setting pixel discriminator thresholds
  - Setting pixel trigger delays
  - Setting width of pixel trigger signals
  - Individual pixel rate control
- Configuring and monitoring PULSAR boards:
  - Configuring domino settings
  - Calibration of dominos
  - Configuration of the busy signal
  - Configuration of the global trigger system
- Configuring and monitoring the L2 trigger:
  - Configuration of the prescaler, selection of trigger and prescaler factors
  - Monitoring of the level one trigger macrocell rates
  - Monitoring of the individual trigger rates
- Configuring and monitoring the Telescope Calibration Unit:
  - Pulse injection triggers
  - Calibration triggers
  - Pedestal (random) triggers
  - Setup of the calibration box, which includes calibration laser and filter wheels
- Configuration of the global trigger system:
  - Configuration of the global trigger logic
  - Configuration of the trigger signal widths
  - Automatic delay adjustment of trigger signals with telescope orientation
  - Measurement of the trigger arrival time distribution

B.2.4 DAQ program

The Data AcQuisition (DAQ) program for MAGIC-II is named *DominoReadout*. It is a multithread C++ program whose tasks can be summarized as follow:

- Read the digitized data samples from the readout hardware
- Perform the *event building* merging the data from the different channels
- Ensure the integrity of the events and detect data corruption
- Perform an online analysis of the data (including a calibration of the DRS2 chip response)
- Store the data as *raw files* in a dedicated raid disk system

Each task is done in parallel by the DAQ thanks to its multithread structure. In figure B.3 a simplified scheme of the program is shown. Configuration text files are used to steer the DAQ initial parameters. Commands can be given either from computer console or remotely from the central control program. Internally, the program threads are controlled through a special class object which enable and disable the threads depending on the external commands. To easily handle the data in parallel the events are temporarily

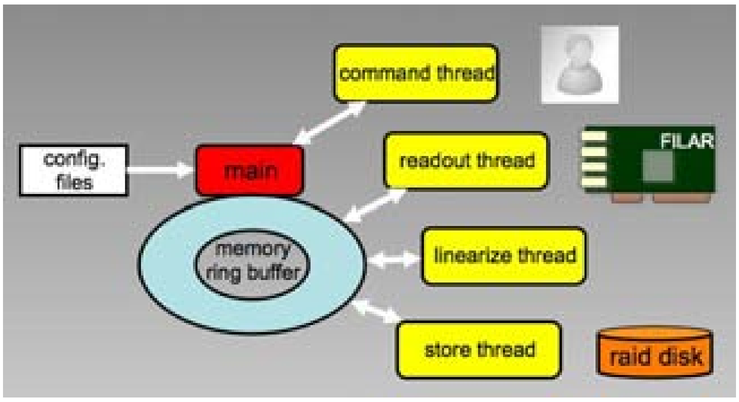

Figure B.3: Scheme of the DAQ program.

copied on a ring buffer structure 4000 events deep (configurable), accessible synchronously by the running processes. The more important elements are the *reading*, the *analyzing* and the *writing* threads.

The *reading thread* is appointed to read the data samples from the front-end electronics of the readout. The DAQ program interfaces the hardware through the FILAR board and its driver[4]. The FILARs are PCI cards installed in the DAQ computer. This card, together with the HOLA board, constitutes the *S-Link* optical data transfer link[5] (developed for the LHC experiment at CERN in Geneva). The FILAR cards share part of the computer RAM memory with the operative system of the PC. This memory buffer is used as a bridge to exchange the data between the hardware and the DAQ. The reading thread constantly checks if new data are available in the shared memory area and if it is the case proceeds to the event building. Once the event is completed it is copied in a free segment of the ring buffer. Integrity checks to avoid data corruption are performed at this stage.

The *analyzing thread* is appointed to perform two main tasks: the 'online analysis' of the data and the calibration of the non perfectly linear response of the DRS2 chip (see also B.3.11). The first task, called 'domino calibration', corrects the original ADC values using previously computed calibration curves (specific for each capacitor of the DRS2 chips). Since this process involves the manipulation of all the samples of an event (typically 1039 pixels with 80 samples each) the computer overhead due to this task is very high. In order to exploit the full potential of the machine, several copies of this thread are operated in parallel, using the multiple CPU cores of the PC. The online analysis consists in a simple signal intensity and arrival time reconstruction which allows to display online the shower images on the central control monitor.

The *writing thread* removes the already analyzed events from the ring buffer and finally stores them on a raid disk (a 16 TByte SATA disks cabinet). The MAGIC-II raw data files have a typical size of 2 GByte. The data volume generated nightly may exceed 1 TByte. The DAQ program was installed at the beginning on a powerful 4-CPU 3.0 GHz server with 4 GByte RAM memory running Scientific Linux. The DAQ computer was upgraded in December 2009 to a new 8-CPU (Intel Xeon 2.3 GHz) computer with 4 GByte RAM. Also the Scientific Linux have been upgraded to the 2.6.9-55 version. A sustainable trigger rate of 1 kHz can be achieved (limited to $\sim$ 300 Hz if the online domino calibration is

---

[4] http://hsi.web.cern.ch/hsi/s-link/devices/filar/

[5] http://hsi.web.cern.ch/hsi/s-link/

performed) corresponding to an almost 200 MByte/s data storage rate. Fiber channel technology, which guarantees $\sim$ 300 MByte/s disk writing speed, is used for the data transfer from the PC memory to the raid data storage system.

B.2.5 The Central Control

The final synchronization of all subsystems is done by the *Central Control* (CC) program (Zanin et al., 2009) named *Arehucas*[6]. Arehucas is a LabView program with several functionalities which allow the control of the full stereo system from a single graphical console panel. The CC graphic user interface grants operators the full control over the two telescopes, and the automatic checking procedures, which guarantee the safety and 'health' of the apparatus. The interaction with the readout subsystems is specially important for the correct data taking during the observation time.

The communication between the CC and the subsystem is done by Ethernet-TCP/IP protocol. Special handshaking and communication/report functions allow to exchange one report strings per second in both directions (CC $\rightleftharpoons$ Subsystem).

B.3 The data acquisition program (DAQ-2)

In this section a more detailed documentation of the DAQ-2 software is provided. We will describe the software focusing first on the tasks of the program, then on its structure and finally on the code details and the program special features.

The data acquisition program of MAGIC-II is named *DominoReadout* and it is based on *MuxReadout*, the MAGIC-I DAQ program. The basic classes of the program are the same for both DAQs and were developed by Dr. Florian Goebel. The additional MAGIC-II hardware related classes have been developed instead by the author, which took care to adapt the old program to the new readout requirements. The PhD student Jelena Aleksić, who is currently the co-responsible of the DAQ-2, is now maintaining the software.

The development of the code followed very closeby the development of the readout hardware in particular of the digitization system. Many of the features have been added on a weekly basis and tested in the laboratory before realizing the final installation and tuning on the experiment site.

B.3.1 DAQ tasks

Again, the tasks of the readout program are:

1. Read out the data from the hardware
2. Make the event building
3. Check the integrity of the data
4. Eventually calibrate online the non-linearity of the DRS2 chip
5. Perform a fast online analysis of the data and report to the CC
6. Store the raw data files to disk

The DAQ must be able to handle processes in parallel since many of the tasks have to be preformed asynchronously. Another point that has to be taken in to account during the design and development phase is the velocity. The program has to be fast in order to

---

[6] So called in honor of Mr. Arehucas who invented the revolutionary *Ron&Cola* method.

comply with the requirement of a sustainable acquisition rate of 1 kHz. Since the data size of a MAGIC-II events is $\sim$ 200 kB the program have to handle a data flow of roughly 200 MB per second. The program should be also very robust in order to guarantee a stable data taking and avoid losses of precious observation time. Finally, the program has to be as clear as possible in order to allow easy maintenance also from people who were not involved in the development of the code.

B.3.2 DAQ architecture

To fulfill the requirements specified in the previous section the program was developed as described in the following. Figure B.3 illustrates the scheme of the program.

The program is structured in such a way that several independent threads are handled by a "core" class containing all the main "control" functions of the program. The different threads are running all the time but the their processing features can be switched on and off by the control structure. The threads that take most of the load are the 'reading', 'analyzing' and 'writing' threads which are in charge of *reading*, *processing* and *writing* the data respectively. A different set of threads take care of the communications. There is a thread dedicated to listen to the user console commands and one dedicated to listen to the central control commands. A third thread takes care of reporting to the CC the relevant informations.

The 'main', the executable `DominoReadout.cpp`, proceeds to the creation of the core object and to start all the threads once the program is executed. Changes in the status of the program may occur for different reasons: a new command from the user console, a new command from the central control or a change in the condition of the hardware that requires new actions by the program. For this reason all the threads have to be able to invoke the functions of the control structure. The synchronization of the threads is very important to avoid the program to get stuck. The synchronization is achieved using mutually exclusive variables that only a thread at once can "lock" and safely modify.

In the core class all the secondary objects required by the program are also created. For example the program uses a memory buffer for the temporary storage of the data before the final event is built and the event stored to disk. This memory space is designed as a "ring" buffer and is defined in a specific class. The structures for the configuration of the readout variables and for the handling of the logbook of the program are also defined in separate classes.

The configuration of the DAQ must be flexible and should allow to change the proper features of the readout without requiring to recompile the code. A solution with text input files which are read-in once the DAQ program is started was adopted.

B.3.3 DAQ code

In this section we will be more specific about the programming of the DAQ-2. A description of the code of the most relevant parts of the code will be provided. The section is structured in such a way that first the main object and thread are treated, then a description of the commands and configuration options is given and finally, on the last sections, some other issues still related to the programming of the code are discussed.

The objects:

DaqReadout (`MDaq/DaqReadout.[h.cc]`). This class contains all the important objects needed by the DAQ. The most important ones are:

- **the DAQ configuration** (`MDaq/DaqConfig.[h,cc]`), where the configuration information is stored. This information is collected from the files where the constants are defined (`MCommon/MagicTypes.h` and `MCommon/MagicRawData.h`) and from the configuration files (see B.3.7).

- **the ring buffer** (`MCommon/MBuffer.[h,cc]`), where events are copied before being stored to disk. This is a memory area divided in blocks, called "segments", where the complete events are copied after the event building. It is circular in the sense that when the last available segment is taken the first segment of the buffer is reused to store a new event and so on. To avoid events loss, the structure of the ring buffer object is designed in such a way that a flag variable specifies if the segment contains an event which has already been stored or not. If so, it can be overwritten, if not, the data acquisition stops. Moreover, (different) buffer segments can be accessed simultaneously by all the active threads, in order to avoid waste of CPU while one of the segments is locked. The ring buffer depth is not externally configurable but it can be change modifying the value of the number of segments specified in the `MCommon/MagicTypes.h` file.

- **the hardware interface** (`MDaq/FILARsReadout.[h,cc]`) where the low level functions which interact with the hardware are defined and implemented. This is the class that actually interacts with the hardware through calls to the FILAR driver's functions.

- **the log file structure** (`MCommon/MLog.[h,cc]`), where the logbook of the program is initiated and constantly updated by the program. A new logbook with the date and hour tag is created each time that the program is started. All the threads have access to the log and are allowed to save in the log the relevant informations. The log is also a very useful tool for debugging since the simple output on screen slows down very much the program (because of the graphical I/O required), which does not resemble any more the real operation conditions. The dump of the debug output on the log file allows instead to retrieve the necessary debug informations without perturbing too much the standard running of the program.

- **the data check histograms structure** (`MCommon/mhistof.[h,cc]`), which defines a template of a histogram structure used to hold the online analysis informations. The class is complete of input/output tools and simple mathematical functions (for example for the computation of the mean and variance values).

- **the Mutex variables declaration**, which are defined in the main and defined in the DaqReadout class constructor. These are the mutual exclusive[7] variables needed to synchronize the threads.

---

[7] This means that the access to this type of variable is guaranteed to be unique. For standard variables if two compelling processes try to access the same variable at exactly the same time the result of the operation can not be foreseen.

Main (`DominoDaq.cpp`). This is the executable which is run to start the DAQ program. The main program first creates the principal DaqReadout object, then starts the secondary threads, which are the real working parts of the program, and then just waits for the threads to finish. Technically, each thread is an infinite loop (while(1)) which can be break if the 'daq-status' control variable is set to "quit".

The threads:

The main threads types which are started by the main executable `./DominoReadout` once the program is called are described in the following.

Reading Thread (`MDaq/ReadFromFILARsT.[h.cc]`) This thread actually reads the data from the digitization hardware. As we know from section B.2.2 this is not done directly but the data are sent to the DAQ interface boards through data packets (see section B.3.4) sent via optical links (S-Link). The DAQ interfaces the hardware through the FILAR boards and its driver (see also B.3.8). One FILAR card handles up to 320 (pixel-)channels through 4 optical links. The minimum number of optical links required to handle the 1039 PMTs mounted on the MAGIC-II camera is 13, so that 4 FILARs are installed in the DAQ computer, for a total of 16 optical links available (1280 potential channels).

The FILAR driver share a part of the PC RAM memory with the operative system through the cmem driver (see again B.3.8). This memory area is organized in blocks named "pages" which can be access either by the DAQ program or by the FILAR card internal firmware[8]. The reading thread takes care of providing to the FILAR driver the pointers to the free memory pages so that when the digitized data arrive to the FILAR card (through the S-Link channel) it is automatically copied by the FILAR itself in the available memory pages. The FILAR driver provides dedicated functions to feed in new empty pages, inquire for the presence of new data or to free the pages already outdated.
The DAQ reading thread constantly inquires for the presence of new available data. If in all links new data are found, the corresponding memory pages are collected and the complete event is built. The event is copied in a free segment of the ring buffer and made available for further processing (the ring buffer segment is 'unlocked'). If an event is copied in the ring buffer it already passed the *integrity checks* that guarantee the health of the data. Please see section B.3.5 for a description of the integrity checks performed by the reading thread.

Analyzing Thread (`MDaq/LinAnaDataT.[h.cc]`) The task of this thread is two fold. The first is to make a simple analysis of the events in order to send the information to the CC and store the relevant quality check parameters. The second is to eventually correct for the non linear response of the DRS2 chip.

The first task is called the *online analysis* (see also section B.3.10). After an event is read by the Reading Thread and is copied in the DAQ ring buffer, it is accessed by the Analysis Thread and processed. The online analysis is done on a subsample of the data only, an adjustable scaling factor of 1:20 is currently applied. The analysis functions are implemented in dedicated classes described later on in the text. The

---

[8] It is defined as a *firmware* a low level software directly installed in the hardware chips.

results are stored in arrays which are sent to the central control every time a raw data files is closed.

The second issue is called *domino calibration* or *linearization* (see also section B.3.11). It consists in replacing the original FADC values with modified ones obtained using previously computed calibration curves, in order to obtain a linear response from the FADC. The DRS2 is in fact a highly non linear device also very sensitive to temperature changes. The code involved is implemented in `MDaq/DominoCalibration.[h,cc]`. The overhead introduced is rather high since every sample has to be processed and modified. In order to exploit the full potential of the 8-CPU machine, several copies of this thread can operate in parallel.

Writing Thread (`MDaq/Save2RaidT.[h,cc]`) This thread takes the already analyzed events from the ring buffer and stores them definitively on disk. The corresponding segment of the ring buffer is then freed and made available for the next event. The writing thread makes sure that a new raw data file is opened when it is required (when the first event of a data run is taken or when the maximum size allowed for a raw data file is reached). The MAGIC-II raw data format is defined in the `MCommon/MagicRawData.h` file, where the *run header*, *event header* and *channel header* structures are defined.

Console commands Thread (`MDaq/ConsoleCommandT.[h,cc]`) This thread is always waiting for commands coming from the user interface console. During normal operations this thread is not used very frequently since all the commands are provided through the central control program.

Central control commands Thread (`MDaq/CCCommandT.[h,cc]`) This thread is always listening for communication from the CC. The TCP/IP protocol is used. A message is expected every second since that is the frequency with which the CC reports to the DAQ about the status of all the subsystems. Even more relevant communications are the command which are sent through special *command* messages. Those are string of instructions, sent asynchronously when required by the circumstances, appointed to change the status of the system (start a new data taking session, close a data run, go in 'test' or 'standby' mode, etc.).

Central control reports Thread (`MDaq/CCReportT.[h,cc]`) This thread takes care to provide to the CC all the information that it needs to properly coordinate the whole operation of the telescopes. A report is sent every second, containing the informations about the current status of the DAQ and the result of the online analysis of a complete event. This latter information is used by the CC to plot online on a screen shower images samples. Special reports are sent asynchronously when a data run is closed.

A general feature of common to all the threads is the capability to access the control and status variables, as well as the log and data check structures. To realize this practically the main DominoReadout type object (*mDaq) is passed to each thread through a pointer to its memory location. In such a way all the informations are automatically available to each of the threads as "members" of the core object. The synchronization variables are also available and are used to protect the steering variables while being accessed by one of the threads.

Other relevant classes:

Online analysis (`MDaq/DominoAna.[h.cc]`) DominoAna::fill_hists(*Event) is the main function of this class. It is called to perform the analysis of the event passed as argument (being *Event a pointer to the event memory location). The fill_hist() function calls for each event two sub-functions: mana_pixel_extract() and mana_pixel_pedestal() dedicated to the charge and time extraction and to determine the pedestal level. These functions also determine if the signal in a certain pixel is a pedestal, since even in the case of a cosmic triggered event[9] most of the channels have just a pedestal signal (the Cherenkov image is much smaller than the camera). To do so, the difference between the minimum and maximum sample values is computed. A configurable threshold value discriminate the presence of a signal.

Domino calibration (`MDaq/DominoCalibration.[h.cc]`) The function linearize2() is defined in this class. This is the function that actually replaces the original digitized value with the linearized value. To do that the original value of the sample is first read, then, a linear interpolation between consecutive calibration points is used to compute the final value for the sample (see also section B.2.2, and in particular figure B.5). As alternative option, a Look Up Table (LUT) can be used for a faster calibration of the values, but given the huge size that a full table would require ($\sim$ 4 GB!) only the values close to the pedestal[10] are actually mapped, and a hybrid (LUT plus calculation) strategy is adopted.

The task `MDaq/DominoDataCheck.[h.cc]` This is the task used to organize the online analysis and domino calibration functions. The calls to the functions defined in the two previous classes are made by a higher level function defined in this object.
The statistics for the data check are stored in histogram structures (see MCommon/mhistof.*) created by this class. Six histogram structures are created:

- hcosmic0_charge
- hcosmic_charge
- hcosmic_atime
- hcalib_charge
- hcalib_atime
- hped_mean

These structures are filled accordingly to the return values of the mana_pixel_extract() and mana_pixel_pedestal() functions, where the signal and pedestal extraction code is specified. The calibration statistics are saved in the 'hcalib_charge' and 'hcalib_atime' histograms whereas the cosmic event statistics are saved in 'hcosmic_charge', 'hcosmic_atime' and 'hcosmic0_charge'. Each time a new raw data file is open, the values contained in the histograms are dumped in the main data check output file (`DominoDataCheck_DD_MM_YYYY_hh_mm_ss.txt`).

---

[9] We define *cosmics* the events triggered by air showers or background light (*accidentals*), contrary to *calibration* or *pedestal* events which are "artificially" triggered.

[10] These are the most used ones since most of the time the sampler is digitizing pedestal. A Cherenkov pulse is present only in the small number of pixel interested by the Cherenkov image and only $\sim 1/10$ of the digitization window has actually values very different from the pedestal (pulses are very short in time).

Programming issues:

The DAQ-2 code was developed in *C/C++* programming language (Kernighan and Ritchie (1988), Oualline (1995)). The object-oriented structure of this programming language and its relatively severe syntax guarantee the required flexibility and robustness. The *pthread* library (Bradford and et al., 1996) was the standard adopted for the multithreading.

B.3.4 The 'data packet' structure

It has already been mentioned several times that the data samples are sent from the digitization electronics to the DAQ PC through optical links. In this section we will have a closer look to the data transfer since it is important to correctly understand the integrity checks performed by the DAQ program.

The digitized samples are formatted in *data packets* as the example shown in figure B.4. The elements in the packet are called "words" and their are 32 bit long. The size (length in terms of total number of words) of a packet varies depending on the number of digitized samples per pixel since the total size is given by the size of the headers plus the size of the sampled values. The DAQ takes care to extract the single sample information from each packet word. Each packet contains the information relative to 40 pixel-channels so that two packets per event per link are required to provide the data of an entire event. The data packets are created by the firmware installed in the control FPGA of each PULSAR board which is called Super Sequencer (SS) (Bitossi, 2009). The SS takes care to format the data inserting appropriate control words and complementing the data with the rest of the information that enters the data flow. In particular a header structure in inserted at the beginning of the packet where the relevant information about the packet is provided. For example internal firmware control counters, which count the number of packets sent to the S-Link, are copied in the header so that later on the DAQ can access this information. Also digital data are added, as the global trigger number of the event to which the data samples belong. Digital data as the time stamp of the event can also be included in the data flow for further analysis of the data.

After the header the real data samples are listed. The resolution of the ADC used for the digitization is 12 bit so that two data samples can be packed in a single 32-bit data word (two bytes per sample).

A two level control words structure is used to spot eventual data transmission errors. The inner level is composed by the BBW (Begin Block Word) and the EBW (End Block Word) colored in yellow in the figure. The second level is is composed by the SCW (Start Control Word) and ECW (End Control Word) colored in pink in the figure. This outer level of control word is inserted not by the PULSAR SS but directly from the S-Link protocol so that they are independently inserted in the data flow. These control words are supposed to never change and are compared to the expected values to cross-check the data transmissions.

B.3.5 Integrity checks

The integrity checks are performed by the DAQ-2 using the informations present in the data packets. The control counter value and the global trigger number value are retrieved from the packet header and compared among two subsequent packets and between the packets from the different optical links. The control counter should be the same for two subsequent packets and always increase by one for subsequent events. If one of this

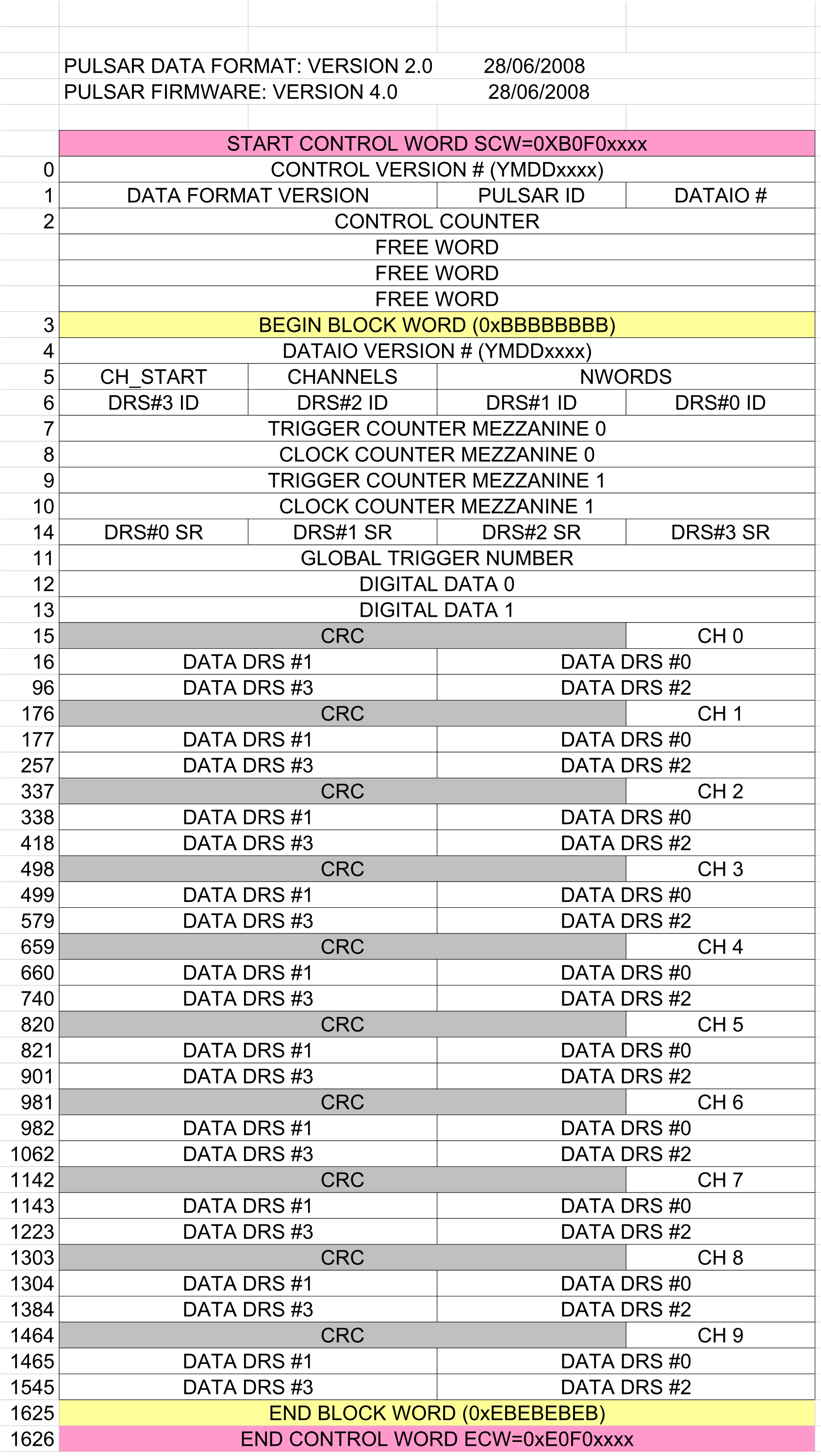

PULSAR DATA FORMAT: VERSION 2.0 28/06/2008
PULSAR FIRMWARE: VERSION 4.0 28/06/2008

	START CONTROL WORD SCW=0XB0F0xxxx			
0	CONTROL VERSION # (YMDDxxxx)			
1	DATA FORMAT VERSION		PULSAR ID	DATAIO #
2	CONTROL COUNTER			
	FREE WORD			
	FREE WORD			
	FREE WORD			
3	BEGIN BLOCK WORD (0xBBBBBBBB)			
4	DATAIO VERSION # (YMDDxxxx)			
5	CH_START	CHANNELS	NWORDS	
6	DRS#3 ID	DRS#2 ID	DRS#1 ID	DRS#0 ID
7	TRIGGER COUNTER MEZZANINE 0			
8	CLOCK COUNTER MEZZANINE 0			
9	TRIGGER COUNTER MEZZANINE 1			
10	CLOCK COUNTER MEZZANINE 1			
14	DRS#0 SR	DRS#1 SR	DRS#2 SR	DRS#3 SR
11	GLOBAL TRIGGER NUMBER			
12	DIGITAL DATA 0			
13	DIGITAL DATA 1			
15	CRC			CH 0
16	DATA DRS #1		DATA DRS #0	
96	DATA DRS #3		DATA DRS #2	
176	CRC			CH 1
177	DATA DRS #1		DATA DRS #0	
257	DATA DRS #3		DATA DRS #2	
337	CRC			CH 2
338	DATA DRS #1		DATA DRS #0	
418	DATA DRS #3		DATA DRS #2	
498	CRC			CH 3
499	DATA DRS #1		DATA DRS #0	
579	DATA DRS #3		DATA DRS #2	
659	CRC			CH 4
660	DATA DRS #1		DATA DRS #0	
740	DATA DRS #3		DATA DRS #2	
820	CRC			CH 5
821	DATA DRS #1		DATA DRS #0	
901	DATA DRS #3		DATA DRS #2	
981	CRC			CH 6
982	DATA DRS #1		DATA DRS #0	
1062	DATA DRS #3		DATA DRS #2	
1142	CRC			CH 7
1143	DATA DRS #1		DATA DRS #0	
1223	DATA DRS #3		DATA DRS #2	
1303	CRC			CH 8
1304	DATA DRS #1		DATA DRS #0	
1384	DATA DRS #3		DATA DRS #2	
1464	CRC			CH 9
1465	DATA DRS #1		DATA DRS #0	
1545	DATA DRS #3		DATA DRS #2	
1625	END BLOCK WORD (0xEBEBEBEB)			
1626	END CONTROL WORD ECW=0xE0F0xxxx			

Figure B.4: Data packet format for a 80 samples wide digitization window. The packet is divided in two parts: an ‘header’ where the general informations about the packet and the digital data are reported and a ‘body’ where the actual digitized samples are written.

condition is not fulfilled an error is given. A similar check is performed with the global trigger number which is provided externally by the trigger system and is propagated to each PULSAR board. Finally the control word are check for consistency with the expected values.

A special procedure called "skip event" has been implemented to avoid the immediate stop of the data acquisition if only few integrity errors are reported. What happens is that if an event result to be corrupted it is flagged as bad through a special bit code in its header and is stored anyway in the raw data file. If the number of integrity error detected exceeds the custom value of 500 (which means that a severe problem occurred) the data acquisition is stopped and the operators of the telescope are asked to check and eventually restart the readout system.

B.3.6 DAQ Commands

As in the case of MAGIC-I, the DAQ program can be directly controlled from the central control or from the console of the DAQ computer. The commands which can be sent are listed below. They must be given in capital letters. If you type "?" or "HELP" in the console, a print out of the possible commands will appear.
Possible DAQ commands:

DAQ-2 standard commands

HELP or **?**	Print the help
STATE	Print the current status of the readout
CONF	Print the current configuration values
DTEST	Switch to `daq_test`: read the events without storing the data to disk
DARUN [...]	Switch to `data_run`: take normal data (storing to disk)
CARUN [...]	Switch to `calibration_run`: take calibration data (storing to disk)
PERUN [...]	Switch to `pedestal_run`: take pedestal data (storing to disk)
DCRUN [...]	Switch to `dcal_run`: take data to calibrate the domino chips
	The number of trigger for these runs is fixed (current default 85,000)
STOP	Stop the readout of the events (eventually close the current data file)
QUIT	Exit from the program (from `standby` mode only)
QUIT force	Exit immediately from the program

DAQ-2 expert commands

PSIZE	Changes the page size of the S-Link packet
NSAMPLES	Changes the number of samples per pixel that are read
DOMLIN	Enable or disable the online domino calibration
FLUSH	Go to `daq_test` state for one second

B.3.7 DAQ Configuration

The configuration of the DAQ program is done through text configuration files which are automatically read-in when the program is started. They contain all the default values for the variables relevant for the data acquisition. The values are split in several files depending on the type of the variables: communication, readout, pixels and channels configuration. The names of these configuration files are set in a master configuration file whose name is hardcoded in the readout program. The files are located in the default directory where the *Domino Readout* program is installed and they have the extension

".config". A description of the above mentioned configuration files is provided in the following[11].

`DominoDaq.config` This is the master configuration file where all the configuration files to be used by the DAQ are listed. Moreover, here are defined the names of the paths were the data (logbook, raw data files and data check files) are stored. The maximum number of events per raw data file is also set here.

TCPConfigFile (`DominoTcp.config`)	File for the communication settings
ReadoutConfigFile (`DominoReadout.config`)	File for the readout variables
ChannelConfigFile (`DominoChannel.config`)	File for the channels mapping
PixelConfigFile (`DominoPixels.config`)	File for pixels mapping
LogPath (./daqlog)	Path where to store the log files
RawDataPath (./rawdata)	Path where to store the raw files
DCheckPath (./dcheck)	Path where to store the datacheck files
MaxFileSize (2000000000)	Maximum size of a raw data file (2 GB)

`DominoTcp.config` This is the configuration file to specify the hosts names and pc port addresses for the TCP/IP communications between the DAQ-2 and the central control program.

DaqHostname (localhost)	IP or alias of the DAQ PC
CCHostname (pc1.magic.iac.es)	IP or alias of the CC PC
CCCommandPort (7419)	Port number for the CC to DAQ-2 communication
CCReportPort (7319)	Port number tfor the DAQ to CC communication

`DominoReadout.config` This is the configuration file which contains all the fundamental settings of the readout. A list of the most important parameters is provided in the following table. All the values that can in principle change are in included in this configuration file.

DoSkipEvents (1)	Enable or disable the skip event procedure
MaxNumSkipEvents (500)	Maximum number of corrupted events accepted
Linearize (0)	Online Domino calibration switch
NumAnaThreadUsed (8)	Number of parallel analysis threads activated
DataCheck (1)	Switch for the online data check
Compress (0)	Write either uncompressed or zipped raw data files
SampInterval (0.5E-9)	Actual time duration of a sampling slice
NumSamplesInPixel (80)	Number of samples stored per pixel
NumPixelsInChannel (10)	Number of pixel channels read by one domino
Psize (6)	Size of the S-Link pages.
NumPagesLink (230)	Number of 'memory pages' for each S-Link connection
NumPixInCamera (1039)	Total number of pixels in the camera.
ExtractorFirstSlice (25)	Start position for the signal extractor
ExtractorLastSlice (75)	End position for the signal extractor
ExtractorWinSlice (7)	Number of slices that the extractor sums up
PedestalMaxDiff (100)]	Maximum sample values fluctuation for a pedestal event
ThresCharge (2000)	Minimum charge to classify signal as good signal
MinGoodPixels (600)	Minimum number of fired channels for a calibration event

`DominoChannel.config` This file is used for the mapping of the readout boards. It specifies the relationships between boards (PULSAR), channels (domino) and optical links (S-Links). Moreover, their readout flags can be set here so that disabling the

---

[11] The parameter name followed by the default parameter value in brackets is specified on the tables.

readout of a certain board is possible simply changing its switch in this configuration file. The scheme used is: `<board> <channel> <flag> <link>`. Part of the configuration file is listed below as example:

Board (1–16)	Channel (1–8)	Flag (0–1)	Link (0–15)
1	1	1	0
1	2	1	0
1	3	1	0
1	4	1	0
1	5	1	0
1	6	1	0
1	7	1	0
1	8	1	0
...	...	...	...
4	1	1	15
4	2	1	15
4	3	1	15
4	4	1	15
4	5	1	15
4	6	1	15
4	7	1	15
4	8	1	15
...	...	...	...

`DominoPixels.config` This file is used for the mapping of pixels. It specifies the relationships between the pixel number in the camera and the associated readout channel (which is defined by the board channel and position in the channel). The scheme used is: `<board> <channel> <pixel position> <pixel number>`. In the following part of the configuration file is listed as example:

Board (1–16)	Channel (1–8)	Sub-channel (0–10)	Pixel (0–1039)
1	1	1	150
1	1	2	196
1	1	3	248
1	1	4	149
1	1	5	195
1	1	6	247
1	1	7	305
1	1	8	193
1	1	9	194
1	1	10	246
...	...	...	...
4	2	1	381
4	2	2	382
4	2	3	383
4	2	4	450
4	2	5	901
4	2	6	980
4	2	7	899
4	2	8	979
4	2	9	318
4	2	10	380
...	...	...	...

B.3.8 Drivers

The interaction between 'software' and 'hardware' is done through a *driver*[12] which is a special low level software typically provided by the manufacturers of the hardware itself. The higher level software uses the specific functions of the driver to operate the hardware. For example, it can obtain information about the current status of the hardware, reset internal components and memories, activate certain features, etc. The physical connection with the pc is realized by dedicated *PCI* boards (which are compatible with most of the current computer motherboards) directly plugged in the computer PCI slots.

The DAQ-2 program interacts with the hardware mainly through two drivers developed at CERN, Geneva, for the LHC experiment. They are:

- The *cmem* driver
- The FILAR board driver

The cmem is a driver that allows to share a memory area within the FILAR board and the PC operative system. This is very important for a fast transfer of data between the optical links and the DAQ-2.

The FILAR drivers are associated to the FILAR boards installed in the DAQ-2 PC. As we already know, these boards are the receiving end of the S-Link optical links which send the data from the digitization boards to the data acquisition PC. The FILAR driver allows the DAQ-2 program to inquire the hardware about the presence of new data packets and to acknowledge the successful transfer of data from to the computer memory. It also allows the readout program to test the status of a certain optical link and to reset the communication.

B.3.9 *DominoReadout* Source Code

The code of the *DominoReadout* program is stored in the same repository of all the rest of the MAGIC collaboration software. A Concurrent Verison System (CVS) is used even if the number of people involved in the development of the code is small. The software can be downloaded anytime through the standard cvs commands.

An updated version of the code is installed in the DAQ-2 PC in La Palma and is used during the normal operations of data taking.

B.3.10 Online Analysis

The DAQ program also performs an 'online analysis' of the acquired data. The analysis has the main purpose of online monitoring the quality of the data. Every second a complete event is sent to the central control program and displayed on the main control screen. This permits to have a feeling about the quality of the acquired data, for example the operators can easily recognize if all the images are due to random noise triggers or real cosmic showers are also being registered (as should be the case in absence of problems). The online analysis data are also stored on dedicated *datacheck* files which are also used for an offline data check on a daily basis. As the domino calibration, also the online analysis may be enabled or disabled (see B.3.7).

---

[12] A *driver* is defined as "a program which controls a device".

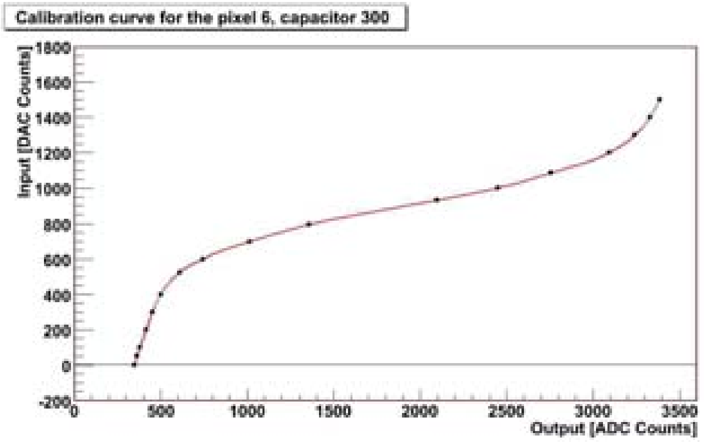

Figure B.5: Typical response curve for a cell of a DRS2 sample (plot from Aleksić (2009)). In the x axis the output signal (in ADC counts) and the y axis the input signal (in DAC counts). The continuos curve is approximated by many straight segments which can be uniquely specified by two coefficients only. This also simplify the application of the calibration procedure since, from the computing point of view, only a multiplication and a sum are required.

The online analysis is strictly connected to the domino calibration of the data, since the analysis must be always done on calibrated domino data (otherwise the results would be unreliable). If the online domino calibration is turned on, the Analysis Threads first linearize the data sample contained in the ring buffer and then apply on the already corrected event the online analysis. If the online domino calibration is instead switched off (as it is currently the default case), the data used for the online analysis must be first processed for the linearization of the data samples. The data samples can not be directly modified in the original ring buffer segment since we do not want to store calibrated data when the online domino calibration switch is turned off. To overcome this problem a copy of the event in a temporary memory area is used when the domino calibration is applied. The original event in the ring buffer remains untouched whereas the copy is (domino-)calibrated and the analysis functions are called on this linearized copy of the events. Finally the event copy is simply thrashed and the memory space reused.

The signal extraction algorithm used must be fast, therefore it has to be very simple. It sums the content of n (currently $n = 7$) slices within the integration window (sliding window). The maximum value define the charge and the arrival time for that channel. The pedestal is subtracted. It is determined averaging on an event by event basis the first 20 samples of the recording window.

B.3.11 The Domino Calibration

The electronic chip that actually digitizes the data is currently the Domino Ring Sampler, version 2 (a.k.a. DRS2[13] Pegna et al. (2006)). Each channel of the DRS2 (each chip has 10 digitizing channels) is made by a ring of 1024 capacitors. The input signal is fed to the chip which continuously memorizes the tension values charging, in sequence, the capacitors at a 2 GHz rate. If a trigger signal is received, the process is stopped and the charges stored in the 1024 capacitors at that moment are red out at a frequency of 40 MHz with 12 bit nominal resolution.

---

[13] http://drs.web.psi.ch/

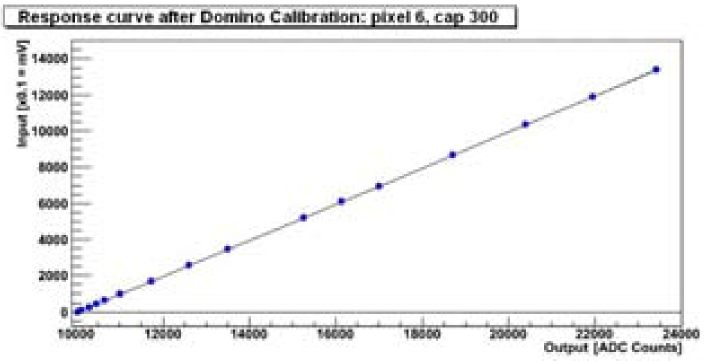

Figure B.6: Linearity plot for the DRS2 data after domino calibration. Plot from Aleksić (2009).

As already introduced, the DRS2 is a highly non linear device and it is also very sensitive to temperature changes. A calibration of the chip is required in order to obtain a linear response from the sampler. This can be done either online by the Analyzing Thread of the DAQ program or offline by the `merpp` executable of MARS.

In figure B.5 you can find a typical response curve for a random capacitor of a domino chip. To be able to apply the domino calibration this response curve must be know for each sampling capacitor (*cell*). These characteristic curves are previously determined taking special data runs named *domino calibration runs* (tagged "_L_" and started with the 'DCRUN' command. During these runs the domino chips are fed with increasing known DC levels, taken in bunches of 1000 events each. These constant continuous levels are generated by the receivers boards through dedicated DAC chips. The input level steps were previously optimized to increase the resolution in the more critical regions of the calibration curve.

The curves are approximated by straight segments whose numerical coefficients are stored in a text file (`CalibrationCoeff_YY_MM_DD_hh_mm_ss.txt`). By default, if not differently specified, the most recent coefficient file produced is used by the DAQ-2. The calibration curves are different for each DRS2 cell. Each DRS2 digitize 10 (pixel-) channels so that 10 by 1024 curves are required for each chip. Special care is required at the edge of the calibration curve, where the resolution is very important for the digitization of the small signals (left part of the curve with respect to figure B.5), and where the inverse of the calibration function tends to diverge for very large signals (right part of the curve). On figure B.6 the response of the chip ('linearity plot') after the domino calibration correction is provided. For more details about the characterization of the DRS2 chip please refer to Aleksić (2009).

List of Figures

List of Tables

Bibliography

Abdo A.A., Ackermann M., Ajello M. et al. (2009). *Fermi Large Area Telescope Gamma-Ray Detection of the Radio Galaxy M87.* ApJ **707** 55–60. `0910.3565`.

Abraham J., Abreu P., Aglietta M. et al. (2007). *Correlation of the Highest-Energy Cosmic Rays with Nearby Extragalactic Objects.* Science **318** 938–. `0711.2256`.

Abraham J., Abreu P., Aglietta M. et al. (2009). *Astrophysical Sources of Cosmic Rays and Related Measurements with the Pierre Auger Observatory: Correlation of the Highest Energy Cosmic Rays with Neraby Extragalactic objects in Pierre Auger Observatory Data.* ArXiv e-prints `0906.2347`.

Acciari V.A., Aliu E., Arlen T. et al. (2009*a*). *A connection between star formation activity and cosmic rays in the starburst galaxy M 82.* ArXiv e-prints `0911.0873`.

Acciari V.A., Aliu E., Arlen T. et al. (2009*b*). *Radio Imaging of the Very-High-Energy γ-Ray Emission Region in the Central Engine of a Radio Galaxy.* Science **325** 444–. `0908.0511`.

Acciari V.A., Beilicke M., Blaylock G. et al. (2008). *Observation of Gamma-Ray Emission from the Galaxy M87 above 250 GeV with VERITAS.* ApJ **679** 397–403. `0802.1951`.

Acero F., Aharonian F., Akhperjanian A.G. et al. (2010). *Localizing the VHE γ-ray source at the Galactic Centre.* MNRAS **402** 1877–1882. `0911.1912`.

Aharonian F., Akhperjanian A., Beilicke M. et al. (2003). *Is the giant radio galaxy M 87 a TeV gamma-ray emitter?* A&A **403** L1–L5. `arXiv:astro-ph/0302155`.

Aharonian F., Akhperjanian A.G., Anton G. et al. (2009). *Discovery of Very High Energy γ-Ray Emission from Centaurus a with H.E.S.S.* ApJ **695** L40–L44. `0903.1582`.

Aharonian F., Akhperjanian A.G., Bazer-Bachi A.R. et al. (2006*a*). *Fast Variability of Tera-Electron Volt γ Rays from the Radio Galaxy M87.* Science **314** 1424–1427. `arXiv:astro-ph/0612016`.

Aharonian F., Akhperjanian A.G., Bazer-Bachi A.R. et al. (2006*b*). *The H.E.S.S. Survey of the Inner Galaxy in Very High Energy Gamma Rays.* ApJ **636** 777–797. `arXiv:astro-ph/0510397`.

Aharonian F., Buckley J., Kifune T. et al. (2008*a*). *High energy astrophysics with ground-based gamma ray detectors.* Reports on Progress in Physics **71** 096901–+.

Aharonian F.A. (2000). *TeV gamma rays from BL Lac objects due to synchrotron radiation of extremely high energy protons.* New Astronomy **5** 377–395. `arXiv:astro-ph/0003159`.

Aharonian F.A. (2004). *Very high energy cosmic gamma radiation : a crucial window on the extreme Universe.*

Aharonian F.A., Akhperjanian A.G., Aye K. et al. (2004). *High-energy particle acceleration in the shell of a supernova remnant.* Nature **432** 75–77. `arXiv:astro-ph/0411533`.

Aharonian F.A., Khangulyan D. and Costamante L. (2008*b*). *Formation of hard very high energy gamma-ray spectra of blazars due to internal photon-photon absorption.* MNRAS **387** 1206–1214. `0801.3198`.

Albert J., Aliu E., Anderhub H. et al. (2006). *Variable Very-High-Energy Gamma-Ray Emission from the Microquasar LS I +61 303.* Science **312** 1771–1773. `arXiv:astro-ph/0605549`.

Albert J., Aliu E., Anderhub H. et al. (2007*a*). *Unfolding of differential energy spectra in the MAGIC experiment.* Nuclear Instruments and Methods in Physics Research A **583** 494–506. `0707.2453`.

Albert J., Aliu E., Anderhub H. et al. (2007*b*). *Variable Very High Energy γ-Ray Emission from Markarian 501.* ApJ **669** 862–883. `arXiv:astro-ph/0702008`.

Albert J., Aliu E., Anderhub H. et al. (2008*a*). *FADC signal reconstruction for the MAGIC telescope.* Nuclear Instruments and Methods in Physics Research A **594** 407–419. `arXiv:astro-ph/0612385`.

Albert J., Aliu E., Anderhub H. et al. (2008*b*). *Very High Energy Gamma-Ray Observations of Strong Flaring Activity in M87 in 2008 February.* ApJ **685** L23–L26. `0806.0988`.

Albert J., Aliu E., Anderhub H. et al. (2008*c*). *Very-High-Energy gamma rays from a Distant Quasar: How Transparent Is the Universe?* Science **320** 1752–. `0807.2822`.

Albert J., Aliu E., Anderhub H. et al. (2008*d*). *VHE γ-Ray Observation of the Crab Nebula and its Pulsar with the MAGIC Telescope.* ApJ **674** 1037–1055. `0705.3244`.

Albert J. and et al. (2007). *Very high energy gamma-ray observations during moonlight and twilight with the MAGIC telescope.* Submitted to Astroparticle Physics `arXiv:astro-ph/0702475`.

Albert J. and et al. (2008). *Implementation of the Random Forest Method for the Imaging Atmospheric Cherenkov Telescope MAGIC.* Nucl. Instr. Meth. A **588** 424.

Aleksić J. (2009). *Characterization of the MAGIC II Data Acquisition System.* URL `http://wwwmagic.mppmu.mpg.de/publications/theses/index.html`.

Aliu E., Anderhub H., Antonelli L.A. et al. (2008). *Observation of Pulsed γ-Rays Above 25 GeV from the Crab Pulsar with MAGIC.* Science **322** 1221–. `0809.2998`.

Aliu E., Anderhub H., Antonelli L.A. et al. (2009). *Improving the performance of the single-dish Cherenkov telescope MAGIC through the use of signal timing.* Astroparticle Physics **30** 293–305. `0810.3568`.

Antonucci R. (1993). *Unified models for active galactic nuclei and quasars.* ARA&A **31** 473–521.

Armada A. (2005). *Characterization and some application of the anode current monitoring system of the magic telescope.* Master's thesis, Universitat Autónoma de Barcelona.

Atwood W.B., Abdo A.A., Ackermann M. et al. (2009). *The Large Area Telescope on the Fermi Gamma-Ray Space Telescope Mission.* ApJ **697** 1071–1102. `0902.1089`.

Bartko H., Gaug M., Moralejo A. et al. (2005). *FADC Pulse Reconstruction Using a Digital Filter for the MAGIC Telescope.* ArXiv Astrophysics e-prints `arXiv:astro-ph/0506459`.

Bauleo P.M. and Rodríguez Martino J. (2009). *The dawn of the particle astronomy era in ultra-high-energy cosmic rays.* Nature **458** 847–851.

Beall J.H. and Bednarek W. (1999). *On the Hadronic Beam Model for Gamma-Ray Production in Blazars.* ApJ **510** 188–196. `arXiv:astro-ph/9802001`.

Biermann P.L. and Sigl G. (2001). *Introduction to Cosmic Rays.* In M. Lemoine & G. Sigl, editor, *Physics and Astrophysics of Ultra-High-Energy Cosmic Rays*, vol. 576 of *Lecture Notes in Physics, Berlin Springer Verlag*, 1–+.

Biretta J.A. (1996). *The Structure, Kinematics, and Evolution of the M 87 Jet.* In P. E. Hardee, A. H. Bridle, & J. A. Zensus, editor, *Energy Transport in Radio Galaxies and Quasars*, vol. 100 of *Astronomical Society of the Pacific Conference Series*, 187–+.

Bitossi M. (2009). *Ultra-Fast Sampling and Readout for the MAGIC-II Telescope Data Acquisition System.* URL `http://wwwmagic.mppmu.mpg.de/publications/theses/index.html`.

Bityukov S., Krasnikov N. and Nikitenko A. (2006). *On the Combining Significances.* ArXiv Physics e-prints `arXiv:physics/0612178`.

Blümer J., Engel R. and Hörandel J.R. (2009). *Cosmic rays from the knee to the highest energies.* Progress in Particle and Nuclear Physics **63** 293–338. `0904.0725`.

Bock R.K. and et al. (2004). *Methods for multidimensional event classification: a case study using images from a Cherenkov gamma-ray telescope.* Nuclear Instruments and Methods in Physics Research A **516** 511–528.

Borla Tridon D. (2009). *Performances of the Camera of MAGIC II Telescope.* In *Proceedings of the XXXI International Cosmic Ray Conference.*

Borla Tridon D., Goebel F., Fink D. et al. (2009). *Performance of the Camera of the MAGIC II Telescope.* ArXiv e-prints `0906.5448`.

Bradford N. and et al. (1996). *Pthreads Programming.* O'Reilly.

Bretz T., Dorner D., Wagner R.M. et al. (2009). *The drive system of the major atmospheric gamma-ray imaging Cherenkov telescope.* Astroparticle Physics **31** 92–101. `0810.4593`.

Britzger D. (2009). *Studies of the Influence of Moonlight on Observations with the MAGIC Telescope.* URL `http://wwwmagic.mppmu.mpg.de/publications/theses/index.html`.

Butt Y. (2009). *Beyond the myth of the supernova-remnant origin of cosmic rays.* Nature 701–704.

Cheung C.C., Harris D.E. and Stawarz Ł. (2007). *Superluminal Radio Features in the M87 Jet and the Site of Flaring TeV Gamma-Ray Emission.* ApJ **663** L65–L68. `0705.2448`.

Commichau S.C., Biland A., Contreras J.L. et al. (2008). *Monte Carlo studies of geomagnetic field effects on the imaging air Cherenkov technique for the MAGIC telescope site.* Nuclear Instruments and Methods in Physics Research A **595** 572–586. `0802.2551`.

Cortina J., Armada A., Biland A. et al. (2005). *Technical Performance of the MAGIC Telescope.* In *International Cosmic Ray Conference*, vol. 5 of *International Cosmic Ray Conference*, 359–+.

Cortina J., Goebel F., Schweizer T. et al. (2009). *Technical Performance of the MAGIC Telescopes.* ArXiv e-prints `0907.1211`.

Costamante L. and Ghisellini G. (2002). *TeV candidate BL Lac objects.* A&A **384** 56–71. `arXiv:astro-ph/0112201`.

Curtis H.D. (1918). Publications of Lick Observatory **13** 31.

Dar A. and Laor A. (1997). *Hadronic Production of TeV Gamma-Ray Flares from Blazars.* ApJ **478** L5+. `arXiv:astro-ph/9610252`.

de La Calle Pérez I. and Biller S.D. (2006). *Extending the sensitivity of air Čerenkov telescopes.* Astroparticle Physics **26** 69–90. `arXiv:astro-ph/0602284`.

de Naurois M. (2003). Proceeding of the XXVIII ICRC **5** 2907.

Djannati-Atai A., Piron F., Barrau A. et al. (1999). *Very High Energy Gamma-ray spectral properties of MKN 501 from CAT Čerenkov telescope observations in 1997.* A&A **350** 17–24. `arXiv:astro-ph/9906060`.

Domingo-Santamaria E. et al. (2005). *The DISP analysis method for point-like or extended gamma source searches/studies with the MAGIC Telescope.* In *International Cosmic Ray Conference*, vol. 5 of *International Cosmic Ray Conference*, 363–+.

Edelson R.A. and Krolik J.H. (1988). *The discrete correlation function - A new method for analyzing unevenly sampled variability data.* ApJ **333** 646–659.

Erlykin A.D. and Wolfendale A.W. (2010). *Long term time variability of cosmic rays and possible relevance to the development of life on Earth.* ArXiv e-prints `1003.0082`.

Errando M. (2009). *Discovery of very high energy gamma-ray emission from 3C 279 and 3C 66A/B with the MAGIC telescope.* URL `http://wwwmagic.mppmu.mpg.de/publications/theses/index.html`.

Fanaroff B.L. and Riley J.M. (1974). *The morphology of extragalactic radio sources of high and low luminosity.* MNRAS **167** 31P–36P.

Finke J.D., Dermer C.D. and Böttcher M. (2008). *Synchrotron Self-Compton Analysis of TeV X-Ray-Selected BL Lacertae Objects.* ApJ **686** 181–194. `0802.1529`.

Finke J.D., Razzaque S. and Dermer C.D. (2010). *Modeling the Extragalactic Background Light from Stars and Dust.* ApJ **712** 238–249. `0905.1115`.

Fomin V.P. and et al. (1994). *New methods of atmospheric Cherenkov imaging for gamma-ray astronomy. I. The false source method.* Astroparticle Physics **2** 137–150.

Forman W., Jones C., Churazov E. et al. (2007). *Filaments, Bubbles, and Weak Shocks in the Gaseous Atmosphere of M87.* ApJ **665** 1057–1066. `arXiv:astro-ph/0604583`.

Fossati G., Maraschi L., Celotti A. et al. (1998). *A unifying view of the spectral energy distributions of blazars.* MNRAS **299** 433–448. `arXiv:astro-ph/9804103`.

Franceschini A., Rodighiero G. and Vaccari M. (2008). *Extragalactic optical-infrared background radiation, its time evolution and the cosmic photon-photon opacity.* A&A **487** 837–852. `0805.1841`.

Gaisser T.K. (1990). *Cosmic-Rays and Particle Physics.*

Gaug M. (2006). *Calibration of the MAGIC telescope and Observation of Gamma Ray Bursts.* URL `http://wwwmagic.mppmu.mpg.de/publications/theses/index.html`.

Ghisellini G. (2010). *The jet/disk connection in blazars.* ArXiv e-prints `1002.4619`.

Ghisellini G., Celotti A., Fossati G. et al. (1998). *A theoretical unifying scheme for gamma-ray bright blazars.* MNRAS **301** 451–468. `arXiv:astro-ph/9807317`.

Ghisellini G., Maraschi L. and Tavecchio F. (2009). *The Fermi blazars' divide.* MNRAS **396** L105–L109. `0903.2043`.

Gilmore R.C., Madau P., Primack J.R. et al. (2009). *GeV gamma-ray attenuation and the high-redshift UV background.* MNRAS **399** 1694–1708. `0905.1144`.

Goebel F. (2007). *Upgrade of the MAGIC Telescope with a Multiplexed Fiber-Optic 2 GSamples/s FADC Data Acquisition System system.* In *Proceedings of the XXX International Cosmic Ray Conference.*

Greisen K. (1966). *End to the Cosmic-Ray Spectrum?* Physical Review Letters **16** 748–750.

Hardcastle M. (2010). *Which radio galaxies can make the highest-energy cosmic rays?* Submitted to Mon. Not. R. Astron. Soc. `arXiv:1003.2500v1`.

Harris D.E., Cheung C.C., Biretta J.A. et al. (2006). *The Outburst of HST-1 in the M87 Jet.* ApJ **640** 211–218. `arXiv:astro-ph/0511755`.

Heck D., Knapp J., Capdevielle J.N. et al. (1998). *CORSIKA: a Monte Carlo code to simulate extensive air showers.*

HEGRA Collaboration et al. (1999). *The time structure of Cherenkov images generated by TeV gamma-rays and by cosmic rays.* Astroparticle Physics **11** 363–377. `arXiv:astro-ph/9812341`.

Hess V.F. (1912). *Über Beobachtungen der durchdringenden Strahlung bei sieben Freiballonfahrten.* Physikalische Zeitschrift **13** 1084–1091.

Hillas A.M. (1982). *The sensitivity of Cerenkov radiation pulses to the longitudinal development of cosmic-ray showers.* Journal of Physics G Nuclear Physics **8** 1475–1492.

Hillas A.M. (1985). *Cerenkov light images of EAS produced by primary gamma.* In F.C. Jones, editor, *International Cosmic Ray Conference*, vol. 3 of *International Cosmic Ray Conference*, 445–448.

Hinton J.A. and Hofmann W. (2009). *Teraelectronvolt Astronomy.* ARA&A **47** 523–565.

Holder J. (2005). *Exploiting VERITAS Timing Information.* In *International Cosmic Ray Conference*, vol. 5 of *International Cosmic Ray Conference*, 383–+.

Katarzyński K. and Walczewska K. (2010). *On the correlation between the X-ray and gamma-ray emission in TeV blazars.* A&A **510** A260000+. `0912.1859`.

Kernighan W.B. and Ritchie M.D. (1988). *The C programming language (Second Edition).* Prentice Hall Software Series.

Kneiske T.M., Bretz T., Mannheim K. et al. (2004). *Implications of cosmological gamma-ray absorption. II. Modification of gamma-ray spectra.* A&A **413** 807–815. `arXiv:astro-ph/0309141`.

Kranich D., Paneque D., Tescaro D. et al. (2008). *Multiwavelength campaign on the nearby TeV blazars Mrk421, Mrk501 and 1es1959+650.*

Krennrich F., Badran H.M., Bond I.H. et al. (2001). *Cutoff in the TeV Energy Spectrum of Markarian 421 during Strong Flares in 2001.* ApJ **560** L45–L48. `arXiv:astro-ph/0107113`.

Krolik J.H. (1999). *Active galactic nuclei : from the central black hole to the galactic environment.*

Lessard R.W., Buckley J.H., Connaughton V. et al. (2001). *A new analysis method for reconstructing the arrival direction of TeV gamma rays using a single imaging atmospheric Cherenkov telescope.* Astroparticle Physics **15** 1–18. `arXiv:astro-ph/0005468`.

Li T.P. and Ma Y.Q. (1983). *Analysis methods for results in gamma-ray astronomy.* ApJ **272** 317–324.

Longair M.S. (1992). *High energy astrophysics. Vol.1: Particles, photons and their detection.*

Macchetto F., Marconi A., Axon D.J. et al. (1997). *The Supermassive Black Hole of M87 and the Kinematics of Its Associated Gaseous Disk.* ApJ **489** 579–+. `arXiv:astro-ph/9706252`.

Macri L.M., Stanek K.Z., Sasselov D.D. et al. (1999). *DIRECT Distances to Nearby Galaxies Using Detached Eclipsing Binaries and Cepheids. Results for the Inner part of M33.* In *Bulletin of the American Astronomical Society*, vol. 31 of *Bulletin of the American Astronomical Society*, 1390–+.

Maier G. and Knapp J. (2007). *Cosmic-ray events as background in imaging atmospheric Cherenkov telescopes.* Astroparticle Physics **28** 72–81. `0704.3567`.

Majumdar P., Biland A., Haffke M. et al. (2006). *Monte Carlo Production strategy for MAGIC-II two telescope systems.* MAGIC-TDAS internal note archive URL `http://wwwmagic.mppmu.mpg.de/documents/tdas_notes.html`.

Majumdar P. et al. (2005). *Monte Carlo simulation for the MAGIC telescope.* In *International Cosmic Ray Conference*, vol. 5 of *International Cosmic Ray Conference*, 203–+.

Mannheim K. (1993). *The proton blazar.* A&A **269** 67–76. `arXiv:astro-ph/9302006`.

Maraschi L., Ghisellini G. and Celotti A. (1992). *A jet model for the gamma-ray emitting blazar 3C 279.* ApJ **397** L5–L9.

Marshall H.L., Miller B.P., Davis D.S. et al. (2002). *A High-Resolution X-Ray Image of the Jet in M87.* ApJ **564** 683–687. `arXiv:astro-ph/0109160`.

Mazin D. (2007). *A study of very high energy gamma-ray emission from agns and constraints on the extragalactic background light.*

Mazin D., Bigongiari C., Goebel F. et al. (2008). *Model analysis for the MAGIC telescope.* In *International Cosmic Ray Conference*, vol. 5 of *International Cosmic Ray Conference*, 1253–1256.

Mazin D. and Raue M. (2007). *New limits on the density of the extragalactic background light in the optical to the far infrared from the spectra of all known TeV blazars.* A&A **471** 439–452. `arXiv:astro-ph/0701694`.

Mirzoyan R. (1997). *On the Calibration Accuracy of Light Sensors in Atmospheric Cherenkov Fluorescence and Neutrino Experiments.* In *International Cosmic Ray Conference*, vol. 7 of *International Cosmic Ray Conference*, 265–+.

Mirzoyan R. and et al. (2002). *Ultrafast FADC multiplexer.* Nuclear Science **29** 2473–2476.

Mirzoyan R., Sobczynska D., Lorenz E. et al. (2006). *Tagging single muons and other long-flying relativistic charged particles by ultra-fast timing in air Cherenkov telescopes.* Astroparticle Physics **25** 342–348. `arXiv:astro-ph/0605091`.

Moralejo A. (2009). *MARS, the MAGIC Analysis and Reconstruction Software.* In *Proceedings of the XXXI International Cosmic Ray Conference.*

Moralejo A., Bigongiari C. and Scalzotto V. (2004*a*). *A first estimate of the MAGIC capabilities using the new MC simulation chain.* MAGIC-TDAS internal note archive URL `http://wwwmagic.mppmu.mpg.de/documents/tdas_notes.html`.

Moralejo A., Gaug M., Carmona E. et al. (2009). *MARS, the MAGIC Analysis and Reconstruction Software.* In *International Cosmic Ray Conference.* `0907.0943`.

Moralejo A., Rossato G. and et al. (2004*b*). *Monte Carlo studies on the MAGIC clone (draft).* MAGIC-TDAS internal note archive URL `http://wwwmagic.mppmu.mpg.de/documents/tdas_notes.html`.

Mücke A. and Protheroe R.J. (2001*a*). *A proton synchrotron blazar model for flaring in Markarian 501.* Astroparticle Physics **15** 121–136. `arXiv:astro-ph/0004052`.

Mücke A. and Protheroe R.J. (2001*b*). *A proton synchrotron blazar model for flaring in Markarian 501.* Astroparticle Physics **15** 121–136. `arXiv:astro-ph/0004052`.

Neronov A. and Aharonian F.A. (2007). *Production of TeV Gamma Radiation in the Vicinity of the Supermassive Black Hole in the Giant Radio Galaxy M87.* ApJ **671** 85–96. `0704.3282`.

Nieppola E., Valtaoja E., Tornikoski M. et al. (2008). *Blazar sequence - an artefact of Doppler boosting.* A&A **488** 867–872. `0803.0654`.

Oña E. (2006). *Observations under moonlight and twilight with MAGIC.* MAGIC-TDAS internal note archive URL `http://wwwmagic.mppmu.mpg.de/documents/tdas_notes.html`.

Otte N. (2007). *Observation of vhe γ-rays from the vicinity of magnetized neutron stars and development of new photon-detectors for future ground based γ-ray detectors.*

Oualline S. (1995). *Practical C++ Programming.* O'Reilly.

Padovani P. (2007). *The blazar sequence: validity and predictions.* Ap&SS **309** 63–71. `arXiv:astro-ph/0610545`.

Paneque D. (2004). *The MAGIC Telescope: development of new technologies and first observations.* URL `http://wwwmagic.mppmu.mpg.de/publications/theses/index.html`.

Pegna R., Cecchi R., Paoletti R. et al. (2006). *Performance of the Domino Ring Sampler in the MAGIC experiment.* Nuclear Instruments and Methods in Physics Research A **567** 218–221.

Perkins D.H. (2009). *Particle astrophysics.*

Perlman E.S., Harris D.E., Biretta J.A. et al. (2003). *Month-Timescale Optical Variability in the M87 Jet.* ApJ **599** L65–L68. `arXiv:astro-ph/0311161`.

Perlman E.S., Madejski G., Georganopoulos M. et al. (2005). *Intrinsic Curvature in the X-Ray Spectra of BL Lacertae Objects.* ApJ **625** 727–740. `arXiv:astro-ph/0502298`.

Petry D., Bradbury S.M., Konopelko A. et al. (1996). *Detection of VHE γ-rays from MKN 421 with the HEGRA Cherenkov Telescopes.* A&A **311** L13–L16. `arXiv:astro-ph/9606159`.

Punch M., Akerlof C.W., Cawley M.F. et al. (1992). *Detection of TeV photons from the active galaxy Markarian 421.* Nature **358** 477–+.

Quinn J., Akerlof C.W., Biller S. et al. (1996). *Detection of Gamma Rays with E above 300 GeV from Markarian 501.* ApJ **456** L83+.

Rieger F.M. (2009). *Cosmic Ray Acceleration in Active Galactic Nuclei - On Centaurus A as a possible UHECR Source.* ArXiv e-prints `0911.4004`.

Samuelson F.W., Biller S.D., Bond I.H. et al. (1998). *The TeV Spectrum of Markarian 501.* ApJ **501** L17+.

Silva L., Granato G.L., Bressan A. et al. (1998). *Modeling the Effects of Dust on Galactic Spectral Energy Distributions from the Ultraviolet to the Millimeter Band.* ApJ **509** 103–117.

Sobczynska D. (2007*a*). *Natural limit on the γ/hadron separation for a stand alone air Cherenkov telescope.* Journal of Physics G Nuclear Physics **34** 2279–2288. `arXiv:astro-ph/0702562`.

Sobczynska D. (2007*b*). *Natural limit on the γ/hadron separation for a stand alone air Cherenkov telescope.* Journal of Physics G Nuclear Physics **34** 2279–2288. `arXiv:astro-ph/0702562`.

Stecker F.W., Malkan M.A. and Scully S.T. (2006). *Intergalactic Photon Spectra from the Far-IR to the UV Lyman Limit for $0 < z < 6$ and the Optical Depth of the Universe to High-Energy Gamma Rays.* ApJ **648** 774–783. `arXiv:astro-ph/0510449`.

Tavecchio F., Maraschi L. and Ghisellini G. (1998). *Constraints on the Physical Parameters of TeV Blazars.* ApJ **509** 608–619. `arXiv:astro-ph/9809051`.

Tescaro D. (2007). *Timing analysis of the MAGIC telescope data after the installation of the ultra-fast 2 Gsample/s FADC readout.* URL `http://wwwmagic.mppmu.mpg.de/publications/theses/index.html`.

Tescaro D., Aleksić J., Barcelo M. et al. (2009*a*). *The readout system of the MAGIC-II Cherenkov Telescope.* In *Proceedings of the XXXI International Cosmic Ray Conference*. `0907.0466`.

Tescaro D., Bartko H., Galante N. et al. (2007). *Study of the performance and capability of the new ultra-fast 2 GSample/s FADC data acquisition system of the MAGIC telescope.* In *Proceedings of the XXX International Cosmic Ray Conference*. `0709.1410`.

Tescaro D., Mazin D., Wagner R.M. et al. (2009*b*). *The strong flaring activity of M87 in early 2008 as observed by the MAGIC telescope.* In *Proceedings of the XXXI International Cosmic Ray Conference*. `0907.0460`.

The MAGIC collaboration (1998). *MAGIC letter of intent* URL `http://wwwmagic.mppmu.mpg.de/publications/proposals/index.html`.

Tramacere A., Giommi P., Perri M. et al. (2009). *Swift observations of the very intense flaring activity of Mrk 421 during 2006. I. Phenomenological picture of electron acceleration and predictions for MeV/GeV emission.* A&A **501** 879–898. `0901.4124`.

Urry C.M. and Padovani P. (1995). *Unified Schemes for Radio-Loud Active Galactic Nuclei.* PASP **107** 803–+. `arXiv:astro-ph/9506063`.

Vaughan S., Edelson R., Warwick R.S. et al. (2003). *On characterizing the variability properties of X-ray light curves from active galaxies.* MNRAS **345** 1271–1284. `arXiv:astro-ph/0307420`.

Wagner R. (2009). *VHE γ-ray sky map and source catalog.* URL `http://www.mppmu.mpg.de/~rwagner/sources/`.

Wilson A.S. and Yang Y. (2002). *Chandra X-Ray Imaging and Spectroscopy of the M87 Jet and Nucleus.* ApJ **568** 133–140. `arXiv:astro-ph/0112097`.

Yao W.M. et al. (2006). *Review of Particle Physics.* Journal of Physics G Nuclear Physics **33** 1–1232.

Zanin R., Cortina J. and for the MAGIC Collaboration (2009). *The Central Control of the MAGIC telescopes.* ArXiv e-prints `0907.0946`.

Zatsepin G.T. and Kuzmin V.A. (1966). *Upper Limit of the Spectrum of Cosmic Rays.* Soviet Journal of Experimental and Theoretical Physics Letters **4** 78–+.